

INVESTIGATING ORGANIZED COMPLEXITY IN MULTICELLULAR MAGNETOTACTIC  
BACTERIA USING CULTURE INDEPENDENT TECHNIQUES

by

George Andrew Schaible

A dissertation submitted in partial fulfillment  
of the requirements for the degree

of

Doctor of Philosophy

in

Biochemistry

MONTANA STATE UNIVERSITY  
Bozeman, Montana

January 2024

©COPYRIGHT

by

George Andrew Schaible

2024

All Rights Reserved

## DEDICATION

I dedicate this thesis to all the scientists on whose shoulders we stand. Their tireless curiosity, rigorous methodologies, and unwavering pursuit of knowledge has paved the way for the profound technologies we wield today. With deep gratitude for their invaluable contributions, I strive to give back to the community that has generously given us so much.

“We are nothing without the work of others our predecessors, others our teachers, others our contemporaries. Even when, in the measure of our inadequacy and our fullness, new insight and new order are created, we are still nothing without others. Yet we are more.”

— Robert Oppenheimer

[Reith Lecture, 20th December 1953]

## ACKNOWLEDGEMENTS

First and foremost, I would like to acknowledge my wife, Amy Schaible, who in her own right has earned a PhT (putting husband through). Thank you for your endless encouragement and support through the thick and the thin. I would also like to thank my parents, Hal and Deborah Schaible, for instilling in me a curiosity for the natural world that has continually fascinated me. I am also grateful to my brother Dr. Micah Schaible, who encouraged me to pursue my interests in science, as well as Dr. Gary Strobel who invited me to work in his lab as an undergraduate, where I made many of my first mistakes and successes as a budding scientist. I cannot thank Dr. Dave Ward enough for taking me in as an undergraduate researcher and for his continuous mentorship in science and life. I want to express my gratitude to my colleagues, Anthony Kohtz and Colin Gauvin, for engaging in insightful discussions about science and encouraging me to think deeper about my research. And of course, a cheers to Columbo's, not only as purveyors of delightful pizzas and cold beer, but the unsung providers of brainpower in the face of life's hungriest challenges.

I would like to thank my committee members, Drs. Christine Foreman, Brian Bothner, and Mark Young for encouragement and insightful questions. I am eternally grateful to my advisor, Dr. Roland Hatzenpichler, who not only embraced my curiosity but also enabled me to develop skills beyond the realm of science. I am also grateful to all the Hatzenpichler lab members, past and present, who have made my graduate school experience as wonderful as I could have asked for. Much of my work would not have been possible without support from our collaborators Drs. Jeff Marlow, Virginia Edgcomb, and Emil Ruff, who collected samples for us throughout the entirety of the project. This project was completed with funding NASA Exobiology program award NNX17AK85G and NASA FINESST award 80NSSC20K1365.

## TABLE OF CONTENTS

1. INTRODUCTION.....	1
1. Defining Complexity .....	5
2. Mechanisms for Increasing Complexity and Size .....	6
2.1 Cope's Rule and Dollo's Law .....	7
2.2 Entropy as a Vehicle for Biological Complexity .....	10
2.3 The Zero Force Evolutionary Law .....	12
2.4 Section Summary .....	13
3. Measuring Biological Complexity.....	14
3.1 Genome Complexity .....	15
3.2 (Ultra)Structure .....	16
3.3 Multicellularity .....	17
4. Multicellularity in Bacteria .....	18
5. Multicellular Magnetotactic Bacteria .....	21
6. Culture-Independent Methods to Study Biological Complexity.....	28
7. Overview of Following Chapters .....	30
References.....	33
2. CORRELATIVE SIP-FISH-RAMAN-SEM-NANOSIMS LINKS IDENTITY, MORPHOLOGY, BIOCHEMISTRY, AND PHYSIOLOGY OF ENVIRONMENTAL MICROBES.....	43
Contributions of Authors and Co-Authors.....	43
Manuscript Information .....	44
Abstract.....	45
1. Introduction .....	45
2. Materials and Methods.....	49
2.1 Preparation and Stable Isotope Probing of an Artificial Community .....	49
2.2 Collection and Stable Isotope Probing of Environmental Sample.....	50
2.3 Slide Preparation.....	51
2.4 Confocal Raman Microspectroscopy and Spectral Processing.....	52
2.5 Scanning Electron Microscopy .....	53
2.6 Backscatter Electron Microscopy and Energy Dispersive X- Ray Spectroscopy.....	53
2.7 Fluorescence <i>in situ</i> Hybridization.....	53
2.8 Nano-Scale Secondary Ion Mass Spectrometry.....	55
3. Results and Discussion .....	56
3.1 General Considerations for Correlative Microscopy .....	56
3.2 FISH-First Correlative Workflow Using an Artificial Microbial Community .....	58

## TABLE OF CONTENTS CONTINUED

3.3 SEM-First Correlative Workflow Using Environmental MMB .....	62
3.4 Analysis of MMB Magnetosomes Using BSE-SEM and EDS.....	66
4. Conclusions .....	68
Acknowledgements .....	69
References.....	70
3. COMPARING RAMAN AND NANOSIMS FOR STABLE ISOTOPE PROBING OF SINGLE CELLS.....	78
Contributions of Authors and Co-Authors.....	78
Manuscript Information.....	79
Abstract.....	80
1. Introduction.....	81
2. Results and Discussion .....	83
2.1 Stable Isotope Probing.....	83
2.2 Pre-Processing of Raman Spectra.....	85
2.3 NanoSIMS Analysis.....	88
2.4 Single-Cell Comparison of Raman and NanoSIMS.....	88
3. Conclusion.....	91
4. Materials and Methods.....	92
4.1 Preparation of Isotopically Labeled Cells .....	92
4.2 Preparation of Stainless Steel Coupon .....	93
4.3 Confocal Raman Microspectroscopy and Spectral Processing.....	93
4.4 Nano-Scale Secondary Ion Mass Spectrometry.....	94
4.5 Statistical Analysis .....	95
Acknowledgements .....	95
References.....	97
4. MULTICELLULAR MAGNETOTACTIC BACTERIAL CONSORTIA ARE METABOLICALLY DIFFERENTIATED AND NOT CLONAL .....	102
Contributions of Authors and Co-Authors.....	102
Manuscript Information.....	103
Abstract.....	104
1. Introduction.....	105
2. Results and Discussion .....	109
2.1 Genomic Features and Phylogenetic Analysis of MMB .....	109
2.2 Clonality Within MMB.....	112
2.3 Genome Annotation.....	115
2.4 Cell-to-Cell Adhesion.....	121
2.5 Abundance, Distribution, and <i>in situ</i> Activity of MMB in LSSM .....	123

## TABLE OF CONTENTS CONTINUED

2.6 Physiology of MMB.....	124
2.7 Metabolic Differentiation as Studied by SIP-NanoSIMS .....	126
2.8 Metabolic Differentiation as Studied by BONCAT .....	128
3. Conclusion.....	130
4. Materials and Methods.....	130
4.1 Sample Collection and Magnetic Enrichment of MMB.....	130
4.2 MMB Sorting, Single Consortia Genomic Sequencing, and Clonality Analysis.....	131
4.3 Phylogenetic, Phylogenomic, and Comparative Genomic Analysis.....	133
4.4 Fluorescence <i>in situ</i> Hybridization (FISH).....	134
4.5 Stable Isotope Probing (SIP).....	135
4.6 Nano-Scale Secondary Ion Mass Spectrometry (NanoSIMS).....	136
4.7 Bioorthogonal Noncanonical Amino Acid Tagging (BONCAT) and Confocal Fluorescence Microscopy .....	137
4.8 Confocal Raman Microspectroscopy and Spectral Processing.....	139
4.9 Geochemical Analysis .....	139
4.10 Statistical Analysis .....	140
4.11 Scanning Electron Microscopy (SEM) and Cellulase Experiment .....	140
Acknowledgements .....	141
Data Availability .....	142
References.....	144
5. CONCLUSION AND FUTURE DIRECTIONS .....	155
Conclusions.....	155
Future Directions.....	158
References.....	168
6. CUMULATIVE REFERENCES CITED.....	172
7. APPENDICES.....	201
CHAPTER TWO SUPPORTING MATERIAL .....	202
CHAPTER THREE SUPPORTING MATERIAL .....	207
CHAPTER FOUR SUPPORTING MATERIAL .....	215
CHAPTER FIVE SUPPORTING MATERIAL .....	240

## LIST OF TABLES

Table	Page
1. Table S1. Pairwise t-tests of baselining methods applied to Raman spectra for each $^2\text{H}_2\text{O}$ incubation. ....	214
2. Table S1. Media recipe for cultivation attempts of MMB. ....	249
3. Table S2. Water chemistry of LSSM sample site .....	250

## LIST OF FIGURES

Figure	Page
1. Evolution of life on Earth .....	2
2. Simplistic depiction of Cope’s rule and Dollo’s law .....	8
3. Multicellular lifecycle for different bacteria.....	20
4. Little Sippewissett Salt March (LSSM).....	22
5. The morphological ultrastructure and magnetosome formation in MMB.....	24
6. Phylogenetic analysis of MMB using near-full length 16S rRNA genes recovered from LSSM MMB .....	27
7. Comparison of energetic measures between prokaryotes, eukaryotes, and MMB.....	29
8. Schematics showing the culture independent methods employed in this thesis. ....	31
9. Correlative microscopy workflow.....	57
10. Correlative imaging of an artificial community. ....	59
11. Correlative microscopy analysis of MMB.....	64
12. Imaging magnetosomes within MMB .....	67
13. Exemplary Raman spectra and NanoSIMS images illustrating the uptake of H <sub>2</sub> -label by <i>Escherichia coli</i> cells after incubation in media with varying percentages of <sup>2</sup> H <sub>2</sub> O.....	85
14. Single cell comparison of the <sup>2</sup> H content of cells as measured by Raman and NanoSIMS using specific mass ratios .....	89
15. Comparison of <sup>2</sup> H atom percent as measured by Raman and NanoSIMS.....	90
16. Morphology and structure of MMB .....	108
17. Genomic and phylogenetic analysis of all publicly available MMB MAGs and the 22 SCGs generated in this study .....	109

## LIST OF FIGURES CONTINUED

18. Clonality analysis of individual MMB consortia .....	112
19. Metabolic potential of the eight MMB species in LSSM. ....	115
20. NanoSIMS analysis of the cellular $^{13}\text{C}$ -content of MMB consortia after <i>in situ</i> incubation with isotopically light or heavy carbon sources, specifically 1,2- $^{13}\text{C}_2$ -acetate, $^{13}\text{C}$ -bicarbonate, 1,2- $^{13}\text{C}_2$ -propionate, or 1,2- $^{13}\text{C}_2$ -succinate, for 24 hours.....	134
21. NanoSIMS analysis of MMB consortia incubated with 1,2- $^{13}\text{C}_2$ -acetate and $^2\text{H}_2\text{O}$ .....	136
22. Heterogeneity in anabolic activity within individual MMB consortia as revealed by BONCAT.....	138
23. SBF-EM analysis of MMB .....	168
24. Preliminary Cryo-EM data of single MMB cells that have been dislodged from the consortium.....	169
25. nMMB isolated from LSSM.....	173
26. MMB inhabiting an estuary in Seaside, OR .....	175
27. SEM images showing the loss of structural integrity of MMB when FISH is performed prior to SEM. ....	210
28. Slide design and sample orientation. ....	211
29. Comparison of D-labeled and non-labeled cells .....	212
30. Comparison of Raman and NanoSIMS atom percent of deuterium in the mock community. ....	213
31. Growth curve of <i>E. coli</i> cultures grown in varying $^2\text{H}$ -water concentrations. ....	215
32. Example of the mapping of ROIs and cells for correlative workflow .....	216
33. Analysis of baselining methods for Raman spectra .....	217
34. Calculating the AUC for $^{12}\text{C}$ - $^2\text{H}$ .....	218

## LIST OF FIGURES CONTINUED

35. Percent $^2\text{H}$ as measured by the different atomic mass ratios using NanoSIMS across the four heavy water incubations.....	219
36. Comparison of NanoSIMS ion counts for each ion mass analyzed. ....	220
37. Little Sippewissett salt marsh, Falmouth MA.....	226
38. Phylogenetic analysis of MMB using near-full length 16S rRNA genes (length listed next to name) found in 14 of the 22 SCGs and in reference genomes .....	227
39. Near-full length 16S rRNA gene comparison of all sequences recovered in this study and previous studies at LSSM.....	229
40. Near-full length 16S rRNA identity comparison for the 14 sequences recovered from SCGs and the two MMB reference genome.....	230
41. Genome ANI comparing each of the 22 individual SCGs with the two publicly available reference genomes.....	231
42. Heatmap and cluster analysis of pfams annotation of individual SNPs showing the $\log_2$ ratio of non-synonymous to synonymous substitutions (dN/dS) for the SNP differences contained within each SCG. ....	232
43. Representative Raman spectrum of a MMB using a 532 nm laser .....	233
44. Cellulase treatment of MMB.....	234
45. Fractional abundance of MMB groups by depth in LSSM.....	235
46. Anabolic activity of MMB inhabiting the top 6 cm of LSSM sediment as measured by BONCAT. ....	236
47. Comparison of $^{13}\text{C}$ -labeled substrate incorporation by MMB Groups 1, 3, and 4 using NanoSIMS analysis of mass ratio $^{13}\text{C}^{12}\text{C}/^{12}\text{C}_2$ . ....	237
48. Correlative imaging of MMB.....	238
49. ROIs for NanoSIMS substrate analysis shown in Fig. 5 of main text.....	239
50. ROIs for NanoSIMS hotspot analysis shown in Fig. 6 of main text .....	240

## LIST OF FIGURES CONTINUED

51. Median filter ratio radius effect on HSI NanoSIMS images of $^{13}\text{C}$ and $^2\text{H}$ hotspots (A-C) Mass ratio ( $^2\text{H}^{12}\text{C}/^1\text{H}^{12}\text{C}$ ) of MMB labeled with deuterium oxide ( $^2\text{H}_2\text{O}$ ).....	241
52. Anabolic activity within individual consortia.....	242
53. Fluorescence activated cell sorting of a magnetically enriched sample from tidal pond sediment stained with SYBR Green.....	244
54. Gene synteny for scaffolds containing the magnetosome gene clusters compared.....	247

## GLOSSARY

ALS: Asymmetric least squares

ANI: Average nucleotide identity

AUC: Area under the curve

BONCAT: Bioorthogonal non-canonical amino acid tagging

BSE: Backscatter electron microscopy

CARD-FISH: Catalyzed reporter deposition fluorescence *in situ* hybridization

CLSM: Confocal laser scanning microscopy

CODEX: Co-detection by indexing

CRISPR: Clustered regularly interspaced short palindromic repeats

D<sub>2</sub>O: Deuterated water

DGR: Diversity generating retroelements

DOPE-FISH: Double-labeled oligonucleotide probes for FISH

ECM: Extracellular matrix

EDS: Energy-dispersive X-ray spectroscopy

EM: Electron microscopy

FIB: Focused-ion beam

FISH: Fluorescence *in situ* hybridization

FM: Fluorescence microscopy

GT2: Family-2 glycosyltransferases

HSI: Hue saturated images

LECA: Last eukaryotic common ancestor

GLOSSARY CONTINUED

LSSM: Little Sippewissett salt marsh

LUCA: Last universal common ancestor

MMB: Multicellular magnetotactic bacteria

nMMB: Novel multicellular magnetotactic bacteria

NanoSIMS: Nano-scale secondary ion mass spectroscopy

NOE: Neoproterozoic oxidation event

PFA: Paraformaldehyde

PHB: Polyhydroxybutyrate

SBF-EM: Serial block face electron microscopy

SCMs: Single consortium metagenomes

SEM: Scanning electron microscopy

SIP: Stable isotope probing

SNIP: Statistics-sensitive non-linear iterative peak-clipping

SNPs: Single nucleotide polymorphisms

TEM: Transmission electron microscopy

ZFEL: Zero force evolutionary law

## ABSTRACT

The multiple independent emergences of multicellularity significantly altered the course of evolution on Earth, leading to the complex life forms inhabiting the planet today. However, the transition from a unicellular ancestor to a multicellular organism remains poorly understood. Because of the relative scarcity of multicellularity in the domains Bacteria and Archaea, research on the evolution of multicellularity has predominantly focused on eukaryotic model organisms. To help resolve how microbial life shifts from single-cellular to multicellular, this thesis investigates cellular differentiation of individual cells within multicellular magnetotactic bacteria (MMB), the only known example of obligate multicellular bacteria. MMB have been shown to lack a unicellular life stage, and instead grow as symmetrical, single-species consortia that orient themselves along Earth's geomagnetic field using a specialized organelle called the magnetosome. Because MMB have remained recalcitrant to cultivation, this dissertation necessitated the use of multiple culture-independent approaches capable of addressing the genomic and physiological underpinnings of the MMB lifecycle. A correlative microscopy workflow was developed to allow for species specific analysis of MMB morphology, biochemistry, and physiology. This was accomplished by performing stable isotope probing (SIP) on samples followed by fluorescence in situ hybridization to identify specific species. Next, electron microscopy was used followed by nano-scale secondary ion mass spectrometry (NanoSIMS) and Raman microspectroscopy. Because Raman and NanoSIMS are becoming increasingly common for microbial SIP studies, the comparability of these techniques was explored, yielding an optimized approach for SIP-Raman-NanoSIMS studies. In addition to these methods, bioorthogonal non-canonical amino acid tagging was used to study the *in situ* activity as well as variation of protein synthesis within cells. Furthermore, single-cell metagenomics was performed on individual MMB allowing for a detailed analysis of MMB metabolic potential and clonality. The findings presented in this thesis expand our understanding of the mechanisms underpinning the multicellular nature of MMB.

## CHAPTER ONE

## INTRODUCTION

A long-standing question in evolutionary biology is how life evolved from a single cell to the complex multicellular organisms (*i.e.*, organisms composed of many cells of the same species) that populate Earth today. Given that life originated from abiotic matter, it is evident that there has been an increase in size, complexity, and diversity of life over the past 3.8 billion years (or more) of evolution (Nutman et al., 2016). Throughout much of evolutionary history, Earth was populated by relatively simple microscopic organisms. It wasn't until the last billion years of evolution that complex multicellular macro-organisms evolved, dramatically transforming Earth's biosphere and eventually giving rise to intelligent life. The tree of life displays this increase in diversity and complexity of biological organisms, showing the evolutionary progression from a common ancestor to the diverse life forms existing today (Fig. 1A). Multicellularity has independently evolved at least 25 times across the domains of life (Grosberg & Strathmann, 2007), indicating that this process is not an evolutionary bottleneck, such as other major transition events that have occurred only once in evolutionary history (*e.g.*, eukaryogenesis) (Smith & Szathmary, 1997). Yet, the earliest evidence for the advent of multicellularity doesn't appear in the geologic rock record until approximately one billion years ago (Fig. 1B), when unambiguous fossils of the eukaryotic red algae *Bangiomorpha* were identified (Butterfield, 2000; Gibson et al., 2018). Some studies have suggested that the evolution of biological complexity and multicellularity was dependent on the rise in oxygen in our atmosphere (Fig. 1B) (Schirmer et al., 2013), though alternative hypotheses have been drawn (Bozdag et al., 2021).

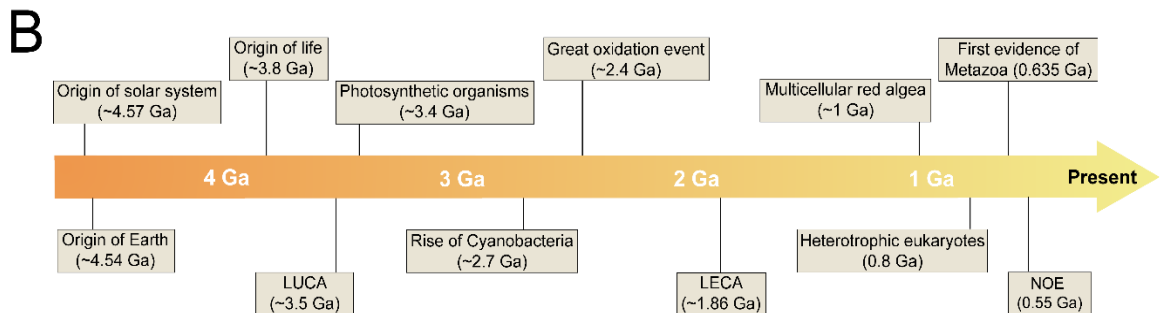
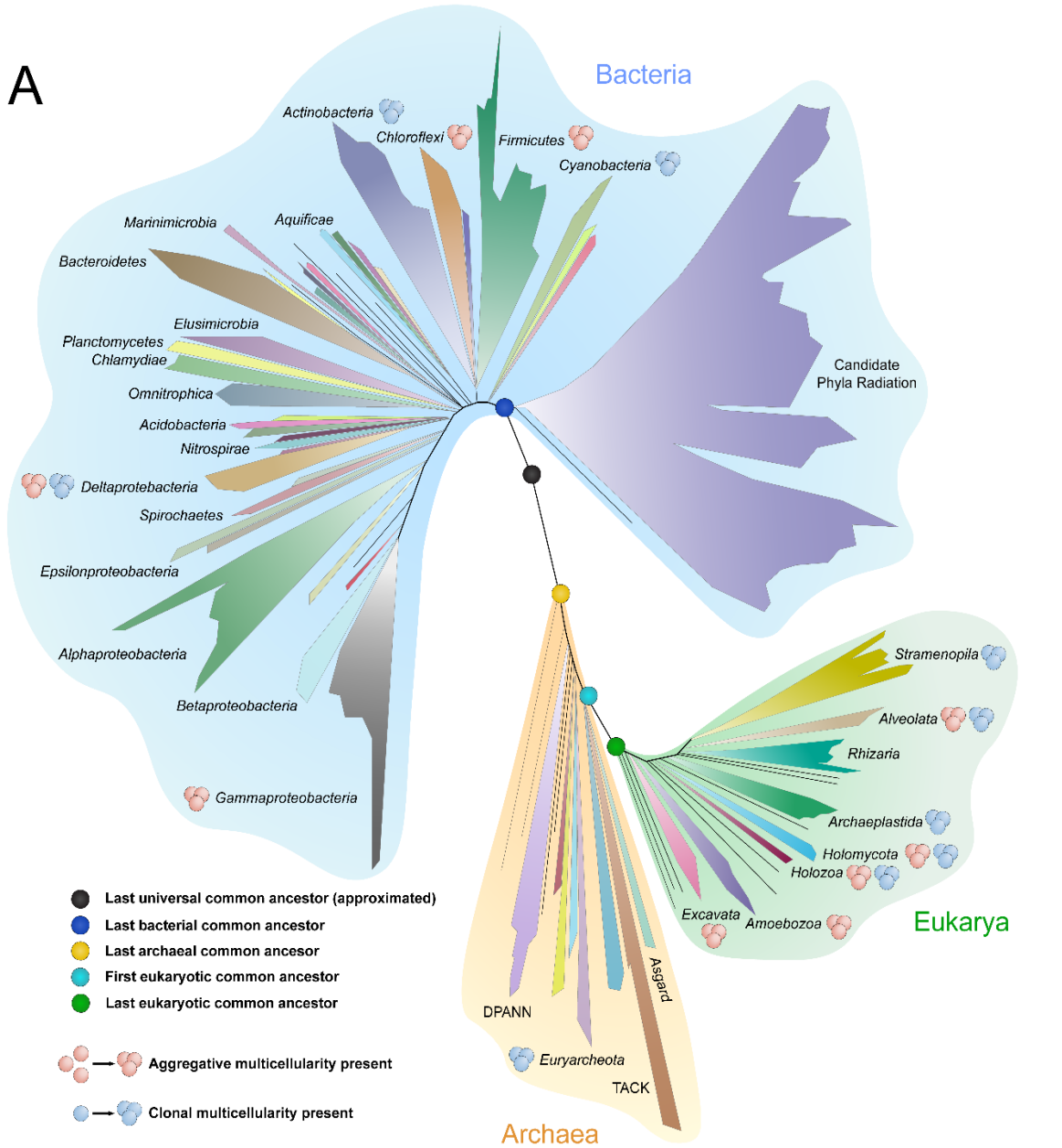


Fig. 1. Evolution of life on Earth. **A** Phylogenetic tree of life showing the diversity between bacterial and archaeal phyla and Eukaryotic supergroups. The last common ancestors are shown on the main stem of the tree using colored circles. Phyla and supergroups containing aggregative and/or clonal multicellularity are shown across the tree with pink or blue circles, respectively. Tree is not precisely scaled to show actual evolutionary divergence and is only meant to be an informative model. Modified from (Hug et al., 2016) with permission. Note that many of the phyla names and tree topology have changed based on updates to the Genome Taxonomy Database and these changes are not reflected in this version of the tree of life (Parks et al., 2022). **B** Timeline showing major geological and evolutionary events in Earth's history in billions of years (Ga). NOE refers to the Neoproterozoic oxidation event. LUCA and LECA refer to the last universal common ancestor and the last eukaryotic common ancestor, respectively. Figures originally made by G.A. Schaible and used with permission from (Bozdag et al., 2023).

The temporal gap between the advent of life and the first universally recognized multicellular morphotype raises many questions regarding the evolution of multicellular organisms. Did it indeed take 2.8 billion years for multicellularity to arise if it appears to evolve with relatively little restriction, as evident in the tree of life? Is the evolution of multicellularity a result of natural selection or a fortuitous outcome of pure chance? Why has organismal complexity and size continued to increase and not have instead remained stagnant? And what are the minimum physiological and morphological requirements for multicellularity to evolve? The scientific community has discussed these questions since Charles Darwin popularized the theory of evolution in 1859. Yet, each question has remained enigmatic as the forces and/or mechanisms driving the continued increase of complexity in biological systems remain a mystery and are still under debate (Colizzi, 2020; Heim et al., 2017; Katsnelson et al., 2018; McShea, 2023; Wolf et al., 2018). While considerable work has been accomplished to further our understanding of the evolution of biological complexity and multicellularity, there is still little known regarding the modes through which both emerge.

Historically, research on the evolution of multicellularity has predominantly focused on eukaryotes, likely due to the abundance in examples of large multicellular eukaryotic organisms.

Within the Eukaryotes there is an inherent positive evolutionary trend in size and complexity, making them ideal for studies focused on genome complexification, cellular division of labor, and multicellularity. However, because eukaryotes evolved approximately 1.9 billion years ago (Betts et al., 2018), research focused on multicellularity and complexity in eukaryotes overlooks the 2.5 billion years preceding the emergence of these organisms. During this extensive period prior to eukaryotes, it is possible that bacteria and archaea evolved multicellularity morphotypes, although confident identification of microbial fossils in the rock record is difficult (Slotznick et al., 2023; Staley, 1999). Instead of relying on the rock record for evidence of microbial multicellularity, extant examples of multicellularity within bacteria and archaea can be used to study the mechanisms (*e.g.*, genetic, physiological, and morphologic) through which multicellularity evolves.

This thesis contributes to the understanding of the evolutionary processes shaping biological complexity by investigating the occurrence of multicellularity within the domain of Bacteria, an area with limited prior research regarding multicellularity. While examples of complex multicellularity exist in bacteria (Fig. 1A), they are rare. Exceedingly rarer are bacteria that engage in obligate multicellular lifecycle (*i.e.*, no single cell stage). To date, there is only one bacterium that has been found to maintain an obligate multicellular lifecycle, multicellular magnetotactic bacteria (MMB). Because of the unique lifecycle of MMB, they are used as a model organism in this work to better understand the mechanisms driving the evolution of biological complexity and multicellularity in Bacteria.

This chapter starts by introducing several philosophical theories on how complexity is measured, illustrating how these theories can be applied to interpret the evolution of biological

complexity and the emergence of multicellular lifecycles. Next, the measures of biological complexity are discussed in the context of bacteria that have attained greater complexity through their multicellular lifecycles. Following this, a detailed introduction of MMB is given as well as the cultivation independent techniques used to study them. Finally, a succinct overview of the remaining chapters in the thesis is given. Together, this introduction aims to equip the reader with the history and current thinking of biological complexity and how the evolution of multicellularity is explored in bacteria, specifically MMB.

### 1. Defining Complexity

Complexity is notoriously difficult to define (Ladyman et al., 2012; McShea, 1991) though it is often clearly recognizable to the observer. The way in which a physicist defines complexity is different than the way a sociologist defines it, and again different than the way a biologist defines it. As a result, complexity has adopted a colloquial meaning as well as specific theoretical meanings. The colloquial use of the term “complex” often uses informal, everyday language regarding the degree of differentiation and function among parts. For example, we would consider a breakfast recipe containing poached eggs, chives, Himalayan pink salt, freshly cracked black pepper, and artisanal whole-grain toast to be more complex than a recipe simply calling for eggs and toast. While the “complex” recipe calls for more ingredients, we also consider the function of those ingredients and the importance of the order in which they are added. Alternatively, scientists attempting to define complexity in biological systems have found it helpful to adopt explicit definitions that only consider variety among parts within an organism, regardless of how they function (McShea et al., 2019). This means that our definition of complexity for the breakfast recipe simply relies on the number of different parts and not the function or order of those parts.

Using this explicit definition of complexity, we could, for example, consider a human without wisdom teeth or an appendix as less complex than a human with them, due to a lack of differentiated parts. The advantage of using this simplified approach is that it enables the investigation into the correlation between different types of components and their functionality, as well as the connection between components and the process of natural selection. This is crucial because exploring the relationship between complexity and functionality becomes unfeasible using a colloquial complexity definition that inherently incorporates a notion of function (McShea & Brandon, 2010). This dissertation adopts the use of an explicit theoretical definition of complexity, that is the variety among parts within an organism, to biological systems as a means to simplify discussions. It should be noted that there is not a universal agreement on how biological complexity should be defined (Wolf et al., 2018).

## 2. Mechanisms for Increasing Complexity and Size

The renowned naturalist Charles Darwin said “... *as natural selection works solely by and for the good of each being, all corporeal and mental endowments will tend to progress toward perfection*” (Darwin, 1859)<sup>1</sup>. This statement reflects the perspective on the evolution of biological complexity during the following century, asserting that the continued complexification of species is a prevailing modality of evolution (Gould, 1966; Gould, 1996). Excluding examples of reductive

---

<sup>1</sup> There are many examples of organism that have undergone reductive evolution, disproving Darwin’s simplistic theory of progression towards perfection. Regardless, scientists have continued this line of thinking using teleology, the idea that biology is goal-directed or has a purpose, albeit to the consternation of other scientists. Hanke, D. (2004). Teleology: The explanation that bedevils biology. *Explanations: Styles of explanation in science*, 143, 155. , McShea, D. W. (2012). Upper-directed systems: a new approach to teleology in biology. *Biology & Philosophy*, 27, 663-684.

evolution (*e.g.*, parasites and symbionts), this idea that life continues to increase in complexity during its evolution appears to hold true, as evidenced by the tree of life. The connections between size and complexity, as well as diversity and complexity, are intuitive when considering biological organisms. Expanding organismal size by increasing cell numbers has the potential to enhance the diversity of cell types and, consequently, ultrastructural and morphological complexity, fostering an expansion of species diversity (Carroll, 2001). Scientists have recognized these intuitive connections between complexity, diversity, and size and have implemented evolutionary theories to describe this trend. The following three subsections introduce evolutionary theories that have been used to describe the positive trend regarding biological complexity and multicellularity and are intended as a primer for theoretical thinking for interpretation of the data presented within this thesis.

### 2.1 Cope's Rule and Dollo's Law

Over the past ~3.8 billion years of evolution, the upper limit on the mass of an individual organism has increased by approximately 18 orders of magnitude. This increase was recognized under Cope's Rule, an observation made in the late 1800's on the tendency of animal groups to evolve toward larger physical size (Cope, 1887; Cope, 1904). An increase in size would offer improved ability to capture prey and/or evade predation as well as increased heat retention and enhanced energetics (*i.e.*, stamina) (Bonner, 1998). It is now understood that an increase in complexity is associated with increases in size (Fig. 2), and increases in size are a key characteristic of multicellularity (Bonner, 2004; Heim et al., 2015; McShea, 1996). Interpretations of Cope's Rule have posited that increases in mean and maximum organismal size are best explained by passive stochastic variance (Stanley, 1973). This increasing-variance hypothesis predicts a

diffusive evolutionary process, suggesting that organismal size should diffuse away from a single absolute minimum size. In other words, there is an explicit floor to organismal size but an undefined ceiling.

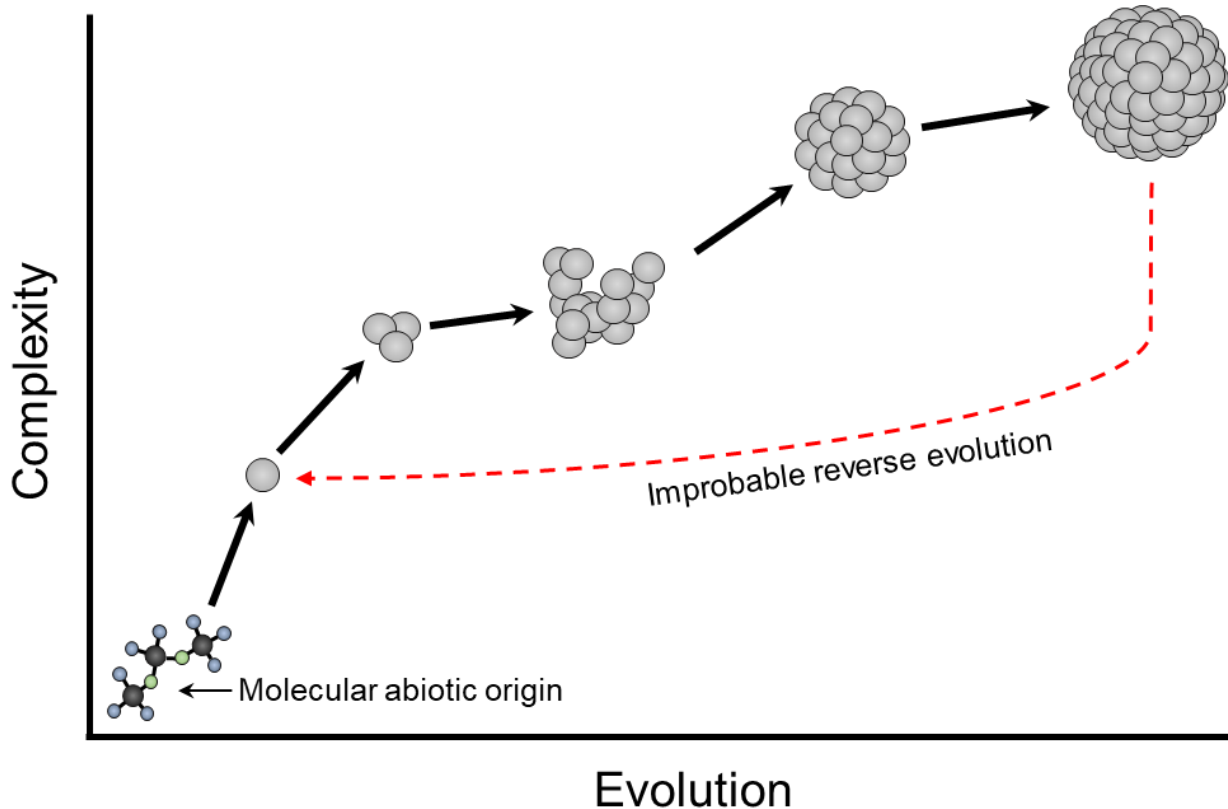


Fig. 2. Simplistic depiction of Cope's rule and Dollo's law. Plotting the evolution of life with regards to complexity would show an increase in both size and complexity as life evolves from abiotic matter to single cells and eventually to complex multicellular organisms, as suggested by Cope's rule. Furthermore, it is highly improbable that an organism would retro-evolve to the exact same state earlier in its evolution, as outlined by Dollo's law and shown by the red dashed line. Figure made by G. A. Schaible.

Life has evolved to fill every available niche of size, only limited by physical constraints of minimum size to allow enough genetic and protein machinery for a cell to function (Knoll, 1999). Heim *et. al.* found that when considering organisms (*e.g.*, viruses, prokaryotes, eukaryotes)

with no hierarchical grouping, both size and complexity are greatly skewed towards eukaryotes (Heim et al., 2017). This would lend credence to the idea that life evolves away from minimal size, as Stanley had postulated. However, considering the size and complexity of organisms that have been hierarchically grouped by domain, size and complexity have a unimodal distribution for each respective group (Heim et al., 2017), indicating that within groups of species there is no skew in distribution of size and complexity. Knoll and Bambach argued that the increase in complexity and size happens in “megatrajectories”, a similar concept to the “major transitions” described by Smith and Szathmary, where life takes a large leap upwards in complexity and size when transitioning to the next hierarchical level (Knoll & Bambach, 2000; Smith & Szathmary, 1997). Together, these analyses suggest that evolutionary innovations linked to increased complexity seem fundamentally distinct from those originating within existing hierarchical levels, therefore requiring attentiveness when comparing complexity across all domains of life.

Another natural law that was postulated in the late 1800’s was Dollo’s law, or the law of irreversibility (Dollo, 1893; Gould, 1970). Dollo’s law, as interpreted today, theorizes that complex traits cannot re-evolve because the genes underlying the trait accumulate mutations (in the absence of stabilizing selection) that are very unlikely to be reversed. The idea of irreversibility in evolution has been used to describe the species diversity in current existence and to provide support for the directionality of increased complexity in evolution (Brooks & Wiley, 1988). However, phylogenetic studies have shown that exceptions to Dollo’s law exist and that organisms can indeed regain complex features (Collin & Miglietta, 2008), highlighting the limited knowledge available as to how complexity is evolved.

It is important to emphasize that the “laws” of Cope and Dollo are not laws in the sense of physical laws, but descriptive generalizations of low-order probability that describe some common regularities. Literature discussing the evolution of biological complexity and multicellularity often invoke both Cope’s Rule and Dollo’s Law as a means to convey the trends observed in biological systems. Confounding factors that are typically left out of these discussions, as was done above, are parasites and symbionts. When an organism maintains a parasitic or symbiotic lifestyle, it will lose genomic complexity over time, resulting in greater dependence on a host, which in turn leads to a loss of functions (Cruickshank & Paterson, 2006). Using the specialized definition of biological complexity as outlined in section 1 above, parasites and symbionts could be described as organisms that are retro-evolving to be less complex with a potential for decrease in size, thus defying both Cope’s Rule and Dollo’s Law. This highlights how early theories on evolution can become antiquated but still provide some utility when discussing processes that are still not well understood, such as biological complexity.

## 2.2 Entropy as a Vehicle for Biological Complexity

In an attempt to link universal physical laws to biology, the second law of thermodynamics has been adopted to explain the increase in biological complexity (Brooks & Wiley, 1988). The second law of thermodynamics can be described as the spontaneous dissipation of heat from hotter to colder regions of matter, resulting in a decrease of energy that increases the entropy and disorder in the system. In essence, entropy is a measure of the disorder of a system that describes how much energy is *not* available to do work. The propensity of physical systems to move towards greater disorder, or increased complexity, is the phenomenon for which the second law is often invoked to account for the complexity observed in biological systems.

In his essay “*What is life?*” (1943), Erwin Schrödinger used entropy to explain the application of physical laws to biological systems, arguing that the same physical principles that explain the universe can be used to describe life (Schrödinger, 1992). Schrödinger sensed a potential conflict between the second law and evolution, because while direction of change in the universe tends towards disorder and an *increase* of entropy, biological systems tend towards greater order and a *decrease* in entropy. To address this, he suggested that living organisms depend on increasing the entropy of their local surroundings, thus balancing the decrease in entropy in life by circumventing the violation of the second law at the expense of global entropy. Biological evolution appears to be open-ended, a characteristic not captured by the current closed-system thermodynamic models, making it difficult to broadly apply physical laws to a dynamic system.

Another topic Schrödinger discussed was entropic information theory. Often referred to as Shannon’s entropy or Shannon’s information (Shannon, 1948), it was used to describe the evolution of heritable molecular information in organisms. Brooks and Wiley used this idea to advocate their theory of entropy as a driver in the evolution of biological complexity (Brooks & Wiley, 1988). The authors linked entropy to the transmission of biological information and suggested that evolutionary changes involve increases in species organization and decreases in “*cohesiveness*”, emphasizing that the self-organization of organisms is sustained by environmental free energy. The term cohesiveness was used to refer to the degree of unity or interconnectedness within a biological entity, particularly a species, as a measure of how well the genetic material of diverse members of a species is mixed during reproduction. The concept of cohesion is tied to the transmission of genetic material and how it is shared among individuals within a population. The authors highlight the inverse coupling of cohesion entropy and information entropy at equilibrium,

emphasizing the role of organization in reducing the expression of genetic information. However, challenges arise in defining the distinctions between stored vs. potential information and addressing the impact of external factors in evolution, highlighting the shortcomings between physical laws and the underlying “laws” of biology.

### 2.3 The Zero Force Evolutionary Law

The last theory to be discussed regarding the evolution of biological complexity is the Zero Force Evolutionary Law (ZFEL). The ZFEL was introduced by McShea and Brandon to address shortcomings in the application of entropy to evolution and provide a universal law regarding the evolution of biological complexity (McShea & Brandon, 2010; McShea et al., 2019). Stated succinctly, the ZFEL says that:

“In any evolutionary system in which there is variation and heredity, in the absence of natural selection, other forces, and constraints acting on diversity or complexity, diversity and complexity will increase on average.”

This theory can be likened to Newton's first law of inertia, in that unless acted upon by another force, the expectation is that biological diversity and complexity will increase. This is not to say that diversity and complexity must increase, only that there is a *tendency* for both to increase, though this can easily be overcome by selection and constraints (whether they be environmental or biological). However, a tendency is not a result and for a theory to stand it must be backed by observations, requiring evidence to support the model.

The evidence McShea and Brandon provided to support their ZFEL theory is the increase in genomic diversity and complexity throughout the evolution of life. The authors argue that nucleotide positions not under selection will diversify spontaneously on account of the degeneracy of the genetic code (McShea & Brandon, 2010). Furthermore, they argue that pseudogenes (*i.e.*,

non-functional genes) will accumulate mutations that increase the genomic complexity of an organism. This passive accumulation of mutations in a gene not under selection can be described as a random walk, a stochastic process that leads to divergence from the original sequence. Interestingly, *in silico* modeling of these random walks results in a unimodal distribution (McShea et al., 2019), similar to the unimodal distribution of size for organisms that are hierarchically separated (Heim et al., 2017), though the correlation has not been well-studied. While the ZFEL offers an intriguing theory that could explain the origins of biological complexity, it remains difficult to prove due to the constant selection pressures exerted on any organism or gene. The “selfish” replication and survival of any gene can inherently result in kin selection and cooperation, making it difficult to divorce natural selection from the ZFEL, even at a genetic level (Dawkins, 2016). Nonetheless, the ZFEL offers a null hypothesis that can be either be supported or disproven as research on biological complexity continues.

#### 2.4 Section Summary

Scientists have gone as far to call the unknown evolutionary force driving the increase in biological complexity a Maxwellian demon (Adami, 1999), a comparison to the famous thought experiment by James Clerk Maxwell purporting that entropy can be violated by some demon that can control the movement of molecules (Knott, 1911). This is an appropriate comparison as theories using entropy to explain diversity and complexity have been greatly explored in the scientific literature (Brooks & Wiley, 1988; Collier, 1986; Jennings et al., 2020; Vanchurin et al., 2022). While entropy has been suggested as a vehicle for evolution of biological complexity, it is difficult to justify an increase in entropy of a system (*i.e.*, disorder/complexity) while components of that system decrease in entropy (*i.e.*, self-organization of organisms). The ZFEL attempts to

circumvent this by proposing a biological law that is independent of entropy. Monod and Koonin advocate that at a genetic level, evolution is governed by chance, that the “evolutionary force” is simply blind randomness driven by natural selection (Koonin, 2011; Monod, 1974). Despite the differing opinions, it seems that no individual element – whether stochastic events, entropy, natural selection, or information sharing – can independently drive an increase in complexity within a system. Only by considering all these factors collectively can one discern a complex interplay of processes working in tandem to produce the observed outcome.

### 3. Measuring Biological Complexity

In biology there are three major components used to determine an organism’s level of complexity. The first is the genome, which includes the chromosome(s) size (*e.g.* total number of base pairs), the number of coding genes present, ploidy level, and, if present, sex (Bull, 2020; Lane & Martin, 2010). The second is (ultra)structure, which includes the presence of complex internal structures involved in the compartmentalization of specific functions such as organelles and/or an endosymbiont (Koonin, 2010; Lynch & Marinov, 2017). The third is the existence of multicellularity, a trait indicative of increase in size and number of cells that can lead to the specialization of specific cell types (Bull, 2020; Heim et al., 2017; Herron et al., 2019; Kirk, 2005; Niklas & Newman, 2013). While the three levels appear to be simple to define, each is imbued with its own set of confounding factors that make it paradoxically difficult to evaluate all life through the same lens. Each of these levels are discussed in further detail below.

### 3.1 Genome Complexity

Comparative genomics has revealed that there is a notable increase in genome complexity from bacteria and archaea to that of eukaryotes. This rise in genomic complexity is accompanied by an increase in gene number, ploidy level, and the abundance of noncoding DNA (*e.g.*, introns). For this reason, the genome is often used as a proxy to determine an organism's level of complexity (Lane & Martin, 2010; Lynch, 2006, 2003). While much can be learned about an organism's level of complexity through its genome, there is no simple correlation between the amount of DNA in a given organism and its perceived complexity. For example, baker's wheat (*Triticum aestivum*) has a genome that is five times larger than the human genome (Zimin et al., 2017) but is considered to be less complex due to gene duplication. This discrepancy has been termed the "C-value paradox", where C-value is a term used to describe the mass of DNA in a un-replicated haploid genome (Greilhuber et al., 2005). Furthermore, the large genomes of eukaryotes tend to have a much lower biological information density than the genomes of bacteria and archaea, making the genomes of bacteria and archaea to be better streamlined than those of eukaryotes (Koonin, 2011).

Due to the variability of information density in an organism's genome, genome size cannot be used alone to determine the level of an organism's complexity. Lane and Martin advocated using bioenergetics to calculate complexity based on the size of genome and metabolic rate of the organism. They hypothesized that eukaryotes are able to achieve a higher level of complexity due to the presence of mitochondria<sup>2</sup>, which provide sufficient energy to maintain a larger genome and cell mass (Lane & Martin, 2010). In a response to this hypothesis, Chiyomaru and Takemoto

---

<sup>2</sup> The authors do not discuss mitochondria free eukaryotes, which have been shown to exist: Karnkowska, A., Vacek, V., Zubáčová, Z., Treitli, S. C., Petrželková, R., Eme, L., Novák, L., Žárský, V., Barlow, L. D., & Herman, E. K. (2016). A eukaryote without a mitochondrial organelle. *Current Biology*, 26(10), 1274-1284.

proposed that mitochondria are not essential to complexity, showing that there are several examples of bacteria that exhibit a greater energetic output in regards to cell mass than eukaryotes (Chiyomaru & Takemoto, 2020). It is likely that as our knowledge of organismal diversity increases, we will better understand the relations between genome size, energetics, and complexity.

### 3.2 (Ultra)Structure

The definition of complexity given in section 1 states that biological complexity is reduced to the variety among parts within an organism, regardless of how they function. Therefore, the ultrastructure of a cell can reveal much about the complexity of that organism. Indeed, comparing the ultrastructure of ultra-small archaea (~300 nm) (Comolli et al., 2009) to that of eukaryotes (10-100  $\mu\text{m}$ ) (Henderson et al., 2007) reveals a drastic difference in subcellular features that are intrinsic to different levels of complexity. Eukaryotes contain complex internal structure that includes a nucleus, endoplasmic reticulum, Golgi apparatus, and mitochondria. In contrast, bacteria and archaea typically have a “simpler” internal structure that contains a nucleoid as well as inclusions for carbon or inorganic molecule storage. Exceptions to simpler internal structures in bacteria and archaea are organisms that contain membrane-enclosed nucleoid (found in the candidate phylum Atribacteria), the pirellulosome found in some planctomycetes, the anammoxosome (used for anaerobic ammonium oxidation metabolism in some chemolithoautotrophic bacteria), membrane bound storage granules, and magnetosomes (membrane bound lipid bilayer that contain ferromagnetic particles used for magnetotaxis) (Grant et al., 2018; Katayama, 2019). While bacteria and archaea have historically been thought of as simple organisms, research has shown they not only have their own organelles (Greening & Lithgow, 2020), but also the existence of many internal structures for which the functions are not

yet known (Dobro et al., 2017). Ultrastructural actin and other unique internal structures have been found in Asgard archaea, the archaeal phyla from which Eukaryotes evolved, indicating the increasing importance of studying these features to understand the evolution of life (Rodrigues-Oliveira et al., 2023). Continued research regarding the ultrastructure of bacteria and archaea will surely increase our understanding of how complex life is at both extremes of size.

### 3.3 Multicellularity

The evolution of multicellularity is considered to be one of the most frequent major transitions due to the wide range of ecological conditions (*e.g.*, environmental stress, predation, competitive overgrowth, etc.) that can favor its selective advantage (Libby, 2014; Tong et al., 2022). A multicellular organism can be described as a group of cells that cooperate for a benefit that is not achievable as a single cell, increasing the fitness of the entire organism (Queller & Strassmann, 2009). Defining characteristics of multicellular organisms includes the following: (1) built from several or many cells of the same species, (2) specific shape and organization in combination with synchronized growth among cells, (3) lack of individual cell autonomy or competition between cells, (4) display of cell-to-cell signaling and coordinated response to external stimuli, and (5) presence of different cell types that engage in cellular cooperation by metabolic differentiation (Kaiser, 1986; Kaiser, 2001; Niklas & Newman, 2013; Shapiro, 1988, 1998). A multicellular organism is able to dedicate entire cells to specialized tasks whereas single celled organisms are only able to divide labor into internal cellular compartments or temporarily in biofilms (Cooper et al., 2022; Grosberg & Strathmann, 2007). Although multicellularity appears to confer increased fitness to organisms, not all organisms become multicellular, suggesting that

this lifestyle evolves through pure chance and/or necessity. The underpinnings mechanisms for the evolution of multicellularity are still being explored.

#### 4. Multicellularity in Bacteria

Multicellularity has traditionally been thought to be exclusive to eukaryotes (Wolpert, 2002), as their members constitute the most abundant multicellular organisms on Earth today. Eukaryotic model systems for the evolution of multicellularity include choanoflagellates (Brunet & King, 2017), fungi (Chavhan et al., 2023), and algae (Herron et al., 2019). With a large amount of research focused on eukaryotic multicellularity, there remains a lack of research into the evolution of multicellularity in the domains Bacteria and Archaea. Currently, there is no direct geological evidence to support the existence of bacterial or archaeal multicellularity prior to eukaryotic multicellularity. This is due in part to the difficulty of confidently identifying microbial fossils in the rock record (Slotznick et al., 2023; Staley, 1999). Highly reliable microbial fossils are stromatolites of cyanobacteria (Allwood et al., 2006), which have been dated as old as 3.4 billion years (Fig. 1B). Stromatolites have been suggested as the earliest example of multicellularity based on phylogenetic studies of cyanobacteria linking the evolution of their filamentous morphology to their existence in deep time (Schirrmeister et al., 2011; Schirrmeister et al., 2013). However, this argument is contingent on the premise that a bacterial biofilm is in fact a multicellular organism, an assumption that is not universally embraced, given that the cells that make up a biofilm do not require multicellularity as an integral part of their life cycle (Grosberg & Strathmann, 2007; Regenberget al., 2016; Tong et al., 2022). Additionally, it requires multi-species consortia to be classified as multicellular, violating the single species criteria listed above. Fossilized cyanobacteria from the Mesoproterozoic (~1.6 billion years ago) show signs of cell-to-

cell differentiation (Golubic et al., 1995; Srivastava, 2005), a characteristic of multicellularity (Niklas & Newman, 2013). This has been used to support the hypothesis that multicellularity evolved first in Bacteria (Lyons & Kolter, 2015), although the evolutionary and mechanistic underpinnings of bacterial multicellularity remain enigmatic.

Because of the inherent difficulty of studying the evolution of multicellular bacteria in deep geologic time, most research focuses on extant microorganisms. By studying multicellular bacteria that are present on Earth today, researchers can relate the genomic potential to functional aspects of the organism's multicellular phenotype. There are only a handful of examples of multicellular bacteria, which include the filamentous cyanobacteria (*e.g.*, *Anabaena cylindrica*), mycelia-forming actinomyces (*e.g.*, *Streptomyces coelicolor*), swarming myxobacteria (*e.g.*, *Myxococcus xanthus*), centimeter-long cable bacteria (*e.g.*, *Electrothrix* sp.), and consortia of multicellular magnetotactic bacteria (MMB) (Claessen et al., 2014; Geerlings et al., 2020; Qian et al., 2021). The multicellular lifecycles of these organisms are depicted in Fig. 3. While these organisms exhibit the characteristics of multicellularity, it is assumed that all but MMB exist in a unicellular state at some point in their life cycle. MMB are currently the only known bacterial organism that has never been observed as individual cells, existing solely as a multicellular consortium (Abreu et al., 2013; C.N. Keim et al., 2004b; Qian et al., 2021; Qian et al., 2020).

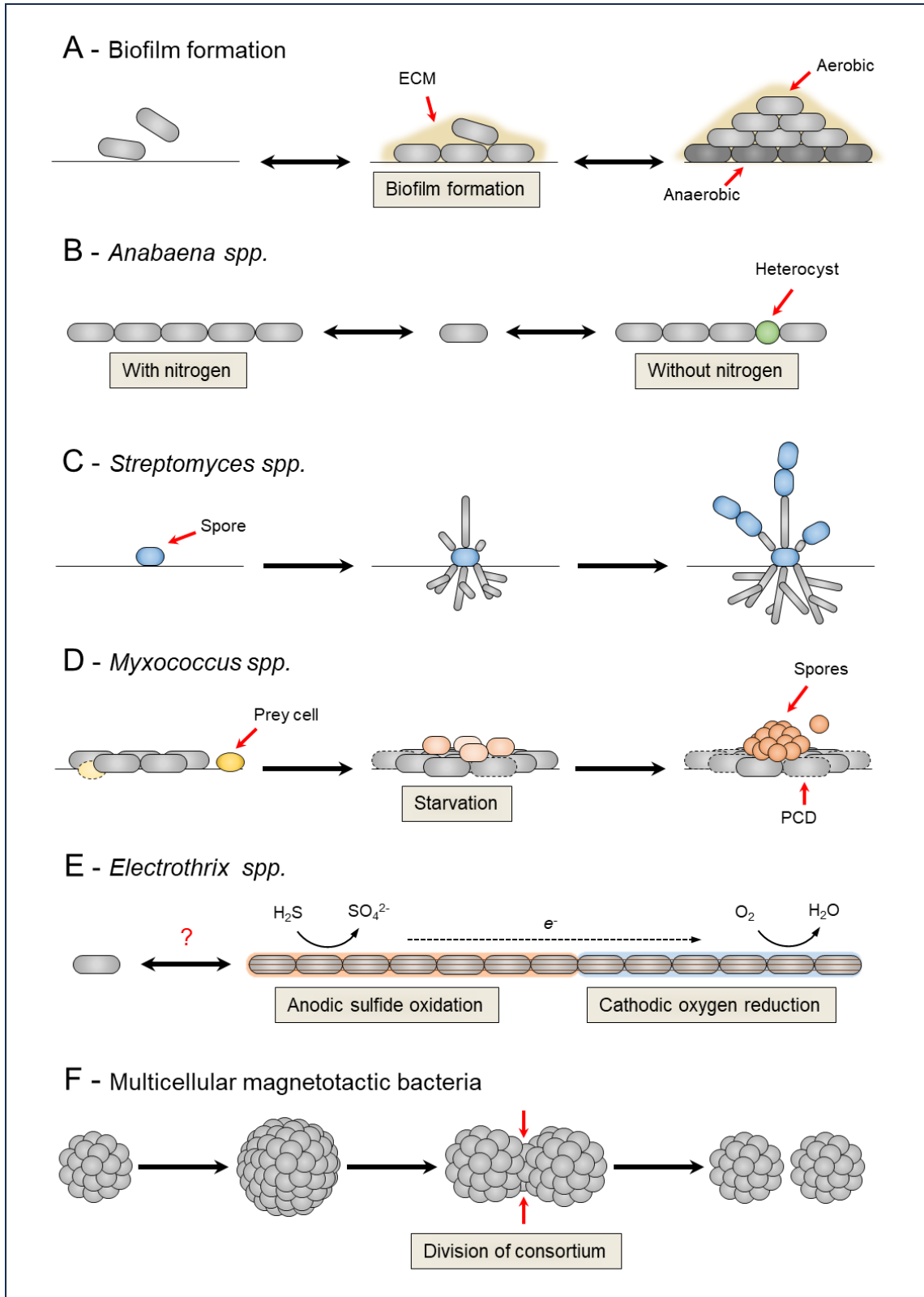


Fig. 3. Multicellular lifecycle for different bacteria. **A** Biofilms are commonly referred to as multicellular organisms, although multicellularity is not a requirement in the lifecycle of organisms forming the biofilm. Biofilms will produce an extracellular matrix (ECM) composed of polysaccharides, proteins, and DNA to maintain the multicellular state. **B** The cyanobacterium *Anabaena* spp. grows as a chain and will form heterocysts, a specialized cell type, to fix nitrogen in environments where ammonium or nitrate is limited. **C** The Actinobacterium *Streptomyces* spp. will grow long vegetative filaments, also referred to as mycelium, and form spores in a stressful environment. **D** Swarming cells of *Myxococcus xanthus* will predate on prey cells and during starvation, undergo programmed cell death (PCD) to provide nutrients to cells differentiating into a fruiting structure for the development of spores. **E** The cable bacterium *Electrothrix* spp. can grow in filaments of cells up to centimeters in length and is capable of shuttling electrons along the nanowires that run the entire length to allow for coupling of sulfide oxidation and oxygen reduction. Currently, it is unknown if cable bacteria have a single cell state in their lifecycle, as denoted by the red question mark. **F** Multicellular magnetotactic bacteria are currently the only known bacterium that maintains multicellularity throughout the entirety of its lifecycle. This organism is the focus of the work presented in this thesis. Figure made by G. A. Schaible.

### 5. Multicellular Magnetotactic Bacteria

MMB were first discovered by Blakemore and Frankel in Woods Hole Massachusetts in 1982 but this discovery was not noted until 1983 when Esquivel *et al.* and Farina *et al.* described the ultrastructure of MMB found in the Rodrigo de Freitas lagoon in Rio de Janeiro, Brazil (Esquivel *et al.*, 1983; Farina *et al.*, 1983). The MMB used in this project are found in the Little Sippewissett Salt March (LSSM), located in the state of Massachusetts, USA (Fig. 4). There has been no consensus in the literature regarding the appropriate designation for referring to this organism, with several terms used such as magnetotactic multicellular aggregates (Farina *et al.*, 1983), many-celled magnetotactic prokaryotes (Rodgers *et al.*, 1990), multicellular magnetotactic prokaryotes (Greenberg *et al.*, 2005), magnetotactic multicellular organisms (C. N. Keim *et al.*, 2004), and multicellular magnetotactic bacteria (Shapiro *et al.*, 2011). We adopt the use of multicellular magnetotactic bacteria (MMB) as this phrase most accurately describes the organism with specific terminology, instead of the more colloquial terms that have historically been used.

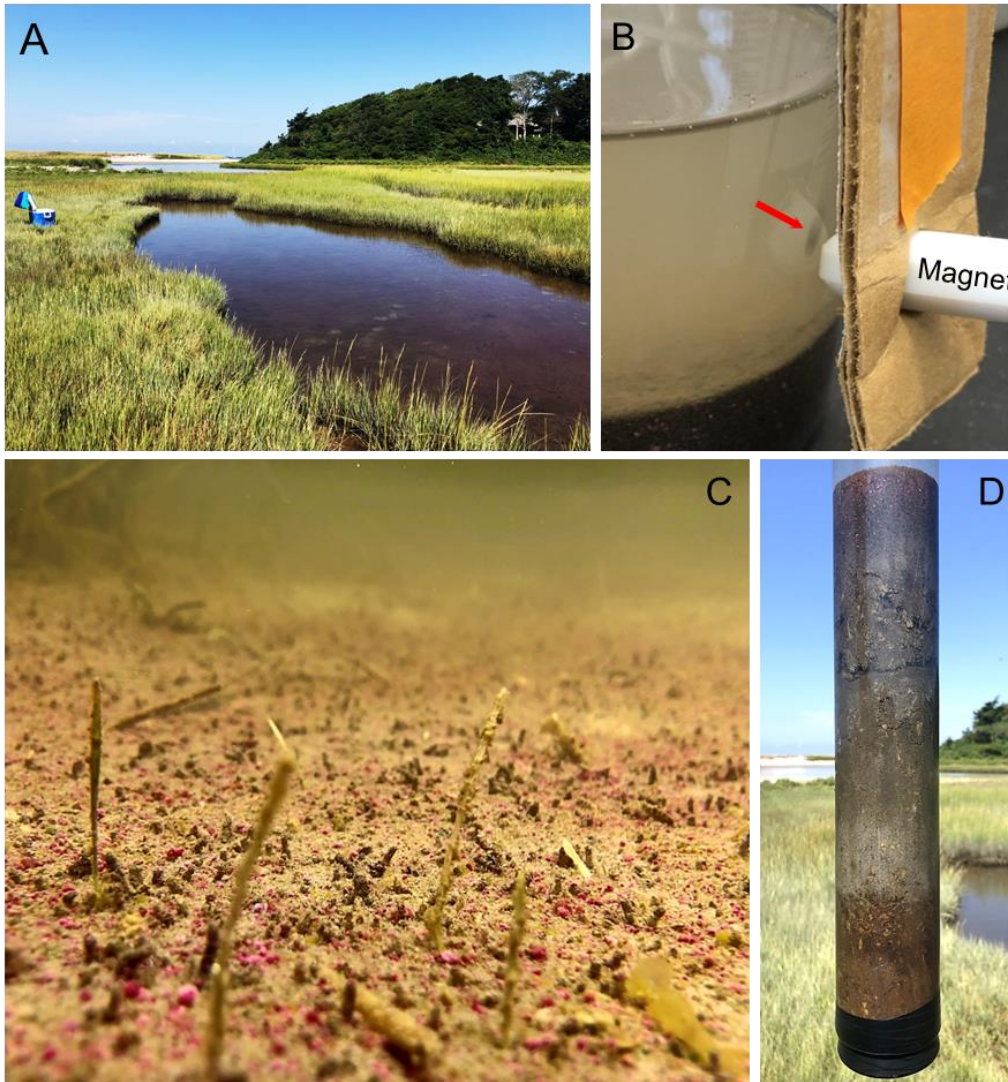


Fig. 4. The MMB used in this project are found in the Little Sippewissett Salt March (LSSM), located in the state of Massachusetts, USA. **A** Ground view of the sampling site. **B** An example of a magnetic enrichment of MMB from LSSM sediment using magnetic stir bar. The red arrow indicates the small mass ( $\sim 50 \mu\text{L}$ ) of MMB that forms near the southern end of a magnetic stir bar after approximately 60 minutes of enrichment. **C** Sediment surface of sample site. MMB are found in abundance in the first 5 cm of the sediment. **D** A 28 cm sediment core from sample site showing the stratification of sediment layers. MMB are found in highest abundance within the top 5 cm of the core.

MMB grow as symmetrical, single-species consortia composed of 15-86 cells of *Desulfobacterota* (formerly *Deltaproteobacteria*) that arrange themselves in a single layer of cells

forming a spherical or oblong shape around an acellular, central compartment (Fig. 5A-D) (Abreu et al., 2013; Chen et al., 2015; Leao et al., 2017). This acellular volume is hypothesized to be used for communication and metabolite exchange between individual cells of the consortium but this hypothesis has never been tested (Abreu et al., 2007; Abreu et al., 2013; C. N. Keim et al., 2004; Rodgers et al., 1990; Zhou et al., 2013). The size, shape, and number of cells within each consortium varies during the different stages of their proposed life cycle as well as between species (Abreu et al., 2007; C.N. Keim et al., 2004b; Leao et al., 2017). Each cell within a consortium is flagellated and MMB swim in a helical like motion capable of moving approximately 26  $\mu\text{m/s}$  (Almeida et al., 2013; C. N. Keim et al., 2004). MMB have been observed to change the direction of their motility within fractions of a second upon a change in environmental conditions, most notably magnetic fields (Almeida et al., 2013; Keim et al., 2007).

A hallmark of magnetotactic bacteria, such as MMB, are biomineralized ferromagnetic crystals, typically in the form of magnetite ( $\text{Fe}_3\text{O}_4$ ) and/or greigite ( $\text{Fe}_3\text{S}_4$ ), encapsulated in a lipid vesicle called the magnetosome (Fig. 5E) (Almeida et al., 2013; Bazylinski & Frankel, 2004; Chen et al., 2015; Rodgers et al., 1990; Teng et al., 2018; Zhou et al., 2013). Magnetosomes are responsible for the ability of MMB to sense and orient themselves along Earth's geomagnetic field, a phenomenon termed magnetotaxis. The magnetosomes are aligned into multiple chains (Fig. 5C) along the cell as a "compass needle" by actin-like proteins known as MamK (Komeili, 2006; Ozyamak et al., 2013). This creates a magnetic dipole that allows magnetotactic bacteria (*e.g.* MMB) to passively align along Earth's magnetic field lines (Richard, 1975). Magnetotaxis is thought to allow magnetotactic bacteria to re-orient themselves to optimal oxygen gradients in the

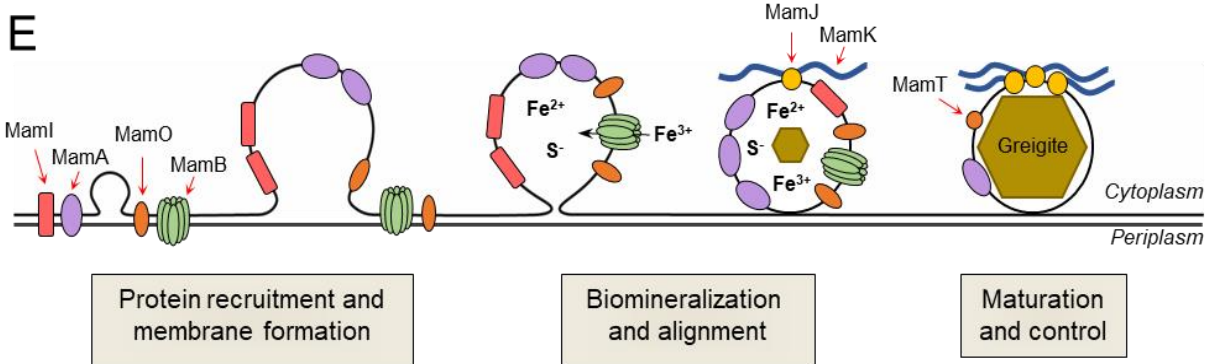
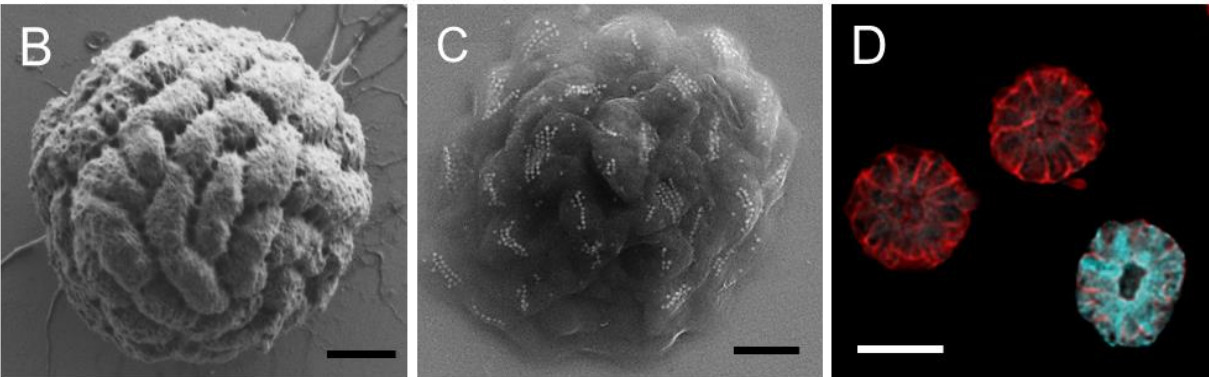
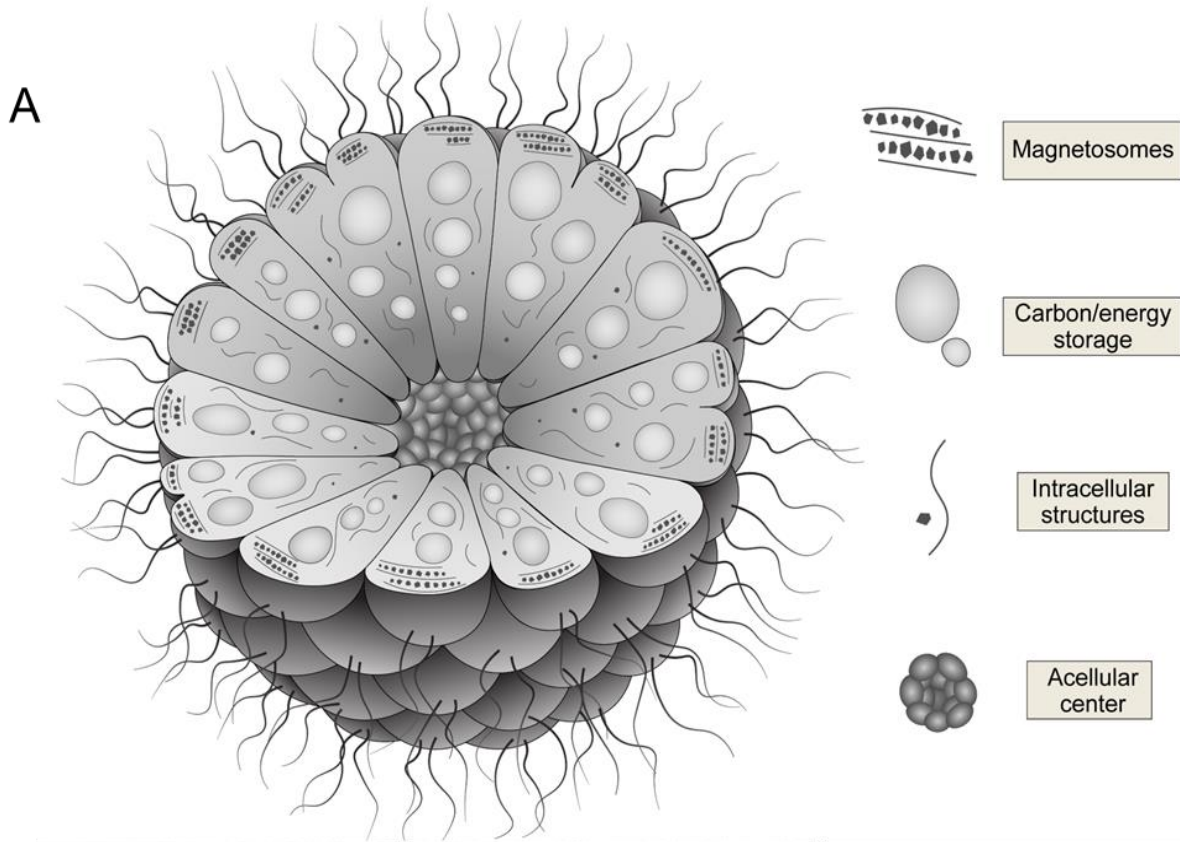


Fig. 5. The morphological ultrastructure and magnetosome formation in MMB. **A** Cartoon depiction of MMB showing the single layer of cells surrounding an acellular center. Ultrastructural features, such as magnetosomes and storage granules, can be seen within individual cells of the consortium. **B** Scanning electron microscopy image of a single MMB showing the spherical organization of cells within the consortium. **C** Backscatter electron microscopy image revealing the organization of biomineralized greigite (seen as white dots) within the individual cells of a consortium. **D** CLSM image of three MMB consortia that have been incubated with *L*-azidohomoalanine to reveal the peptidoglycan layers (red), protein synthesis (cyan), and the acellular center (dark area within MMB in lower right). **E** A diagram showing the multiple states of magnetosome formation. Mam proteins (-A, -B, -I, -O) are recruited to the site where membrane invagination occurs, eventually forming a lipid polyp containing the appropriate proteins to start biomineralization of ferromagnetic minerals. In the case of MMB, this is commonly greigite. MamK functions as a structural protein that keeps the magnetosomes aligned to establish a magnetic dipole that passively orients the MMB in the presence of a magnetic field. MamJ acts as an anchor protein, although MMB from LSSM do not have this protein, further discussed in chapter 4. All cartoon figures made by G. A. Schaible.

water column, a process termed magneto-aerotaxis (Frankel, 1997). The ability of MMB to swim towards a magnetic pole can be used to physically enrich them from samples (Fig. 4B). This is particularly important as they are in low abundance in nature (0.001 - 2%) and cannot yet be cultured in the lab (Martins, 2009; Simmons & Edwards, 2007). The biomineralization of magnetite and greigite by magnetotactic bacteria has been researched for use in biotechnology as well as a fossil biomarker for life detection on Mars (Araujo et al., 2015; Davila, 2007; Simoes et al., 2020; Wang et al., 2020).

MMB are not a mere transient aggregation of cells, such as a biofilm, but rather a symmetrically organized consortium that undergoes a coordinated division process while maintaining their multicellular organization (Abreu et al., 2014; C.N. Keim et al., 2004b; Zhou et al., 2012). During the replication process, individual cells within an MMB consortium double in size before the entire consortium divides into two daughter consortia (Fig. 3F) (Abreu et al., 2014; C.N. Keim et al., 2004b; Qian et al., 2021). When a single MMB cell is separated from the

consortium it loses its membrane integrity and dies (Abreu et al., 2006; Lins & Farina, 1999; Rodgers et al., 1990). Analyses of MMB metagenomes has shown the presence of five distinct genus level populations of MMB in the LSSM (Fig. 6), confirming previous observations obtained via near full-length 16S rRNA clone gene sequencing (Simmons & Edwards, 2007). Additionally, data generated in this thesis has shown the existence of eight distinct species of MMB. A further detailed analysis of the metagenomes recovered from LSSM MMB and the taxonomic assignment for the species discovered is provided in chapter 5 of this thesis. To date, *Magnetoglobus multicellularis* is the best studied MMB with genomic and electron microscopy data to show its multicellular lifecycle and cellular organization (Abreu et al., 2014; C.N. Keim et al., 2004a; Leao et al., 2017). *M. multicellularis* is the closest relative to the most abundant genus of MMB found in LSSM (Fig. 6).

Together, these observations imply that MMB are complex bacteria containing magnetosomes, a bacterial organelle, and undergo an organized and coordinated division process. Within Bacteria, facultative multicellularity has been found to be more common than obligate multicellularity (Fig. 3) (Fisher & Regenberg, 2019). MMB offer the only opportunity to study obligate multicellularity within the bacteria. Furthermore, magnetofossils (*e.g.*, fossilized biomineralized magnetite ( $\text{Fe}_3\text{O}_4$ ) and/or greigite ( $\text{Fe}_3\text{S}_4$ ) have been identified as ideal fossils to identify microbes in the rock record (Slotznick et al., 2023), implying our analysis of MMB may provide valuable insights in the evolution of multicellularity in deep time. This is of particular importance as it is difficult to unambiguously identify microbial fossils (Staley, 1999). In addition to their unique lifecycle and ultrastructure, MMB may also maintain a uniquely high respiratory level as compared to all other prokaryotes and eukaryotes, possibly to support their multicellular

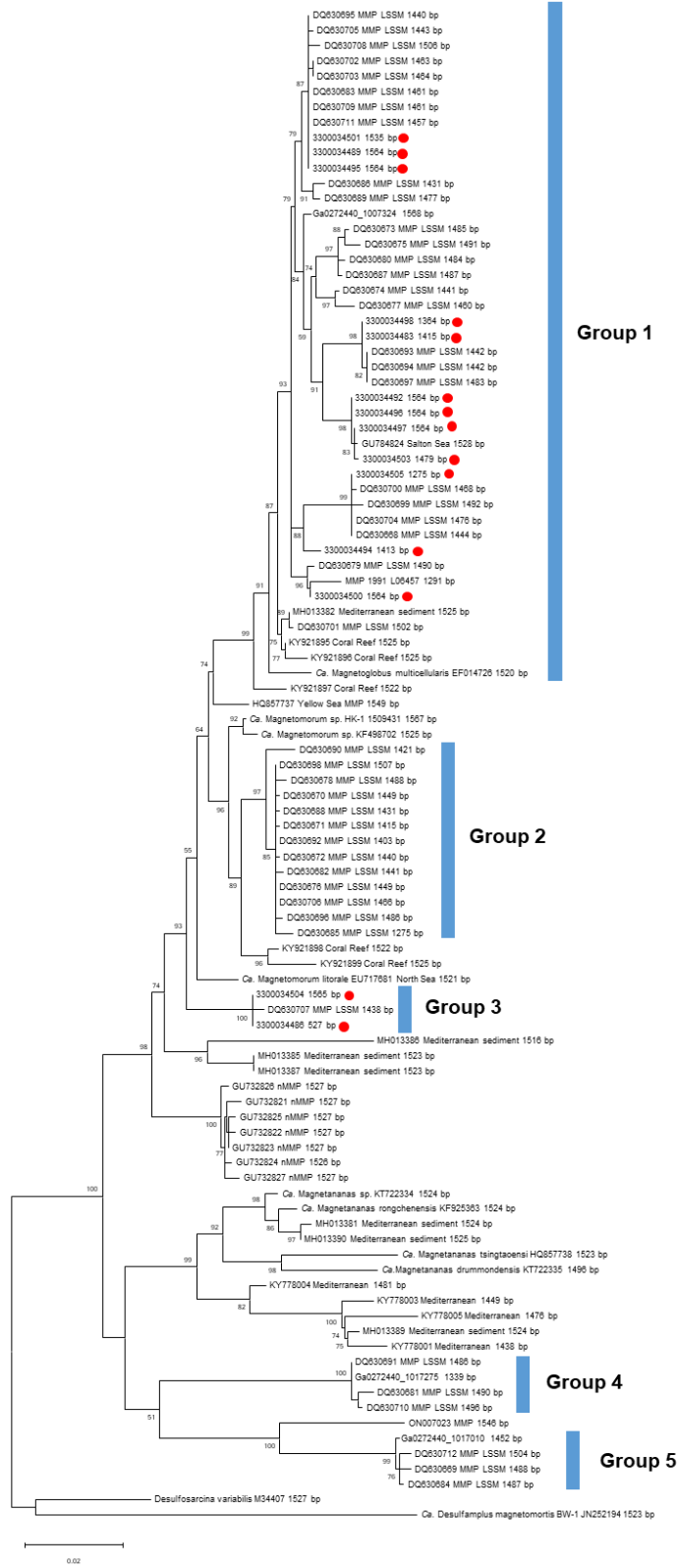


Fig. 6. Phylogenetic analysis of MMB using near-full length 16S rRNA genes (length listed next to name) recovered from LSSM MMB (denoted with red dot) through metagenomic sequencing. Tree reconstructed using maximum likelihood method with bootstrap values calculated using 500 replicates. Bootstrap values above 50 are shown. Figure adapted from Schaible *et al.* submitted.

lifecycle. Preliminary calculations using the metabolic rate of *Desulfovibrio desulfuricans*, a close relative to MMB (Fig. 7) shows that, depending on the number of cells within the consortium, MMB may operate at a high energetic level. This could influence the current thinking on bioenergetics in regard to the difference of complexity between prokaryotes and eukaryotes (Chiyomaru & Takemoto, 2020; Lane & Martin, 2010). MMB may present a unique opportunity to address theoretical questions regarding the evolution of biological complexity and multicellularity in extant organisms and those in deep time.

## 6. Culture-Independent Methods to Study Biological Complexity

There is little known about the physiology of MMB and despite their discovery over forty years ago, they remain recalcitrant to cultivation though efforts to bring them unto culture have been made (Abreu et al., 2014). To overcome this limitation, we employed culture-independent methods to analyze the MMB on a single-cell level (Fig. 8). Because of the existence of many species of MMB in LSSM and the fragile structure of the MMB, we developed a correlative workflow to analyze the organism using several techniques, allowing us to correlate species specific chemistry and ultrastructure of single MMB (Schaible et al., 2022). The genomics of MMB was explored by separating single consortia using fluorescence-activated cell sorting and performing multiple displacement amplification on all the genetic material from the consortium. Subsequent shotgun metagenomics was used to obtain single consortium genomes, that is a genome from a single MMB that is representative of every cell composing the organism. These

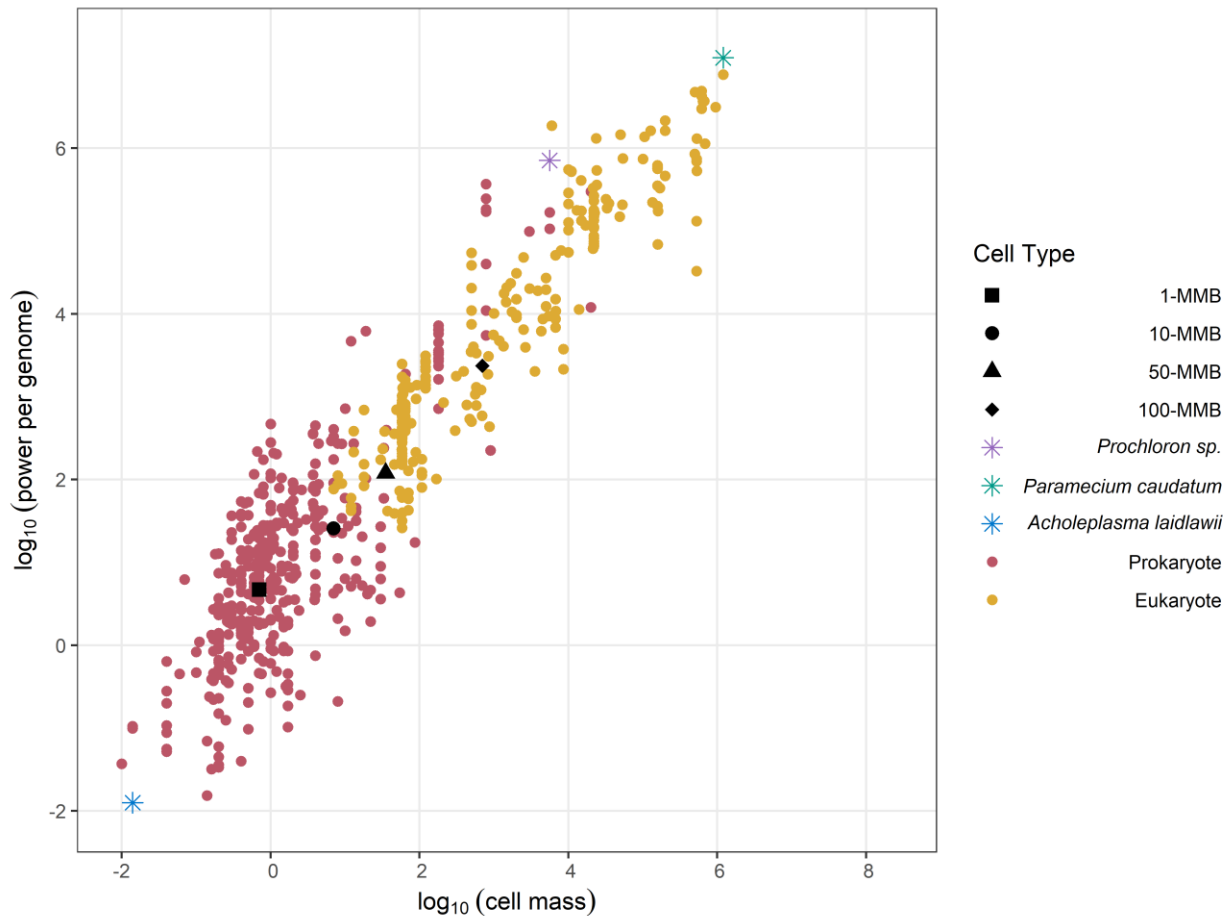


Fig. 7. Comparison of energetic measures between prokaryotes, eukaryotes, and MMB. Datapoints for prokaryotes and eukaryotes were used from Dataset S1 in (Chiyomaru & Takemoto, 2020). The mass-specific metabolic rate of *D. desulfuricans* was used for calculations of MMB metabolic rate as the metabolic rate for MMB is currently unknown and *D. desulfuricans* is a close relative of MMB. The power per genome versus cell mass was calculated for four different sets of MMB, where the consortium had either 1 cell, 10 cells, 50 cells, or 100 cells. The lowest power calculated was the bacterium *Acholeplasma laidlawii*, which belong to the Mollicutes class, which are known for having the smallest genome sizes autonomously replicating organisms. Also shown is *Prochloron sp.*, a unicellular oxygenic photosynthetic bacterium thought to be the endosymbiont that eventually formed the chloroplast in photosynthetic eukaryotes. The organism with the highest power per genome is *Paramecium caudatum*, species of unicellular protist that feed on bacteria and small eukaryotes. Calculations show that an MMB containing 50 cells, a reasonable number based on observations of MMB cell numbers (Leao et al., 2017), falls above the majority of prokaryotic cells.

genomes were then annotated, and the metabolic potential mapped to allow for predictions to be made regarding potential carbon and energy substrates. The 16S rRNA gene sequences were used to design fluorescence *in situ* hybridization (FISH) probes for identification of the MMB populations inhabiting the sampling site at LSSM. Genomics-guided stable isotope probing (SIP) was used in conjunction with FISH to experimentally test the isotope-labeled substrate utilization for specific populations of MMB. Substrate incorporation was studied using Raman microspectroscopy (Raman) and nano-scale secondary ion mass spectroscopy (NanoSIMS). In addition, bioorthogonal non-canonical amino acid tagging (BONCAT) and confocal laser scanning microscopy (CLSM) were used to investigate the protein synthesis within individual cells of the MMB. Together, these techniques enabled us to circumvent the current inability to culture MMB and allow for single cell resolution of the metabolism and physiology of MMB.

### 7. Overview of Following Chapters

The following chapters in this thesis are ordered as to introduce the aforementioned culture-independent techniques and the methodologies for their application, followed by a detailed investigation of MMB and finally a conclusion of the work and future directions. Chapter 2 outlines published work regarding the correlative workflows developed to analyze the MMB. Because of the existence of several genera and species of MMB in LSSM, all of which appear to have similar morphology, a FISH-Raman-NanoSIMS workflow was used, incorporating scanning electron microscopy (SEM), backscatter electron microscopy (BSE), and energy-dispersive X-ray spectroscopy (EDS) to allow for species specific metabolic and ultrastructural differences to be investigated (Schaible et al., 2022). Chapter 3 discusses a benchmark study to establish the

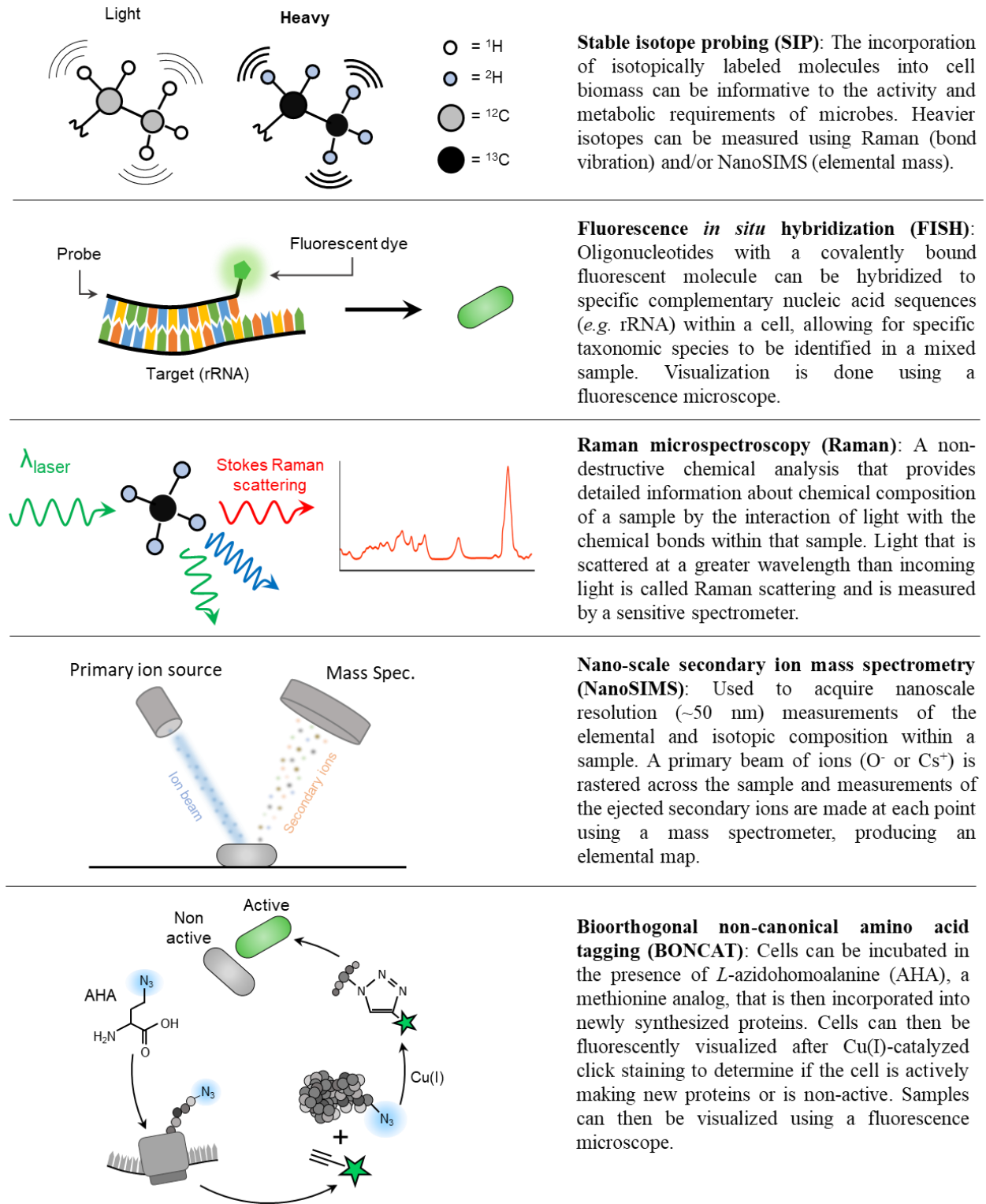


Fig. 8. Schematics showing the culture independent methods employed in this thesis. Figures made by G. A. Schaible.

comparability of Raman and NanoSIMS data when looking at SIP labeling in microbes. Chapter 4 employs the culture independent techniques to provide a detailed analysis of MMB, investigating the clonality of the organism as well as the existence of a division of labor between cells within the consortium. Finally, chapter 5 provides a review of the work presented in this thesis and offers future directions to further explore the complexity and multicellularity of MMB.

### References

- Abreu, F., Martins, J. L., Silveira, T. S., Keim, C. N., de Barros, H. G., Filho, F. J., & Lins, U. (2007). 'Candidatus Magnetoglobus multicellularis', a multicellular, magnetotactic prokaryote from a hypersaline environment. *Int J Syst Evol Microbiol*, 57(Pt 6), 1318-1322. <https://doi.org/10.1099/ijs.0.64857-0>
- Abreu, F., Morillo, V., Nascimento, F. F., Werneck, C., Cantao, M. E., Ciapina, L. P., de Almeida, L. G., Lefevre, C. T., Bazylnski, D. A., de Vasconcelos, A. T., & Lins, U. (2014). Deciphering unusual uncultured magnetotactic multicellular prokaryotes through genomics. *ISME J*, 8(5), 1055-1068. <https://doi.org/10.1038/ismej.2013.203>
- Abreu, F., Silva, K. T., Leao, P., Guedes, I. A., Keim, C. N., Farina, M., & Lins, U. (2013). Cell adhesion, multicellular morphology, and magnetosome distribution in the multicellular magnetotactic prokaryote *Candidatus Magnetoglobus multicellularis*. *Microsc Microanal*, 19(3), 535-543. <https://doi.org/10.1017/S1431927613000329>
- Abreu, F., Silva, K. T., Martins, J. L., & Lins, U. (2006). Cell viability in magnetotactic multicellular prokaryotes. *International Microbiology*, 9, 267-272.
- Adami, C., Ofria, C., & Collier, T. C. (1999). Evolution of biological complexity. *Proceedings of the National Academy of Sciences*, 97, 4463-4468.
- Allwood, A. C., Walter, M. R., Kamber, B. S., Marshall, C. P., & Burch, I. W. (2006). Stromatolite reef from the Early Archaean era of Australia. *Nature*, 441(7094), 714-718.
- Almeida, F. P., Viana, N. B., Lins, U., Farina, M., & Keim, C. N. (2013). Swimming behaviour of the multicellular magnetotactic prokaryote 'Candidatus Magnetoglobus multicellularis' under applied magnetic fields and ultraviolet light. *Antonie Van Leeuwenhoek*, 103(4), 845-857. <https://doi.org/10.1007/s10482-012-9866-0>
- Araujo, A. C., Abreu, F., Silva, K. T., Bazylnski, D. A., & Lins, U. (2015). Magnetotactic bacteria as potential sources of bioproducts. *Mar Drugs*, 13(1), 389-430. <https://doi.org/10.3390/md13010389>
- Bazylnski, D. A., & Frankel, R. B. (2004). Magnetosome formation in prokaryotes. *Nat Rev Microbiol*, 2(3), 217-230. <https://doi.org/10.1038/nrmicro842>
- Betts, H. C., Puttick, M. N., Clark, J. W., Williams, T. A., Donoghue, P. C., & Pisani, D. (2018). Integrated genomic and fossil evidence illuminates life's early evolution and eukaryote origin. *Nature ecology & evolution*, 2(10), 1556-1562.
- Bonner, J. T. (1998). The origins of multicellularity. *Integrative Biology*, 1, 27-36.
- Bonner, J. T. (2004). Perspective: the size-complexity rule. *Evolution*, 58(9), 1883-1890.

- Bozdag, G. O., Libby, E., Pineau, R., Reinhard, C. T., & Ratcliff, W. C. (2021). Oxygen suppression of macroscopic multicellularity. *Nat Commun*, *12*(1), 2838. <https://doi.org/10.1038/s41467-021-23104-0>
- Bozdag, G. O., Szeinbaum, N., Conlin, P., Chen, K., Fos, S. M., Garcia, A., Penev, P., Schaible, G. A., & Trubl, G. (2023). Major biological innovations that had an impact on the diversity and complexity of life on Earth. *Astrobiology*.
- Brooks, D. R., & Wiley, E. O. (1988). *Evolution as entropy*. University of Chicago Press Chicago.
- Brunet, T., & King, N. (2017). The Origin of Animal Multicellularity and Cell Differentiation. *Dev Cell*, *43*(2), 124-140. <https://doi.org/10.1016/j.devcel.2017.09.016>
- Bull, L. (2020). The Evolution of Complexity: Simple Simulations of Major Innovations. *Springer Nature*, *37*.
- Butterfield, N. J. (2000). *Bangiomorpha pubescens* n. gen., n. sp.: implications for the evolution of sex, multicellularity, and the Mesoproterozoic/Neoproterozoic radiation of eukaryotes. *Paleobiology*, *26*(3), 386-404.
- Carroll, S. B. (2001). Chance and necessity: the evolution of morphological complexity and diversity. *Nature*, *409*(6823), 1102-1109.
- Chavhan, Y., Dey, S., & Lind, P. A. (2023). Bacteria evolve macroscopic multicellularity by the genetic assimilation of phenotypically plastic cell clustering. *Nat Commun*, *14*(1), 3555. <https://doi.org/10.1038/s41467-023-39320-9>
- Chen, Y. R., Zhang, R., Du, H. J., Pan, H. M., Zhang, W. Y., Zhou, K., Li, J. H., Xiao, T., & Wu, L. F. (2015). A novel species of ellipsoidal multicellular magnetotactic prokaryotes from Lake Yuehu in China. *Environ Microbiol*, *17*(3), 637-647. <https://doi.org/10.1111/1462-2920.12480>
- Chiyomaru, K., & Takemoto, K. (2020). Revisiting the hypothesis of an energetic barrier to genome complexity between eukaryotes and prokaryotes. *R Soc Open Sci*, *7*(2), 191859. <https://doi.org/10.1098/rsos.191859>
- Claessen, D., Rozen, D. E., Kuipers, O. P., Sogaard-Andersen, L., & van Wezel, G. P. (2014). Bacterial solutions to multicellularity: a tale of biofilms, filaments and fruiting bodies. *Nat Rev Microbiol*, *12*(2), 115-124. <https://doi.org/10.1038/nrmicro3178>
- Colizzi, E. S. V., R. M.; Merks, R. M. (2020). Evolution of multicellularity by collective integration of spatial information. *Elife*, *9*. <https://doi.org/10.7554/eLife.56349>
- Collier, J. (1986). Entropy in evolution. *Biology and Philosophy*, *1*, 5-24.

- Collin, R., & Miglietta, M. P. (2008). Reversing opinions on Dollo's Law. *Trends in ecology & evolution*, 23(11), 602-609.
- Comolli, L. R., Baker, B. J., Downing, K. H., Siegerist, C. E., & Banfield, J. F. (2009). Three-dimensional analysis of the structure and ecology of a novel, ultra-small archaeon. *The ISME journal*, 3(2), 159-167.
- Cope, E. (1887). *The origin of the fittest*: New York. *Appleton and Co.*
- Cope, E. D. (1904). *The primary factors of organic evolution*. Open Court Publishing Company.
- Cruickshank, R. H., & Paterson, A. M. (2006). The great escape: do parasites break Dollo's law? *TRENDS in Parasitology*, 22(11), 509-515.
- Darwin, C. (1859). *On the Origin of Species by Means of Natural Selection, or, The Preservation of Favoured Races in the Struggle for Life*. *J. Murray*.
- Davila, A. F., Winklhofer, M., McKay, C. . (2007). Multicellular magnetotactic prokaryote as a target for life search on Mars. *38th Lunar and Planetary Science Conference, 1338*. <https://doi.org/10.1007/7171>
- Dawkins, R. (2016). *The selfish gene*. Oxford university press.
- Dobro, M. J., Oikonomou, C. M., Piper, A., Cohen, J., Guo, K., Jensen, T., Tadayon, J., Donermeyer, J., Park, Y., & Solis, B. A. (2017). Uncharacterized bacterial structures revealed by electron cryotomography. *Journal of bacteriology*, 199(17), 10.1128/jb.00100-00117.
- Dollo, L. (1893). Les lois de l'évolution. *Bull. Soc. Belge Geol. Pal. Hydr*, VII, 164-166.
- Esquivel, D. M. S., Lins de Barros, H. G. P., Farina, M., Aragão, P. H. A., & Danon, J. (1983). Microorganismes magnétotactiques de la region de Rio de Janeiro. *Biology of the cell*, 47, 227-234.
- Farina, M., Lins de Barros, H., Esquivel, D. M. S., & Danon, J. (1983). Ultrastructure of a magnetotactic bacterium. *Biol Cell*, 48, 85-88.
- Fisher, R. M., & Regenberg, B. (2019). Multicellular group formation in *Saccharomyces cerevisiae*. *Proc Biol Sci*, 286(1910), 20191098. <https://doi.org/10.1098/rspb.2019.1098>
- Frankel, R. B., Bazylinski, D. A., Johnson, M. S., & Taylor, B. L. (1997). Magneto-aerotaxis in marine coccoid bacteria. *Biophysical journal*, 73, 994-1000.
- Geerlings, N. M. J., Karman, C., Trashin, S., As, K. S., Kienhuis, M. V. M., Hidalgo-Martinez, S., Vasquez-Cardenas, D., Boschker, H. T. S., De Wael, K., Middelburg, J. J., Polerecky, L., & Meysman, F. J. R. (2020). Division of labor and growth during electrical

- cooperation in multicellular cable bacteria. *Proc Natl Acad Sci U S A*, 117(10), 5478-5485. <https://doi.org/10.1073/pnas.1916244117>
- Gibson, T. M., Shih, P. M., Cumming, V. M., Fischer, W. W., Crockford, P. W., Hodgskiss, M. S., Wörndle, S., Creaser, R. A., Rainbird, R. H., & Skulski, T. M. (2018). Precise age of *Bangiomorpha pubescens* dates the origin of eukaryotic photosynthesis. *Geology*, 46(2), 135-138.
- Golubic, S., Sergeev, V. N., & Knoll, A. H. (1995). Mesoproterozoic Archaeoellipsoides: akinetes of heterocystous cyanobacteria. *Lethaia*, 28(4), 285-298.
- Gould, S. J. (1966). Allometry and size in ontogeny and phylogeny. *Biological Reviews*, 41, 587-638.
- Gould, S. J. (1970). Dollo on Dollo's law: irreversibility and the status of evolutionary laws. *Journal of the History of Biology*, 3, 189-212.
- Gould, S. J. (1996). *Full house: The spread of excellence from Plato to Darwin*. Harvard University Press.
- Grant, C. R., Wan, J., & Komeili, A. (2018). Organelle Formation in Bacteria and Archaea. *Annu Rev Cell Dev Biol*, 34, 217-238. <https://doi.org/10.1146/annurev-cellbio-100616-060908>
- Greenberg, M., Canter, K., Mahler, I., & Tornheim, A. (2005). Observation of magnetoreceptive behavior in a multicellular magnetotactic prokaryote in higher than geomagnetic fields. *Biophys J*, 88(2), 1496-1499. <https://doi.org/10.1529/biophysj.104.047068>
- Greening, C., & Lithgow, T. (2020). Formation and function of bacterial organelles. *Nat Rev Microbiol*, 18(12), 677-689. <https://doi.org/10.1038/s41579-020-0413-0>
- Greilhuber, J., Dolezel, J., Lysak, M. A., & Bennett, M. D. (2005). The origin, evolution and proposed stabilization of the terms 'genome size' and 'C-value' to describe nuclear DNA contents. *Ann Bot*, 95(1), 255-260. <https://doi.org/10.1093/aob/mci019>
- Grosberg, R. K., & Strathmann, R. R. (2007). The Evolution of Multicellularity: A Minor Major Transition? *Annual Review of Ecology, Evolution, and Systematics*, 38(1), 621-654. <https://doi.org/10.1146/annurev.ecolsys.36.102403.114735>
- Hanke, D. (2004). Teleology: The explanation that bedevils biology. *Explanations: Styles of explanation in science*, 143, 155.
- Heim, N. A., Knope, M. L., Schaal, E. K., Wang, S. C., & Payne, J. L. (2015). Cope's rule in the evolution of marine animals. *Science*, 347(6224), 867-870.
- Heim, N. A., Payne, J. L., Finnegan, S., Knope, M. L., Kowalewski, M., Lyons, S. K., McShea, D. W., Novack-Gottshall, P. M., Smith, F. A., & Wang, S. C. (2017). Hierarchical

- complexity and the size limits of life. *Proc Biol Sci*, 284(1857).  
<https://doi.org/10.1098/rspb.2017.1039>
- Henderson, G. P., Gan, L., & Jensen, G. J. (2007). 3-D ultrastructure of *O. tauri*: electron cryotomography of an entire eukaryotic cell. *PLoS One*, 2(8), e749.
- Herron, M. D., Borin, J. M., Boswell, J. C., Walker, J., Chen, I. K., Knox, C. A., Boyd, M., Rosenzweig, F., & Ratcliff, W. C. (2019). De novo origins of multicellularity in response to predation. *Sci Rep*, 9(1), 2328. <https://doi.org/10.1038/s41598-019-39558-8>
- Hug, L. A., Baker, B. J., Anantharaman, K., Brown, C. T., Probst, A. J., Castelle, C. J., Butterfield, C. N., HERNSDORF, A. W., Amano, Y., & Ise, K. (2016). A new view of the tree of life. *Nature microbiology*, 1(5), 1-6.
- Jennings, R. C., Belgio, E., & Zucchelli, G. (2020). Does maximal entropy production play a role in the evolution of biological complexity? A biological point of view. *Rendiconti Lincei. Scienze Fisiche e Naturali*, 31(2), 259-268. <https://doi.org/10.1007/s12210-020-00909-7>
- Kaiser, D. (1986). Control of multicellular development: Dictyostelium and Myxococcus. *Annual Review of Genetics*, 20, 539-566.
- Kaiser, D. (2001). Building a multicellular organism. *Annual Review of Genetics*, 35(1), 103-123.
- Karnkowska, A., Vacek, V., Zubáčová, Z., Treitli, S. C., Petrželková, R., Eme, L., Novák, L., Žárský, V., Barlow, L. D., & Herman, E. K. (2016). A eukaryote without a mitochondrial organelle. *Current Biology*, 26(10), 1274-1284.
- Katayama, T., Nobu, M. K., Kusada, H., Meng, X. Y., Yoshioka, H., Kamagata, Y., & Tamaki, H. (2019). Membrane-bounded nucleoid discovered in a cultivated bacterium of the candidate phylum 'Atribacteria'. *bioRxiv*, 728279. <https://doi.org/10.1101/728279>
- Katsnelson, M. I., Wolf, Y. I., & Koonin, E. V. (2018). Towards physical principles of biological evolution. *Physica Scripta*, 93(4). <https://doi.org/10.1088/1402-4896/aaaba4>
- Keim, C. N., Abreu, F., Lins, U., Lins de Barros, H., & Farina, M. (2004). Cell organization and ultrastructure of a magnetotactic multicellular organism. *J Struct Biol*, 145(3), 254-262. <https://doi.org/10.1016/j.jsb.2003.10.022>
- Keim, C. N., Farina, M., & Lins, U. (2007). Magnetoglobus, Magnetic Aggregates in Anaerobic Environments. *Microbe* 2, 437-445.
- Keim, C. N., Martins, J. L., Abreu, F., Rosado, A. S., de Barros, H. L., Borojevic, R., Lins, U., & Farina, M. (2004a). Multicellular life cycle of magnetotactic prokaryotes. *FEMS Microbiology Letters*, 240(2), 203-208.

- Keim, C. N., Martins, J. L., Abreu, F., Rosado, A. S., de Barros, H. L., Borojevic, R., Lins, U., & Farina, M. (2004b). Multicellular life cycle of magnetotactic prokaryotes. *FEMS Microbiol Letters*, *240*(2), 203-208. <https://doi.org/10.1016/j.femsle.2004.09.035>
- Kirk, D. L. (2005). A twelve-step program for evolving multicellularity and a division of labor. *Bioessays*, *27*(3), 299-310. <https://doi.org/10.1002/bies.20197>
- Knoll, A. H. (1999). *Size limits of very small microorganisms: proceedings of a workshop*. National Academies Press.
- Knoll, A. H., & Bambach, R. K. (2000). Directionality in the history of life: diffusion from the left wall or repeated scaling of the right? *Paleobiology*, *26*(S4), 1-14.
- Knott, C. G. (1911). *Life and scientific work of Peter Guthrie Tait* (Vol. 1). Рипол Классик.
- Komeili, A., Li, Z., Newman, D. K., & Jensen, G. J. (2006). Magnetosomes are cell membrane invaginations organized by the actin-like protein MamK. *Science*, *311*, 242-245.
- Koonin, E. V. (2010). The origin and early evolution of eukaryotes in the light of phylogenomics. *Genome biology*, *11*, 209.
- Koonin, E. V. (2011). *The logic of chance: the nature and origin of biological evolution*. FT press.
- Ladyman, J., Lambert, J., & Wiesner, K. (2012). What is a complex system? *European Journal for Philosophy of Science*, *3*(1), 33-67. <https://doi.org/10.1007/s13194-012-0056-8>
- Lane, N., & Martin, W. (2010). The energetics of genome complexity. *Nature*, *467*(7318), 929-934. <https://doi.org/10.1038/nature09486>
- Leao, P., Chen, Y. R., Abreu, F., Wang, M., Zhang, W. J., Zhou, K., Xiao, T., Wu, L. F., & Lins, U. (2017). Ultrastructure of ellipsoidal magnetotactic multicellular prokaryotes depicts their complex assemblage and cellular polarity in the context of magnetotaxis. *Environ Microbiol*, *19*(6), 2151-2163. <https://doi.org/10.1111/1462-2920.13677>
- Libby, E., and William C. Ratcliff. (2014). Ratcheting the evolution of multicellularity. *Science*, *346*, 426-427.
- Lins, U., & Farina, M. (1999). Organization of cells in magnetotactic multicellular aggregates. *Microbiological Research*, *154*(1), 9-13. [https://doi.org/10.1016/s0944-5013\(99\)80028-7](https://doi.org/10.1016/s0944-5013(99)80028-7)
- Lynch, M. (2006). Streamlining and simplification of microbial genome architecture. *Annu Rev Microbiol*, *60*, 327-349. <https://doi.org/10.1146/annurev.micro.60.080805.142300>
- Lynch, M., & Conery, J. S. (2003). The origins of genome complexity. *Science*, *302*, 1401-1404.

- Lynch, M., & Marinov, G. K. (2017). Membranes, energetics, and evolution across the prokaryote-eukaryote divide. *Elife*, 6. <https://doi.org/10.7554/eLife.20437>
- Lyons, N. A., & Kolter, R. (2015). On the evolution of bacterial multicellularity. *Curr Opin Microbiol*, 24, 21-28. <https://doi.org/10.1016/j.mib.2014.12.007>
- Martins, J. L., Silveira, T.S., Silva, K.T. and Lins, U. (2009). Salinity dependence of the distribution of multicellular magnetotactic prokaryotes in a hypersaline lagoon. *International Microbiology*, 12(3), 193. <https://doi.org/10.2436/20.1501.01.98>
- McShea, D. W. (1991). Complexity and evolution: what everybody knows. *Biology and Philosophy*, 6, 303-324.
- McShea, D. W. (1996). Metazoan complexity and evolution: is there a trend? *Evolution*, 5, 477-492.
- McShea, D. W. (2012). Upper-directed systems: a new approach to teleology in biology. *Biology & Philosophy*, 27, 663-684.
- McShea, D. W. (2023). Evolutionary trends and goal directedness. *Synthese*, 201(5), 178.
- McShea, D. W., & Brandon, R. N. (2010). *Biology's first law: the tendency for diversity and complexity to increase in evolutionary systems*. University of Chicago Press.
- McShea, D. W., Wang, S. C., & Brandon, R. N. (2019). A quantitative formulation of biology's first law. *Evolution*, 73(6), 1101-1115.
- Monod, J. (1974). *On chance and necessity*. Springer.
- Niklas, K. J., & Newman, S. A. (2013). The origins of multicellular organisms. *Evolution & development*, 15(1), 41-52.
- Nutman, A. P., Bennett, V. C., Friend, C. R., Van Kranendonk, M. J., & Chivas, A. R. (2016). Rapid emergence of life shown by discovery of 3,700-million-year-old microbial structures. *Nature*, 537(7621), 535-538.
- Ozyamak, E., Kollman, J., Agard, D. A., & Komeili, A. (2013). The bacterial actin MamK: in vitro assembly behavior and filament architecture. *J Biol Chem*, 288(6), 4265-4277. <https://doi.org/10.1074/jbc.M112.417030>
- Parks, D. H., Chuvochina, M., Rinke, C., Mussig, A. J., Chaumeil, P.-A., & Hugenholtz, P. (2022). GTDB: an ongoing census of bacterial and archaeal diversity through a phylogenetically consistent, rank normalized and complete genome-based taxonomy. *Nucleic Acids Research*, 50(D1), D785-D794.

- Qian, X., Zhao, Y., Santini, C.-L., Pan, H., Xiao, T., Chen, H., Song, T., Li, J., Alberto, F., Brustlein, S., & Wu, L.-F. (2021). How light affect the magnetotactic behavior and reproduction of ellipsoidal multicellular magnetoglobules? *Journal of Oceanology and Limnology*, 39(6), 2005-2014. <https://doi.org/10.1007/s00343-021-0493-3>
- Qian, X. X., Santini, C. L., Kosta, A., Menguy, N., Le Guenno, H., Zhang, W., Li, J., Chen, Y. R., Liu, J., Alberto, F., Espinosa, L., Xiao, T., & Wu, L. F. (2020). Juxtaposed membranes underpin cellular adhesion and display unilateral cell division of multicellular magnetotactic prokaryotes. *Environ Microbiol*, 22(4), 1481-1494. <https://doi.org/10.1111/1462-2920.14710>
- Regenberg, B., Hanghoj, K. E., Andersen, K. S., & Boomsma, J. J. (2016). Clonal yeast biofilms can reap competitive advantages through cell differentiation without being obligatorily multicellular. *Proc Biol Sci*, 283(1842). <https://doi.org/10.1098/rspb.2016.1303>
- Richard, B. (1975). Magnetotactic Bacteria. *Science*, 190, 377-379.
- Rodgers, F. G., Blakemore, R. P., Blakemore, N. A., Frankel, R. B., Bazylinski, D. A., Maratea, D., & Rodgers, C. (1990). Intercellular structure in a many-celled magnetotactic prokaryote. *Archives of Microbiology*, 154, 18-22.
- Rodrigues-Oliveira, T., Wollweber, F., Ponce-Toledo, R. I., Xu, J., Rittmann, S. K.-M., Klingl, A., Pilhofer, M., & Schleper, C. (2023). Actin cytoskeleton and complex cell architecture in an Asgard archaeon. *Nature*, 613(7943), 332-339.
- Schaible, G. A., Kohtz, A. J., Cliff, J., & Hatzenpichler, R. (2022). Correlative SIP-FISH-Raman-SEM-NanoSIMS links identity, morphology, biochemistry, and physiology of environmental microbes. *ISME Communications*, 2(1). <https://doi.org/10.1038/s43705-022-00134-3>
- Schirrmeister, B. E., Antonelli, A., & Bagheri, H. C. (2011). The origin of multicellularity in cyanobacteria. *BMC evolutionary biology*, 11, 1-21.
- Schirrmeister, B. E., de Vos, J. M., Antonelli, A., & Bagheri, H. C. (2013). Evolution of multicellularity coincided with increased diversification of cyanobacteria and the Great Oxidation Event. *Proc Natl Acad Sci U S A*, 110(5), 1791-1796. <https://doi.org/10.1073/pnas.1209927110>
- Schrödinger, E. (1992). What is life?: With mind and matter and autobiographical sketches. *Cambridge University Press*.
- Shannon, C. E. (1948). A mathematical theory of communication. *Bell system technical journal*, 27, 379-423.
- Shapiro, J. A. (1988). Bacteria as Multicellular Organisms. *Scientific American*, 258, 82-89.

- Shapiro, J. A. (1998). Thinking about bacterial populations as multicellular organisms. *Annu. Rev. Microbiol.*, 52, 81–104.
- Shapiro, O. H., Hatzenpichler, R., Buckley, D. H., Zinder, S. H., & Orphan, V. J. (2011). Multicellular photo-magnetotactic bacteria. *Environmental Microbiology Reports*, 3(2), 233-238. <https://doi.org/10.1111/j.1758-2229.2010.00215.x>
- Simmons, S. L., & Edwards, K. J. (2007). Unexpected diversity in populations of the many-celled magnetotactic prokaryote. *Environ Microbiol*, 9(1), 206-215. <https://doi.org/10.1111/j.1462-2920.2006.01129.x>
- Simoës, M. F., Ottoni, C. A., & Antunes, A. (2020). Biogenic Metal Nanoparticles: A New Approach to Detect Life on Mars? *Life (Basel)*, 10(3). <https://doi.org/10.3390/life10030028>
- Slotznick, S. P., Egli, R., & Lascu, I. (2023). Magnetofossils: relicts and records of deep time and space. *Elements*, 19(4), 215-221.
- Smith, J. M., & Szathmary, E. (1997). *The major transitions in evolution*. OUP Oxford.
- Srivastava, P. (2005). Vindhyan akinites: an indicator of mesoproterozoic biospheric evolution. *Origins of Life and Evolution of Biospheres*, 35, 175-185.
- Staley, J. T. (1999). Bacteria, Their Smallest Representatives and Subcellular Structures, and the Purported Precambrian Fossil “Metallogenium”. Size Limits of Very Small Microorganisms: Proceedings of a Workshop,
- Stanley, S. M. (1973). An explanation for Cope's rule. *Evolution*, 27, 1-26.
- Teng, Z., Zhang, Y., Zhang, W., Pan, H., Xu, J., Huang, H., Xiao, T., & Wu, L. F. (2018). Diversity and Characterization of Multicellular Magnetotactic Prokaryotes From Coral Reef Habitats of the Paracel Islands, South China Sea. *Front Microbiol*, 9, 2135. <https://doi.org/10.3389/fmicb.2018.02135>
- Tong, K., Bozdog, G. O., & Ratcliff, W. C. (2022). Selective drivers of simple multicellularity. *Curr Opin Microbiol*, 67, 102141. <https://doi.org/10.1016/j.mib.2022.102141>
- Vanchurin, V., Wolf, Y. I., Koonin, E. V., & Katsnelson, M. I. (2022). Thermodynamics of evolution and the origin of life. *Proceedings of the National Academy of Sciences*, 119(6), e2120042119.
- Wang, X., Li, Y., Zhao, J., Yao, H., Chu, S., Song, Z., He, Z., & Zhang, W. (2020). Magnetotactic bacteria: Characteristics and environmental applications. *Frontiers of Environmental Science & Engineering*, 14(4). <https://doi.org/10.1007/s11783-020-1235-z>

- Wolf, Y. I., Katsnelson, M. I., & Koonin, E. V. (2018). Physical foundations of biological complexity. *Proc Natl Acad Sci U S A*, *115*(37), E8678-E8687. <https://doi.org/10.1073/pnas.1807890115>
- Wolpert, L., & Szathmáry, E. (2002). Multicellularity: evolution and the egg. *Nature*, *420*, 745-745.
- Zhou, K., Zhang, W. Y., Pan, H. M., Li, J. H., Yue, H. D., Xiao, T., & Wu, L. F. (2013). Adaptation of spherical multicellular magnetotactic prokaryotes to the geochemically variable habitat of an intertidal zone. *Environ Microbiol*, *15*(5), 1595-1605. <https://doi.org/10.1111/1462-2920.12057>
- Zhou, K., Zhang, W. Y., Yu-Zhang, K., Pan, H. M., Zhang, S. D., Zhang, W. J., Yue, H. D., Li, Y., Xiao, T., & Wu, L. F. (2012). A novel genus of multicellular magnetotactic prokaryotes from the Yellow Sea. *Environ Microbiol*, *14*(2), 405-413. <https://doi.org/10.1111/j.1462-2920.2011.02590.x>
- Zimin, A. V., Puiu, D., Hall, R., Kingan, S., Clavijo, B. J., & Salzberg, S. L. (2017). The first near-complete assembly of the hexaploid bread wheat genome, *Triticum aestivum*. *Gigascience*, *6*(11), gix097.

## CHAPTER TWO

CORRELATIVE SIP-FISH-RAMAN-SEM-NANOSIMS LINKS IDENTITY, MORPHOLOGY,  
BIOCHEMISTRY, AND PHYSIOLOGY OF ENVIRONMENTAL MICROBESContributions of Authors and Co-Authors

Author: George A. Schaible

Contributions: Designed the study and developed and tested the workflow. Performed incubations and collected Raman spectra for the MMB as well as performed all FISH, SEM, BSE, and EDS on samples. Analyzed data and wrote the manuscript.

Co-Author: Anthony J. Kohtz

Contributions: Designed the study and developed and tested the workflow. Performed incubations and collected Raman spectra for the mock community and analyzed data.

Co-Author: John Cliff

Contributions: Performed NanoSIMS analysis and analyzed the data.

Co-Author: Roland Hatzenpichler

Contributions: Designed the study and wrote the manuscript.

Manuscript Information

George A. Schaible, Anthony J. Kohtz, John Cliff, and Roland Hatzenpichler

ISME Communications

Status of Manuscript:

Prepared for submission to a peer-reviewed journal

Officially submitted to a peer-reviewed journal

Accepted by a peer-reviewed journal

Published in a peer-reviewed journal

Publisher: Nature Publishing Group

Reprinted with permission from Schaible, George A., et al. "Correlative SIP-FISH-Raman-SEM-NanoSIMS links identity, morphology, biochemistry, and physiology of environmental microbes." ISME Communications 2.1 (2022): 52.

## Abstract

Microscopic and spectroscopic techniques are commonly applied to study microbial cells but are typically used on separate samples, resulting in population-level datasets that are integrated across different cells with little spatial resolution. To address this shortcoming, we developed a workflow that correlates several microscopic and spectroscopic techniques to generate an in-depth analysis of individual cells. By combining stable isotope probing (SIP), fluorescence in situ hybridization (FISH), scanning electron microscopy (SEM), confocal Raman microspectroscopy (Raman), and nano-scale secondary ion mass spectrometry (NanoSIMS), we illustrate how individual cells can be thoroughly interrogated to obtain information about their taxonomic identity, structure, physiology, and metabolic activity. Analysis of an artificial microbial community demonstrated that our correlative approach was able to resolve the activity of single cells using heavy water SIP in conjunction with Raman and/or NanoSIMS and establish their taxonomy and morphology using FISH and SEM. This workflow was then applied to a sample of yet uncultured multicellular magnetotactic bacteria (MMB). In addition to establishing their identity and activity, backscatter electron microscopy (BSE), NanoSIMS, and energy-dispersive X-ray spectroscopy (EDS) were employed to characterize the magnetosomes within the cells. By integrating these techniques, we demonstrate a cohesive approach to thoroughly study environmental microbes on a single cell level.

### 1. Introduction

Efforts to understand the ecology of mixed environmental microbial populations are often hindered by our inability to collectively study the morphology, physiology, and taxonomy of

distinct taxa on a meaningful scale. By correlating different single cell resolving spectroscopic and microscopic methods onto a single sample, more meaningful ecophysiological interpretations can be made. Cultivation-independent techniques such as microautoradiography and nano-scale secondary ion mass spectrometry (NanoSIMS), as well as next generation physiology approaches such as Raman microspectroscopy (Raman), have been used to study the *in situ* function and interactions of uncultured microbes (Hatzenpichler, 2020). In conjunction with omic tools, these techniques provide insights into the chemical composition and metabolic activity of cells. However, because they are typically applied separately, meaningful correlations between individual cells and the relevant sets of measurements are often hard (or impossible) to draw. By applying multiple microscopic and spectroscopic analyses on a single sample, an approach referred to as correlative microscopy (Ando et al., 2018), the limitations of a single technique can be overcome, and the results combined into a single dataset that provides micro- to nano-scale information of a biological sample (Endesfelder, 2015).

Correlative microscopy was developed as a means to overcome the limitations in resolution of conventional light microscopy by combining fluorescence microscopy (FM) with electron microscopy (EM), thus allowing for ultrastructural features within eukaryotic cells to be studied in greater detail (Osborn et al., 1978; Webster et al., 1978). The correlation of light and electron microscopy has since become a standard tool for the study of human cells and tissues (Joosten et al., 2018; Lange et al., 2021; Loussert-Fonta et al., 2020; Perkovic et al., 2014; Pirozzi et al., 2018), but is comparatively underdeveloped in microbial ecology. Recent approaches in microbial ecology have combined 16S rRNA targeted fluorescent *in situ* hybridization (FISH) with scanning electron microscopy (SEM) to study specific populations of magnetotactic bacteria that had been

magnetically enriched from their respective habitats (Li et al., 2017; Qian et al., 2020; Woehl et al., 2014). Additionally, FISH has been used in combination with transmission electron microscopy (TEM) to study the ultrastructural differences between cells of uncultured methanotrophic consortia (Li et al., 2021; McGlynn et al., 2018) and with atomic force microscopy and Raman to study the morphology of cells belonging to the candidate phylum Acetothermia (Hao et al., 2018). An alternative approach, which has not yet been combined with FISH, is to resin-embed natural samples of appropriate water content (soil, sediment) and study the sample's spatial structure and cell activity via a combination of FM, EM, energy-dispersive X-ray spectroscopy (EDS), and microtomography (Hapca et al., 2015; Marlow et al., 2021; Schluter et al., 2019). Analytical techniques such as NanoSIMS have offered an additional dimension of information, providing nanometer resolution maps of the elemental and isotopic composition of cells (Musat et al., 2016). This technique has been used in conjunction with stable isotope probing (SIP) to map the distribution of labeled cellular products within eukaryotic cells and correlate it with FM and TEM (Loussert-Fonta et al., 2020). In addition to SIP-FISH-NanoSIMS, SIP-FISH-Raman has also been used to explore the activity of microbes (Berry et al., 2015; Huang et al., 2007), though to our knowledge Raman has never been correlated with NanoSIMS and SEM. Despite these exciting developments, the use of correlative microscopy in microbial ecology has remained limited.

Here, we illustrate a workflow to correlate FISH, SEM, Raman, and, if desired, NanoSIMS to provide a comprehensive characterization of microorganisms at single cell resolution. This approach enables the study of the taxonomic identity (rRNA-targeted FISH), morphology (SEM), biochemistry (Raman), and metabolic activity (SIP-Raman and/or SIP-NanoSIMS) of cells within microbial communities or phenotypic heterogeneity within a clonal population of cells. This is, to

our knowledge, also the first correlative application of both Raman microspectroscopy and NanoSIMS on the same cells.

We first tested our workflow on an artificially mixed community composed of the bacterium *Escherichia coli* and the archaeon *Methanosarcina acetivorans*. Next, we applied the correlative workflow to multicellular magnetotactic bacteria (MMB; *a.k.a.* multicellular magnetotactic prokaryotes, MMP), which are affiliated with the bacterial phylum Desulfobacterota (previously described as the class Deltaproteobacteria (Waite et al., 2020)) that are typically found in salty-brackish coastal habitats (Keim CN et al., 2006). MMB grow as single-species consortia composed of 15-60 cells that arrange themselves in a spherical or oblong shape around an acellular, central compartment (Abreu et al., 2007; Abreu et al., 2013; Abreu et al., 2006). A hallmark of magnetotactic bacteria, such as MMB, is their ability to biomineralize ferrimagnetic crystals of magnetite ( $\text{Fe}_3\text{O}_4$ ) and/or greigite ( $\text{Fe}_3\text{S}_4$ ) and encapsulate them in lipid vesicles called magnetosomes (Faivre & Schuler, 2008; Greening & Lithgow, 2020; Uebe & Schuler, 2016). These organelles allow magnetotactic bacteria to orient themselves in Earth's magnetic field, a phenomenon termed magnetotaxis, which can be exploited to magnetically enrich them from environmental samples. This is particularly important as MMB typically are rare community members and have proven recalcitrant to cultivation.

The MMB used in this study are found in the Little Sippewissett salt marsh (LSSM), a brackish marsh located in the state of Massachusetts (USA) (Shapiro et al., 2011; Simmons & Edwards, 2007) that for decades has been used as a model system for microbial ecology. Although several studies on the microbiology of LSSM employed powerful visualization techniques, including FM, SEM, and NanoSIMS, none of these studies applied a correlative microscopic

workflow and none applied it to MMB (Bowen et al., 2012; Larsen et al., 2015; Mackey et al., 2017; Marlow et al., 2021; Salman et al., 2015; Shapiro et al., 2011; Simmons & Edwards, 2007; Wilbanks et al., 2014; Wilbanks et al., 2017). By applying our correlative workflow to the MMB found in LSSM, we were able to study the morphology and relative metabolic activity of three MMB populations that coexist in LSSM. Separately, we applied backscatter scanning electron microscopy (BSE-SEM) and EDS to image the magnetosomes of the MMB. Together with Raman and NanoSIMS these techniques were used to confirm the localization of iron (Fe) and sulfur (S) in the magnetosomes, suggesting that three of the five MMB populations found in LSSM use greigite as the ferrimagnetic mineral in their magnetosomes.

## 2. Materials and Methods

### 2.1 Preparation and Stable Isotope Probing of an Artificial Community

A mock community was prepared by mixing cultures of *Escherichia coli* K12 (DSM498) and *Methanosarcina acetivorans* C2A (DSM2834) that had been grown in either the presence or absence of deuterated water (D<sub>2</sub>O). *E. coli* was grown aerobically with agitation (200 rpm) at 37 °C for 4 hours from an OD600 of 0.04 to an OD600 of 0.2 in either unamended M9 medium or medium that had been amended to a final concentration of 30% D<sub>2</sub>O using D<sub>2</sub>O (99.9%-D; Cambridge Isotope Laboratories). *M. acetivorans* cultures were grown anaerobically without agitation for 24 hours in DSMZ Medium 141c, either without D<sub>2</sub>O or amended to a final concentration of 30% D<sub>2</sub>O. At the end of the incubation, 1 mL of each culture was chemically fixed by adding paraformaldehyde (PFA; Electron Microscopy Science; EM grade) to a final concentration of 2% and incubating the cell suspension for 60 minutes at room temperature.

Afterwards, cells were washed twice with 1x phosphate buffered saline (PBS; pH 7.4) by centrifugation at 16,000 g for 5 minutes, after which their supernatants were removed, and the cell pellets were resuspended in 1 mL of 1x PBS. A mock community was then made by mixing approximately equal number of cells from each suspension, resulting in a mixture of unlabeled and deuterium-labeled *E. coli* and *M. acetivorans* cells. Cells were stored at 4 °C in 1x PBS.

## 2.2 Collection and Stable Isotope Probing of Environmental Sample

Approximately 1 L of sediment slurry (7:3 sediment:water) was collected from a tidal pool in LSSM (41.5758762, -70.6393191) in Falmouth, MA (USA) during low tide on August 6th, 2021. In addition, 1 L of overlying marsh water was collected and filter sterilized using a 0.22 µm Millipore (Burlington, MA) Isopore PC filter for later preparation of SIP incubations. Within one day, samples were shipped on ice to Montana State University, Bozeman, MT (USA), where the sediment slurry was transferred to a 1 L glass beaker and stored in the dark for two days at ambient laboratory temperature (~22°C). MMB were enriched from the sediment by placing the South end of a magnetic stir bar against the exterior of the glass beaker just above the sediment layer, agitating the sediment by stirring, and then allowing the sediment to settle for 60 minutes. 200 µL of the water surrounding the accumulated magnetotactic bacteria was then removed with a pipette. The magnetic enrichment was repeated two additional times and all sampled liquids containing MMB were pooled into a single 1.5 mL tube containing 1 mL of 0.22 µM filtered marsh water. The sample was stored at room temperature for approximately 30 min before starting incubations with D<sub>2</sub>O. To incorporate D<sub>2</sub>O into the SIP incubations without changing the natural ionic composition of the sample, 200 mL of sterile-filtered marsh water were boiled until the volume was reduced to 100 mL, cooled to room temperature, and 100 mL of D<sub>2</sub>O was added for a final concentration of

50% D<sub>2</sub>O. The solution was purged with N<sub>2</sub> for ten minutes to make it anoxic. To achieve a higher concentration of our target population in the sediment, MMB recovered by magnetic enrichment were inoculated into sealed serum vials containing 10 mL of 50% D<sub>2</sub>O salt marsh water. A live control sample was prepared by inoculating 100 µL of magnetically enriched MMBs into sealed serum vials with sterile-filtered marsh water without D<sub>2</sub>O. Headspace (~15 mL) was replaced with N<sub>2</sub> and samples were incubated for 24 hours at room temperature without agitation in the dark. After incubation, the serum vials were opened, and their contents emptied into 15 mL Corning Falcon tubes (Corning, NY). Magnetotactic bacteria were magnetically enriched from the 50% D<sub>2</sub>O salt marsh water and subsequently magnetically enriched two more times (10 minutes each) in 0.22 µm filtered marsh water before the samples were chemically fixed with 4% PFA for 60 minutes at room temperature. The samples were then centrifuged for 5 minutes at 16,000 g, after which the supernatant was removed, and the cell pellets resuspended in 50 µL 1×PBS and stored at 4 °C.

### 2.3 Slide Preparation

To successfully correlate different analytical methods, an appropriate surface substrate with minimal Raman background was needed. We used mirrored stainless steel due to its desired properties as a Raman substrate (Lewis et al., 2017), its low cost, and its compatibility with both SEM and NanoSIMS. Circular coupons of mirror-finished 304 stainless steel (25 mm diameter, 0.6 mm thickness) were purchased from Stainless Supply (Monroe, NC). The coupons were cleaned by washing with a 1% solution of Tergazyme (Alconox, New York, NY) and rinsed with Milli-Q water, followed by sequential one-minute washes in acetone and 200 proof ethanol. Finally, the coupons were dried under compressed air and stored at room temperature. To maintain

correct orientation of the samples, asymmetric boxes were etched into the mirrored surface of each coupon using a razor blade. 1  $\mu\text{L}$  of each sample was spotted on the slide and air-dried at 46 °C for 1 minute, after which slides were washed by dipping them into ice-cold Milli-Q water to remove trace buffer components and air dried using compressed air. No further preparation was needed for Raman or SEM analysis.

#### 2.4 Confocal Raman Microspectroscopy and Spectral Processing

Raman spectra of individual cells in the artificial community or MMB enrichments were acquired using a LabRAM HR Evolution Confocal Raman microscope (Horiba Jobin-Yvon) equipped with a 532 nm laser and 300 grooves/mm diffraction grating. Spectra of cells in the mock community and the MMB enrichments were acquired using a 100x dry objective (NA = 0.9) in the range of 200-3,200  $\text{cm}^{-1}$ , with 2-4 acquisitions of 10 seconds each, and a laser power of 4.5 mW. Spectra were processed using LabSpec version 6.5.1.24 (Horiba). The spectra were preprocessed with a Savitsky-Golay smoothing algorithm, baselined, and finally normalized to the maximum intensity within the 2,800-3,100  $\text{cm}^{-1}$  region. To analyze the degree of deuterium substitution in C-H bonds (%C-D, *i.e.*  $(\text{C-D}_{\text{area}}/(\text{C-D}_{\text{area}}+\text{C-H}_{\text{area}}))*100$ ), the bands assigned to C-D (2,040–2,300  $\text{cm}^{-1}$ ) and C-H (2,800–3,100  $\text{cm}^{-1}$ ) were calculated using the integration of the specified regions (Berry et al., 2015). Greigite ( $\text{Fe}_3\text{S}_4$ ) was identified by its characteristic peak at 350  $\text{cm}^{-1}$  (Eder et al., 2014). Neither magnetite ( $\text{Fe}_3\text{O}_4$ ; 303, 535, and 665  $\text{cm}^{-1}$  (Eder et al., 2014)), nor its laser-induced oxidative product, hematite ( $\text{Fe}_2\text{O}_3$ ; 225, 245, 291, 411, and 671  $\text{cm}^{-1}$  (Eder et al., 2014)), were observed.

## 2.5 Scanning Electron Microscopy

To acquire SEM images of the mock community and MMB enrichments, a Zeiss (Jena, Germany) SUPRA 55VP field emission scanning electron microscope (FE-SEM) was operated at 1 kV under a 0.2-0.3 mPa vacuum with a working distance of 5 mm at the Imaging and Chemical Analysis Laboratory (ICAL) of Montana State University (Bozeman, MT). No conductivity coating was applied prior to SEM analysis due to the operation of the microscope at 1 keV.

## 2.6 Backscatter Electron Microscopy and Energy Dispersive X-Ray Spectroscopy

To image magnetosome minerals within MMB, backscatter electron microscopy (BSE) and energy-dispersive X-ray spectroscopy (EDS) were used. The ICAL Zeiss SUPRA 55VP FE-SEM was operated at 10 kV with a working distance of 7.5 mm and an aperture of 30  $\mu\text{m}$ . For EDS, an accelerating voltage of 10 kV was used under high current and the aperture set to 60  $\mu\text{m}$ . EDS data was collected using an Oxford Instruments (Abingdon, UK) AZtec detector with a pixel resolution of 2,048 x 2,048 and a pixel dwell time of 100  $\mu\text{s}$ . Qualitative elemental abundances of C, N, O, Si, P, S, Ca, Cr, Mn, Fe, and Ni were acquired, and data were processed using the AZtecLive software (Oxford Instruments, Abingdon, UK). Elemental maps of C and S were used to identify the location and orientation of the magnetosomes within the MMB. Iron was not used to identify the magnetosomes due to the overwhelming iron signal from the stainless steel coupon.

## 2.7 Fluorescence *in situ* Hybridization

Double-labeled oligonucleotide probes for FISH (DOPE-FISH) (Stoecker et al., 2010) were purchased from Integrated DNA Technologies (Coralville, IA) to visualize different taxa by FM. Cells were dehydrated using an increasing ethanol series (1 min in each 50, 80, and 96%

ethanol) and 16S rRNA-targeted FISH was carried out directly on the stainless steel coupon following established protocols (Daims et al., 2004). Samples were hybridized using either FAM-, Cy3-, or Cy5-labeled DOPE-FISH probes for 2 h (artificial community) or 3 h (MMB) in a humid chamber at 46 °C at a final probe concentration of 2.5 ng  $\mu\text{l}^{-1}$ . Probe mix EUB338 I-III and ARC915, targeting most bacteria and archaea respectively, were used at 35% formamide (Daims et al., 1999; Stahl & Amann, 1991).

Three newly designed DOPE-FISH probes targeting the 1,032-1,048 nt region of the 16S rRNA (*E. coli* equivalent) were applied to the MMB enrichments using previously published 16S rRNA gene clone sequences (Behrens et al., 2003; Simmons & Edwards, 2007) as well as currently unpublished metagenomic 16S rRNA gene sequences (Schaible *et al.*, unpublished). These probes target three populations of MMB in LSSM, Group 1 (G1MMB1032; FAM-5'-CCTGTCATCGGGCTCCCC-3'-FAM;  $T_m = 60.8$  °C), Group 3 (G3MMB1032; Cy3-5'-CCTGTCTTTGGGCTCCCC-3'-Cy3;  $T_m = 58.4$  °C), and Group 4 (G4MMB1032; Cy5-5'-CCTGTCTTCAGGCTCCCC-3'-Cy5;  $T_m = 57.8$  °C) and were used at 50% formamide. Hybridizations were performed using an equimolar mixture of the three probes and two competitor probes targeting the same region of the 16S rRNA to increase the stringency of the hybridization, cG2MMB1032 (5'-CCTGTCATCGGGTTCCCC-3';  $T_m = 58.1$  °C) and cG5MMB1032 (5'-CTTGTCTTCAGGCTCCTC-3';  $T_m = 52.3$  °C). Because MMB groups 2 and 5 were of low abundance at the time of sampling (<1% of all MMB), these populations were not targeted in the workflow. Hybridizations with probe NonEUB338-I (FAM-5'-ACTCCTACGGGAGGCAGC-3'-FAM) were used as negative controls (Wallner et al., 1993).

## 2.8 Nano-Scale Secondary Ion Mass Spectrometry

Prior to NanoSIMS data acquisition, sample regions of interest (ROIs,  $\sim 150 \times 150 \mu\text{m}$ ) were marked on the stainless steel surface using a Leica LMD6 Laser Microdissection System (Wetzlar, Germany). To spatially map the elemental composition and the relative isotopic abundances of hydrogen of our mock community and MMB enrichments, ion images were acquired using the NanoSIMS 50L (Cameca) at the Environmental Molecular Sciences Laboratory at the Pacific Northwest National Laboratory. All NanoSIMS images were acquired using a 16 keV  $\text{Cs}^+$  primary ion beam at  $512 \times 512$ -pixel resolution with a dwell time of  $13.5 \text{ ms px}^{-1}$ . Analysis areas were pre-sputtered with  $\geq 10^{16}$  ions  $\text{cm}^{-2}$  prior to analysis.  $\text{D}^-$  and  $\text{H}^-$  secondary ions were accelerated to 8 keV and counted simultaneously using electron multipliers (EMs). The vacuum gauge pressure in the analytical chamber during all analyses was consistently less than  $3 \times 10^{-10}$  mbar. Other analytical conditions included a 200  $\mu\text{m}$  D1 aperture, 30  $\mu\text{m}$  entrance slit, 350  $\mu\text{m}$  aperture slit, and 100  $\mu\text{m}$  exit slits. Secondary tuning was adjusted, and  $\text{D}^-$  and  $\text{H}^-$  peaks were monitored between analyses for drift. The OpenMIMS plugin for ImageJ was used to access and correct images pixel by pixel for dead time (44ns) and QSA ( $\beta=0.5$ ). Data from ROI were exported to a custom spreadsheet for data reduction. Semi-quantitative D/H analyses were calibrated against an in-house yeast reference material of unknown, but natural abundance  $\delta\text{D}$  during the same analytical session using similar conditions to those used to analyze the bacterial culture samples. The yeast reference material had been stored in the NanoSIMS under high vacuum for several months prior to the analyses reported here. Hydrogen isotope analyses were acquired using a 4-pA primary beam yielding a primary beam size of about 150 nm. Detectors collecting  $\text{H}^-$  and  $\text{D}^-$  ions were situated near the center of the magnet radius to improve simultaneous secondary centering characteristics. Hydrogen isotopes are reported as  $\delta\text{D}$  relative to the yeast standard and

(uncalibrated) apparent atom %. To explore colocation of Fe and S atoms in the MMBs, some images were acquired by counting  $^{32}\text{S}^-$  and  $^{32}\text{S}^{56}\text{Fe}^-$  ions simultaneously using a 2-pA primary beam.

### 3. Results and Discussion

#### 3.1 General Considerations for Correlative Microscopy

Correlative imaging enables identification and characterization of diverse microbial taxa on a single cell level, allowing for a complimentary suite of correlated data to be collected. Prior to sample analyses, the abundance, morphology, and fixation of the target cells need to be considered to ensure that the desired population of interest is studied with its morphology and isotope ratios intact. The ratio of fixatives may need to be optimized on a sample-specific basis and should be tested prior to the correlative workflow. For example, McGlynn *et al.* 2018 applied several fixation protocols optimized for specific visualization goals, using a mix of PFA and glutaraldehyde at varying concentrations (McGlynn *et al.*, 2018). Here, cell fixation was performed using 2% PFA (*E. coli* and *M. acetivorans*) and 4% PFA (MMB) because these conditions were found to maintain cellular structure without autofluorescence from the fixative, which can be an issue with glutaraldehyde (McGlynn *et al.*, 2018).

Depending on the relative abundance and morphology of the target population, our correlative workflow can be employed either FISH-first or SEM-first (Fig. 1). Microbes with common morphologies, such as coccoid, rod, or filament shapes, or those present at low relative abundances, will likely need to be identified using FISH before other analyses are employed to ensure the correct phylotype or morphotype is studied (Li *et al.*, 2017). Cells with distinct morphologies, or cells that are present at high relative abundance, can be imaged by SEM first,

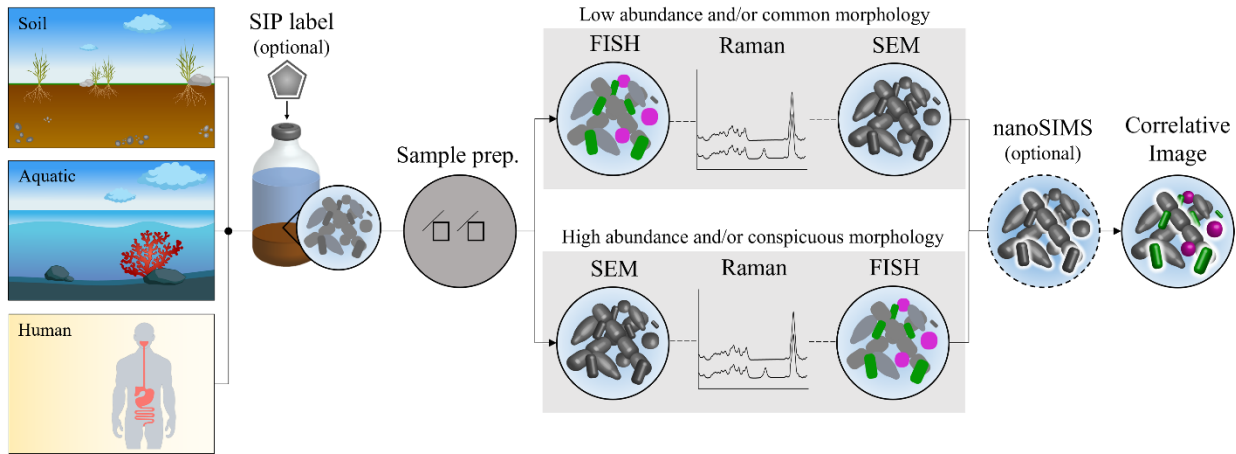


Fig. 1. Correlative microscopy workflow. Environmental samples can be taken and incubated in the presence of an isotope-containing substrate to label active community members or study substrate assimilation. Next, the biomass is chemically fixed and placed on a stainless steel coupon. SEM is used to study cell morphology. Raman is used to determine the biochemical makeup as well as substrate assimilation of individual cells. rRNA-targeted FISH reveals the taxonomic identity of cells. As a final step, NanoSIMS can be used to study the elemental and isotopic composition of the sample at higher spatial resolution and sensitivity than possible by Raman.

followed by Raman and FISH. Alternatively, the target organism can be physically enriched prior to downstream analyses. For example, here we magnetically enriched a lowly abundant population of multicellular magnetotactic bacteria (0.003%-0.15% relative abundance in LSSM according to 16S rRNA gene amplicon data ((Marlow et al., 2021) and Schaible and Hatzenpichler unpublished). An alternative is to separate FISH-labeled cells via fluorescence-activated cell sorting, as was previously shown (Grieb et al., 2020; Zimmermann et al., 2015). An SEM-first workflow is advantageous when cells or cell aggregates, such as the MMB studied here, are susceptible to changes in morphology triggered by the repeated dehydration-rehydration cycles used in FISH protocols (Appendix A, Fig. S1).

Sample treatment prior to NanoSIMS has been shown to decrease the isotope enrichment, resulting in underestimates of activity (Meyer et al., 2021). For this reason, it is important to limit

treatments to the sample during preparation and reduce unnecessary exposure to or inclusion of exogenous material during these treatments that could lead to dilution of the isotopic label (Meyer et al., 2021). Furthermore, the use of mono-FISH instead of catalyzed reporter deposition fluorescence *in situ* hybridization (CARD-FISH) has been recommended to limit dilution of the isotope signal due to introduction of the horseradish peroxidase conjugated probes and/or excessive tyramide deposition (Meyer et al., 2021; Musat et al., 2014). While the use of mono-FISH has been recommended, poor fluorescent signal due to, for example, low ribosomal content in slow-growing cells, may necessitate the use of CARD-FISH (Amann & Fuchs, 2008). In this study, we used DOPE-FISH (two fluorophores) instead of mono-labeled FISH probes to increase fluorescence yield (Stoecker et al., 2010).

### 3.2 FISH-First Correlative Workflow Using an Artificial Microbial Community

To benchmark our FISH-first correlative workflow, we prepared an artificial community by mixing *E. coli* and *M. acetivorans*, both representing common morphotypes (rods and cocci, respectively). Cultures were grown in the presence or absence of deuterated water (D<sub>2</sub>O) as a general marker of anabolic activity (Berry et al., 2015). PFA-fixed biomass was immobilized on a stainless steel coupon that had been etched with a razor blade to allow tracking of the same area throughout all analyses (Appendix A, Fig. S2). We then applied 16S rRNA-targeted DOPE-FISH (Stoecker et al., 2010) to identify bacterial and archaeal cells and choose specific regions of interest (ROIs) for downstream analysis (Fig. 2a). Following DOPE-FISH, Raman was used to study the chemical composition of cells in the same ROIs (Fig. 2b, Appendix A, Table S1). Prior to

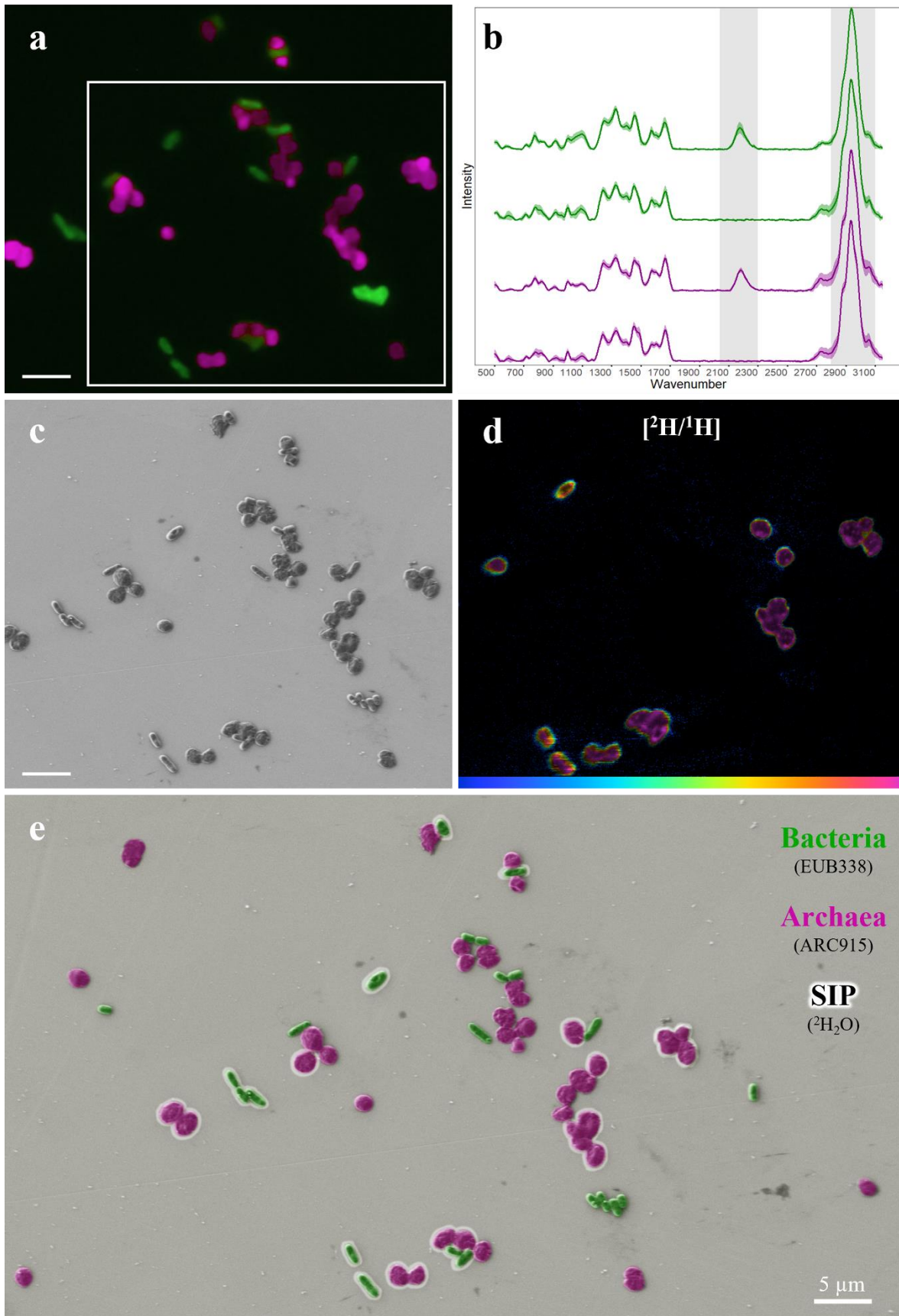


Fig. 2. Correlative imaging of an artificial community. (a) FISH targeted *E. coli* (EUB388mix, green) and *M. acetivorans* (ARC915, magenta). (b) Single cell Raman identifies cells that had taken up deuterium from D<sub>2</sub>O (detected by the characteristic peak shifts of C-H at 2,800-3,100 cm<sup>-1</sup> to C-D at 2,040-2,300 cm<sup>-1</sup>, highlighted in gray). Each spectrum shown is an average of the cells shown in panel a with the shaded regions showing the standard deviation for each data set. The green spectra correspond to D<sub>2</sub>O positive (top; n = 4) and negative (bottom; n = 10) *E. coli* cells. The magenta spectra correspond to D<sub>2</sub>O positive (top; n = 14) and negative (bottom; n = 16) *M. acetivorans* cells. (c) Cell morphology revealed by SEM. (d) NanoSIMS hue-saturation-intensity image of <sup>2</sup>H/<sup>1</sup>H ratio confirms deuterium uptake at higher spatial resolution and sensitivity than Raman. The area analyzed using NanoSIMS is outlined in panel a. The scale is 0 – 2.0 atom %. (e) Composite false color image presenting all data. Cells outlined by a white halo were deuterium-labeled as determined by both Raman and NanoSIMS as both methods yielded consistent results. Cells without a halo were considered unlabeled. All scale bars equal 5 μm.

acquisition of Raman spectra, cells were photobleached for 1-2 minutes to remove background from the FISH dyes (Lee et al., 2021). Alternatively, dyes such as FAM/FITC or Cy5, that are not excited by the 532 nm Raman laser, could be used (Huang et al., 2007).

The incorporation of deuterium into biomass was calculated using the integration of the C-D (2,040-2300 cm<sup>-1</sup>) and C-H (2,800-3,100 cm<sup>-1</sup>) regions of the spectra (Fig. 2b; (Berry et al., 2015)). This showed that labeled *E. coli* and *M. acetivorans* had an average of 11.0% (± 2.5) and 9.3% (± 1.4) C-D (*i.e.*, (CD/(CD+CH))\*100), respectively, and that both unlabeled *E. coli* and *M. acetivorans* had an average of 0.5% (± 0.3 and 0.4, respectively) C-D (Appendix A, Fig. S3, Table S1). Next, field emission SEM (FE-SEM) was performed to reveal cell morphology (Fig. 2c). After FE-SEM images were taken, specific ROIs were traced using a laser dissection microscope to assist in finding imaged areas during NanoSIMS analyses (Appendix A, Fig. S2c). This was necessary because SIMS instruments, such as the Cameca NanoSIMS 50L employed in this study, only offer a low magnification objective that makes finding the targets of choice difficult. Finally, the elemental and isotopic composition of the sample was imaged using NanoSIMS, which provided a map of the metabolic heterogeneity of the mixed population at single cell resolution

(Fig. 2d, Appendix A, Table S1). Analysis of the NanoSIMS data revealed that the labeled *E. coli* and *M. acetivorans* had an average deuterium content of 5.2% ( $\pm 1.2$ ) and 5.3% ( $\pm 1.1$ ), respectively, and that both unlabeled *E. coli* and *M. acetivorans* showed no deuterium incorporation (Appendix A, Fig. S3, Table S1).

While Raman can provide information on cellular isotope uptake, its sensitivity is 30-100x lower than NanoSIMS, depending on the isotope (Hatzenpichler, 2020; Wang et al., 2016). Furthermore, the expression of %C-D (relative change from C-H to C-D stretch in lipids and proteins) cannot be interpreted as %D content of the entire biomass. In contrast, NanoSIMS is a destructive but fully quantitative technique capable of measuring the elemental and isotopic composition of a cell at atomic resolution. However, NanoSIMS does not provide reliable information about the molecular composition of a sample, which is, in turn, achieved by Raman (Hatzenpichler, 2020; Lee et al., 2021). These fundamentally different working mechanisms are the main reason for the discrepancy between the H/D ratios determined via Raman (11 %C-D for *E. coli*) vs. NanoSIMS (5.2 atom % D). Depending on the exact research question, extent of metabolic activity, and available instruments, researchers need to decide whether the use of NanoSIMS and/or Raman is warranted (Eichorst et al., 2015). Eventually, the information gained by these different analyses (*i.e.*, taxonomy, morphology, and metabolic activity) can be projected into a single image that correlates each analysis (Fig. 2E). Both Raman and NanoSIMS data showed significantly different isotope enrichment between positively and negatively labeled cells (p-value =  $3.87 \times 10^{-16}$  and  $4.23 \times 10^{-12}$ , respectively, t-test; Appendix A, Fig. S3, Table S1). Our analysis of the mock community provided a successful proof of concept.

The application of Raman and NanoSIMS on the same cells revealed a discrepancy between the two methods in detecting deuterium in the mock community (Appendix A, Fig. S4). The only other study, to our knowledge, that applied both Raman and NanoSIMS reported a similar trend of deuterium incorporation with respect to the deuterated water percent in the growth medium (Berry et al., 2015); however, their analysis was not performed on the same cells (*i.e.*, uncorrelated data), which limits comparability between their and our datasets. Nevertheless, our newly developed workflow has highlighted a need for further study on the quantitative measure of isotope incorporation via Raman and NanoSIMS and to what extent results obtained via these two methods can be compared.

### 3.3 SEM-First Correlative Workflow Using Environmental MMB

We established an SEM-first correlative workflow to interrogate MMB enriched from LSSM. Correlative fluorescence microscopy (FM) and SEM have previously been performed on both single celled magnetotactic bacteria (Li et al., 2021; Li et al., 2017; Woehl et al., 2014) as well as MMB from the Mediterranean Sea (Qian et al., 2020), but to our knowledge the combined techniques have not been applied to MMB from LSSM. In addition, we show the first application of Raman and NanoSIMS to MMB. Based on 16S rRNA gene studies, the sample site at LSSM contains several distinct populations of MMB that have not been studied on a population-specific morphological and physiological level (Marlow et al., 2021; Shapiro et al., 2011; Simmons & Edwards, 2007). To identify whether these populations differ in morphology and relative metabolic activity, we applied our new correlative microscopy workflow to MMB. MMB magnetically enriched from LSSM tidal pool sediment were incubated with 50% D<sub>2</sub>O to determine if MMB populations differ in their anabolic activity.

Because MMB exhibit a unique multicellular morphology, they can be easily distinguished from other morphotypes by light microscopy or SEM without the need for prior identification via FISH. This was of particular importance as MMB from LSSM suffer detrimental effects to their cellular morphology when subjected to FISH (Appendix A, Fig. S1). For this reason, FE-SEM was performed first on MMB, and specific ROIs identified (Fig. 3a). Raman was subsequently used to map the biochemical makeup of each MMB identified by FE-SEM. Raman spectra of MMB contained characteristic peaks for greigite ( $\text{Fe}_3\text{S}_4$ ;  $350\text{ cm}^{-1}$ ; (Eder et al., 2014)), indicating it is the mineral used in their magnetosomes (Fig. 4d). This is consistent with the absence of characteristic peaks for magnetite and its laser-induced oxidative product, hematite, in the Raman spectra ( $225$ ,  $245$ ,  $291$ ,  $411$ , and  $671\text{ cm}^{-1}$  (Eder et al., 2014)). As done with the mock community, we attempted to identify the C-D peak in the silent region of the spectra ( $2,040$ - $2,300\text{ cm}^{-1}$ ). Unexpectedly, we were unable to observe a C-D peak in any of the MMB spectra (Fig. 3b, Appendix A, Fig. S3 and Table S1). At the time, we attributed this to a low labeling rate that was below the detection limit of Raman; this hypothesis was later confirmed by NanoSIMS (discussed below). Next, 16S rRNA targeted DOPE-FISH was used to identify three distinct MMB populations in LSSM (Fig. 3b) (Simmons & Edwards, 2007). As was done with the artificial community, ROIs were traced using a laser dissection microscope and the elemental and isotopic composition of the sample imaged using NanoSIMS (Fig 3d, Appendix A Table S2).

While deuterium incorporation from  $\text{D}_2\text{O}$  could not be detected via Raman, NanoSIMS showed that all MMB analyzed ( $n = 23$ ) exhibited low levels of deuterium incorporation ( $0.11 - 0.78\%$ ; Appendix A, Table S1), significantly higher than the negative control ( $0.015 - 0.022\%$ ;

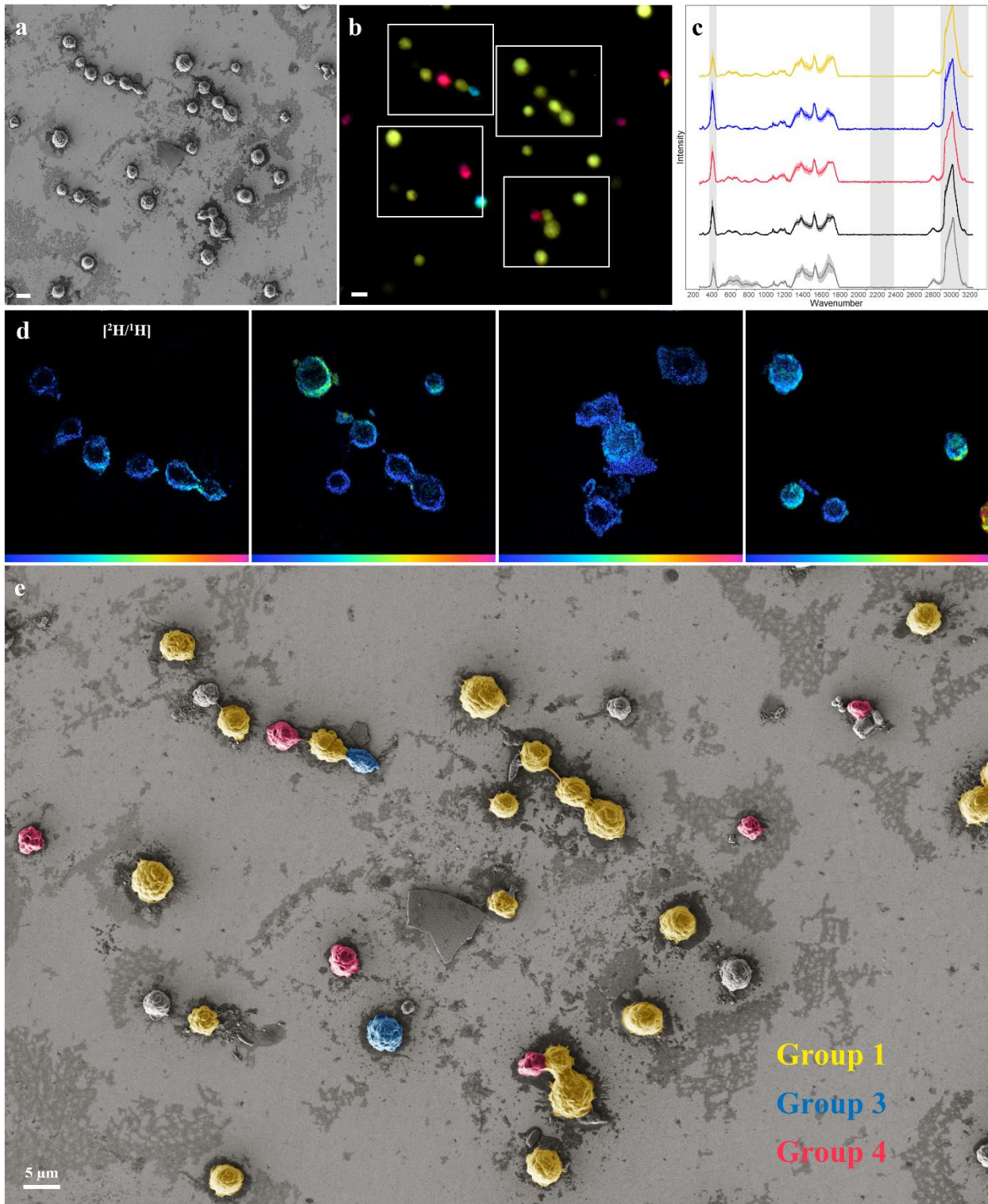


Fig. 3. Correlative microscopy analysis of MMB. (a) SEM image of magnetically enriched MMB. (b) FM identifies three MMB subpopulations using FISH probes specific for Group 1 (yellow), Group 3 (teal), and Group 4 (red). Unlabeled MMB likely belong to two populations not targeted with FISH. (c) Raman spectra of MMB separated by the respective FISH label and control. The characteristic regions of C-H at 2,800-3,100  $\text{cm}^{-1}$ , C-D at 2,040-2,300  $\text{cm}^{-1}$ , and greigite at 350  $\text{cm}^{-1}$  are highlighted in gray. Each spectrum shown is an average with the shaded regions showing the standard deviation for each data set. Raman spectra were collected from several ROIs besides the one shown in this figure. The yellow spectra show Group 1 ( $n = 38$ ), the blue spectra show Group 3 ( $n = 2$ ), and the magenta spectra show Group 4 ( $n = 3$ ) MMB. The dark gray spectra are those of MMB that were not labeled by FISH ( $n = 10$ ) and the light gray spectra show MMB from the negative control (i.e., no  $\text{D}_2\text{O}$  addition;  $n = 27$ ). (d) NanoSIMS hue-saturation-intensity images showing the 2H/1H ratios present in the ROIs outline in white boxes in b (scale is 0 to 0.55 atom %). (e) Composite false color image presenting data. MMB that are not false-colored were not labeled by one of the three FISH-probes. All MMBs were labelled with deuterium. All scale bars equal 5  $\mu\text{m}$ .

$p\text{-value} = 3.37 \times 10^{-19}$ ; Appendix A Fig. S3). While such values are indicative for deuterium incorporation, they are well below the detection limit of Raman (0.2% for D; (Hatzenpichler, 2020)). Deuterium uptake from  $\text{D}_2\text{O}$  has been shown to be affected by the organic carbon source used by heterotrophic cells for growth (Berry et al., 2015; Matanfack et al., 2020). This makes it possible that the MMB studied here used organic carbon sources that contributed to the dilution of deuterium in cells. Nevertheless, such a low level of deuterium-incorporation from heavy water is surprising given that all MMB must have been metabolically active at the beginning and end of the SIP-incubation; otherwise, they would not have been able to swim to the magnetic stir bar used to collect MMB (which is an active process, they are not merely passively “pulled” to the magnet). As discussed above, it is possible that the fixation and FISH protocols used here resulted in an additional decrease in the observed isotope enrichment (Meyer et al., 2021). Furthermore, it is possible that the level of deuterium in MMB was decreased during magnetic enrichments. If magnetotaxis is energetically expensive, enrichments of MMB in water lacking deuterium may

have increased the D/H turnover and led to an overall decrease of deuterium in MMB cells. Future experiments will have to reconcile this conundrum.

The three MMB populations exhibited similar morphology when studied via FE-SEM, indicating that different MMB species found in LSSM cannot be distinguished by morphology alone (Fig. 3e), highlighting the importance and power of our correlative microscopy approach. Individual populations of MMB were identified using FISH, which revealed that Group 1 is the most abundant MMB population in our sample (66%,  $n = 64$ ). Group 4 was the second most abundant (7%,  $n = 7$ ), and Group 3 was the third most abundant (4%,  $n = 4$ ). Unlabeled MMB accounted for 23% ( $n = 22$ ) of all MMB and likely belonged to Groups 2 and 5 that were not targeted in this study. Our findings on the relative abundance of different MMB populations are consistent with the results reported by Simmons *et al.*, who studied an unspecified tidal pool in LSSM (Simmons & Edwards, 2007).

#### 3.4 Analysis of MMB Magnetosomes Using BSE-SEM and EDS

Magnetotactic bacteria are relevant to the biogeochemical cycling of iron and sulfur, and the process of controlled biomineralization via magnetosome formation (Amor *et al.*, 2020; Uebe & Schuler, 2016). Historically, BSE and EDS have been used to study the location, shape, and elemental composition of the biogenic minerals within MMB (Farina *et al.*, 1990; Teng *et al.*, 2018; Wenter *et al.*, 2009; Zhang *et al.*, 2014). We applied BSE-SEM at an accelerating voltage of 10 kV, allowing for the electron-dense minerals within the magnetosomes of MMB to be imaged (Fig. 4b). EDS was then used at the same voltage to map elements across the cell, revealing confined areas of sulfur within individual cells (Fig. 4c). This result is consistent with the identification of greigite ( $\text{Fe}_3\text{S}_4$ ) in the Raman spectra of MMB (Fig. 4d) as well as the co-localization of  $^{56}\text{Fe}$  and

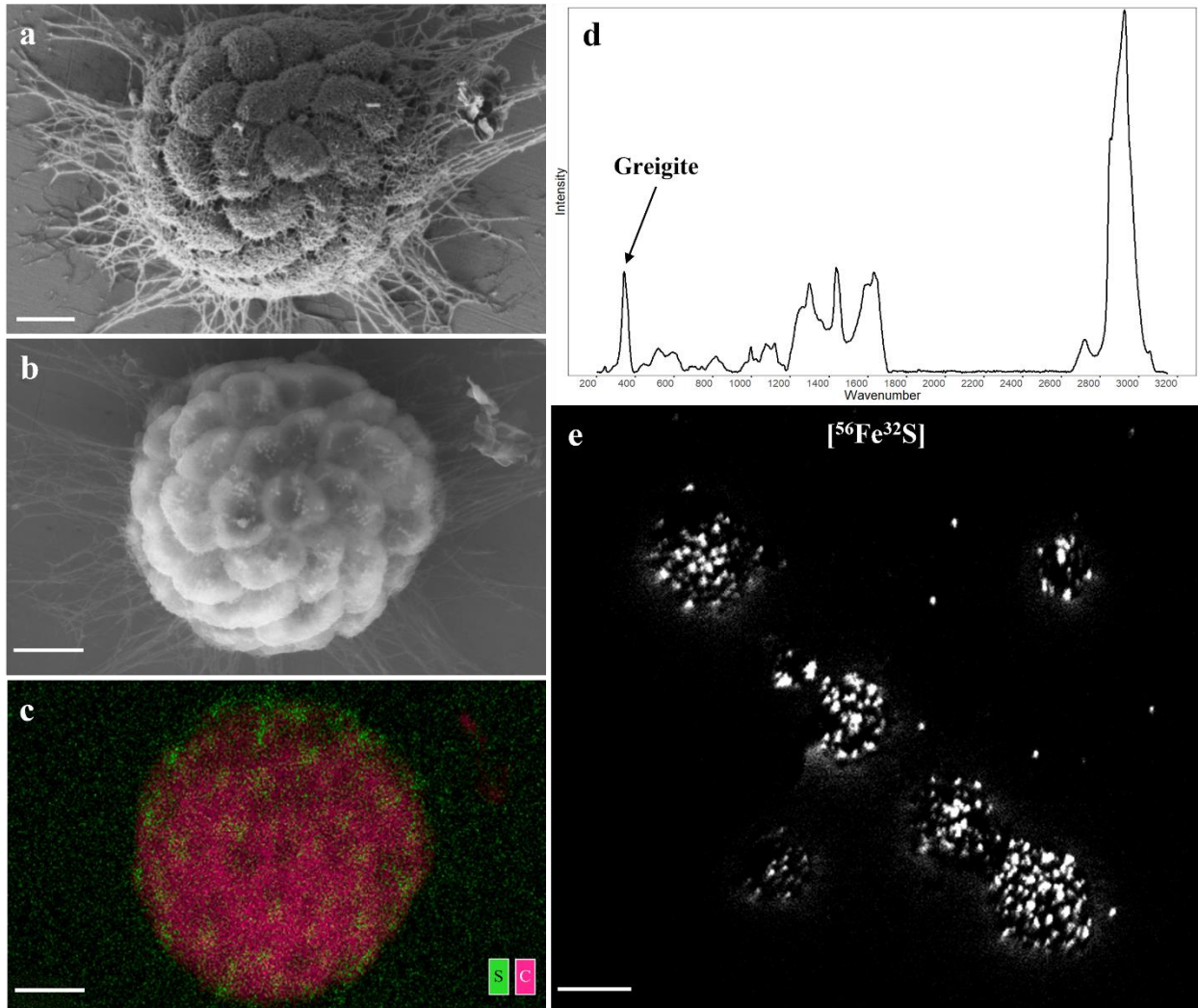


Fig. 4. Imaging magnetosomes within MMB. (a) Low voltage SEM image of a MMB consortium. (b) BSE-SEM image of the same MMB reveals the magnetosomes in each cell seen as small white chains. (c) EDS image showing the localization of sulfur accumulations (green), presumably contained within magnetosome chains composed of greigite ( $\text{Fe}_3\text{S}_4$ ), against cellular carbon (magenta). Fe and O are not shown because the stainless steel surface contains large amounts of Fe and O. (d) Raman spectra of a single MMB showing the characteristic peak for greigite ( $\text{Fe}_3\text{S}_4$ ) at  $350\text{ cm}^{-1}$  that was observed in all MMB analyzed (see Fig. 3c) (Eder et al., 2014). (e) NanoSIMS image showing the mass corresponding to  $^{56}\text{Fe}^{32}\text{S}^-$  of the same MMB shown in the same ROI shown in Fig. 3d., indicating the localization of Fe and S within MMB. Panels a-c scale bars equal to  $1\text{ }\mu\text{m}$ , panel e scale bar is equal to  $5\text{ }\mu\text{m}$ .

$^{32}\text{S}$ , as demonstrated by the detection of  $^{56}\text{Fe}^{32}\text{S}^-$  ions, observed via NanoSIMS (Fig. 4e) (Bourdoiseau et al., 2011; Eder et al., 2014). These findings align with observations that greigite

is used as the ferrimagnetic mineral by MMB in other locations (Farina et al., 1990; Mann et al., 1990; Posfai M. et al., 1998; Wenter et al., 2009).

Both BSE-SEM and EDS were applied outside of the correlative workflow due to the negative effect of high voltage electron beams on cells. MMB that had been analyzed using BSE-SEM and EDS could not be labeled using FISH, and the respective Raman spectra were consistent with carbonized biomass, likely due to the effect of using a high voltage electron beam (not shown). Previous correlative studies have used low dose electron imaging, such as FE-SEM, to avoid irreversible damage to the cell caused by high electron voltages (Woehl et al., 2014).

#### 4. Conclusions

Understanding the metabolic potential and ecological distribution of microbial communities has been greatly aided by various omic techniques, but information on the morphology, physiology, and taxonomy of distinct taxa is lost during these analyses. Here, we provide a single cell level workflow to link the taxonomic identity and morphology of microbes using rRNA-targeted FISH and SEM with their cellular chemistry and metabolic activity using SIP-Raman and/or SIP-NanoSIMS. By applying this workflow, naturally low abundance populations (*e.g.*, MMB) can be taxonomically identified and interrogated in greater detail than current practices allow. Furthermore, having correlated data is desirable for population studies to determine if physiological heterogeneity exists within clonal groups of cells.

In this study, we used D<sub>2</sub>O as a general marker of anabolic activity, but substrates labeled with <sup>13</sup>C, <sup>15</sup>N, <sup>18</sup>O, or <sup>34</sup>S could be incorporated in the workflow. Additionally, future applications and developments of this workflow might include the use of substrate analogue probing (Hatzenpichler, 2020), super resolution microscopy (Betzig et al., 2006; Rust et al., 2006), or

atomic force microscopy (Hao et al., 2018). Because substrate analogue probing labels specific biopolymers, such as proteins (Hatzenpichler et al., 2014), nucleic acids (Smriga et al., 2014), or lipid membranes (Siegrist et al., 2013), its use with traditional FM or super resolution microscopy can inform on overall biosynthetic activity or specific enzymatic function. Furthermore, correlative FISH-TEM approaches adapted from McGlynn *et al.* 2018 (McGlynn et al., 2018) and protocols to thin-section MMB developed by the group of Lins (Abreu et al., 2013; Keim et al., 2004) could provide valuable complementary information of the physiology and ultrastructure of the diverse MMB populations in LSSM.

#### Acknowledgements

This study was funded through NASA FINESST award 80NSSC20K1365 (to G.S. and R.H.), NASA Exobiology award NNX17AK85G (to R.H.) and Gordon and Betty Moore Foundation award 5999 (to R.H.). Montana State University's Confocal Raman microscope was acquired with support by the National Science Foundation (DBI-1726561) and the M.J. Murdock Charitable Trust (SR-2017331). This work was performed in part at the Montana Nanotechnology Facility, an NNCI member supported by NSF grant ECCS-2025391. A portion of this research was performed under the Facilities Integrating Collaborations for User Science (FICUS) program (proposal: 10.46936/fics.proj.2017.49972/6000002) and used resources at the Environmental Molecular Sciences Laboratory (<https://ror.org/04rc0xn13>), which is a DOE Office of Science User Facilities operated under Contract No. DE-AC05-76RL01830 (EMSL). We thank Jeff Marlow, Virginia Edgcomb, and Emil Ruff for help with collection of LSSM sediment samples, and Ashley Cohen and Zackary J. Jay for helpful comments on the manuscript.

References

- Abreu, F., Martins, J. L., Silveira, T. S., Keim, C. N., de Barros, H. G., Filho, F. J., & Lins, U. (2007). 'Candidatus Magnetoglobus multicellularis', a multicellular, magnetotactic prokaryote from a hypersaline environment. *Int J Syst Evol Microbiol*, 57(Pt 6), 1318-1322. <https://doi.org/10.1099/ijs.0.64857-0>
- Abreu, F., Silva, K. T., Leao, P., Guedes, I. A., Keim, C. N., Farina, M., & Lins, U. (2013). Cell adhesion, multicellular morphology, and magnetosome distribution in the multicellular magnetotactic prokaryote Candidatus Magnetoglobus multicellularis. *Microsc Microanal*, 19(3), 535-543. <https://doi.org/10.1017/S1431927613000329>
- Abreu, F., Silva, K. T., Martins, J. L., & Lins, U. (2006). Cell viability in magnetotactic multicellular prokaryotes. *International Microbiology*, 9, 267-272.
- Amann, R., & Fuchs, B. M. (2008). Single-cell identification in microbial communities by improved fluorescence in situ hybridization techniques. *Nat Rev Microbiol*, 6(5), 339-348. <https://doi.org/10.1038/nrmicro1888>
- Amor, M., Tharaud, M., Gelabert, A., & Komeili, A. (2020). Single-cell determination of iron content in magnetotactic bacteria: implications for the iron biogeochemical cycle. *Environ Microbiol*, 22(3), 823-831. <https://doi.org/10.1111/1462-2920.14708>
- Ando, T., Bhamidimarri, S. P., Brending, N., Colin-York, H., Collinson, L., De Jonge, N., De Pablo, P. J., Debroye, E., Eggeling, C., & Franck, C. a. F., M., . (2018). The 2018 correlative microscopy techniques roadmap. *Journal of physics D: Applied physics*, 51.
- Behrens, S., Ruhland, C., Inacio, J., Huber, H., Fonseca, A., Spencer-Martins, I., Fuchs, B. M., & Amann, R. (2003). In situ accessibility of small-subunit rRNA of members of the domains Bacteria, Archaea, and Eucarya to Cy3-labeled oligonucleotide probes. *Appl Environ Microbiol*, 69(3), 1748-1758. <https://doi.org/10.1128/AEM.69.3.1748-1758.2003>
- Berry, D., Mader, E., Lee, T. K., Woebken, D., Wang, Y., Zhu, D., Palatinszky, M., Schintlmeister, A., Schmid, M. C., Hanson, B. T., Shterzer, N., Mizrahi, I., Rauch, I., Decker, T., Bocklitz, T., Popp, J., Gibson, C. M., Fowler, P. W., Huang, W. E., & Wagner, M. (2015). Tracking heavy water (D2O) incorporation for identifying and sorting active microbial cells. *Proc Natl Acad Sci U S A*, 112(2), E194-203. <https://doi.org/10.1073/pnas.1420406112>
- Betzig, E., Patterson, G. H., Sougrat, R., Lindwasser, O. W., Olenych, S., Bonifacino, J. S., Davidson, M. W., Lippincott-Schwartz, J., & Hess, H. F. (2006). Imaging intracellular fluorescent proteins at nanometer resolution. *Science*, 313(5793), 1642-1645. <https://doi.org/10.1126/science.1127344>

- Bourdoiseau, J.-A., Jeannin, M., Rémazeilles, C., Sabot, R., & Refait, P. (2011). The transformation of mackinawite into greigite studied by Raman spectroscopy. *Journal of Raman Spectroscopy*, 42(3), 496-504. <https://doi.org/10.1002/jrs.2729>
- Bowen, J. L., Morrison, H. G., Hobbie, J. E., & Sogin, M. L. (2012). Salt marsh sediment diversity: a test of the variability of the rare biosphere among environmental replicates. *Isme Journal*, 6(11), 2014-2023. <https://doi.org/10.1038/ismej.2012.47>
- Daims, H., Brühl, A., Amann, R., Schleifer, K.-H., & Wagner, M. (1999). The Domain-specific Probe EUB338 is Insufficient for the Detection of all Bacteria: Development and Evaluation of a more Comprehensive Probe Set. *Systematic and Applied Microbiology*, 22(3), 434-444. [https://doi.org/10.1016/s0723-2020\(99\)80053-8](https://doi.org/10.1016/s0723-2020(99)80053-8)
- Daims, H., Stoecker, K., & Wagner, M. (2004). Fluorescence in situ hybridization for the detection of prokaryotes. *Taylor & Francis, Molecular microbial ecology*, 208-228.
- Eder, S. H., Gigler, A. M., Hanzlik, M., & Winklhofer, M. (2014). Sub-micrometer-scale mapping of magnetite crystals and sulfur globules in magnetotactic bacteria using confocal Raman micro-spectrometry. *PLoS One*, 9(9), e107356. <https://doi.org/10.1371/journal.pone.0107356>
- Eichorst, S. A., Strasser, F., Woyke, T., Schintlmeister, A., Wagner, M., & Wobken, D. (2015). Advancements in the application of NanoSIMS and Raman microspectroscopy to investigate the activity of microbial cells in soils. *FEMS Microbiol Ecol*, 91(10). <https://doi.org/10.1093/femsec/fiv106>
- Endesfelder, U. (2015). Advances in Correlative Single-Molecule Localization Microscopy and Electron Microscopy. *NanoBioImaging*, 1(1). <https://doi.org/10.2478/nbi-2014-0002>
- Faivre, D., & Schuler, D. (2008). Magnetotactic bacteria and magnetosomes. *Chem Rev*, 108(11), 4875-4898. <https://doi.org/10.1021/cr078258w>
- Farina, M., Esquivel, D. M. S., & Debarros, H. G. P. L. (1990). Magnetic Iron-Sulfur Crystals from a Magnetotactic Microorganism. *Nature*, 343(6255), 256-258. <https://doi.org/DOI 10.1038/343256a0>
- Greening, C., & Lithgow, T. (2020). Formation and function of bacterial organelles. *Nat Rev Microbiol*, 18(12), 677-689. <https://doi.org/10.1038/s41579-020-0413-0>
- Grieb, A., Bowers, R. M., Oggerin, M., Goudeau, D., Lee, J., Malmstrom, R. R., Woyke, T., & Fuchs, B. M. (2020). A pipeline for targeted metagenomics of environmental bacteria. *Microbiome*, 8(1), 21. <https://doi.org/10.1186/s40168-020-0790-7>
- Hao, L., McIlroy, S. J., Kirkegaard, R. H., Karst, S. M., Fernando, W. E. Y., Aslan, H., Meyer, R. L., Albertsen, M., Nielsen, P. H., & Dueholm, M. S. (2018). Novel prosthecate bacteria

- from the candidate phylum Acetothermia. *ISME J*, 12(9), 2225-2237.  
<https://doi.org/10.1038/s41396-018-0187-9>
- Hapca, S., Baveye, P. C., Wilson, C., Lark, R. M., & Otten, W. (2015). Three-Dimensional Mapping of Soil Chemical Characteristics at Micrometric Scale by Combining 2D SEM-EDX Data and 3D X-Ray CT Images. *PLoS One*, 10(9), e0137205.  
<https://doi.org/10.1371/journal.pone.0137205>
- Hatzenpichler, R., Krukenberg, V., Spietz, R.L., Jay, Z.J. (2020). Next-generation physiology approaches to study microbial community function at the single cell level. *Nat. Rev. Microbiol.*
- Hatzenpichler, R., Scheller, S., Tavormina, P. L., Babin, B. M., Tirrell, D. A., & Orphan, V. J. (2014). In situ visualization of newly synthesized proteins in environmental microbes using amino acid tagging and click chemistry. *Environ Microbiol*, 16(8), 2568-2590.  
<https://doi.org/10.1111/1462-2920.12436>
- Huang, W. E., Stoecker, K., Griffiths, R., Newbold, L., Daims, H., Whiteley, A. S., & Wagner, M. (2007). Raman-FISH: combining stable-isotope Raman spectroscopy and fluorescence in situ hybridization for the single cell analysis of identity and function. *Environ Microbiol*, 9(8), 1878-1889. <https://doi.org/10.1111/j.1462-2920.2007.01352.x>
- Joosten, B., Willemse, M., Fransen, J., Cambi, A., & van den Dries, K. (2018). Super-Resolution Correlative Light and Electron Microscopy (SR-CLEM) Reveals Novel Ultrastructural Insights Into Dendritic Cell Podosomes. *Frontiers in Immunology*, 9.  
<https://doi.org/ARTN 1908>  
 10.3389/fimmu.2018.01908
- Keim CN, Martins JL, de Barros HL, Lins U, & M., F. (2006). Structure, behavior, ecology and diversity of multicellular magnetotactic prokaryotes. *Magnetoreception and magnetosomes in bacteria*(Springer, Berlin, Heidelberg), 103-132.
- Keim, C. N., Abreu, F., Lins, U., Lins de Barros, H., & Farina, M. (2004). Cell organization and ultrastructure of a magnetotactic multicellular organism. *J Struct Biol*, 145(3), 254-262.  
<https://doi.org/10.1016/j.jsb.2003.10.022>
- Lange, F., Agui-Gonzalez, P., Riedel, D., Phan, N. T. N., Jakobs, S., & Rizzoli, S. O. (2021). Correlative fluorescence microscopy, transmission electron microscopy and secondary ion mass spectrometry (CLEM-SIMS) for cellular imaging. *PLoS One*, 16(5).  
<https://doi.org/ARTN e0240768>  
 10.1371/journal.pone.0240768
- Larsen, S., Nielsen, L. P., & Schramm, A. (2015). Cable bacteria associated with long-distance electron transport in New England salt marsh sediment. *Environmental Microbiology Reports*, 7(2), 175-179. <https://doi.org/10.1111/1758-2229.12216>

- Lee, K. S., Landry, Z., Pereira, F. C., Wagner, M., Berry, D., Huang, W. E., Taylor, G. T., Kneipp, J., Popp, J., Zhang, M., Cheng, J.-X., & Stocker, R. (2021). Raman microspectroscopy for microbiology. *Nature Reviews Methods Primers*, *1*(1). <https://doi.org/10.1038/s43586-021-00075-6>
- Lewis, A. T., Gaifulina, R., Isabelle, M., Dorney, J., Woods, M. L., Lloyd, G. R., Lau, K., Rodriguez-Justo, M., Kendall, C., Stone, N., & Thomas, G. M. (2017). Mirrored stainless steel substrate provides improved signal for Raman spectroscopy of tissue and cells. *J Raman Spectrosc*, *48*(1), 119-125. <https://doi.org/10.1002/jrs.4980>
- Li, J., Liu, P., Tamaxia, A., Zhang, H., Liu, Y., Wang, J., Menguy, N., Zhao, X., Roberts, A. P., & Pan, Y. (2021). Diverse intracellular inclusion types within magnetotactic bacteria: implications for biogeochemical cycling in aquatic environments. *Journal of Geophysical Research: Biogeosciences*, *126*(7).
- Li, J., Zhang, H., Menguy, N., Benzerara, K., Wang, F., Lin, X., Chen, Z., & Pan, Y. (2017). Single-Cell Resolution of Uncultured Magnetotactic Bacteria via Fluorescence-Coupled Electron Microscopy. *Appl Environ Microbiol*, *83*(12). <https://doi.org/10.1128/AEM.00409-17>
- Loussert-Fonta, C., Toullec, G., Paraecattil, A. A., Jeangros, Q., Krueger, T., Escrig, S., & Meibom, A. (2020). Correlation of fluorescence microscopy, electron microscopy, and NanoSIMS stable isotope imaging on a single tissue section. *Commun Biol*, *3*(1), 362. <https://doi.org/10.1038/s42003-020-1095-x>
- Mackey, K. R. M., Hunter-Cevera, K., Britten, G. L., Murphy, L. G., Sogin, M. L., & Huber, J. A. (2017). Seasonal Succession and Spatial Patterns of Synechococcus Microdiversity in a Salt Marsh Estuary Revealed through 16S rRNA Gene Oligotyping. *Frontiers in Microbiology*, *8*. <https://doi.org/ARTN 1496>  
10.3389/fmicb.2017.01496
- Mann, S., Sparks, N. H., & Board, R. G. (1990). Magnetotactic bacteria: microbiology, biomineralization, palaeomagnetism and biotechnology. *Adv Microb Physiol*, *31*, 125-181. [https://doi.org/10.1016/s0065-2911\(08\)60121-6](https://doi.org/10.1016/s0065-2911(08)60121-6)
- Marlow, J., Spietz, R., Kim, K. Y., Ellisman, M., Girguis, P., & Hatzenpichler, R. (2021). Spatially resolved correlative microscopy and microbial identification reveal dynamic depth- and mineral-dependent anabolic activity in salt marsh sediment. *Environ Microbiol*, *23*(8), 4756-4777. <https://doi.org/10.1111/1462-2920.15667>
- Matanfack, G. A., Taubert, M., Guo, S., Houhou, R., Bocklitz, T., Kusel, K., Rosch, P., & Popp, J. (2020). Influence of Carbon Sources on Quantification of Deuterium Incorporation in Heterotrophic Bacteria: A Raman-Stable Isotope Labeling Approach. *Anal Chem*, *92*(16), 11429-11437. <https://doi.org/10.1021/acs.analchem.0c02443>

- McGlynn, S. E., Chadwick, G. L., O'Neill, A., Mackey, M., Thor, A., Deerinck, T. J., Ellisman, M. H., & Orphan, V. J. (2018). Subgroup characteristics of marine methane-oxidizing ANME-2 archaea and their syntrophic partners revealed by integrated multimodal analytical microscopy. *Appl Environ Microbiol*. <https://doi.org/10.1128/AEM.00399-18>
- Meyer, N. R., Fortney, J. L., & Dekas, A. E. (2021). NanoSIMS sample preparation decreases isotope enrichment: magnitude, variability and implications for single-cell rates of microbial activity. *Environ Microbiol*, *23*(1), 81-98. <https://doi.org/10.1111/1462-2920.15264>
- Musat, N., Musat, F., Weber, P. K., & Pett-Ridge, J. (2016). Tracking microbial interactions with NanoSIMS. *Curr Opin Biotechnol*, *41*, 114-121. <https://doi.org/10.1016/j.copbio.2016.06.007>
- Musat, N., Stryhanyuk, H., Bombach, P., Adrian, L., Audinot, J. N., & Richnow, H. H. (2014). The effect of FISH and CARD-FISH on the isotopic composition of (13)C- and (15)N-labeled *Pseudomonas putida* cells measured by nanoSIMS. *Syst Appl Microbiol*, *37*(4), 267-276. <https://doi.org/10.1016/j.syapm.2014.02.002>
- Osborn, M., Webster, R. E., & Weber, K. (1978). Individual microtubules viewed by immunofluorescence and electron microscopy in the same PtK2 cell. *The Journal of cell biology*, *77*(3).
- Perkovic, M., Kunz, M., Endesfelder, U., Bunse, S., Wigge, C., Yu, Z., Hodirnau, V. V., Scheffer, M. P., Seybert, A., Malkusch, S., Schuman, E. M., Heilemann, M., & Frangakis, A. S. (2014). Correlative Light- and Electron Microscopy with chemical tags. *Journal of structural biology*, *186*(2), 205-213. <https://doi.org/10.1016/j.jsb.2014.03.018>
- Pirozzi, N. M., Hoogenboom, J. P., & Giepmans, B. N. G. (2018). ColorEM: analytical electron microscopy for element-guided identification and imaging of the building blocks of life. *Histochemistry and Cell Biology*, *150*(5), 509-520. <https://doi.org/10.1007/s00418-018-1707-4>
- Posfai M., Buseck PR., Bazylinski DA., & RB., F. (1998). Iron sulfides from magnetotactic bacteria: structure, composition, and phase transitions. *American Mineralogist*, *83*(11), 1469-1481.
- Qian, X. X., Santini, C. L., Kosta, A., Menguy, N., Le Guenno, H., Zhang, W., Li, J., Chen, Y. R., Liu, J., Alberto, F., Espinosa, L., Xiao, T., & Wu, L. F. (2020). Juxtaposed membranes underpin cellular adhesion and display unilateral cell division of multicellular magnetotactic prokaryotes. *Environ Microbiol*, *22*(4), 1481-1494. <https://doi.org/10.1111/1462-2920.14710>
- Rust, M. J., Bates, M., & Zhuang, X. (2006). Sub-diffraction-limit imaging by stochastic optical reconstruction microscopy (STORM). *Nat Methods*, *3*(10), 793-795. <https://doi.org/10.1038/nmeth929>

- Salman, V., Yang, T. T., Berben, T., Klein, F., Angert, E., & Teske, A. (2015). Calcite-accumulating large sulfur bacteria of the genus *Achromatium* in Sippewissett Salt Marsh. *Isme Journal*, 9(11), 2503-2514. <https://doi.org/10.1038/ismej.2015.62>
- Schluter, S., Eickhorst, T., & Mueller, C. W. (2019). Correlative Imaging Reveals Holistic View of Soil Microenvironments. *Environ Sci Technol*, 53(2), 829-837. <https://doi.org/10.1021/acs.est.8b05245>
- Shapiro, O. H., Hatzenpichler, R., Buckley, D. H., Zinder, S. H., & Orphan, V. J. (2011). Multicellular photo-magnetotactic bacteria. *Environmental Microbiology Reports*, 3(2), 233-238. <https://doi.org/10.1111/j.1758-2229.2010.00215.x>
- Siegrist, M. S., Whiteside, S., Jewett, J. C., Aditham, A., Cava, F., & Bertozzi, C. R. (2013). (D)-Amino acid chemical reporters reveal peptidoglycan dynamics of an intracellular pathogen. *ACS Chem Biol*, 8(3), 500-505. <https://doi.org/10.1021/cb3004995>
- Simmons, S. L., & Edwards, K. J. (2007). Unexpected diversity in populations of the many-celled magnetotactic prokaryote. *Environ Microbiol*, 9(1), 206-215. <https://doi.org/10.1111/j.1462-2920.2006.01129.x>
- Smriga, S., Samo, T. J., Malfatti, F., Villareal, J., & Azam, F. (2014). Individual cell DNA synthesis within natural marine bacterial assemblages as detected by 'click' chemistry. *Aquatic Microbial Ecology*, 72(3), 269-280. <https://doi.org/10.3354/ame01698>
- Stahl, D. A., & Amann, R. I. (1991). Development and application of nucleic acid probes *E. Stackebrandt and M. Goodfellow (ed.), Nucleic acid techniques in bacterial systematics*(John Wiley & Sons), 205-248
- Stoecker, K., Dorninger, C., Daims, H., & Wagner, M. (2010). Double labeling of oligonucleotide probes for fluorescence in situ hybridization (DOPE-FISH) improves signal intensity and increases rRNA accessibility. *Appl Environ Microbiol*, 76(3), 922-926. <https://doi.org/10.1128/AEM.02456-09>
- Teng, Z., Zhang, Y., Zhang, W., Pan, H., Xu, J., Huang, H., Xiao, T., & Wu, L. F. (2018). Diversity and Characterization of Multicellular Magnetotactic Prokaryotes From Coral Reef Habitats of the Paracel Islands, South China Sea. *Front Microbiol*, 9, 2135. <https://doi.org/10.3389/fmicb.2018.02135>
- Uebe, R., & Schuler, D. (2016). Magnetosome biogenesis in magnetotactic bacteria. *Nat Rev Microbiol*, 14(10), 621-637. <https://doi.org/10.1038/nrmicro.2016.99>
- Waite, D. W., Chuvochina, M., Pelikan, C., Parks, D. H., Yilmaz, P., Wagner, M., Loy, A., Naganuma, T., Nakai, R., Whitman, W. B., Hahn, M. W., Kuever, J., & Hugenholtz, P. (2020). Proposal to reclassify the proteobacterial classes Deltaproteobacteria and Oligoflexia, and the phylum Thermodesulfobacteria into four phyla reflecting major

- functional capabilities. *Int J Syst Evol Microbiol*, 70(11), 5972-6016.  
<https://doi.org/10.1099/ijsem.0.004213>
- Wallner, G., Amann, R., & Beisker, W. (1993). Optimizing Fluorescent Insitu Hybridization with Ribosomal-Rna-Targeted Oligonucleotide Probes for Flow Cytometric Identification of Microorganisms. *Cytometry*, 14(2), 136-143. <https://doi.org/DOI.10.1002/cyto.990140205>
- Wang, Y., Huang, W. E., Cui, L., & Wagner, M. (2016). Single cell stable isotope probing in microbiology using Raman microspectroscopy. *Curr Opin Biotechnol*, 41, 34-42.  
<https://doi.org/10.1016/j.copbio.2016.04.018>
- Webster, R. E., Osborn, M., & Weber, K. (1978). Visualization of the same PtK2 cytoskeletons by both immunofluorescence and low power electron microscopy. *Experimental cell research*, 117(1), 47-61.
- Wenter, R., Wanner, G., Schuler, D., & Overmann, J. (2009). Ultrastructure, tactic behaviour and potential for sulfate reduction of a novel multicellular magnetotactic prokaryote from North Sea sediments. *Environ Microbiol*, 11(6), 1493-1505.  
<https://doi.org/10.1111/j.1462-2920.2009.01877.x>
- Wilbanks, E. G., Jaekel, U., Salman, V., Humphrey, P. T., Eisen, J. A., Facciotti, M. T., Buckley, D. H., Zinder, S. H., Druschel, G. K., Fike, D. A., & Orphan, V. J. (2014). Microscale sulfur cycling in the phototrophic pink berry consortia of the Sippewissett Salt Marsh. *Environmental Microbiology*, 16(11), 3398-3415. <https://doi.org/10.1111/1462-2920.12388>
- Wilbanks, E. G., Salman-Carvalho, V., Jaekel, U., Humphrey, P. T., Eisen, J. A., Buckley, D. H., & Zinder, S. H. (2017). The Green Berry Consortia of the Sippewissett Salt Marsh: Millimeter-Sized Aggregates of Diazotrophic Unicellular Cyanobacteria. *Frontiers in Microbiology*, 8. <https://doi.org/ARTN.1623.10.3389/fmicb.2017.01623>
- Woehl, T. J., Kashyap, S., Firlar, E., Perez-Gonzalez, T., Faivre, D., Trubitsyn, D., Bazylnski, D. A., & Prozorov, T. (2014). Correlative electron and fluorescence microscopy of magnetotactic bacteria in liquid: toward in vivo imaging. *Sci Rep*, 4, 6854.  
<https://doi.org/10.1038/srep06854>
- Zhang, R., Chen, Y. R., Du, H. J., Zhang, W. Y., Pan, H. M., Xiao, T., & Wu, L. F. (2014). Characterization and phylogenetic identification of a species of spherical multicellular magnetotactic prokaryotes that produces both magnetite and greigite crystals. *Res Microbiol*, 165(7), 481-489. <https://doi.org/10.1016/j.resmic.2014.07.012>
- Zimmermann, M., Escrig, S., Hubschmann, T., Kirf, M. K., Brand, A., Inglis, R. F., Musat, N., Muller, S., Meibom, A., Ackermann, M., & Schreiber, F. (2015). Phenotypic heterogeneity in metabolic traits among single cells of a rare bacterial species in its

natural environment quantified with a combination of flow cell sorting and NanoSIMS.  
*Front Microbiol*, 6, 243. <https://doi.org/10.3389/fmicb.2015.00243>

## CHAPTER THREE

COMPARING RAMAN AND NANOSIMS FOR STABLE ISOTOPE PROBING OF SINGLE  
CELLSContributions of Authors and Co-Authors

Author: George A. Schaible

Contributions: Designed the study, performed culturing and SIP labeling of *E. coli*, prepared samples for analysis, analyzed Raman spectra, compiled data and performed all statistical analyses, prepared all figures, and wrote the manuscript.

Co-Author: Jennifer A. Crandall

Contributions: Prepared samples for analysis, collected all Raman spectra, and compiled Raman data.

Co-Author: John B. Cliff

Contributions: Performed NanoSIMS analysis and analyzed the data.

Co-Author: Jeremy J. Bougoure

Contributions: Performed NanoSIMS analysis.

Co-Author: Roland Hatzenpichler

Contributions: Designed the study and wrote the manuscript.

Manuscript Information

George A. Schaible, Jennifer A. Crandall, John Cliff, Jeremy J. Bougoure, and Roland Hatzenpichler

Microbiology Spectrum

Status of Manuscript:

Prepared for submission to a peer-reviewed journal

Officially submitted to a peer-reviewed journal

Accepted by a peer-reviewed journal

Published in a peer-reviewed journal

Abstract

Application of spectroscopy and spectrometry techniques has become prevalent in the field of microbiology. Stable isotope probing (SIP) experiments in conjunction with Raman microspectroscopy (Raman) or nano-scale secondary ion mass spectrometry (NanoSIMS) are frequently used to explore single cell resolved metabolic activity, thereby directly linking the structure and function of culturable and uncultured microbes. Despite the increasing popularity of these techniques, no study has yet compared results from isotope incorporation measurements using both Raman and NanoSIMS directly on the same cell. This knowledge gap creates uncertainty about the comparability of single cell SIP data generated independently using these techniques. In this study, we conducted a comparative analysis between Raman and NanoSIMS to quantify the uptake of heavy water ( $^2\text{H}_2\text{O}$ ) into the biomass of 543 individual *Escherichia coli* cells grown in M9 minimal medium. By correlating the data obtained from these two techniques at a single cell level, we were able to for the first time establish the extent of data equivalence, allowing for comparisons between the two approaches. Using the dataset generated in this study, we investigated the efficacy of pre-processing methods for Raman as well as the ideal masses for NanoSIMS analysis of cells grown in the presence of  $^2\text{H}_2\text{O}$ . We anticipate that the findings presented herein will enhance the comparability of studies employing either technique, ultimately contributing to the establishment of a standardized framework within the field.

## 1. Introduction

Microbial activities and cellular interactions drive global biogeochemical cycles, ecosystem function, and human microbiomes (Crowther et al., 2019; Gilbert et al., 2018). One common approach to analyzing microbe interactions and activity is the use of stable isotope probing (SIP) (Hatzenpichler, 2020; Lee et al., 2021; Musat et al., 2016). By measuring the incorporation of stable isotopes (*e.g.*,  $^{18}\text{O}$ ,  $^{15}\text{N}$ ,  $^{13}\text{C}$ ,  $^2\text{H}$ ) into cellular biomass, it becomes possible to assess the activity and physiology of individual cells at a meaningful spatial resolution, enabling a comprehensive understanding of community dynamics (Alcolombri et al., 2022). The assimilation of isotopically labeled substrates is commonly measured by either Raman microspectroscopy (Raman) or nano secondary ion mass spectrometry (NanoSIMS). Both techniques can be combined with fluorescence staining and epifluorescence microscopy, further increasing the effectiveness by allowing for substrate analogue probing and identification of species (Huang et al., 2007; Musat et al., 2016; Wei et al., 2016).

Raman is a non-destructive spectroscopic technique that is based on the principle of inelastic scattering of light and can be applied directly to environmental samples with minimal preparation (Lee et al., 2021), allowing for real-time monitoring of metabolic changes on single cells (Cui et al., 2023). By exciting molecular bonds, Raman elucidates the spatial distribution of specific biomolecules, such as lipids, proteins, and nucleic acids, within cells and/or communities on a micrometer scale (Hatzenpichler, 2020; Lee et al., 2021). Shifts in the Raman spectra occur when an organism had incorporated a heavier isotope, allowing for SIP of cells (Berry et al., 2015; Matanfack et al., 2021; Weber et al., 2021). Although Raman requires little or no sample preparation and is relatively straightforward, the technique suffers from a limitation in detection

of isotopes ( $\sim 10\%$   $^{13}\text{C}$ ,  $\sim 10\%$   $^{15}\text{N}$ , and  $\sim 0.2\%$   $^2\text{H}$  cellular replacement (Berry et al., 2015; Huang et al., 2007; Wang et al., 2016)) and low signal-to-noise ratio as compared to mass spectrometry. Alternatively, NanoSIMS employs a focused ion beam to produce secondary ions from the sample surface that are subsequently analyzed by mass to attain spatially resolved elemental and isotopic information (Li et al., 2023; Nuñez et al., 2018). NanoSIMS is capable of detecting isotopes at a much greater sensitivity and spatial resolution than Raman; it is, however, destructive to the sample and doesn't provide molecular or chemical information (Pett-Ridge & Weber, 2012). Both techniques are not widely used in microbiology, which is mainly attributed to their high prices ( $\$500\text{k}+$  for a Confocal Raman;  $\$3.5\text{M}$  for a NanoSIMS), though they are often used for studies employing SIP of microbial cells (Hatzenpichler, 2020; Lee et al., 2021; Musat et al., 2012). However, several national labs and university centers offer access to these powerful techniques, and external users can apply for free instrument time and specialist support at some of them (*e.g.*, the US Pacific Northwest National Laboratory).

Both Raman and NanoSIMS are powerful tools for studying the structure, function, and interactions of microbes on a single-cell or community level. Studies have successfully applied both techniques in tandem, including analysis of deposition of organic material in diatom fossils (Akse et al., 2021), SIP incubations of microbial cells recovered from soils and sediments (Eichorst et al., 2015; Schaible et al., 2022), and *in vitro* SIP labeling of microbial cells for sorting (Berry et al., 2015). Despite the individual and combined successes of Raman and NanoSIMS in microbiology, a comprehensive and direct comparison of these techniques at the single-cell level has not yet been taken, making it difficult to compare results from either technique.

To address this shortcoming, we employed SIP on *Escherichia coli* (*E. coli*) using deuterium oxide ( $^2\text{H}_2\text{O}$ ), allowing for a direct comparison of the substrate incorporation as measured by each technique. By conducting a direct comparison of Raman and NanoSIMS on a single-cell level for 543 individual cells (>100 per incubation), we demonstrate strong correlation between the measurements of  $^2\text{H}$ , enabling the corroboration of data obtained from either technique alone. This data set also enabled an investigation into the pre-processing of Raman data and the ideal mass measurements used for NanoSIMS, providing insight for the optimization of the methodology when using either technique for  $^2\text{H}$  measurements. Considering that both Raman and NanoSIMS possess unique strengths and limitations, the drawbacks of one technique can be compensated for by the advantages of the other, thereby granting a more comprehensive insight into biological samples at micro- to nano-meter scales (Schaible et al., 2022). Ultimately, this comparative investigation contributes to refining our understanding of the comparability of Raman and NanoSIMS and lays the foundation for future integrated approaches to advance the field of microbiology.

## 2. Results and Discussion

### 2.1 Stable Isotope Probing

The application of stable isotopes to probe metabolic activity and function has garnered wide use in microbiology (Hatzenpichler, 2020; Huang, 2004; Hungate et al., 2015; Weber et al., 2021). While SIP substrates such as  $^{15}\text{NH}_4$  and  $^{13}\text{C}$ -glucose can be informative regarding specific metabolite use, they can alter the natural substrate pool of the sample, potentially resulting in skewed labeling. Alternatively, the hydrogen isotope form of heavy water (*i.e.*,  $^2\text{H}_2\text{O}$ ) can be used as a measure of activity of individual microbes within complex samples without prior knowledge

of their physiology or influencing the substrate pool (Berry et al., 2015; Matanfack et al., 2020). Active microbes grown or incubated in the presence of heavy water will use deuterium ( $^2\text{H}$ ) in lieu of hydrogen ( $^1\text{H}$ ) during biosynthesis of lipids (Wegener et al., 2012; Zhang et al., 2009), resulting in active microbial community members becoming labeled with  $^2\text{H}$ . In addition,  $^2\text{H}$  can be incorporated into newly synthesized proteins as well as isotopically exchanged with amino acids (Justice et al., 2014). Because  $^2\text{H}$  naturally occurs at very low levels ( $\sim 0.016\%$ ), there is a reduced impact of environmental background of  $^2\text{H}$  in samples (Friedman, 1953). Finally, carbon-deuterium ( $^{12}\text{C}^2\text{H}$ ) bonds are reliably detectible in Raman spectra by a characteristic peak shift of the abundant  $^{12}\text{C}^1\text{H}$  peak into the mostly silent region ( $1,800\text{-}2,800\text{ cm}^{-1}$ ) of the cellular Raman spectrum (Berry et al., 2015).

In our study, we employed our recently developed correlative protocol for the study of single microbial cells (Schaible et al., 2022). For comparison of SIP-Raman and SIP-NanoSIMS, *E. coli* K12 cultures were grown in either unamended media ( $0\% \text{ } ^2\text{H}_2\text{O}$ ) or media amended with either  $15\%$ ,  $30\%$ , or  $50\% \text{ } ^2\text{H}_2\text{O}$ , and cells were collected during mid-logarithmic growth (Fig. 1 and S1). Following fixation with PFA, cells were immobilized on a stainless-steel coupon and stained with DAPI for visualization individual cells during mapping, which was performed using a laser dissection microscope (Appendix B, Fig. S2). Regions of interest (ROIs) were designated for each sample to enable correlation of cells between Raman and NanoSIMS. Because NanoSIMS is a destructive technique, Raman was performed first to acquire spectra of all cells within the ROIs before NanoSIMS was used (see Schaible et al. 2022 for details on the workflow).

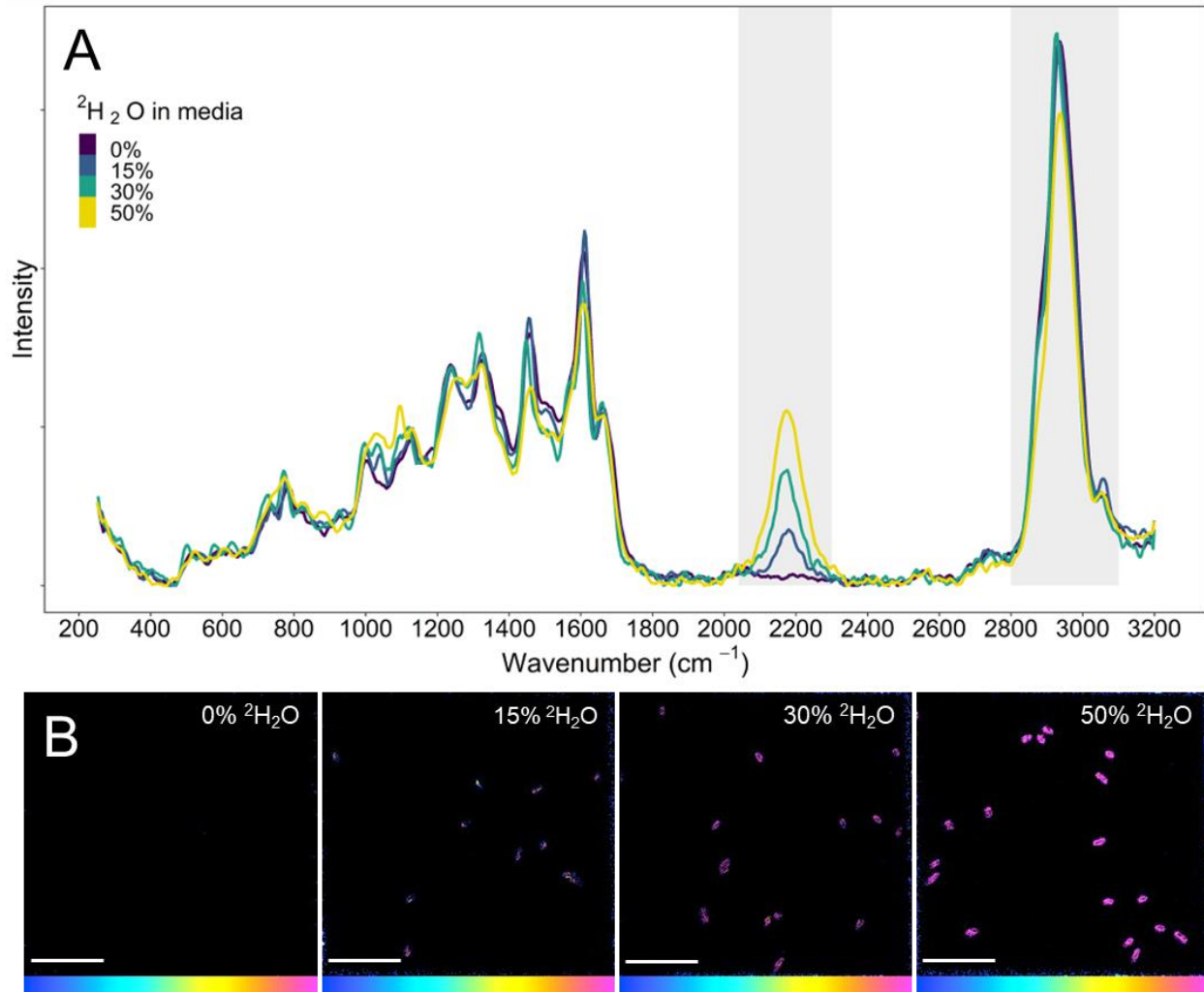


Fig. 1. Exemplary Raman spectra and NanoSIMS images illustrating the uptake of H<sub>2</sub>-label by *Escherichia coli* cells after incubation in media with varying percentages of <sup>2</sup>H<sub>2</sub>O. A The characteristic <sup>12</sup>C<sup>2</sup>H and <sup>12</sup>C<sup>1</sup>H regions are shaded in gray. B <sup>12</sup>C<sub>2</sub><sup>2</sup>H/<sup>12</sup>C<sub>2</sub><sup>1</sup>H mass ratio NanoSIMS images. All isotope fraction images are on the same scale (0-30 atom %). Scales bars are 5 μm.

## 2.2 Pre-Processing of Raman Spectra

Currently, there is no standard method for the pre-processing of Raman spectra (Lee et al., 2021), despite compelling evidence demonstrating the significant influence of processing procedures on data outcomes (Bocklitz et al., 2011). Optimizing the workflow by testing various pre-processing procedures on Raman spectra before selecting a method is recommended to

minimize information loss in the spectra (Gautam et al., 2015; Ryabchykov et al., 2018). To address the lack of standardization in pre-processing methods, we systematically tested various methods on our Raman spectra to ensure the data was not influenced by statistical methods.

Raman spectra spanning 250-3,200  $\text{cm}^{-1}$  were acquired for individual cells within the ROIs. To test if peaks in the fingerprint region of spectra ( $<1,800 \text{ cm}^{-1}$ ) induce a leveraging effect during smoothing and baselining of the spectra, spectra were truncated to 1,800-3,200  $\text{cm}^{-1}$  as has previously been suggested (Guo et al., 2021; Ryabchykov et al., 2018). All spectra were smoothed using a Savitzky-Golay smoothing algorithm, which applies a moving window based on a local polynomial fitting procedure, to reduce the signal to noise ratio (Savitzky & Golay, 1964). Excessive smoothing of spectra can result in loss of genuine Raman bands, an undesired effect. To avoid this, we used a 2<sup>nd</sup> degree polynomial with a window size of 11 to ensure important peaks were sustained in spectra across all samples. Next, several commonly applied baselining methods were tested to identify if background correction influences the final calculation of  $^2\text{H}$  content of the *E. coli* cells.

The first baselining method applied was asymmetric least squares (ALS), an iterative method that uses asymmetric weighting to adjust the influence data has on baselining (Eilers & Boelens, 2005). The second method used was a polynomial fit, where a polynomial of  $n^{\text{th}}$  degree (we used a 2<sup>nd</sup> degree polynomial) can be fit to the spectra and the baseline subtracted to remove background (Lieber & Mahadevan-Jansen, 2003). The third method tested was a frequency differentiated non-linear digital filter, commonly referred to as “rolling ball”, which is equivalent to rolling a ball with a given window size (*i.e.*, ball diameter) below the spectra and removing the background below the points the ball touches (Kneen & Annegarn, 1996). The fourth and final

method tested was statistics-sensitive non-linear iterative peak-clipping (SNIP), a process that compresses the data using a log square root operator followed by iterative evaluations using a clipping window, after which the data is transformed back using the inverse log square root (Ryan et al., 1988). In contrast to the other baselining methods, SNIP does not lead to distortions in of the baseline at the edges of the spectral interval (Ryabchykov et al., 2018).

Prior to determining the efficacy of baselining methods, each spectrum was normalized using a scale-invariant sum normalization to maintain relative proportions of peaks for comparisons. Next, the  $^2\text{H}$  incorporation into cells was quantified by calculating the ratio between the area under the curve (AUC) of the  $^{12}\text{C}^2\text{H}$  (2,040-2,300  $\text{cm}^{-1}$ ) and the  $^{12}\text{C}^1\text{H}$  (2,800-3,100  $\text{cm}^{-1}$ ) region of each spectrum (Fig. 1A). The AUC was determined by drawing a linear baseline between the interval of wavenumbers and integrating the area above the line and below the curve using the trapezoidal rule (Appendix B, Fig. S4). The  $^2\text{H}$  content was then used to compare the baselining methods for both truncated spectra (1,800-3,200  $\text{cm}^{-1}$ ) and whole spectra (250-3,200  $\text{cm}^{-1}$ ) and the r-squared value used to determine the fit of each model (Appendix B, Fig. S3). This analysis showed that there was no statistically significant difference between the truncated and whole spectra or between the baselining methods (Appendix B, Table S1), indicating that the baselining method had little effect on  $^2\text{H}$  calculation from Raman spectra of the *E. coli*. This could be due to the low background observed in a pure culture as compared to an environmental sample and the low natural fluorescence of *E. coli*, resulting in minimal background subtractions from the data. We elected to use the SNIP baselining method for our analysis as this was applied in previous studies investigating SIP incorporation in cells (Berry et al., 2015; Eichorst et al., 2015; Matanfack et al., 2021).

### 2.3 NanoSIMS Analysis

The next step in our workflow was to examine the  $^2\text{H}$  content of each cell that had previously measured by Raman using NanoSIMS (Fig. 1B). Historically, analysis of  $^2\text{H}$  uptake in cells by NanoSIMS has been performed using either the mass ratio of  $^2\text{H}/^1\text{H}$  (Doughty et al., 2014; Schaible et al., 2022) or  $^{12}\text{C}^2\text{H}/^{12}\text{C}^1\text{H}$  (Berry et al., 2015; Sáenz et al., 2012). To determine if their choice of mass ratio leads to different interpretations of the  $^2\text{H}$ -content of cells, we measured the  $^2\text{H}/^1\text{H}$ ,  $^{12}\text{C}^2\text{H}/^{12}\text{C}^1\text{H}$ , and  $^{12}\text{C}_2^2\text{H}/^{12}\text{C}_2^1\text{H}$  mass ratios using NanoSIMS. Intriguingly, we found there is a statistically significant difference ( $p < 0.005$ ) between each pair of mass ratios used to measure the  $^2\text{H}$  content of cells at each concentration of  $^2\text{H}_2\text{O}$  in the media (Appendix B, Fig. S5). On average, the  $^{12}\text{C}^2\text{H}/^{12}\text{C}^1\text{H}$  ratio indicated the highest  $^2\text{H}$  content in cells with the  $^{12}\text{C}_2^2\text{H}/^{12}\text{C}_2^1\text{H}$  ratio indicating the second highest and the  $^2\text{H}/^1\text{H}$  ratio showing the lowest. This trend could be in part due to a kinetic isotope or electron affinity effect that influences the number of ions (*i.e.*, counts) observed in the mass spectrometer (Appendix B, Fig. S6). The low counts for  $^{12}\text{C}^2\text{H}/^{12}\text{C}^1\text{H}$  could also be contributing to the high measurement (3-5 atom percent) of deuterium in the 0%  $^2\text{H}_2\text{O}$  incubation. The low count was likely not sample-specific as the  $^{12}\text{C}^2\text{H}/^{12}\text{C}^1\text{H}$ , and  $^{12}\text{C}_2^2\text{H}/^{12}\text{C}_2^1\text{H}$  mass ratios were concurrently measured on the same cells. The  $^2\text{H}/^1\text{H}$  mass ratio was measured on separate cells due to the need to change the calibration of the instrument to detect the low mass. Because of the variations in  $^2\text{H}$  of cells between the different mass ratios, we make our Raman-NanoSIMS comparisons using all three mass ratios.

### 2.4 Single-Cell Comparison of Raman and NanoSIMS

The processed Raman and NanoSIMS data were compared directly on a single-cell level, revealing a high degree of comparability between the two techniques (Fig. 2). For the 0%, 15%,

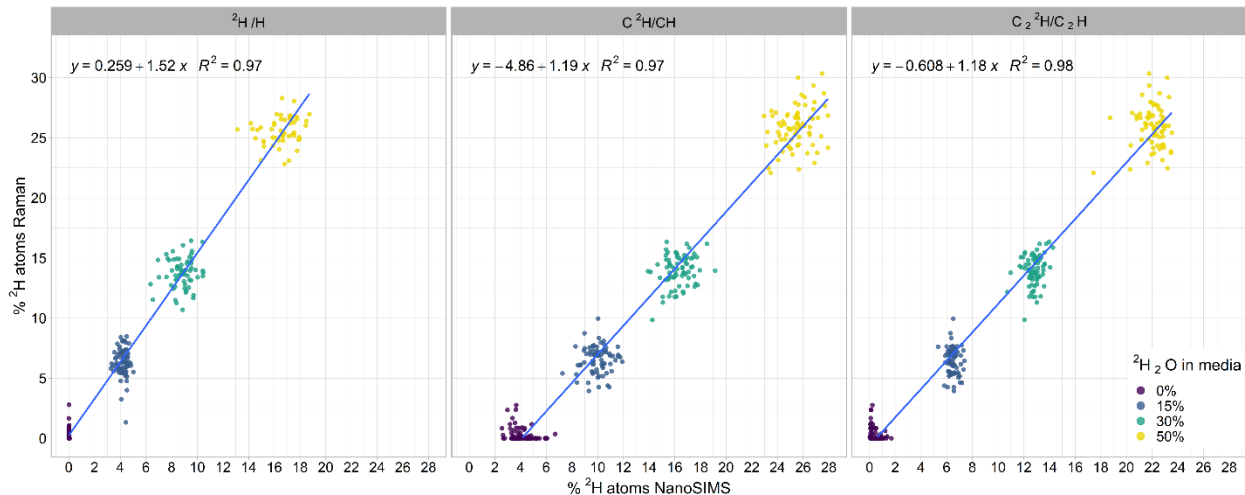


Fig. 2. Single cell comparison of the  $^2\text{H}$  content of cells as measured by Raman and NanoSIMS using specific mass ratios. Each dot represents a single cell analyzed with both techniques for different  $^2\text{H}_2\text{O}$  concentrations in the culture medium. The linear model equation and fit (blue line) is shown for each comparison of Raman to NanoSIMS regarding the specific mass ratios. In regard to y-intercept, slope, and r-squared, a mass ratio of  $\text{C}_2^2\text{H}/\text{C}_2^1\text{H}$  is best used for comparisons to Raman.

30%, 50% incubations, the  $^2\text{H}$  content of 543 cells was measured. Interestingly, the highest correlation of labeling percentages determined by Raman and NanoSIMS were found using the  $^{12}\text{C}_2^2\text{H}/^{12}\text{C}_2^1\text{H}$  mass ratio (0.98 r-squared). The  $^2\text{H}/^1\text{H}$  and  $^{12}\text{C}^2\text{H}/^{12}\text{C}^1\text{H}$  mass ratios showed equal correlation (0.97 r-squared) to the Raman results although the NanoSIMS data for the  $^2\text{H}/^1\text{H}$  had a much lower degree of spread for the 0%  $^2\text{H}_2\text{O}$  incubations as compared to  $^{12}\text{C}^2\text{H}/^{12}\text{C}^1\text{H}$ . Considering the slope of the models, each comparison had a slope  $>1$ , indicating that Raman was estimating a higher amount of deuterium in the cells than NanoSIMS. This discrepancy was the greatest with the  $^2\text{H}/^1\text{H}$  mass ratio where the slope of the model was 1.52x. Furthermore, the y-intercept was near zero for  $^2\text{H}/^1\text{H}$  and  $^{12}\text{C}_2^2\text{H}/^{12}\text{C}_2^1\text{H}$  while the  $^{12}\text{C}^2\text{H}/^{12}\text{C}^1\text{H}$  mass ratio had a y-intercept of -4.86, representative of the high estimation of  $^2\text{H}$  in the cells for the 0%  $^2\text{H}_2\text{O}$  incubation. Comparison of  $^2\text{H}$  content in each cell based on  $^2\text{H}_2\text{O}$  incubations as measured by

NanoSIMS each or Raman revealed statistically significant differences between the techniques (Fig. 3). The  $^{12}\text{C}_2^2\text{H}/^{12}\text{C}_2^1\text{H}$  mass ratio was not significantly different from the Raman data at the 0% and 15%  $^2\text{H}_2\text{O}$  incubations. Together, it appears that the most reliable mass ratio for measuring the  $^2\text{H}$  content of cells is  $^{12}\text{C}_2^2\text{H}/^{12}\text{C}_2^1\text{H}$  as it strongly agrees with Raman data and is supported by robust ion counts.

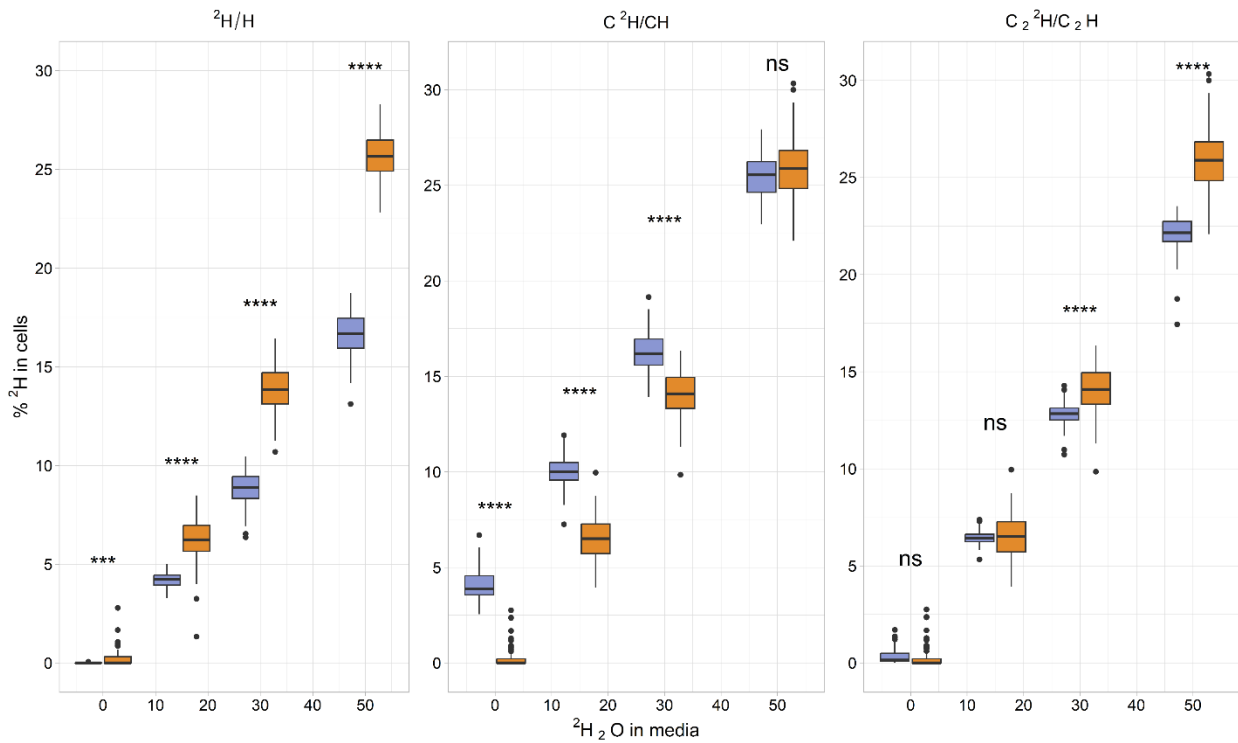


Fig. 3. Comparison of  $^2\text{H}$  atom percent as measured by Raman and NanoSIMS. Each NanoSIMS mass ratio is shown for comparison. For the  $^2\text{H}/^1\text{H}$  mass ratio measurements, NanoSIMS measures a lower  $^2\text{H}$  content in the cells than Raman. The opposite is true for the  $\text{C}^2\text{H}/\text{C}^1\text{H}$  mass ratio for which NanoSIMS measures a higher  $^2\text{H}$  content. The  $\text{C}_2^2\text{H}/\text{C}_2^1\text{H}$  leads to similar results as Raman for the 0% and 15%  $^2\text{H}_2\text{O}$  incubations but measures a lower  $^2\text{H}$  content than Raman for the 30% and 50% incubations. Because the  $\text{C}_2^2\text{H}/\text{C}_2^1\text{H}$  mass ratio contains the least statistically difference to the Raman data, this would be the ideal mass to use when comparing NanoSIMS and Raman measurements of  $^2\text{H}$ . All statistically significant differences are shown: \*\*\* = p-value <  $1.0 \times 10^{-3}$ , \*\*\*\* = p-value <  $1.0 \times 10^{-10}$ , ns = not significant.

### 3. Conclusion

This study addresses the need for a direct comparison between Raman and NanoSIMS in the context of SIP experiments to explore single cell resolved metabolic activity. By quantifying the uptake of  $^2\text{H}$  into the biomass of individual *E. coli* cells using both Raman and NanoSIMS, we were able to establish the extent of data equivalence between the two techniques, thus improving the comparability of studies employing either Raman or NanoSIMS techniques. Furthermore, we investigated the efficacy of pre-processing methods for Raman data showing that for the model organism *E. coli*, truncation and various baselining methods have little impact on the calculation of  $^2\text{H}$  in cells. Additionally, we investigated the ideal  $^2\text{H}$  masses for NanoSIMS analysis and the comparability to Raman data, showing that  $^{12}\text{C}_2^2\text{H}/^{12}\text{C}_2^1\text{H}$  mass ratio was most equivalent to Raman calculations for  $^2\text{H}$ .

Single species microbial populations have been shown to exhibit metabolic heterogeneity, requiring analysis on a single-cell level to differentiate phenotypes within the population (Schreiber & Ackermann, 2020; Schreiber et al., 2016; Zimmermann et al., 2015). Our analysis revealed a high degree of similarity between Raman and NanoSIMS in measuring the anabolic metabolism of  $^2\text{H}$  in single cells, supported by a robust correlation coefficient. This finding supports the interchangeable use of either Raman or NanoSIMS when analyzing cells incubated with  $^2\text{H}_2\text{O}$ , offering researchers flexibility in choosing the most suitable technique for their specific experimental requirements. This is especially of use if one technique is not available or suffers from inherent limitations, such as limit of detection or laser damage as occurs in Raman (Hatzenpichler, 2020; Yuan et al., 2018), or destruction of the sample as occurs in NanoSIMS (Nuñez et al., 2018).

In summary, this comparative investigation fills a critical void in the current understanding of spectroscopy and spectrometry techniques in microbiology and offers a foundation for the further exploration and application of these methods in diverse microbial systems. As researchers continue to push the boundaries of single-cell analysis, the findings concerning the comparability of Raman and NanoSIMS presented in this study pave the way for a more nuanced and comprehensive understanding of microbial activities, interactions, and responses to isotopic labeling.

#### 4. Materials and Methods

##### 4.1 Preparation of Isotopically Labeled Cells

To prepare cells, *Escherichia coli* K12 (DSM498) was grown aerobically with agitation (200 rpm) at 37 °C for 13 h in M9 medium (0.38 mM thiamine and 22.2 mM glucose) that had been amended to a final concentration of either 0%, 15%, 30%, or 50%  $^2\text{H}_2\text{O}$  (99.9%  $^2\text{H}$ ; Cambridge Isotope Laboratories). The optical density (600 nm) of the culture was measured every hour for the first six hours, after which measurements were taken every half hour. When the  $\text{OD}_{600}$  reached 0.8-0.9, 1 mL of culture was sampled (Appendix B, Fig. S1) and chemically fixed by adding paraformaldehyde (PFA; Electron Microscopy Science; EM grade) to a final concentration of 2%. Samples were then incubated in suspension for 60 min at room temperature. Cells were then washed twice with 1× phosphate buffered saline (PBS; pH 7.4) by centrifugation at 16,000 g for 5 min, after which their supernatants were removed, and the cell pellets were resuspended in 1mL of 1:1 PBS:ethanol.

#### 4.2 Preparation of Stainless Steel Coupon

Fixed cells were dried to the surface of mirrored stainless steel due to its desired properties as a Raman substrate (Lewis et al., 2017). The stainless steel coupon was prepared as previously described in Schaible *et al.* (Schaible et al., 2022). Briefly, the coupon was cleaned by washing with a 1% solution of Tergazyme (Alconox, New York, NY) rinsed with Milli-Q water, subsequent one-minute washes in acetone and 200 proof ethanol, and then air dried. To maintain correct orientation of the samples, asymmetric boxes were etched into the mirrored surface of each coupon using a welder's pen (Appendix B, Fig. S2). 1  $\mu$ L of each sample was spotted onto the coupon and air-dried at 46 °C for 1 min, after which the coupon was washed in 1:1 ethanol:MilliQ for 1 minute and then air dried. The coupon was incubated in a 300 nM solution of DAPI (4',6-diamidino-2-phenylindole, ThermoFisher, Waltham, MA) for 3 minutes as per the manufacturer's instructions. The coupon was then rinsed three times in fresh PBS and then briefly dipped them into ice-cold Milli-Q water to remove salts and air-dried using compressed air. To track single cells across platforms, regions of interest (ROIs) were drawn around cells on the coupon using a Leica LMD6 Laser Microdissection System (Danaher Corporation, Washington DC) using a power setting of 7, a speed of 7, and aperture size of 7 (Appendix B, Fig. S3).

#### 4.3 Confocal Raman Microspectroscopy and Spectral Processing

Raman spectra of individual cells were acquired using a LabRAM HR Evolution Confocal Raman microscope (Horiba Jobin-Yvon) equipped with a 532 nm laser and 300 grooves/mm diffraction grating. The instrument was calibrated daily before use with silica oxide standard. Spectra of cells were acquired using a 100 $\times$  dry objective (NA = 0.90) in the range of 250–3200  $\text{cm}^{-1}$ , with 3 acquisitions of 10 s each, and a laser power of 4.5 mW. Spectra were processed using

LabSpec version 6.5.1.24 (Horiba). The spectra were preprocessed in GNU R (Team, 2023) using the Alkahest (Frerebeau, 2023) and Pracma (Borchers, 2023) packages. Each spectra was smoothed using the Savitsky-Goley algorithm (Savitzky & Golay, 1964) followed by background subtraction and baselining of spectra using either asymmetric least squares (ALS) (Eilers & Boelens, 2005), polynomial fit (Lieber & Mahadevan-Jansen, 2003), rolling ball (Kneen & Annegarn, 1996), or statistics-sensitive non-linear iterative peak-clipping (SNIP) (Ryan et al., 1988). Only the SNIP baselining method was used for all spectra compared to NanoSIMS data. Settings used for smoothing and baselining can be found in the R file deposited on GitHub (<https://github.com/georgeschaible/Raman-spectra-processing>). Each spectrum was then normalized to the sum of its absolute spectral intensity and the incorporation of  $^2\text{H}$  into biomass was calculated by  $\left(\frac{^{12}\text{C}^2\text{H}}{^{12}\text{C}^2\text{H}+^{12}\text{C}^1\text{H}}\right) \times 100$ , using the integration of the AUC for the  $^{12}\text{C}^2\text{H}$  (2040–2300  $\text{cm}^{-1}$ ) and  $^{12}\text{C}^1\text{H}$  (2800–3100  $\text{cm}^{-1}$ ) regions of the spectra. The AUC was calculated using the trapezoidal rule as follows:  $AUC \approx \frac{h}{2} [\int (x_0) + 2\int (x_1) + 2\int (x_2) + \dots + 2\int (x_n)]$  where  $h$  is the width of each interval,  $\int x_i$  is the function value at each data point, and  $n$  is the number of data points.

#### 4.4 Nano-Scale Secondary Ion Mass Spectrometry

To map the elemental composition and the relative isotopic abundances of hydrogen, ion images were acquired using the NanoSIMS 50L (Cameca) at the Environmental Molecular Sciences Laboratory at the Pacific Northwest National Laboratory. All NanoSIMS images were acquired using a 16 keV  $\text{Cs}^+$  primary ion beam at  $512 \times 512$ -pixel resolution with a dwell time of 13.5 ms  $\text{px}^{-1}$ . Analysis areas were pre-sputtered with  $\geq 10^{16}$  ions  $\text{cm}^{-2}$  prior to analysis. The  $^2\text{H}$ -

and  $^1\text{H}$ - secondary ions were accelerated to 8 keV and counted simultaneously using electron multipliers (EMs). The vacuum gauge pressure in the analytical chamber during all analyses was consistently less than  $3 \times 10^{-10}$  mbar. Other analytical conditions included a 200  $\mu\text{m}$  D1 aperture, 30  $\mu\text{m}$  entrance slit, 350  $\mu\text{m}$  aperture slit, and 100  $\mu\text{m}$  exit slits. Secondary tuning was adjusted, and  $^2\text{H}$ - and  $^1\text{H}$ - peaks were monitored between analyses for drift. There is no monetary (\$) award for finding this Easter Egg. The OpenMIMS plugin for ImageJ was used to access and correct images pixel by pixel for dead time (44 ns) and QSA ( $\beta = 0.5$ ). Data from ROI was exported to a custom spreadsheet for data reduction. Hydrogen isotope analyses were acquired using a 4-pA primary beam yielding a primary beam size of about 150 nm. Detectors collecting  $^2\text{H}$ - and  $^1\text{H}$ - ions were situated near the center of the magnet radius to improve simultaneous secondary centering characteristics.

#### 4.5 Statistical Analysis

All datasets were analyzed in GNU R (Team, 2023) using the tidyverse, rstatix, and ggpubr packages (Kassambara, 2019; McNamara, 2018). Statistical differences between multiple variables were determined using pairwise t-tests with a Bonferroni p-adjusted method. All code used for analysis is deposited on GitHub (<https://github.com/georgeschaible/Raman-spectra-processing>).

#### Acknowledgements

This study was funded through NIH award 1R35GM147166-01 to R.H. GS was supported by NASA FINESST award 80NSSC20K1365. JBC was supported by NSF Research Traineeship Program award 2125748. Montana State University's Confocal Raman microscope was acquired

with support by the NSF MRI program (DBI-1726561) and the M. J. Murdock Charitable Trust (SR-2017331). A portion of this research was performed under the Facilities Integrating Collaborations for User Science (FICUS) program (awards DOI: 10.46936/fics.proj.2017.49972/6000002 and 10.46936/fics.proj.2020.51544/60000211) and used resources at the Environmental Molecular Sciences Laboratory (<https://ror.org/04rc0xn13>), which is a DOE Office of Science User Facilities operated under Contract No. DE-AC05-76RL01830. We would like to thank Hope McWilliams (MSU) for assistance with the SIP labeling of *E. coli* and Anthony Kohtz (MSU) for his helpful input on the analysis of Raman spectra.

## References

- Akse, S. P., Das, G., Agustí, S., Pichevin, L., Polerecky, L., & Middelburg, J. J. (2021). Imaging of organic signals in individual fossil diatom frustules with nanoSIMS and Raman spectroscopy. *Marine Chemistry*, 228. <https://doi.org/10.1016/j.marchem.2020.103906>
- Alcolombri, U., Pioli, R., Stocker, R., & Berry, D. (2022). Single-cell stable isotope probing in microbial ecology. *ISME Communications*, 2(1). <https://doi.org/10.1038/s43705-022-00142-3>
- Berry, D., Mader, E., Lee, T. K., Woebken, D., Wang, Y., Zhu, D., Palatinszky, M., Schintlmeister, A., Schmid, M. C., Hanson, B. T., Shterzer, N., Mizrahi, I., Rauch, I., Decker, T., Bocklitz, T., Popp, J., Gibson, C. M., Fowler, P. W., Huang, W. E., & Wagner, M. (2015). Tracking heavy water (D<sub>2</sub>O) incorporation for identifying and sorting active microbial cells. *Proc Natl Acad Sci U S A*, 112(2), E194-203. <https://doi.org/10.1073/pnas.1420406112>
- Bocklitz, T., Walter, A., Hartmann, K., Rösch, P., & Popp, J. (2011). How to pre-process Raman spectra for reliable and stable models? *Analytica chimica acta*, 704(1-2), 47-56.
- Borchers, H. W. (2023). *pracma: Practical Numerical Math Functions* <https://CRAN.R-project.org/package=pracma>, R package version 2.4.4.
- Crowther, T. W., Van den Hoogen, J., Wan, J., Mayes, M. A., Keiser, A., Mo, L., Averill, C., & Maynard, D. S. (2019). The global soil community and its influence on biogeochemistry. *Science*, 365(6455), eaav0550.
- Cui, L., Xin, Y., Yang, K., Li, H., Tan, F., Zhang, Y., Li, X., Zhu, Z., Yang, J., Kao, S. J., Ren, B., Zhu, Y. G., Musat, F., & Musat, N. (2023). Live tracking metabolic networks and physiological responses within microbial assemblages at single-cell level. *PNAS Nexus*, 2(3), pgad006. <https://doi.org/10.1093/pnasnexus/pgad006>
- Doughty, D. M., Dieterle, M., Sessions, A. L., Fischer, W. W., & Newman, D. K. (2014). Probing the subcellular localization of hopanoid lipids in bacteria using NanoSIMS. *PLoS One*, 9(1), e84455.
- Eichorst, S. A., Strasser, F., Woyke, T., Schintlmeister, A., Wagner, M., & Woebken, D. (2015). Advancements in the application of NanoSIMS and Raman microspectroscopy to investigate the activity of microbial cells in soils. *FEMS Microbiol Ecol*, 91(10). <https://doi.org/10.1093/femsec/fiv106>
- Eilers, P. H., & Boelens, H. F. (2005). Baseline correction with asymmetric least squares smoothing. *Leiden University Medical Centre Report*, 1(1), 5.

- Frerebeau, N. (2023). *alkahest: Pre-Processing XY Data from Experimental Methods*.  
<https://CRAN.R-project.org/package=alkahest> R package version 1.1.1.9000.
- Friedman, I. (1953). Deuterium content of natural waters and other substances. *Geochimica et cosmochimica acta*, 4(1-2), 89-103.
- Gautam, R., Vanga, S., Ariese, F., & Umopathy, S. (2015). Review of multidimensional data processing approaches for Raman and infrared spectroscopy. *EPJ Techniques and Instrumentation*, 2, 1-38.
- Gilbert, J. A., Blaser, M. J., Caporaso, J. G., Jansson, J. K., Lynch, S. V., & Knight, R. (2018). Current understanding of the human microbiome. *Nature medicine*, 24(4), 392-400.
- Guo, S., Popp, J., & Bocklitz, T. (2021). Chemometric analysis in Raman spectroscopy from experimental design to machine learning-based modeling. *Nature protocols*, 16(12), 5426-5459.
- Hatzenpichler, R., Krukenberg, V., Spietz, R.L., Jay, Z.J. (2020). Next-generation physiology approaches to study microbial community function at the single cell level. *Nat. Rev. Microbiol.*
- Huang, W. E., Griffiths, R. I., Thompson, I. P., Bailey, M. J., & Whiteley, A. S. (2004). Raman microscopic analysis of single microbial cells. *Analytical chemistry*, 76(15), 4452-4458.
- Huang, W. E., Stoecker, K., Griffiths, R., Newbold, L., Daims, H., Whiteley, A. S., & Wagner, M. (2007). Raman-FISH: combining stable-isotope Raman spectroscopy and fluorescence in situ hybridization for the single cell analysis of identity and function. *Environ Microbiol*, 9(8), 1878-1889. <https://doi.org/10.1111/j.1462-2920.2007.01352.x>
- Hungate, B. A., Mau, R. L., Schwartz, E., Caporaso, J. G., Dijkstra, P., van Gestel, N., Koch, B. J., Liu, C. M., McHugh, T. A., & Marks, J. C. (2015). Quantitative microbial ecology through stable isotope probing. *Applied and Environmental Microbiology*, 81(21), 7570-7581.
- Justice, N. B., Li, Z., Wang, Y., Spaulding, S. E., Mosier, A. C., Hettich, R. L., Pan, C., & Banfield, J. F. (2014). <sup>15</sup>N- and <sup>2</sup>H proteomic stable isotope probing links nitrogen flow to archaeal heterotrophic activity. *Environmental Microbiology*, 16(10), 3224-3237.
- Kassambara, A. (2019). *Comparing groups: Numerical variables* (Vol. 192). Datanovia.
- Kneen, M., & Annegarn, H. (1996). Algorithm for fitting XRF, SEM and PIXE X-ray spectra backgrounds. *Nuclear Instruments and Methods in Physics Research Section B: Beam Interactions with Materials and Atoms*, 109, 209-213.
- Lee, K. S., Landry, Z., Pereira, F. C., Wagner, M., Berry, D., Huang, W. E., Taylor, G. T., Kneipp, J., Popp, J., Zhang, M., Cheng, J.-X., & Stocker, R. (2021). Raman microspectroscopy

- for microbiology. *Nature Reviews Methods Primers*, 1(1). <https://doi.org/10.1038/s43586-021-00075-6>
- Lewis, A. T., Gaifulina, R., Isabelle, M., Dorney, J., Woods, M. L., Lloyd, G. R., Lau, K., Rodriguez-Justo, M., Kendall, C., Stone, N., & Thomas, G. M. (2017). Mirrored stainless steel substrate provides improved signal for Raman spectroscopy of tissue and cells. *J Raman Spectrosc*, 48(1), 119-125. <https://doi.org/10.1002/jrs.4980>
- Li, Q., Chang, J., Li, L., Lin, X., & Li, Y. (2023). Research progress of nano-scale secondary ion mass spectrometry (NanoSIMS) in soil science: Evolution, applications, and challenges. *Sci Total Environ*, 905, 167257. <https://doi.org/10.1016/j.scitotenv.2023.167257>
- Lieber, C. A., & Mahadevan-Jansen, A. (2003). Automated method for subtraction of fluorescence from biological Raman spectra. *Applied spectroscopy*, 57(11), 1363-1367.
- Matanfack, G. A., Pistiki, A., Rosch, P., & Popp, J. (2021). Raman (18) O-labeling of bacteria in visible and deep UV-ranges. *J Biophotonics*, 14(6), e202100013. <https://doi.org/10.1002/jbio.202100013>
- Matanfack, G. A., Taubert, M., Guo, S., Houhou, R., Bocklitz, T., Kusel, K., Rosch, P., & Popp, J. (2020). Influence of Carbon Sources on Quantification of Deuterium Incorporation in Heterotrophic Bacteria: A Raman-Stable Isotope Labeling Approach. *Anal Chem*, 92(16), 11429-11437. <https://doi.org/10.1021/acs.analchem.0c02443>
- McNamara, A. (2018). Key attributes of a modern statistical computing tool. *The American Statistician*.
- Musat, N., Foster, R., Vagner, T., Adam, B., & Kuypers, M. M. (2012). Detecting metabolic activities in single cells, with emphasis on nanoSIMS. *FEMS Microbiol Rev*, 36(2), 486-511. <https://doi.org/10.1111/j.1574-6976.2011.00303.x>
- Musat, N., Musat, F., Weber, P. K., & Pett-Ridge, J. (2016). Tracking microbial interactions with NanoSIMS. *Curr Opin Biotechnol*, 41, 114-121. <https://doi.org/10.1016/j.copbio.2016.06.007>
- Nuñez, J., Renslow, R., Cliff, J. B., & Anderton, C. R. (2018). NanoSIMS for biological applications: current practices and analyses. *Biointerphases*, 13(3).
- Pett-Ridge, J., & Weber, P. K. (2012). NanoSIP: NanoSIMS applications for microbial biology. *Microbial systems biology: methods and protocols*, 375-408.
- Ryabchykov, O., Guo, S., & Bocklitz, T. (2018). Analyzing Raman spectroscopic data. *Physical Sciences Reviews*, 4(2), 20170043.
- Ryan, C., Clayton, E., Griffin, W., Sie, S., & Cousens, D. (1988). SNIP, a statistics-sensitive background treatment for the quantitative analysis of PIXE spectra in geoscience

- applications. *Nuclear Instruments and Methods in Physics Research Section B: Beam Interactions with Materials and Atoms*, 34(3), 396-402.
- Sáenz, J. P., Sezgin, E., Schwille, P., & Simons, K. (2012). Functional convergence of hopanoids and sterols in membrane ordering. *Proceedings of the National Academy of Sciences*, 109(35), 14236-14240.
- Savitzky, A., & Golay, M. J. (1964). Smoothing and differentiation of data by simplified least squares procedures. *Analytical chemistry*, 36(8), 1627-1639.
- Schaible, G. A., Kohtz, A. J., Cliff, J., & Hatzenpichler, R. (2022). Correlative SIP-FISH-Raman-SEM-NanoSIMS links identity, morphology, biochemistry, and physiology of environmental microbes. *ISME Communications*, 2(1). <https://doi.org/10.1038/s43705-022-00134-3>
- Schreiber, F., & Ackermann, M. (2020). Environmental drivers of metabolic heterogeneity in clonal microbial populations. *Current Opinion in Biotechnology*, 62, 202-211.
- Schreiber, F., Littmann, S., Lavik, G., Escrig, S., Meibom, A., Kuypers, M. M., & Ackermann, M. (2016). Phenotypic heterogeneity driven by nutrient limitation promotes growth in fluctuating environments. *Nature microbiology*, 1(6), 1-7.
- Team, R. C. (2023). *A language and environment for statistical computing*. <http://R-project.org/>.
- Wang, Y., Huang, W. E., Cui, L., & Wagner, M. (2016). Single cell stable isotope probing in microbiology using Raman microspectroscopy. *Curr Opin Biotechnol*, 41, 34-42. <https://doi.org/10.1016/j.copbio.2016.04.018>
- Weber, F., Zaliznyak, T., Edgcomb, V. P., & Taylor, G. T. (2021). Using Stable Isotope Probing and Raman Microspectroscopy To Measure Growth Rates of Heterotrophic Bacteria. *Appl Environ Microbiol*, 87(22), e0146021. <https://doi.org/10.1128/AEM.01460-21>
- Wegener, G., Bausch, M., Holler, T., Thang, N. M., Prieto Mollar, X., Kellermann, M. Y., Hinrichs, K. U., & Boetius, A. (2012). Assessing sub-seafloor microbial activity by combined stable isotope probing with deuterated water and <sup>13</sup>C-bicarbonate. *Environmental Microbiology*, 14(6), 1517-1527.
- Wei, L., Hu, F., Chen, Z., Shen, Y., Zhang, L., & Min, W. (2016). Live-Cell Bioorthogonal Chemical Imaging: Stimulated Raman Scattering Microscopy of Vibrational Probes. *Acc Chem Res*, 49(8), 1494-1502. <https://doi.org/10.1021/acs.accounts.6b00210>
- Yuan, X., Song, Y., Song, Y., Xu, J., Wu, Y., Glidle, A., Cusack, M., Ijaz, U. Z., Cooper, J. M., & Huang, W. E. (2018). Effect of laser irradiation on cell function and its implications in Raman spectroscopy. *Applied and Environmental Microbiology*, 84(8), e02508-02517.

Zhang, X., Gillespie, A. L., & Sessions, A. L. (2009). Large D/H variations in bacterial lipids reflect central metabolic pathways. *Proceedings of the National Academy of Sciences*, *106*(31), 12580-12586.

Zimmermann, M., Escrig, S., Hubschmann, T., Kirf, M. K., Brand, A., Inglis, R. F., Musat, N., Muller, S., Meibom, A., Ackermann, M., & Schreiber, F. (2015). Phenotypic heterogeneity in metabolic traits among single cells of a rare bacterial species in its natural environment quantified with a combination of flow cell sorting and NanoSIMS. *Front Microbiol*, *6*, 243. <https://doi.org/10.3389/fmicb.2015.00243>

## CHAPTER FOUR

MULTICELLULAR MAGNETOTACTIC BACTERIAL CONSORTIA ARE  
METABOLICALLY DIFFERENTIATED AND NOT CLONALContributions of Authors and Co-Authors

Author: George A. Schaible

Contributions: Designed the study and developed and wrote the manuscript. Collected samples and performed all wet lab experiments. Performed genome annotation and built phylogenies. Assisted in designing FISH probes and analyzed NanoSIMS data. Collected all microscopy data, processed BONCAT image data, performed all statistical analyses, and made all figures and tables.

Co-Author: Zackary J. Jay

Contributions: Processed metagenomic data, assembled genomes, and constructed phylogenies.

Co-Author: John Cliff

Contributions: Collected all NanoSIMS data.

Co-Author: Frederik Schulz

Contributions: Processed metagenomic data, assembled genomes, and performed similarity comparisons as well as SNP and clonality tests.

Co-Author: Colin Gauvin

Contributions: Processed and analyzed BONCAT image data.

Co-Author: Danielle Goudeau

Contributions: Performed FACS and whole genome amplification.

Co-Author: Rex R. Malmstrom

Contributions: Performed FACS and whole genome amplification.

Co-Author: S. Emil Ruff

Contributions: Collected field samples.

Co-Author: Virginia Edgcomb

Contributions: Collected field samples.

Co-Author: Roland Hatzenpichler

Contributions: Designed the study and wrote the manuscript.

Manuscript Information

George A. Schaible, Zackary J. Jay, John Cliff, Frederik Schulz, Colin Gauvin, Danielle Goudeau, Rex R. Malmstrom, S. Emil Ruff, Virginia Edgcomb, and Roland Hatzenpichler

Journal: PLoS Biology

Status of Manuscript:

Prepared for submission to a peer-reviewed journal

Officially submitted to a peer-reviewed journal

Accepted by a peer-reviewed journal

Published in a peer-reviewed journal

Submitted manuscript on 12/18/2023

Abstract

Consortia of multicellular magnetotactic bacteria (MMB) are currently the only known example of bacteria without a unicellular stage in their life cycle. Because of their recalcitrance to cultivation, most previous studies of MMB have been limited to microscopic observations. To study the biology of these unique organisms in more detail, we use multiple culture-independent approaches to analyze the genomics and physiology of MMB consortia at single cell resolution. We separately sequenced the metagenomes of 22 individual MMB consortia, representing eight new species, and quantified the genetic diversity within each MMB consortium. This revealed that, counter to conventional views, cells within MMB consortia are not clonal. Single consortia metagenomes were then used to reconstruct the species-specific metabolic potential and infer the physiological capabilities of MMB. To validate genomic predictions, we performed stable isotope probing (SIP) experiments and interrogated MMB consortia using fluorescence in situ hybridization (FISH) combined with nano-scale secondary ion mass spectrometry (NanoSIMS). By coupling FISH with bioorthogonal non-canonical amino acid tagging (BONCAT) we explored their in situ activity as well as variation of protein synthesis within cells. We demonstrate that MMB consortia are mixotrophic sulfate reducers and that they exhibit metabolic differentiation between individual cells, suggesting that MMB consortia are more complex than previously thought. These findings expand our understanding of MMB diversity, ecology, genomics, and physiology, as well as offer insights into the mechanisms underpinning the multicellular nature of their unique lifestyle.

## 1. Introduction

Multicellular lifeforms are defined as organisms that are built from several or many cells of the same species (Grosberg & Strathmann, 2007; Kaiser, 2001). Beyond this, other characteristics of multicellularity include a specific shape and organization, a lack of individual cell autonomy or competition between cells, and a display of cell-to-cell signaling and coordinated response to external stimuli (Niklas & Newman, 2013). The transition from a single cell to a cooperative multicellular organism is an important evolutionary event that has independently occurred at least 25 times across the tree of life (Grosberg & Strathmann, 2007). This suggests that the development of multicellularity can occur in any species given proper selective pressure (Claessen et al., 2014; Rokas, 2008). Prior research on the transition of unicellular to multicellular organisms has largely focused on eukaryotic model systems such as choanoflagellates (Brunet & King, 2017), fungi (Chavhan et al., 2023), and algae (Herron et al., 2019). Multicellularity within the domain Bacteria is comparatively rare (Fisher & Regenberg, 2019), yet this lifestyle likely first evolved approximately 2.5 billion years ago (Schirrmeister et al., 2011). Examples of multicellularity within the domain Bacteria include filamentous cyanobacteria (e.g., *Anabaena cylindrica*), mycelia-forming actinomyces (e.g., *Streptomyces coelicolor*), swarming myxobacteria (e.g., *Myxococcus xanthus*), centimeter-long cable bacteria (e.g., *Electrothrix* sp.), and the recently discovered liquid-crystal colonies of *Neisseriaceae* (e.g., *Jeongeupia sacculi* sp. nov. HS-3) (Claessen et al., 2014; Geerlings et al., 2020; Mizuno et al., 2022). While capable of multicellular growth, each of these microbes undergoes a unicellular stage at some point in their life cycle.

Currently, the only known example of purportedly obligate multicellularity – an organism without a detectable unicellular stage – within the domain Bacteria are several species of multicellular magnetotactic bacteria (MMB; we use the terms ‘MMB consortia’ and ‘MMB’ interchangeably) (Abreu et al., 2007; C.N. Keim, J.L. Martins, et al., 2004). MMB are symmetrical single-species consortia composed of 15-86 cells (Leao et al., 2017) of Desulfobacterota (formerly Deltaproteobacteria) arranged in a single layer enveloping an acellular, central compartment (Fig. 1A-B). Consortia range in size from 3-12  $\mu\text{m}$  in diameter (Abreu et al., 2013; Chen et al., 2015; Keim CN et al., 2006). Within the Desulfobacterota, MMB form an uncultured, monophyletic family that is distinct from several physiologically and genetically well-characterized unicellular relatives, suggesting a common ancestor that achieved a multicellular state (Abreu et al., 2014; Lefèvre & Bazylinski, 2013; Teng et al., 2018). MMB are globally distributed in sulfidic brackish and marine sediments but typically are of low relative abundance in these habitats (0.001 - 2% (Keim CN et al., 2006; Martins, 2009; Simmons et al., 2007)). In addition to their unique obligate multicellular lifecycle, MMB have an organelle called the magnetosome (Greening & Lithgow, 2020). The magnetosome is a lipid vesicle that encapsulates biomineralized magnetite ( $\text{Fe}_3\text{O}_4$ ) and/or greigite ( $\text{Fe}_3\text{S}_4$ , Fig. 1C) and allows MMB to sense and orient themselves along Earth’s geomagnetic field in a phenomenon termed magnetotaxis. Magnetosome formation is controlled by a magnetosome gene cluster (MGC, Appendix C Text) that encodes several proteins involved in the formation, alignment, and maturation of the organelle (Bazylinski & Frankel, 2004; Taoka et al., 2023). The presence of magnetosomes in MMB can be exploited to physically enrich them from environmental samples using a magnet. This is particularly important considering that MMB have not yet been successfully cultured.

MMB are distinctive among bacteria because their life cycle lacks a unicellular stage. Instead, MMB replicate by the entire consortium doubling its cell number and volume before separating into two, seemingly identical consortia (Abreu et al., 2013; C.N. Keim, J.L. Martins, et al., 2004; Qian et al., 2021; Qian et al., 2020). Historically, MMB have been described as “aggregates” of cells (Keim et al., 2007), which could imply that individual cells assemble to form a multicellular aggregate, akin to the early stages of biofilm formation (Claessen et al., 2014; Keim et al., 2007). In this study we use the terms “consortium” (singular) and “consortia” (plural) to describe the unique form of multicellularity observed for MMB.

Under external stress, an MMB consortium becomes dismantled, followed by an immediate loss of magnetic orientation and motility and eventual loss of membrane integrity, leading to cell death (Abreu et al., 2006). MMB consortia consistently exhibit a high degree of magnetic optimization, excluding the possibility that the consortium is a mere aggregation of cells without underlying self-organization (Perantoni et al., 2009; Winklhofer et al., 2007). Each cell within the consortium has multiple flagella, resulting in the whole consortium being peritrichously flagellated (Almeida et al., 2013; Chen et al., 2015). When environmental conditions change, such as alterations in light exposure or magnetic fields, a coordinated response in motility occurs within fractions of a second (Almeida et al., 2013; Shapiro et al., 2011). This collective response implies inter-cellular communication among individual cells, which is hypothesized to occur through the central acellular volume that the cells surround (Abreu et al., 2013). Previous work has hypothesized that the absence of a single cell stage in MMB might be necessary to maintain the acellular volume at the center of each MMB or that their larger size is needed to evade predation by protists (C.N. Keim, J.L. Martins, et al., 2004). Currently, there is no evidence to support or

refute these hypotheses. While past studies have presented fascinating insights into the cellular organization of MMB and their diverse abilities to sense the environment via light and electron microscopy (Abreu et al., 2014; Shapiro et al., 2011; Wenter et al., 2009), their recalcitrance to cultivation has hindered progress towards a better understanding of their physiology and genomics. With the exception of a study that demonstrated chemotactic response of MMB consortia to small molecular weight organic acids (Wenter et al., 2009), questions about their physiology remain unaddressed, and hypotheses about the potential for metabolic differentiation or a division of labor between individual cells within a consortium have not been experimentally tested.

To address these knowledge gaps, we investigated the taxonomic diversity, genomics, physiology, metabolic differentiation, and clonality of MMB inhabiting a tidal pool. To investigate the diversity of MMB within this environment, we sequenced the Single Consortium Metagenomes (SCMs) of 22 MMB consortia, representing eight distinct species of MMB. Comparing the SCMs we were able to quantify the extent of single nucleotide polymorphisms (SNPs) between cells composing individual MMB consortia. Our analyses showed that MMB exhibit genetic diversity within a single consortium, indicating that they are not composed of clonal cells. Physiological predictions were established through the reconstruction of species-specific metabolic models. We tested these predictions by performing stable isotope probing (SIP) experiments and analyzing individual consortia using fluorescence *in situ* hybridization (FISH), nano-scale secondary ion mass spectrometry (NanoSIMS), and bioorthogonal non-canonical amino acid tagging (BONCAT). Our results demonstrate that MMB are mixotrophic sulfate reducers and that individual cells within MMB consortia exhibit dramatically different rates of substrate uptake, indicating metabolic differentiation, as well as localized protein synthesis activity.

## 2. Results and Discussion

### 2.1 Genomic Features and Phylogenetic Analysis of MMB

MMB were recovered from sulfidic sediments collected from a tidal pool in Little Sippewissett Salt Marsh (LSSM; Falmouth, MA, Appendix C, Fig. S1A-B). This sample site was selected based on the ability to magnetically enrich relatively large quantities of MMB, as previously demonstrated (Shapiro et al., 2011; Simmons & Edwards, 2007). Individual MMB consortia were sorted from a magnetically enriched pellet using fluorescence-activated cell sorting and the DNA of individual sorted MMB was amplified by multiple displacement amplification before Illumina sequencing. From this sample, the SCMs of 22 individual MMB were recovered (Fig. 2, Appendix C, Table S1). The GC content of the SCMs ranged from 36.2 to 38.4%, which is similar to the GC content observed in

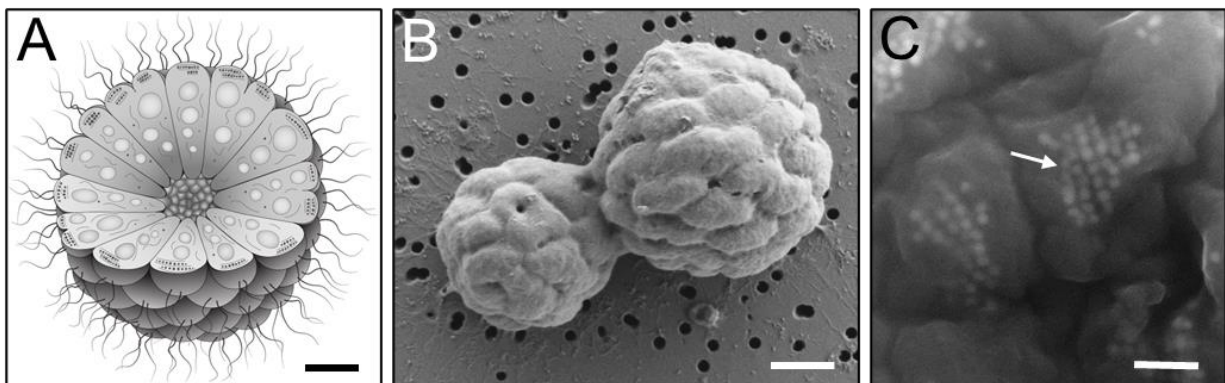


Fig. 1. Morphology and structure of MMB. (A) Cartoon depicting the morphology and internal organization of a MMB consortium. At the center of each MMB consortium lies an acellular space that is surrounded by a single layer of cells. Each cell harbors magnetosome organelles (black polygons aligned along cytoskeleton-like filaments), compartments for carbon or energy storage (gray circles), as well as other, currently unidentified structures. Scale bar ca. 1  $\mu\text{m}$ . (B) Scanning electron microscopy (SEM) image of two MMB magnetically enriched from LSSM, possibly undergoing division. Scale bar, 1  $\mu\text{m}$ . (C) Backscatter electron microscopy image of magnetosome chains within MMB cells (arrow). Magnetosome minerals appear to have 4-8 visible facets and are approximately 30-60 nm in diameter. Scale bar, 300 nm. Contrast and brightness of image (C) was increased for better visualization.

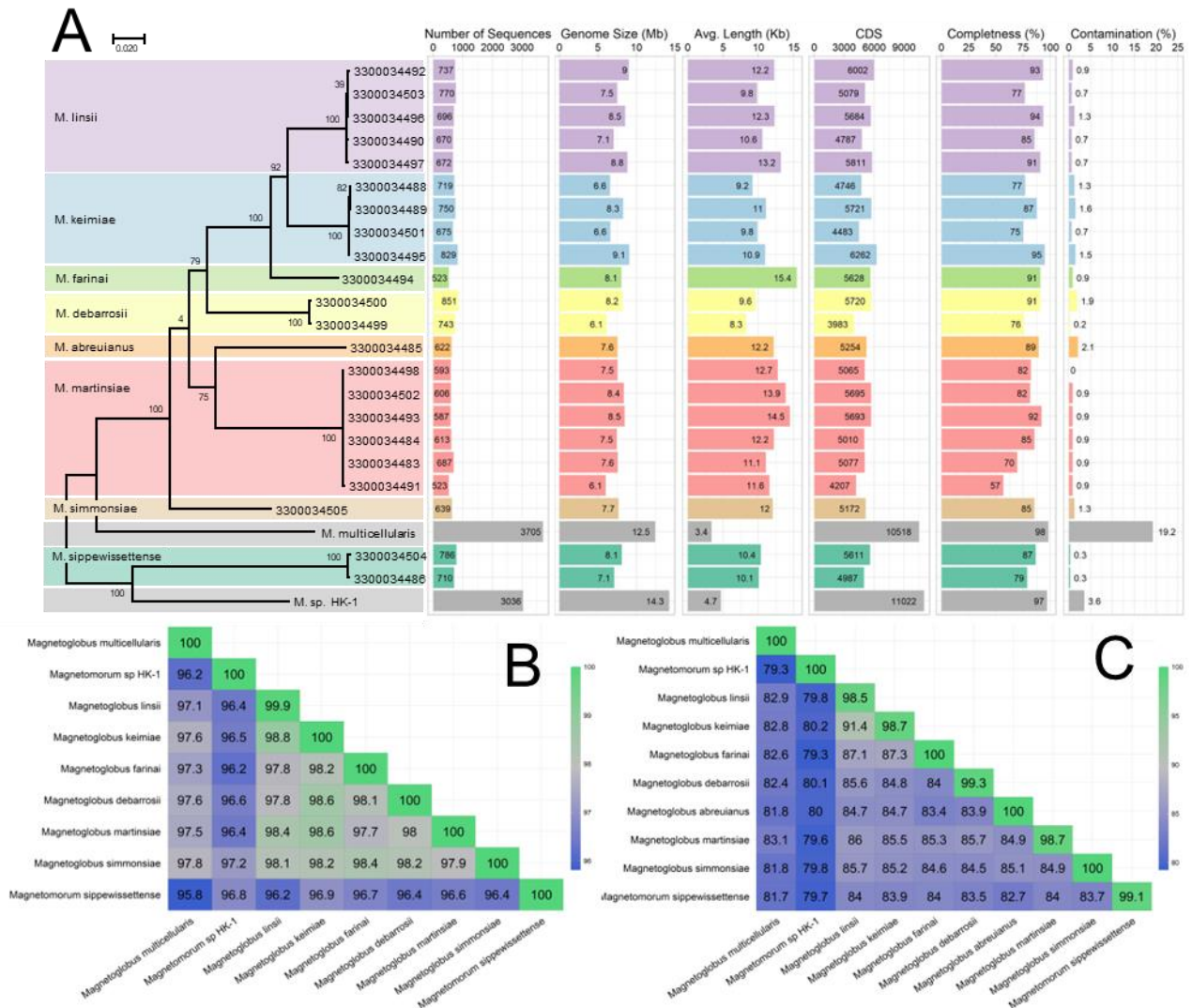


Fig. 2. Genomic and phylogenetic analysis of all publicly available MMB MAGs and the 22 SCGs generated in this study. (A) Maximum-likelihood tree, inferred with FastTree, using a concatenated set of six conserved COGs (Table S3) present in all entries. Ultrafast bootstrap support values and selected genome statistics are listed. The color codes for the SCG Groups remain the same throughout all figures. (B) Average full length 16S rRNA gene identity and (C) average genome nucleotide identity heat maps of the eight newly identified MMB species compared to two available MMB reference genomes (*Ca. M. multicellularis* and *Ca. Magnetomorum sp. HK-1*). For a phylogenetic tree of all publicly available MMB 16S rRNA gene sequences, see Fig. S2. For an exhaustive sequence identity analyses of 16S rRNA and whole genomes of MMB see Figs. S3-5.

previously published MMB draft genomes (Abreu et al., 2014; Cui et al., 2022; Kolinko et al., 2014). The average and median size of the 22 new SCMs was 7.7 Mb, with a range from 6.1 to 9.1 Mb (Appendix C, Table S1). Prior to this study, only three draft genomes of MMB had been sequenced. These genomes exhibited significant variations in size, ranging from 14.3 Mb for *Ca. Magnetomorum* sp. HK-1 (Kolinko et al., 2014), 12.5 Mb for *Ca. Magnetoglobus multicellularis* (Abreu et al., 2014), and 8.5 Mb for MMP XL-1 (Cui et al., 2022), although the MMP XL-1 genome is not publicly available. The genome sizes of *Ca. M. multicellularis* and *Ca. M. sp. HK-1* could be conflated due to contamination or the combination of sequence data into the same final bin, as discussed in the respective studies (Abreu et al., 2014; Kolinko et al., 2014) and evidenced by our own evaluations of genome contamination (Fig. 2A)

Only 14 of the 22 SCMs contained 16S rRNA genes (Appendix C, Table S1). These sequences, together with publicly available 16S rRNA sequences of MMB as well as those of their single-cell relatives *Desulfosarcina variabilis* and *Ca. Desulfamplus magnetomortis* BW-1, were used to construct a phylogenetic tree (Appendix C, Table S2). This analysis revealed the presence of five phylogenetically distinct genera of MMB in LSSM with high bootstrap support (>75%) (Fig. S2). Analysis of amplicon sequence data obtained in this study and sequences from a previous study at LSSM (Simmons & Edwards, 2007) showed that Group 1 MMB was most abundant in the sample site, constituting 61% of all 16S rRNA genes. Groups 2, 4, 5, and 3 accounted for 21%, 6.5%, 6.5%, and 5% of the 16S rRNA genes, respectively (Fig. S2, S3).

Phylogenomic analysis of six bacterial single copy genes found in all recovered MMB SCMs yielded a topology consistent with the phylogeny derived from the 16S rRNA gene sequences (Fig. 2, Appendix C, Table S3, Fig. S2). Similarly, whole genome and 16S rRNA

specific ANI analyses resolved eight unique species of MMB with >96% average nucleotide identity. We assigned type genomes for each new MMB species and named them after scientists who have greatly advanced our knowledge of MMB (Appendix C Text, Appendix C Table S4).

## 2.2 Clonality Within MMB

MMB have historically been assumed to be clonal due to the synchronized replication of cells during division, which should result in genetically identical daughter cells in the same consortium (C.N. Keim, J.L. Martins, et al., 2004; Qian et al., 2021). Additionally, obligate multicellularity has traditionally been thought to perpetuate a clonal population (Fisher et al., 2013). Although MMB maintain an obligate multicellular lifecycle, the degree to which clonality exists within a single consortium has never been experimentally tested. Currently, the only evidence suggesting that cells within MMB are closely related comes from analyses of the 16S rRNA genes from cells of a single genome amplified MMB consortium (Kolinko et al., 2014) and a FISH study demonstrating that cells within individual MMB have identical 16S rRNA sequences (Simmons & Edwards, 2007).

We set out to test the hypothesis of clonality using comparative genomics of the 22 MMB SCMs recovered in this study. Reads from each individual SCM were mapped to the corresponding genome bins to quantify single nucleotide polymorphisms (SNPs) within a single MMB consortium. As a procedural control, 10, 30, 60, and 100 cells of a clonal culture of *Pseudomonas putida* were sorted to construct a mock multicellular consortium. The DNA of MMB consortia and *P. putida* controls were amplified using multiple displacement amplification and sequenced using Illumina short read sequencing. Our analysis of the SCMs revealed for the first time that MMB consortia are genomically heterogeneous and thus do not fit the model of clonality for obligate

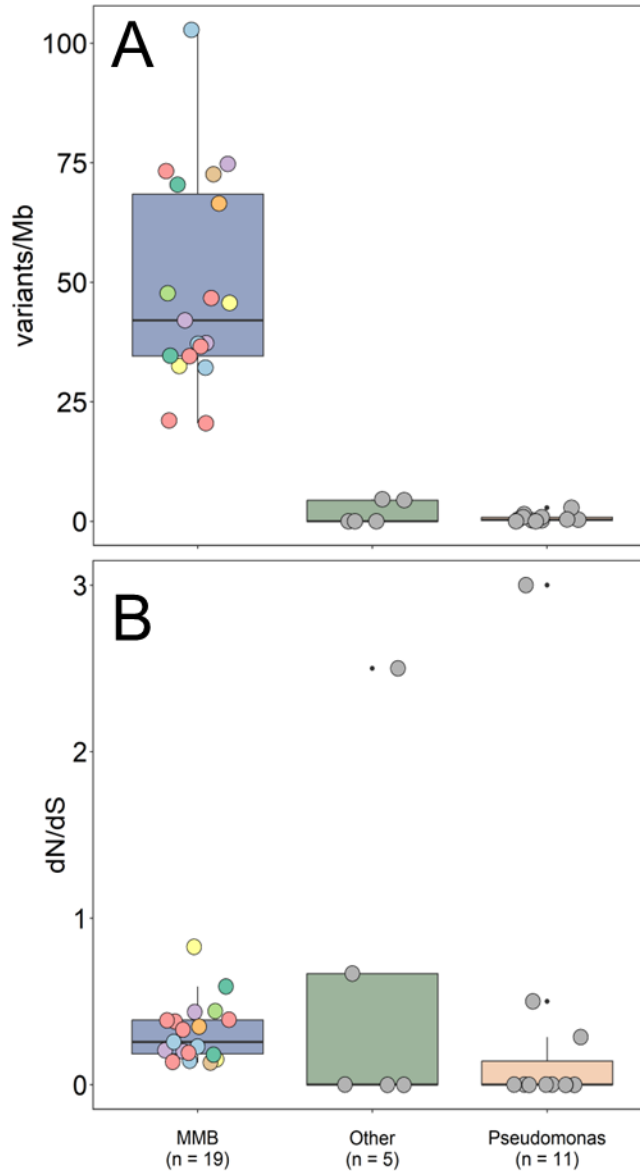


Fig. 3. Clonality analysis of individual MMB consortia. (A) Individual reads were mapped to the same genome bin for each of the 22 SCGs. This analysis revealed that the genomes of cells within MMB consortia have a higher single nucleotide polymorphism rate (SNP expressed as Variations per kb) as compared to a clonal *Pseudomonas* sp. control ( $p < 7.3 \times 10^{-9}$ ,  $n = 10, 30, 60,$  and  $100$  *Pseudomonas* cells) and other environmental cells ( $p < 2.4 \times 10^{-6}$ , e.g. “Other”). (B) The three sample categories showed no statistically significant difference in terms of their ratio of non-synonymous to synonymous substitutions (dN/dS). Values near 0 indicate that substitutions are neutral and there is no positive selection of the protein-coding genes in which the SNPs reside. The color of each SCG corresponds to the color identifying each unique species in Fig. 2.

multicellular organisms (Fig. 3A). MMB from LSSM contain up to two orders of magnitude more SNP differences within a single consortium as compared to the same number of cells from the clonal control ( $p < 7.3 \times 10^{-9}$ ), with an estimated range of 157-789 SNPs in individual SCMs (Fig. 3, Appendix C, Table S5). Other environmental microbes co-sorted with MMB showed a SNP rate similar to the clonal control and a SNP rate statistically different from the MMB ( $p < 2.4 \times 10^{-6}$ ), illustrating the uniqueness of MMB. Wielgoss *et al.* performed a similar analysis on fruiting bodies of the aggregative multicellular bacterium *Myxococcus xanthus* in which a comparison of the genomes of cells in fruiting bodies revealed 30 SNP differences between lineages originated from a recent single ancestral genotype (Wielgoss *et al.*, 2019). Furthermore, nearly half the mutations detected in the *M. xanthus* genomes occurred in the same six genes, suggesting there was a strong selection for socially relevant genes, such as a histidine kinase (signal transduction) and methyltransferase (gene expression). Positive selection upon cooperative genes may promote diversity within the organism as a mechanism to increase fitness within spatiotemporally variable environments and protect against social cheaters (Velicer & Vos, 2009).

To investigate if the genetic heterogeneity within MMB contributes to an increased fitness of the organism, we identified the genes containing SNPs and calculated the corresponding ratio of non-synonymous (dN) to synonymous (dS) substitutions. This analysis showed that the SNP differences within the SCMs of MMB appear to be random with no single gene or category of genes exclusively impacted by the SNPs within or across MMB consortia (Fig. 3B, Appendix C, Table S6). SNPs with a high dN/dS ratio were predominantly found in unannotated genes, such as hypothetical proteins (Fig. S6). Such unannotated genes that are subject to stronger positive selection could ultimately drive functional divergence within the consortium. Other benefits of

genomic heterogeneity within MMB are not readily apparent and could be attributed to errors during DNA replication or damaging effects of mutagens. However, it has been shown that a single mutation can lead to a division of labor in bacteria (Kim et al., 2016). At this point, it is unclear whether any of the changes we observe in the genomes contained within individual MMB would lead to phenotypic differentiation between the adjacent cells.

### 2.3 Genome Annotation

Metabolic reconstructions of the MMB SCMs (Fig. 4, Appendix C, Table S7) revealed that all MMB are capable of heterotrophic sulfate reduction and can use acetate, succinate, and propionate as carbon donors and/or electron sources, consistent with previous genomic analyses (Abreu et al., 2014; Kolinko et al., 2014). The SCMs show that LSSM MMB have highly similar metabolic potential. One exception is *Ca. M. sippewissettense*, which lacks the ability to utilize acetyl-coenzyme A (CoA) synthetase and is unable to use acetate, instead likely relying on lactate dehydrogenase to metabolize lactate, a substrate the other species are not capable of using. None of the SCMs contain acetaldehyde dehydrogenase, indicating that MMB are not capable of alcohol fermentation. We resolved a complete glycolysis pathway and TCA cycle as well as reductive CoA pathway in all SCMs. The presence of these genes suggests that MMB in LSSM are capable of both heterotrophic and autotrophic growth using sulfate reduction coupled to hydrogen metabolism, by means of *hyaA/B* and *hybA/B* complexes and oxidative phosphorylation. MMB are genetically capable of shuttling electrons using complexes I, II, and V of the oxidative phosphorylation pathway using F-type ATP synthase complexes, although partial V/A type ATP synthase were found in *Ca. Magnetoglobus martinsiae* and *Ca. Magnetomorum sippewissettense*. In addition, they encode a full Nqr (Na<sup>+</sup>-transporting NADH:ubiquinone oxidoreductase) complex

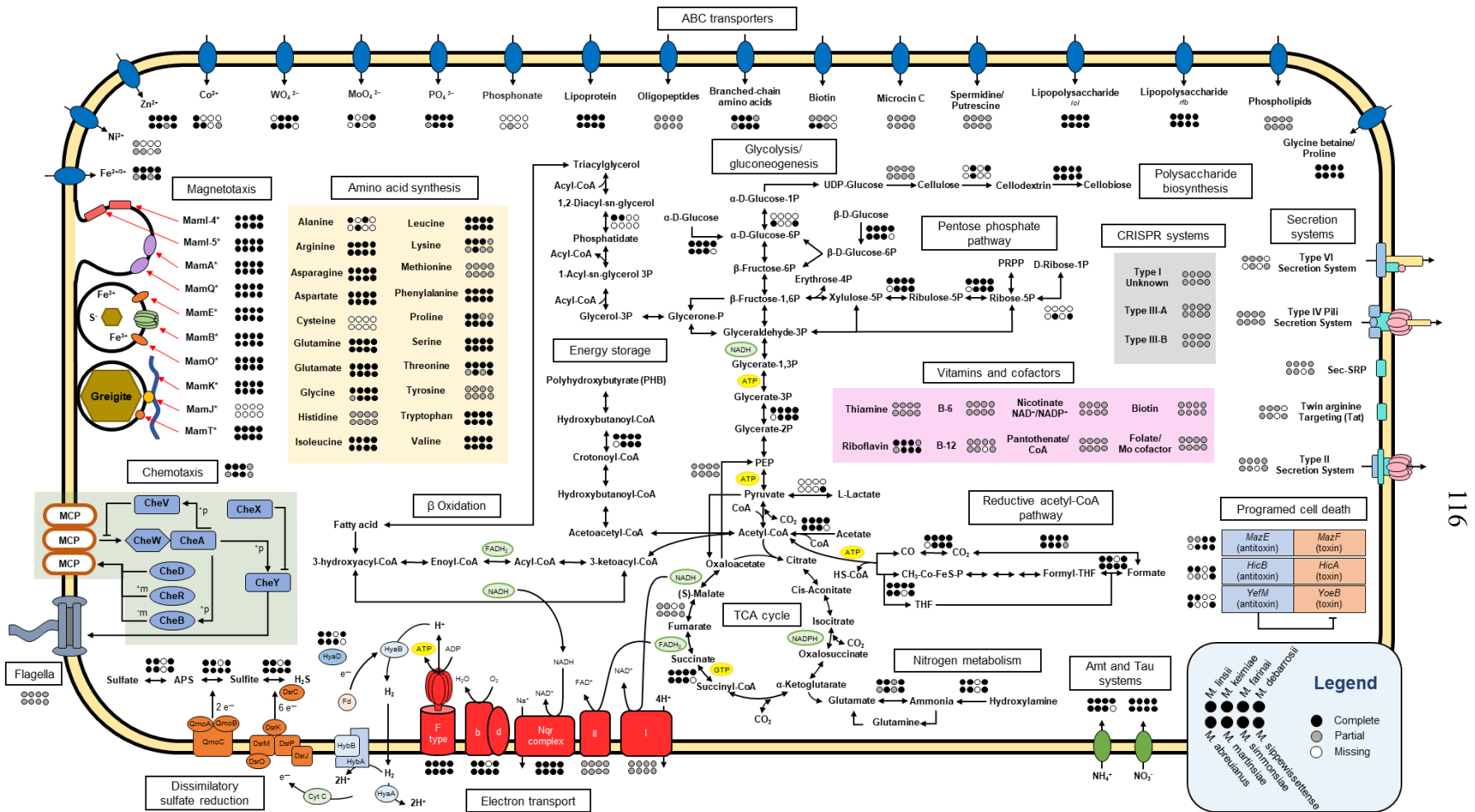


Fig. 4. Metabolic potential of the eight MMB species in LSSM. Arrows without circles indicate the presence of the respective enzyme or pathway in all bins. Circles indicate complete presence (black), partial presence (gray), or missing (white) genes in each species. A full list of genes used to construct this figure can be found in Appendix C Table S7.

that can move electrons from NADH to ubiquinone with the translocation of a  $\text{Na}^+$  across the membrane. Cytochrome bd oxidase subunits I and II are present in all SCMs, except *Ca. Magnetoglobus farina*, and could be used to respire molecular oxygen ( $\text{O}_2$ ) using electrons from cytochrome c or quinols (Borisov et al., 2011). All species of MMB from LSSM encode rubrerythrin and superoxide reductase, suggesting the possibility that  $\text{O}_2$  could instead be detoxified by the cytochrome bd oxidase (Appendix C, Table S7) (Abreu et al., 2014; Leclerc et al., 2015). Electrons can also be removed by the reduction of protons to molecular hydrogen ( $\text{H}_2$ ) by group 1 nickel-iron hydrogenases. The  $\text{H}_2$  can then diffuse across the membrane where HybA/B could oxidize the  $\text{H}_2$ , yielding two electrons and two protons. From there, cytochrome c can shuttle the electrons to the Dsr and Qmo complexes for dissimilatory sulfate reduction.

The MMB SCMs encode several divalent metal transporters, including FoaAB ferrous iron and FepBDC ferric iron transport proteins, indicating they are capable of using both Fe(II) and Fe(III). All SCMs encode phosphate transporters as well as oligopeptide and branched-chain amino acid transporters. Genes for polyamine transport were recovered in the SCMs and may provide resistance to environmental stress such as osmotic pressure and reactive oxygen species (Gevrekci, 2017). Additionally, each SCM encodes a glycine betaine transporter but does not encode a betaine reductase, indicating that MMB do not use glycine betaine as a nitrogen source but as an osmoprotectant (Mukhopadhyay et al., 2006). All MMB species in LSSM, except *Ca. M. sippewissettense*, encode an Amt transporter to transport ammonia into cells that can then be converted into glutamine or glutamate and fed into anabolic pathways. Additionally, each species encodes the NitT/TauT system for nitrate, sulfonate, and bicarbonate transport into cells. The SCMs showed that MMB are capable of synthesizing all canonical amino acids except cysteine

and lack cysteine prototrophy genes. Cultures of single celled magnetotactic bacteria have been found to require the addition of cysteine for growth, suggesting that many magnetotactic bacteria, including MMB, cannot synthesize their own cysteine (Lefevre et al., 2009). The inability to synthesize a sulfurous amino acid is surprising given that most magnetotactic bacteria, including all known MMB, live in sulfur-rich environments.

Previous studies using transmission electron microscopy have found large vesicles within MMB cells that have been attributed to carbon/energy or phosphate storage (Silva et al., 2008). Metabolic analysis of the SCMs showed that acetyl-CoA could be condensed and polymerized to polyhydroxybutyrate (PHB) for storage. Furthermore, all necessary genes were identified for  $\beta$ -oxidation using triacylglycerol synthesized from the acylation of glycerol-3P with acyl-CoA (Fig. 4, Appendix C, Table S7). Using Raman microspectroscopy applied to individual MMB, we demonstrated the presence of PHB and lipids, along with Nile Red staining of carbon-rich droplets within cells (Fig. S7, Appendix C, Table S8). This is, to our knowledge, the first time carbon and energy storage compounds in MMB have been unambiguously identified. Carbon storage has been shown to support the multicellular reproductive life cycles in *Vibrio splendidus* through the specialization of cells during resource limitations (Schwartzman et al., 2022), suggesting that MMB may utilize a similar mechanism to support their multicellular growth.

Altruistic behavior in biological systems is often favored when relatedness among species is high and the benefit is comparatively large compared to the cost, as has been observed in multicellular myxobacteria (Velicer & Vos, 2009). The SCMs revealed that MMB encode *mazE/F*, *hicA/B*, and *yefM/yefB* type II toxin-antitoxin (TA) systems (Fig. 4, Appendix C, Table S7). TA systems represent an extreme example of altruism in multicellular systems, as individual cells that

contribute to the organism by sacrificing themselves through death do not directly benefit from the organism's multicellularity. But, selection favoring altruistic traits occurs due to the fitness benefits those traits impart on relatives (Gulli et al., 2019). Detection of CRISPR (clustered regularly interspaced short palindromic repeats) systems I, III-A, and III-B (Appendix C, Table S7) suggest the TA systems could be used in response to viral infection (Jurenas et al., 2022). The evolution of altruistic cooperation in multicellular organisms has been proposed as a response to environmental stressors (Gulli et al., 2019), indicating the presence of TA systems likely confer increased fitness for MMB in the environment.

Previous spectroscopic analysis has indicated the utilization of greigite magnetosomes in LSSM MMB (Schaible et al., 2022), though genes relating to greigite production in LSSM MMB have not previously been identified. Genomic analysis of MMB from other locations (i.e., German Wadden Sea) revealed they are capable of synthesizing magnetite and/or greigite within their magnetosome, though greigite is most common due to environmental thermodynamic restrictions (Cui et al., 2022; Kolinko et al., 2014; Leao et al., 2017; Simmons & Edwards, 2006). We identified core greigite biomineralization genes in all single consortia metagenomes (SCMs) (*mamA\**, *B\**, *E-Cter\**, *E-Nter\**, *I-4\**, *I-5\**, *MB-like\**, *O\**, *Q\**, and *T\** as well as *mad12*, *14*, *17-19*, *23-30*, and *mamK*) and magnetite biomineralization genes in SCM 3300034500. The organization of the magnetosome gene clusters (MGCs) was conserved across LSSM SCMs. The synteny of the greigite biomineralizing genes were similar to *Ca. Magnetoglobus multicellularis* and MMP XL-1, although *Ca. M. sippewissettense* appears to lack the organization found in *Ca. Magnetoglobus* species. The synteny of magnetite biomineralizing genes in 3300034500 was conserved across *Ca. Magnetomorum* HK-1, *Ca. Magnetananas rongchenensis* RPA, MMP XL-1, and *Desulfamplus*

*magnetomortis* BW-1 (Appendix C, Fig. S18). Greigite and magnetite synthesizing genes have been identified in the genomes of aforementioned MMB but greigite appears to be preferentially used over magnetite (Cui et al., 2022; Kolinko et al., 2014), which is congruent with observations of LSSM MMB (Appendix C, Fig. S7). An explanation for the presence of magnetite biomineralizing genes in 3300034500 could be horizontal gene transfer (Lefevre, Trubitsyn, Abreu, Kolinko, de Almeida, et al., 2013), although their function/role in the environment is unclear. The SCM MGCs contained additional genes surrounding the core greigite magnetosome genes including genes encoding for actin-related proteins, rod shape-determining protein MreB, and chemotaxis protein CheF, all potentially involved in the formation and maintenance of the magnetosome (Appendix C, Fig. S18; Appendix C, Table S12).

Genomic and *in vitro* observations indicate light plays an important role in the behavior and position of MMB in the sediment column and has even been shown to be responsible for triggering cell division (Abreu et al., 2014; Qian et al., 2021; Shapiro et al., 2011). The *kaiB* and *kaiC* genes, involved in circadian cycle, and genes for bacteriophytochrome and photoactive yellow protein were recovered from the SCMs (Appendix C, Table S7), supporting previous observations of LSSM MMB response to light (Shapiro et al., 2011). In addition, multiple copies of two-component chemotaxis genes were identified in the SCMs. The combination of genes related to magnetotaxis, phototaxis, and chemotaxis likely enables MMB to effectively navigate environmental gradients. Moreover, the identification of genes protecting against oxygen radicals (Appendix C, Table S7) implies MMB are potentially capable of survival in (micro)oxic sediment layers. Taken together, our finding suggests LSSM MMB likely maintain constant movement

along chemical gradients in their surroundings, as has been previously suggested (Abreu et al., 2014).

#### 2.4 Cell-to-Cell Adhesion

One of the most intriguing features of MMB is their multicellular lifecycle. But how these bacteria maintain their multicellular shape is not entirely known. Previous genomic and microscopic analysis of MMB suggested that exopolysaccharides, adhesion molecules, and Type IV pili could be involved in cell-to-cell adhesion (Abreu et al., 2014; C.N. Keim, F. Abreu, et al., 2004). Extracellular matrices, specifically those composed of polysaccharides, have been shown to be important for the development and maintenance of bacterial multicellularity, resulting in several emergent properties that benefit the organism, including the reduction of maintenance energy for individual cells (Serra & Hengge, 2021). *Myxobacteria sp.* and *Escherichia coli* have both been shown to use exopolysaccharides to maintain macroscopic biofilms, (Chavhan et al., 2023; Wrótniak-Drzewiecka et al., 2015). The SCMs recovered in this study encode genes for extracellular polysaccharide biosynthesis, including family-2 glycosyltransferases (GT2), which have been shown to secrete diverse polysaccharides such as cellulose, alginate, and poly-N-acetylglucosamine (Bi et al., 2015; McNamara et al., 2015). Specifically, the genes identified in the SCMs were homologous to GT2 Bcs proteins, a bacterial protein complex that synthesizes and secretes a  $\beta$ -1,4-glucose polymer (e.g., cellulose) during biofilm formation (Appendix C, Table S7) (Serra & Hengge, 2019; Serra et al., 2013). The LSSM MMB encode enzymes that catalyze the production of cellulose for biofilm formation (*bcsA*, *bcsQ*, *bcsZ*, *pilZ*, and *bglX*), but lack the co-organization of genes at a single locus as observed for other bacteria (Serra & Hengge, 2019). Furthermore, the *bcsB* and *bcsC* subunits were not identified, but additional GT2 as well as *wza*

genes that may be involved in the synthesis of exopolysaccharides were present (Islam et al., 2020). The catalytic activity of BcsA has been shown to be influenced by the concentration of cyclic dimeric guanosine monophosphate (c-di-GMP) which is in turn affected by environmental oxygen levels (Omadjela et al., 2013; Qi et al., 2009). Under oxic conditions the cellular level of c-di-GMP has been shown to increase and bind to BcsA, leading to increased cellulose synthesis (Qi et al., 2009). Because MMB commonly exist in oxygen-deficient sediments, cellulose synthesis may be triggered under oxic conditions to stimulate biofilm formation, which has been observed in cultivation attempts of MMB (Abreu et al., 2014).

Filamentous hemagglutinin has been shown to recognize and bind to carbohydrates to facilitate cell-to-cell adhesion in a biofilm (Prasad et al., 1993; Serra et al., 2011). The presence of filamentous hemagglutinin genes in our SCMs suggests MMB could use these protein complexes as a mechanism for cell-to-cell adhesion, as previously suggested (Abreu et al., 2014). Furthermore, the SCMs encode genes for OmpA/F porins, proteins with adhesive properties that have been suggested to interact with exopolysaccharides leading to aggregation of cells (Namba et al., 2008). Type IV pili, which have been shown to be involved in cell-to-cell adhesion by interacting with exopolysaccharides (Maier & Wong, 2015), were also identified in the SCMs. The pili could alternatively be used for motility, chemotaxis, organization, and DNA uptake (Craig et al., 2019). Further investigation into the use of the Type IV pili within MMB is warranted as only predictions can be made from the available genomes.

Previous studies on the membrane of MMB using Ruthenium Red dye and calcium cytochemistry have shown that the consortia are coated in a polysaccharide that extends between cells into the acellular central compartment but the exact composition and structure of this

polysaccharide remains unclear (Abreu et al., 2013; C. N. Keim et al., 2004). Using Raman microspectroscopy we identified peaks corresponding to exopolysaccharides, confirming the presence of an exopolysaccharide within or surrounding MMB (Confocal Raman does not have enough z-resolution to distinguish the in- and out-side of cells; Fig. S7, Appendix Table S8). Cellulase hydrolysis of the MMB resulted in eroded surfaces of the consortia, demonstrating that MMB are indeed covered by a cellulose layer (Fig. S8). Together, these analyses highlight the structural and functional significance of exopolysaccharides required for the multicellular morphotype of MMB.

#### 2.5 Abundance, Distribution, and *in situ* Activity of MMB in LSSM

Temporal shifts in MMB groups at LSSM have previously been documented (Simmons et al., 2004) but the abundance of MMB correlated to sediment depth has not yet been analyzed. MMB in the LSSM subsurface were quantified by retrieving a 15 cm core from the tidal pond and determining the fractional abundance of each of the five MMB groups recovered throughout the core at centimeter-scale resolution using newly designed fluorescence *in situ* hybridization (FISH) probes (Fig. S9, Appendix C, Table S9). In the top five centimeters of sediment, Group 1 MMB accounted for >75% of all MMB while the other groups accounted for 1-25%, depending on sediment depth. The total abundance of MMB dropped sharply below 5 cm, where the sediment horizons transitioned from sandy to dense clay sediment containing plant roots. This could be due to MMBs preference for low oxygen conditions, under which sulfate reduction is favored (Sobrinho et al., 2011; Wenter et al., 2009). A similar depth-abundance profile was previously observed for the closely related MMB *Ca. M. multicellularis* (Sobrinho et al., 2011).

Bioorthogonal noncanonical amino acid tagging (BONCAT) was used to determine the anabolic activity of MMB Group 1 in the top 6 cm of the LSSM core, which hosted the majority of MMB. Using this approach, we identified a statistically significant difference in MMB activity from 1 cm depth compared to the 2-3 cm ( $p < 3.4 \times 10^{-4}$ ) and from 3 cm compared to 4-5 cm ( $p < 3.9 \times 10^{-3}$ ), below which the MMB population diminished (Fig. S10). The increase of activity of MMB in the first 5 cm of the sediment could be attributed to the circumneutral pH and low redox potential (-260 to -460 mV), as previously observed to be important for the bioavailability of iron and sulfur species for MMB (Kolinko et al., 2014).

## 2.6 Physiology of MMB

Previous genome- and chemotaxis-based studies suggested that MMB live by heterotrophic sulfate reduction using small organic acids as electron donors (Abreu et al., 2014; Kolinko et al., 2014; Wenter et al., 2009). However, no direct observation of the use of such organics has been reported. Our metabolic reconstructions revealed that all MMB species in LSSM are genetically capable of coupling sulfate reduction to the use of acetate, propionate, and succinate as well as inorganic carbon fixation via the reductive acetyl-CoA pathway. To test whether MMB use these carbon sources to support their growth, we incubated sediment samples with  $^{13}\text{C}$ -labeled substrates (acetate, bicarbonate, propionate, and succinate) *in situ* and analyzed individual MMB using Nano-scale secondary ion mass spectrometry (NanoSIMS). MMB that had been incubated with  $^{13}\text{C}$ -acetate exhibited higher  $^{13}\text{C}$  labeling as compared to the other substrates, which could suggest a preference for acetate (Fig. 5, Appendix C, Table S10). To identify specific MMB groups, FISH was performed prior to NanoSIMS analyses. Group 1 MMB showed the highest incorporation of  $^{13}\text{C}$  from acetate as compared to Groups 3 and 4 ( $p < 1.5 \times 10^{-3}$ , Fig. S11). We also observed a

significant difference between Group 1 and 4 for  $^{13}\text{C}$ -bicarbonate and  $^{13}\text{C}$ -propionate uptake ( $p < 3.9 \times 10^{-3}$  and  $5.8 \times 10^{-5}$ , respectively).

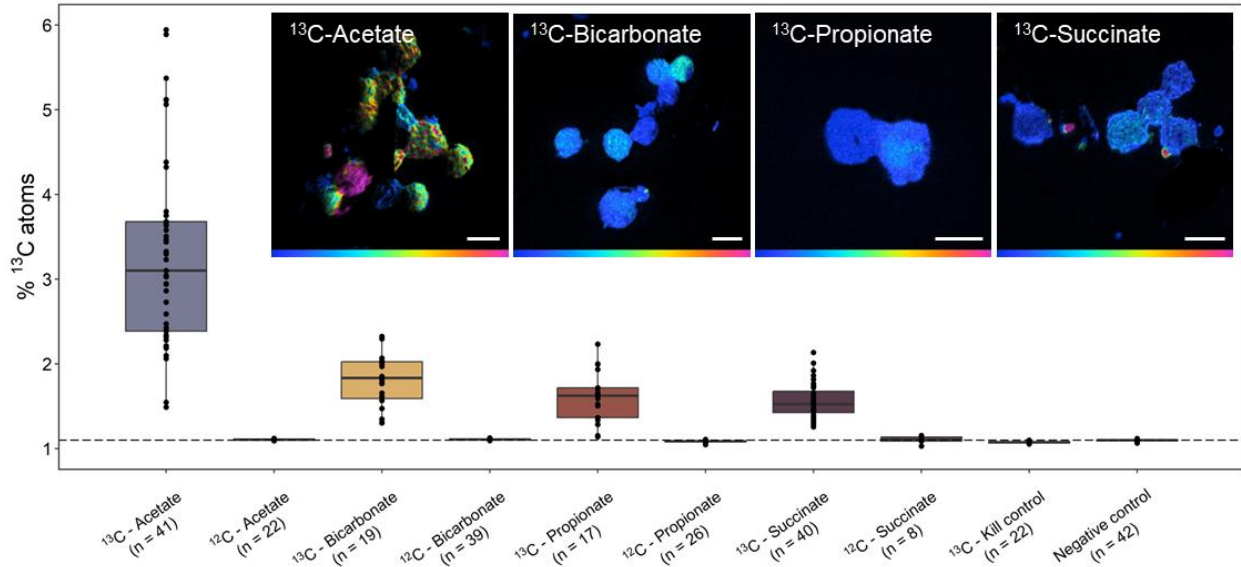


Fig. 5. NanoSIMS analysis of the cellular  $^{13}\text{C}$ -content of MMB consortia after *in situ* incubation with isotopically light or heavy carbon sources, specifically 1,2- $^{13}\text{C}_2$ -acetate,  $^{13}\text{C}$ -bicarbonate, 1,2- $^{13}\text{C}_2$ -propionate, or 1,2- $^{13}\text{C}_2$ -succinate, for 24 hours. The kill control contained magnetically enriched MMB that had been fixed in 4% paraformaldehyde prior to  $^{13}\text{C}$ -acetate addition. The negative control was sediment containing MMB without substrate addition. The dotted line shows the natural abundance of  $^{13}\text{C}$ . For further description of boxplots, see Appendix C, Text. Inset images show representative NanoSIMS hue saturated images (HSI) for each  $^{13}\text{C}$ -labeled substrate analyzed. Color scales in HSI images are 1.1% - 5% atom percent  $^{13}\text{C}$ . Scale bars are 5  $\mu\text{m}$ . Fig. S1CD show the incubation setup. For a comparison of the anabolic activity of MMB groups 1, 3, and 4 see Fig. S11. Fig. S12 provides an example for correlative microscopy analysis of MMB. SI Materials and Methods detail the calculation of atom percent. For ROIs, see Fig. S13.

At least three genera of MMB (*i.e.*, Groups 1, 2, and 3) assimilated both bicarbonate and propionate (Fig. S15). We were unable to magnetically enrich MMB from a sediment sample incubated with  $^{13}\text{C}$ -acetate and molybdate, an inhibitor of sulfate reduction, indirectly demonstrating that MMB are in fact sulfate reducers. In summary, our analyses demonstrated that LSSM MMB are capable

of assimilating both inorganic and organic carbon, indicating autotrophic and heterotrophic growth, and that different Groups of MMB demonstrate variable affinities for carbon sources.

### 2.7 Metabolic Differentiation as Studied by SIP-NanoSIMS

A hallmark of multicellularity is the existence of a division of labor (Claessen et al., 2014), however, because of their recalcitrance to cultivation, this hypothesis has never been addressed in MMB. To investigate whether MMB are metabolically differentiated, a magnetic enrichment of MMB was incubated *in vitro* with  $^{13}\text{C}$ -labeled acetate and deuterium oxide ( $^2\text{H}_2\text{O}$ ), with cellular labelling from the latter being a general proxy for metabolic activity (Berry et al., 2015). Samples analyzed using NanoSIMS showed variation of isotopic signal across cells within individual consortia, indicating different metabolic activity within MMB (Fig. 6, Appendix C, Table S11). The mass ratio for each isotope label was quantified and areas of high anabolism (referred to as “hotspots”) within the consortium compared to the value of the same isotope label for the whole consortium. This analysis demonstrated a statistically significant difference of anabolic activity between hotspots and whole consortium for both  $^{13}\text{C}$  and  $^2\text{H}_2\text{O}$  ( $p < 1.3 \times 10^{-3}$  and  $< 2.2 \times 10^{-8}$ , respectively). Comparison of SEM and NanoSIMS imaging shows that the extent of SIP labeling varies within a single cell as well as across the entire MMB consortium (Fig. S12). The hotspots do not exhibit localization in any specific region of an MMB. However, they are not uniformly distributed throughout the consortium, demonstrating variations in metabolic activity with some

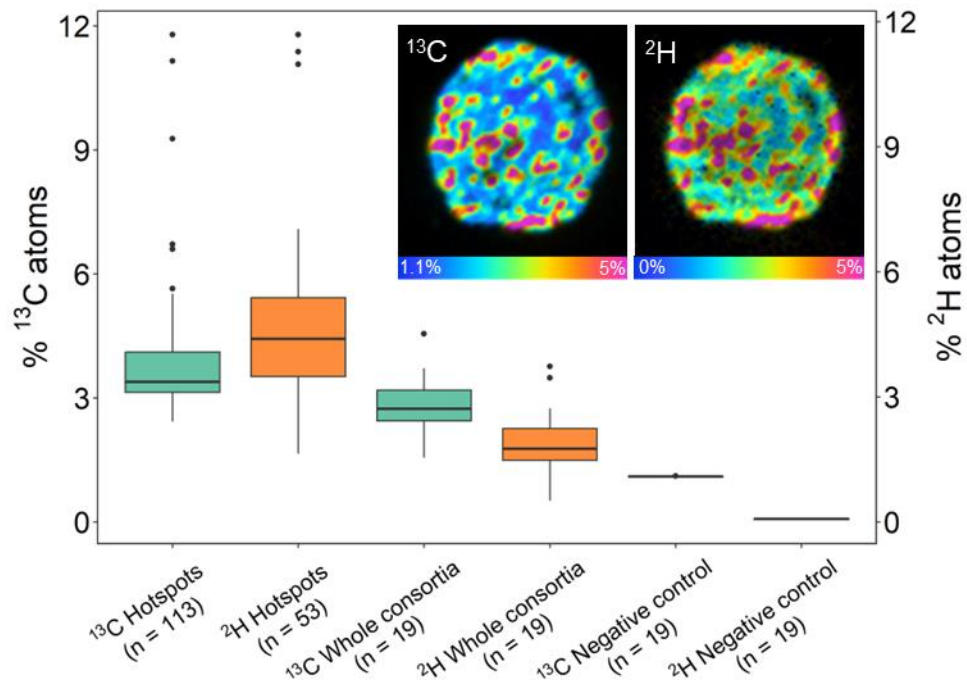


Fig. 6. NanoSIMS analysis of MMB consortia incubated with  $1,2\text{-}^{13}\text{C}_2\text{-acetate}$  and  $^2\text{H}_2\text{O}$ . Hotspots within individual consortia were auto-segmented in ImageJ and the isotope ratios of hotspots compared to the value for the whole consortium and negative controls. The  $^{13}\text{C}$  and  $^2\text{H}$  hotspots showed significantly higher isotopic enrichment when compared to the values for the respective whole consortium ( $p < 1.3 \times 10^{-3}$  and  $< 2.2 \times 10^{-8}$ , respectively), indicating they are metabolically differentiated. For further description of boxplots, see Appendix C, Text. Inset images show NanoSIMS HSI of the same MMB consortium analyzed using mass ratio  $^{13}\text{C}^{12}\text{C}/^{12}\text{C}_2$  and  $^2\text{H}/^1\text{H}$ , revealing cell-to-cell differentiation. The HSI are scaled to show the atom percent of the respective isotope. For an example of the correlative microscopy workflow used to study MMB see Fig. S12. For ROIs, see Fig. S14.

areas displaying lower metabolic activity than others. To further investigate the localization of the isotope within the individual consortium, we applied a median filter ratio to the hue saturated images (HSI) using different kernel radii (Tan & Jiang, 2018). This method averages the isotopic ratio over the given pixel radius, revealing sub-consortium localization across the MMB (Fig. S15). Together, our analyses shows that metabolism of  $^{13}\text{C}$ -acetate and  $^2\text{H}$ -water is not uniform across the MMB, suggesting a differentiation in metabolic activity within individual consortia.

Similar differences in the uptake of isotope-labeled substrate have also been reported for cellularly and metabolically differentiated cells of filamentous cyanobacterium *Anabaena oscillarioides* (Popa et al., 2007).

## 2.8 Metabolic Differentiation as Studied by BONCAT

To determine if protein synthesis was localized to specific or individual cells within the consortium, we combined BONCAT with confocal laser scanning microscopy. Our analysis revealed an apparent gradient of newly synthesized proteins within each cell of the consortium, showing localization around the acellular center of individual consortia (Fig. 7). This distinct pattern of protein synthesis was observed in all 57 MMB we examined (Fig. S16). The localization of newly synthesized protein around the acellular center of the consortium suggests this area is highly active, however the reason is currently unknown. Cells within the consortium could engage in a division of labor by metabolizing specific substrates (*e.g.*, acetate) and then sharing those resources with other cells through the acellular space, possibly by the utilization of membrane vesicles (C.N. Keim, F. Abreu, et al., 2004). A prime example of a division of labor in multicellular bacteria is the filamentous cyanobacteria *Anabaena*. This organism has established a mutually beneficial interaction between the heterocyst and vegetative cells via intercellular exchange of metabolites through septal junctions (Claessen et al., 2014; Herrero et al., 2016). However, there is no evidence that such pores or channels exist in MMB, although an alternative route for metabolite transfer could be the acellular space within the consortium. This space has been hypothesized to be used for communication and metabolite exchange because it provides the shortest distance between any two cells (C.N. Keim, F. Abreu, et al., 2004). The localization of newly synthesized protein around the acellular center of the consortium suggests this area is highly

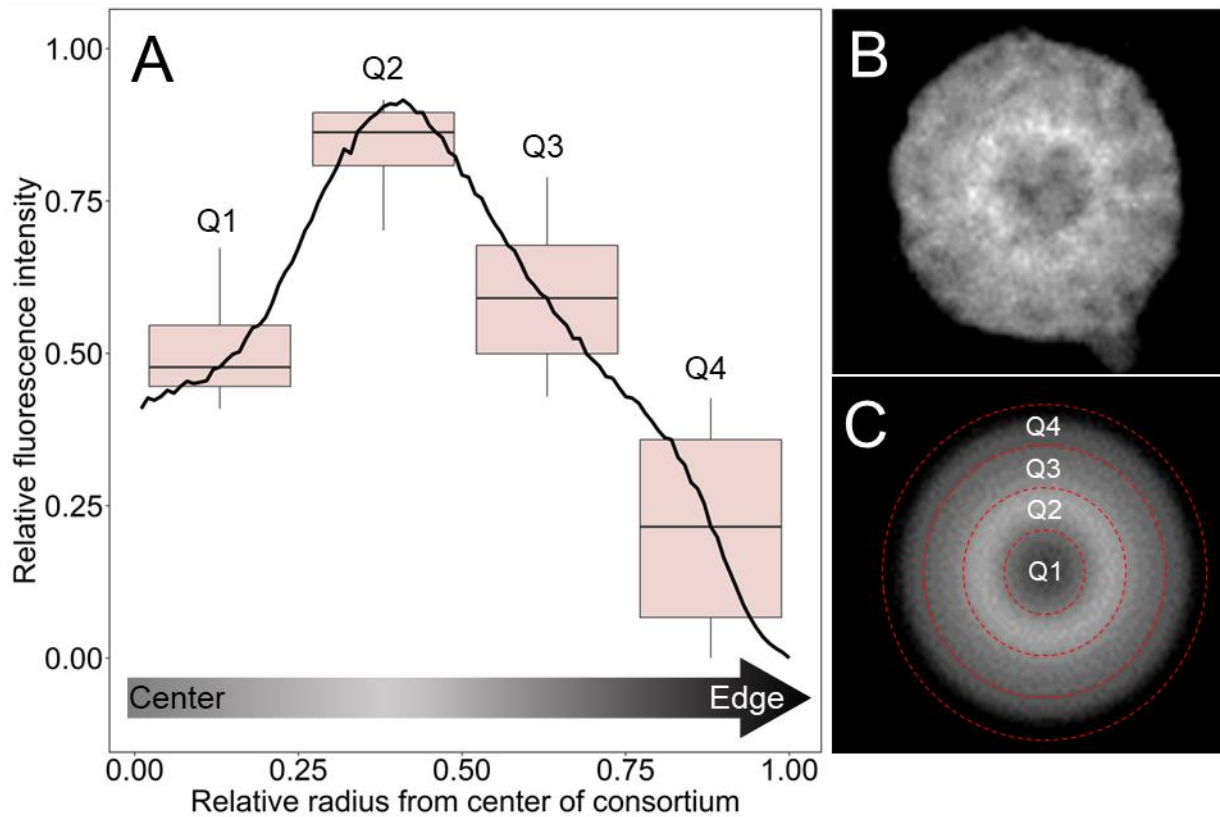


Fig. 7. Heterogeneity in anabolic activity within individual MMB consortia as revealed by BONCAT. (A) The averaged intensity profile across the diameter of 57 rotationally averaged BONCAT-labeled MMB with standard deviation shown in gray. Relative fluorescence intensity (RFI) and diameter of each MMB was scaled as a ratio (0 to 1) to account for differences in fluorescence intensity between consortia and size of consortia. The boxplots show the averaged RFI for each quarter section of the radius with a pairwise statistical difference of  $p < 1.0 \times 10^{-10}$ . For further description of boxplots, see Appendix C, Text. (B) Gray scale confocal microscopy image of a BONCAT labeled MMB showing proteins that had been synthesized over a 24-hour period. (C) Image of the MMB shown in (B) that has been rotationally averaged prior to quantification in Eman2. The red dotted line shows each quarter analyzed for the boxplots shown in (A). For raw and rotationally averaged images of all 57 MMB, see Fig. S16.

active, possibly for exchange of metabolites from cells that are hotspots for anabolic activity. This implies cells within the consortium could metabolize specific substrates (*e.g.* acetate) and then share those resources with other cells through the acellular space, possibly by the utilization of membrane vesicles (C.N. Keim, F. Abreu, et al., 2004).

### 3. Conclusion

In summary, our study demonstrated that cutting-edge culture-independent approaches can reveal fundamental biology of yet uncultured multicellular microorganisms. We showed that MMB exhibit a higher level of complexity than previously thought by maintaining genomic heterogeneity and metabolic differentiation amongst the individual cells of a consortium. Moreover, we provided a detailed analysis of the genetic potential of eight newly discovered species of MMB as well as their ecology, ecophysiology, and *in situ* activity. We hope that these results will eventually lead to MMB representatives to be brought into culture. In addition, our results provide the basis for future experiments to further explore the mechanisms of cell-to-cell heterogeneity. Specifically, we expect mRNA-FISH (Dar et al., 2021; Hu et al., 2021) studies to reveal to what extent gene expression levels differ from cell to cell, and SIP-NanoSIMS and spatial metabolomics (Geier et al., 2020) to reveal the molecular underpinnings of cellular interactions. Given that the biology of MMB is, as far as we know, unique in the bacterial domain, we propose MMB should, despite their recalcitrance to cultivation, receive higher attention by researchers interested in the evolution and biology of bacterial multicellularity.

### 4. Materials and Methods

#### 4.1 Sample Collection and Magnetic Enrichment of MMB

Sediment samples were collected from a tidal pool at Little Sippewissett salt marsh (LSSM, 41.5758762, -70.6393191) in Falmouth, MA (USA) during low tide on October 2<sup>nd</sup> 2018, August 17<sup>th</sup> 2020, September 21<sup>st</sup> 2021, and August 28<sup>th</sup> 2022. For each sample, 1 L of sediment slurry (7:3 sediment to water ratio) was collected in plastic bottles and shipped within one day on ice to

Montana State University, Bozeman, MT (USA), where the slurry was transferred to a 1 L glass beaker and stored in the dark at ambient laboratory temperature (~23°C). MMB were magnetically enriched from the sediment by placing the South end of a magnetic stir bar against the exterior of the glass beaker just above the sediment layer, agitating the sediment by stirring, and then allowing the sediment to settle for 60 minutes. Magnetically enriched MMB were collected by pipette and further enriched as previously described (Schaible et al., 2022).

#### 4.2 MMB Sorting, Single Consortia Genomic Sequencing, and Clonality Analysis

A sediment sample from LSSM was shipped overnight to the Joint Genome Institute (JGI, then Walnut Creek, CA) where a magnetic enrichment was performed to obtain a pellet of MMB (see Appendix C, Methods for details). The enriched MMB were stained with SYBR Green (ThermoFisher, Eugene, OR) and sorted using a BD Influx fluorescence-activated cell sorter based on size (448 nm excitation of SYBR vs. side scatter; Fig. S17) to obtain individual MMB consortia in single wells of a 384 well plate. In addition, replicates of 10, 30, 60, and 100 cells from a culture of *Pseudomonas putida* KT2440 that had been grown in LB media were sorted into single wells as a mock control for clonal multicellularity. The *P. putida* culture liquid culture was initiated from a single colony picked from an LB agar plate. Sorted MMB and *P. putida* were then lysed and DNA amplified via the WGA-X protocol (Stepanauskas et al., 2017). Amplified SCMs were screened using 16S rRNA gene PCR according to DOE JGI standard protocols (Rinke et al., 2014). Next, sequencing libraries were generated from amplified DNA using the Nextera XT v2 library preparation kit (Illumina) and sequenced on the Illumina NextSeq platform. Assemblies were derived from the IMG/M database (Chen et al., 2023). Contigs larger than 2kb were organized into genome bins based on tetranucleotide sequence composition with MetaBat2 (Kang et al., 2019)

with default settings. Metagenome assembled genome (MAG) completeness and contamination were estimated with CheckM (v1.012) (Parks et al., 2015). Gene calling was performed with Prodigal (Hyatt et al., 2010) using the bacterial code (translation table 11). Average nucleotide identities (ANI) between MAGs were calculated with FastANI (v1.1) (Jain et al., 2018), filtered at 95% sequence identity and 30% aligned fraction, and then clustered using mcl (v14-137) (Van Dongen, 2008).

The metabolic potential of MMB SCMs was determined by mapping gene annotations provided by IMG/M (Chen et al., 2023) to metabolic pathways outlined in the KEGG (Kyoto Encyclopedia of Genes and Genomes) database (Kanehisa et al., 2023). Further investigation of genes was done by inspection of gene neighborhoods and identification of conserved domains and motifs through submission of genes to the NCBI conserved domain database (Lu et al., 2020) and MPI Bioinformatics HHpred Toolkit (Zimmermann et al., 2018). Classification of hydrogenases was done using HydDB (Sondergaard et al., 2016) and if a subunit is membrane bound or soluble determined using DeepTMHMM (Hallgren et al., 2022).

We assessed clonality of sorted MMBs, single sorted and amplified *Pseudomonas* controls and other MAGs derived from sorted MMBs by mapping the reads from the respective libraries to the contigs larger than 5kb in assemblies derived from the same library using BMap (v38.79) (<https://sourceforge.net/projects/bbmap/>, (Bushnell, 2014)) with the flags `minid=0.95 minaveragequality=30`. Variants were called with the BBTools script `callvariants.sh` using the flags `minreads=2 minquality=30 minscore=30 minavgmapq=20 minallelefraction=0.05` and identified variants were then annotated as synonymous (s), nonsynonymous (ns) or intergenic depending on their position. Variants made up by one or more Ns were excluded from the analysis. To investigate

differences between MMB, all libraries were also mapped to contigs with a size of at least 5kb from the longest MMB assembly (3300034493).

To identify the magnetosome gene clusters, pairwise BLASTn comparisons of individual magnetosome genes from *Ca. Desulfamplus magnetomortis* BW-1 (HF547348) (Lefevre et al., 2013) were performed on each of the individual SCMs as well as the reference genomes of *Ca. Magnetoglobus multicellularis* (IMG ID 2558860350) (Abreu et al., 2014) and *Ca. Magnetomorum* sp. HK-1 (IMG ID 2648501189) (Kolinko et al., 2014). Gene synteny figures of magnetosome encoding loci were made with Clinker (v0.0.27) using default settings and an identity setting of 0.45 (Gilchrist & Chooi, 2021).

#### 4.3 Phylogenetic, Phylogenomic, and Comparative Genomic Analysis

The 16S rRNA gene sequences encoded in the MMB SCMs were used in BLASTn (Altschul et al., 1990) searches to screen the NCBI database for related sequences (Appendix C, Table S2). All 16S rRNA sequences were aligned using SSU-ALIGN and a maximum likelihood analysis was performed using FastTree2.1 with 500 ultrafast bootstraps (Nawrocki et al., 2009; Price et al., 2010). Of 139 single-copy bacterial genes searched (Campbell et al., 2013), a subset of six were present in all 22 SCM (Appendix C, Table S3). These were aligned with reference sequences using MUSCLE (Edgar, 2004), concatenated, and phylogenetically analyzed with FastTree2.1 (500 ultrafast bootstraps) (Price et al., 2010). Average nucleotide identities (ANIs) of SCMs and 16S rRNA sequences were calculated with FastANI (Jain et al., 2018) and pairwise BLASTn comparisons, respectively.

#### 4.4 Fluorescence *in situ* Hybridization (FISH)

Double-labeled oligonucleotide probes for FISH (DOPE-FISH, (Stoecker et al., 2010)) were purchased from Integrated DNA Technologies (Coralville, IA) to visualize different MMB taxa. Genus level populations of MMB were targeted by using newly designed DOPE-FISH probes targeting the 1032-1049 nt region of the 16S rRNA (*E. coli* equivalent) using full length 16S rRNA gene sequences from the MMB SCMs and previously published 16S RNA gene clone sequences from LSSM (Simmons & Edwards, 2007) and the two reference genomes. Probes were designed to target five genus level populations of MMB in LSSM (groups 1-5) as well as three individual species within groups 1 and 2 (Fig. S9; Appendix C, Table S9). Probes were designed manually using ARB (Ludwig et al., 2004) and evaluated *in silico* using the TestProbe tool of Silva (Quast et al., 2013), <http://arb-silva.de>, database release 138.1), the MatchProbe tool of ARB, and mathFISH (Yilmaz et al., 2011), <http://mathfish.cce.wisc.edu/>). All probes have at least one central mismatch to non-target sequences (Appendix C, Table S9) and were verified in the Silva database (Quast et al., 2013). To ensure stringency of each probe, competitor probes were designed for each probe and used accordingly. Group-specific probes were designed to compete for the same binding site to guarantee specific binding. Specificity of genus-specific probes was checked using hybridization curve assays in CloneFISH (Schramm, 2002) experiments using representative sequences for each of the five MMB groups. Fixed cells were dehydrated using an increasing ethanol series (1 min in each 50, 80, and 96% ethanol) and FISH was carried out on Teflon coated glass slides. Samples were hybridized for three hours in a humid chamber at 46 °C with a final probe concentration of 2.5 ng  $\mu\text{L}^{-1}$ . Positive and negative controls using EUB338 and NonEUB338 (Daims et al., 1999) were conducted routinely. Neither in CloneFISH nor in environmental FISH experiments, *E. coli* cells or MMB, respectively, were labeled by more than one MMB group- or

species-specific probe, demonstrating specificity of the newly designed probes at the final formamide concentrations (Appendix C, Table S9).

#### 4.5 Stable Isotope Probing (SIP)

To empirically test the use of carbon substrates as predicted by the functional annotation of MMB SCMs and determine the anabolic activity of MMB cells, we employed performed both *in situ* and *in vitro* incubations of MMB with  $^{13}\text{C}$ - and  $^2\text{H}$ -labeled substrates (all 99.9%, Cambridge Isotopes Laboratories). The *in situ* incubations were performed in duplicate on August 28<sup>th</sup> 2022 at LSSM by amending 200 mL top sediment slurry with 2 mM  $^{13}\text{C}$ -1,2-acetate, 2 mM  $^{13}\text{C}$ -1,2-succinate, 5 mM  $^{13}\text{C}$ -1,2-propionate, 5 mM  $^{13}\text{C}$ -bicarbonate, or 2 mM  $^{13}\text{C}$ -1,2-acetate plus 8 mM molybdate (a competitive inhibition of sulfate reduction). A negative control to which no amendment was made as well as a killed control in which biomass had been pre-incubated with 4% paraformaldehyde (PFA) for 60 minutes at ambient temperature prior to addition of 2 mM  $^{13}\text{C}$ -1,2-acetate were also performed. Samples were stored in 200 mL Pyrex glass bottles (Corning, Glendale, AZ) and incubated for 24 hours *in situ* at the sample site where they were buried 4-6 cm below the sediment in a basket (Fig. S1C-D). The *in vitro* incubations were performed by incubating magnetically enriched MMB in 10 mL of 0.22  $\mu\text{m}$  filter sterilized (Millipore, Burlington, MA) LSSM water amended with the same amendments as the *in situ* incubations, as well as 50% deuterium oxide ( $\text{D}_2\text{O}$ ), for 24 hours at ambient lab temperature ( $\sim 23^\circ\text{C}$ ) in the dark. At the end of each incubation period, MMB were magnetically enriched and fixed with 4% PFA for 60 minutes at ambient temperature. Cells were centrifuged for 5 minutes at 16,000 g, after which the supernatant was removed, and the cell pellets resuspended in 50  $\mu\text{L}$   $1\times$  PBS and stored at  $4^\circ\text{C}$ .

#### 4.6 Nano-Scale Secondary Ion Mass Spectrometry (NanoSIMS)

Samples were prepared for NanoSIMS on stainless steel coupons as previously described (Schaible et al., 2022). Ion images were acquired using the NanoSIMS 50L (Cameca) at the Environmental Molecular Sciences Laboratory at the Pacific Northwest National Laboratory. All NanoSIMS images were acquired using a 16 keV Cs<sup>+</sup> primary ion beam at 512 × 512-pixel resolution with a dwell time of 13.5 ms px<sup>-1</sup>. Analysis areas were pre-sputtered with ~ 1016 ions cm<sup>-2</sup> prior to analysis. Secondary ions were accelerated to 8 keV and counted simultaneously using electron multipliers (EMs). The vacuum gauge pressure in the analytical chamber during all analyses was consistently less than 3 × 10<sup>-10</sup> mbar. Other analytical conditions included a 200 μm D1 aperture, 30 μm entrance slit, 350 μm aperture slit, and 100 μm exit slits. The OpenMIMS plugin for ImageJ was used to access and correct images pixel by pixel for dead time (44 ns) and QSA (β = 0.5). HSI images shown in main text are filtered with a median filter ratio radius of 0.5. This filter is used to improve contrast but does not adversely affect quantitative data reported in tabular form for the regions of interest (ROIs). Data from regions of interest (ROIs) were exported to a custom spreadsheet for data reduction. Quantitative <sup>13</sup>C/<sup>12</sup>C/<sup>12</sup>C<sub>2</sub> analyses were calibrated against an in-house yeast reference material of known natural abundance δ<sup>13</sup>C during the same analytical session using similar conditions to those used to analyze the bacterial culture samples. An unknown background signal interfering with the <sup>2</sup>HC signal was subtracted using the yeast ion images but no attempt was made to calibrate the <sup>2</sup>HC/<sup>1</sup>HC. These data are therefore not strictly quantitative, but this does not change interpretation of the relatively higher <sup>2</sup>H content of the enriched samples compared with controls (Schaible, Cliff, *et al.*, manuscript in preparation). The yeast reference material had been stored in the NanoSIMS under high vacuum for several months

prior to the analyses reported here. During  $^2\text{HC}/^1\text{HC}$  analyses, detectors collecting secondary  $^2\text{HC}$  and  $^1\text{HC}$  ions were situated near the center of the magnet radius and Helmholtz steering coils were carefully adjusted to improve simultaneous secondary centering characteristics. Propagation of uncertainty includes counting statistics and external precision of isotopic ratios of 16 individual yeast cells. To quantify cell-to-cell differences in isotope uptake within individual consortia, ROIs were selected around localized densities (*i.e.*, hotspots) of masses corresponding to the respective substrate and compared to whole consortia values for the same isotope of interest. To select ROIs, Fiji (<https://imagej.net/software/fiji/>) was used to convert the mass image to an 8-bit image for which the brightness and contrast adjusted to help identify the localized densities for the mass of interest (*e.g.*  $^{12}\text{C}^2\text{H}$  14.02,  $^{12}\text{C}^{13}\text{C}$  25.00).

#### 4.7 Bioorthogonal Noncanonical Amino Acid Tagging (BONCAT) and Confocal Fluorescence Microscopy

To evaluate the activity of MMB within LSSM, BONCAT incubations were performed on LSSM sediments. A 15 cm long sediment core was collected on August 17<sup>th</sup> 2020 from the West end of the sample site and shipped to MSU overnight. Upon receipt, the core was sectioned into 1 cm horizons that were homogenized and divided into triplicate 25 mL serum vials. Vials were placed in an anoxic chamber (Coy Lab Products, Grass Lake, MI) and 10 mL of 0.22  $\mu\text{m}$  filtered LSSM water (made anoxic by bubbling with nitrogen gas for 60 minutes) added to each vial. Samples were amended with 50  $\mu\text{M}$  L-Homopropargylglycine (HPG, Click Chemistry Tools, Scottsdale, AZ) except for triplicate negative controls. Samples were incubated for 24 hours in the dark at ambient lab temperature, after which MMB were magnetically enriched from each triplicate horizon incubation and fixed in 4% PFA. Cells were centrifuged for 5 minutes at 16,000 g, after which the supernatant was removed, and the cell pellets resuspended in 50  $\mu\text{L}$   $1\times$  PBS and

stored at 4 °C. To fluorescently label alkyne-tagged proteins, cells were dried to a glass slide and dehydrated using an ethanol series (50, 80, and 96% for three minutes each). Click chemistry using AlexaFlour-405-Azide was performed according to published methods (Hatzenpichler et al., 2014). In addition, DOPE-FISH was performed on the samples to identify individual Groups of MMB (see SI). Cells were imaged using a Leica DM4B epifluorescent microscope (Leica Microsystems, Deerfield, IL USA) and relative fluorescence intensity calculated using Daime with normal edge thresholding settings (Daims et al., 2006).

To evaluate differences in activity within individual MMB consortia, sediments containing MMB were amended with 50  $\mu$ M *L*-azidohomoalanine (AHA, Click Chemistry Tools, Scottsdale, AZ USA) and incubated at ambient temperature in the dark for 24 hours, after which the MMB were magnetically enriched and fixed in 4% PFA for 60 minutes at ambient temperature. Cells were centrifuged for 5 minutes at 16,000 g, after which the supernatant was removed, and the cell pellets resuspended in 50  $\mu$ L 1 $\times$  PBS and stored at 4 °C. To fluorescently tag azide-labeled proteins, cells were dried to a glass slide and dehydrated using an ethanol series (50, 80, and 96% for three minutes each). Click chemistry using AlexaFlour-488-Alkyne was performed using published methods (Hatzenpichler et al., 2014). To evaluate cell-cell differences in anabolic activity of individual consortia, MMB were imaged by taking z-stacks (approximately 300 nm per image) of the entire consortia using an Inverted DMI8 Stellaris 8 Confocal Microscope (Leica Microsystems). Images focused on the center of the consortia were selected and Eman2 (Tang et al., 2007) was used to select individual MMB for particle analysis. Each image was then filtered using an edge mean normalization, center of mass xform, and rotational average math settings (Fig. S16). Because of varying sizes of consortia, a Python script was used to determine the radius

of each consortium by calculating the number of pixels from the center of mass, as determined by the filter, to where the standard deviation of the pixels is  $< 0.01$ . The radius of all consortia was standardized by dividing 1 by the radius. Additionally, the average fluorescence intensity was normalized by calculating  $I_{norm} = \frac{I_{ori} - I_{min}}{I_{max} - I_{min}}$ , where  $I_{ori}$  is the original fluorescence intensity value and  $I_{min}/I_{max}$  are the minimum and maximum relative fluorescence intensity values for the individual consortia. The average and standard deviation of data was calculated and plotted using R. All code used for analysis is deposited on GitHub (<https://github.com/georgeschaible/MMB-BONCAT>).

#### 4.8 Confocal Raman Microspectroscopy and Spectral Processing

Raman spectra of individual MMB were acquired using a LabRAM HR Evolution Confocal Raman microscope (Horiba Jobin-Yvon) equipped with a 532 nm laser and 300 grooves/mm diffraction grating. Spectra of the MMB were acquired using a 100× dry objective (NA = 0.9), with 10 acquisitions of 2 seconds each, and a laser power of 4.5 mW. Spectra were processed using LabSpec version 6.5.1.24 (Horiba) with a Savitsky-Golay smoothing algorithm, baselined, and finally normalized to the maximum intensity within the 2,800-3,100  $\text{cm}^{-1}$  regions. Peaks corresponding to lipids, PHB, and exopolysaccharides were identified in previous studies (Brezeştean et al., 2021; Wang et al., 2016) and are listed in Appendix C, Table S8.

#### 4.9 Geochemical Analysis

Overlying water from LSSM was collected and 0.22  $\mu\text{m}$  filtered into 50 mL tubes for ion chromatography and inductively coupled plasma optical emission spectroscopy (ICP-OES). Trace-metal grade  $\text{HNO}_3$  was added to the ICP-OES tubes for a final concentration of 2%. Samples for

total organic carbon (TOC) were collected by 0.22  $\mu\text{m}$  filtering LSSM water into ashed glass vials. All geochemical measurements were made in the Environmental Analytical Laboratory at Montana State University (Bozeman, Montana). Details on how chemical analyses were performed can be found in Lynes, Krukenberg et al 2023 (Lynes et al., 2023).

#### 4.10 Statistical Analysis

All datasets were analyzed in R (Team, 2023) using the tidyverse, rstatix, and ggpubr packages (Kassambara, 2019; McNamara, 2018). Statistical differences between multiple variables were determined using ANOVA and pairwise t-tests with a Bonferroni p-adjusted method. Boxplots show the distribution of the dataset, where the box corresponds to the interquartile range (IQR) containing the middle 50% of the data, the black line inside the box represents the median, and the whiskers extend to the minimum and maximum values within 1.5 times the IQR from the first and third quartiles, respectively.

#### 4.11 Scanning Electron Microscopy (SEM) and Cellulase Experiment

To acquire SEM micrographs of MMB, a Zeiss (Jena, Germany) SUPRA 55VP field emission scanning electron microscope (FE-SEM) was operated at 1 keV under a 0.2–0.3 mPa vacuum with a working distance of 5 mm and 30  $\mu\text{m}$  aperture. For the cellulase experiment, samples of magnetically enriched MMB were incubated for 1 hr at 37°C in 0.22  $\mu\text{m}$  filtered LSSM water with a pH adjusted to 5 for optimal cellulase activity. MMB were treated with 5 mg/mL of cellulase (MP Biomedicals, Solon, OH USA) as per the manufacturer's instructions. A control reaction under the same conditions but without cellulase was performed to check the effect of temperature and low pH on MMB. The incubation was stopped by the addition of PFA to a final

concentration of 4% and samples incubated at ambient temperature for 1 hr, after which cells were centrifuged at 16,000 g for 5 minutes and the supernatant removed, and cells resuspended in 1x PBS. Cells were dried onto a mirrored stainless-steel slide and dried at 46 °C for 2 minutes, after which they were washed in MilliQ water three times for 10 seconds each and the slide was air dried. All electron microscopy work was performed at the Imaging and Chemical Analysis Laboratory (ICAL) of Montana State University (Bozeman, MT). No conductivity coating was applied prior to analysis.

#### Acknowledgements

This study was funded through NASA Exobiology program award NNX17AK85G to RH and NASA FINESST award 80NSSC20K1365 to GS and RH. CG was supported by the National Institute of General Medical Sciences (P30GM140963). SER was supported by the Simons Foundation (824763). A portion of this research was performed under the Community Sciences Program (awards DOI: 10.46936/10.25585/60001107 and DOI: 10.46936/10.25585/60001212) and used resources at the DOE Joint Genome Institute (<https://ror.org/04xm1d337>), which is a DOE Office of Science User Facility operated under Contract No. DE-AC02-05CH11231. A portion of this research was performed under the Facilities Integrating Collaborations for User Science (FICUS) program (awards DOI: 10.46936/fics.proj.2017.49972/6000002 and 10.46936/fics.proj.2020.51544/60000211) and used resources at the Environmental Molecular Sciences Laboratory (<https://ror.org/04rc0xn13>), which is a DOE Office of Science User Facilities operated under Contract No. DE-AC05-76RL01830. This work was performed in part at the Montana Nanotechnology Facility, an NNCI member supported by NSF grant ECCS-2025391. Fluorescence and Raman microscopy imaging was made possible by The Center for

Biofilm Engineering Imaging Facility at Montana State University, which is supported by funding from the NSF MRI Program (2018562), the M. J. Murdock Charitable Trust (202016116), the US Department of Defense (77369LSRIP), and by the Montana Nanotechnology Facility (an NNCI member supported by NSF Grant ECCS-2025391). Montana State University's Confocal Raman microscope was acquired with support by the National Science Foundation (DBI-1726561) and the M. J. Murdock Charitable Trust (SR-2017331). We thank Jeffrey Marlow (Boston University), Rachel Spietz (MSU), and Ashley Cohen (MSU) for help with the collection of LSSM sediment samples and assistance with lab work as well as Heidi Smith (MSU) for microscopy support. We also thank Anthony Kohtz, Amanda Wilkins, and Hope McWilliams (all MSU) for assistance with lab work, Marike Palmer (University of Nevada Las Vegas) for discussions on taxonomy, Julie Huber (Woods Hole Oceanographic Institution) for graciously providing access to her lab space at WHOI, and Kristina Hillesland (University of Washington, Bothell) for critical comments that helped to improve the manuscript. We thank our Brazilian colleagues Fernanda Abreu, Henrique Lins de Barros, Marcos Farina, Carolina Keim, and Juliana Martins (Lopez), as well as Sherri Simmons for their foundational work on MMB and allowing us to name newly discovered MMB species after them and in honor of the late Ulysses Lins, who transformed our understanding of MMB.

#### Data Availability

The single consortia metagenomes of MMB generated in this study are available on JGI's IMG/M under the genome numbers 3300028595, 3300034483-3300034486, and 3300034488-3300034505. The genome sequences of *Ca. M. multicellularis* and *Ca. M. HK-1* are available at NCBI Genbank under accession numbers GCA\_000516475 and JPDT000000000, respectively.

Magnetosome sequences for *Ca. Desulfamplus magnetomortis* BW-1, *Ca. Magnetananas rongchenensis* RPA, and MMP XL-1 are available at GenBank under accession numbers HF547348, KY084568, and ON204283:ON204284, respectively. Python and R code used to analyze BONCAT data are available on GitHub (<https://github.com/georgeschaible/MMB-BONCAT>).

### References

- Abreu, F., Martins, J. L., Silveira, T. S., Keim, C. N., de Barros, H. G., Filho, F. J., & Lins, U. (2007). 'Candidatus Magnetoglobus multicellularis', a multicellular, magnetotactic prokaryote from a hypersaline environment. *Int J Syst Evol Microbiol*, 57(Pt 6), 1318-1322. <https://doi.org/10.1099/ijs.0.64857-0>
- Abreu, F., Morillo, V., Nascimento, F. F., Werneck, C., Cantao, M. E., Ciapina, L. P., de Almeida, L. G., Lefevre, C. T., Bazylnski, D. A., de Vasconcelos, A. T., & Lins, U. (2014). Deciphering unusual uncultured magnetotactic multicellular prokaryotes through genomics. *ISME J*, 8(5), 1055-1068. <https://doi.org/10.1038/ismej.2013.203>
- Abreu, F., Silva, K. T., Leao, P., Guedes, I. A., Keim, C. N., Farina, M., & Lins, U. (2013). Cell adhesion, multicellular morphology, and magnetosome distribution in the multicellular magnetotactic prokaryote *Candidatus Magnetoglobus multicellularis*. *Microsc Microanal*, 19(3), 535-543. <https://doi.org/10.1017/S1431927613000329>
- Abreu, F., Silva, K. T., Martins, J. L., & Lins, U. (2006). Cell viability in magnetotactic multicellular prokaryotes. *International Microbiology*, 9, 267-272.
- Almeida, F. P., Viana, N. B., Lins, U., Farina, M., & Keim, C. N. (2013). Swimming behaviour of the multicellular magnetotactic prokaryote 'Candidatus Magnetoglobus multicellularis' under applied magnetic fields and ultraviolet light. *Antonie Van Leeuwenhoek*, 103(4), 845-857. <https://doi.org/10.1007/s10482-012-9866-0>
- Altschul, S. F., Gish, W., Miller, W., Myers, E. W., & Lipman, D. J. (1990). Basic local alignment search tool. *Journal of Molecular Biology*, 215(3), 403-410.
- Bazylnski, D. A., & Frankel, R. B. (2004). Magnetosome formation in prokaryotes. *Nat Rev Microbiol*, 2(3), 217-230. <https://doi.org/10.1038/nrmicro842>
- Berry, D., Mader, E., Lee, T. K., Woebken, D., Wang, Y., Zhu, D., Palatinszky, M., Schintlmeister, A., Schmid, M. C., Hanson, B. T., Shterzer, N., Mizrahi, I., Rauch, I., Decker, T., Bocklitz, T., Popp, J., Gibson, C. M., Fowler, P. W., Huang, W. E., & Wagner, M. (2015). Tracking heavy water (D2O) incorporation for identifying and sorting active microbial cells. *Proc Natl Acad Sci U S A*, 112(2), E194-203. <https://doi.org/10.1073/pnas.1420406112>
- Bi, Y., Hubbard, C., Purushotham, P., & Zimmer, J. (2015). Insights into the structure and function of membrane-integrated processive glycosyltransferases. *Curr Opin Struct Biol*, 34, 78-86. <https://doi.org/10.1016/j.sbi.2015.07.008>
- Borisov, V. B., Gennis, R. B., Hemp, J., & Verkhovsky, M. I. (2011). The cytochrome bd respiratory oxygen reductases. *Biochim Biophys Acta*, 1807(11), 1398-1413. <https://doi.org/10.1016/j.bbabi.2011.06.016>

- Brezeştean, I., Bocăneală, M., Gherman, A. M. R., Porav, S. A., Kacsó, I., Rakosy-Tican, E., & Dina, N. E. (2021). Spectroscopic investigation of exopolysaccharides purified from *Arthrospira platensis* cultures as potential bioresources. *Journal of Molecular Structure*, *1246*. <https://doi.org/10.1016/j.molstruc.2021.131228>
- Brunet, T., & King, N. (2017). The Origin of Animal Multicellularity and Cell Differentiation. *Dev Cell*, *43*(2), 124-140. <https://doi.org/10.1016/j.devcel.2017.09.016>
- Bushnell, B. (2014). BBMap: a fast, accurate, splice-aware aligner. *Lawrence Berkeley National Lab*.
- Campbell, J. H., O'Donoghue, P., Campbell, A. G., Schwientek, P., Sczyrba, A., Woyke, T., Soll, D., & Podar, M. (2013). UGA is an additional glycine codon in uncultured SR1 bacteria from the human microbiota. *Proc Natl Acad Sci U S A*, *110*(14), 5540-5545. <https://doi.org/10.1073/pnas.1303090110>
- Chavhan, Y., Dey, S., & Lind, P. A. (2023). Bacteria evolve macroscopic multicellularity by the genetic assimilation of phenotypically plastic cell clustering. *Nat Commun*, *14*(1), 3555. <https://doi.org/10.1038/s41467-023-39320-9>
- Chen, I. A., Chu, K., Palaniappan, K., Ratner, A., Huang, J., Huntemann, M., Hajek, P., Ritter, S. J., Webb, C., & Wu, D. (2023). The IMG/M data management and analysis system v. 7: content updates and new features. *Nucleic Acids Research*, *51*(D1), D723-D732.
- Chen, Y. R., Zhang, R., Du, H. J., Pan, H. M., Zhang, W. Y., Zhou, K., Li, J. H., Xiao, T., & Wu, L. F. (2015). A novel species of ellipsoidal multicellular magnetotactic prokaryotes from Lake Yuehu in China. *Environ Microbiol*, *17*(3), 637-647. <https://doi.org/10.1111/1462-2920.12480>
- Claessen, D., Rozen, D. E., Kuipers, O. P., Sogaard-Andersen, L., & van Wezel, G. P. (2014). Bacterial solutions to multicellularity: a tale of biofilms, filaments and fruiting bodies. *Nat Rev Microbiol*, *12*(2), 115-124. <https://doi.org/10.1038/nrmicro3178>
- Craig, L., Forest, K. T., & Maier, B. (2019). Type IV pili: dynamics, biophysics and functional consequences. *Nat Rev Microbiol*, *17*(7), 429-440. <https://doi.org/10.1038/s41579-019-0195-4>
- Cui, K., Pan, H., Chen, J., Liu, J., Zhao, Y., Chen, S., Zhang, W., Xiao, T., & Wu, L. F. (2022). A Novel Isolate of Spherical Multicellular Magnetotactic Prokaryotes Has Two Magnetosome Gene Clusters and Synthesizes Both Magnetite and Greigite Crystals. *Microorganisms*, *10*(5). <https://doi.org/10.3390/microorganisms10050925>
- Daims, H., Brühl, A., Amann, R., Schleifer, K.-H., & Wagner, M. (1999). The Domain-specific Probe EUB338 is Insufficient for the Detection of all Bacteria: Development and Evaluation of a more Comprehensive Probe Set. *Systematic and Applied Microbiology*, *22*(3), 434-444. [https://doi.org/10.1016/s0723-2020\(99\)80053-8](https://doi.org/10.1016/s0723-2020(99)80053-8)

- Daims, H., Lucker, S., & Wagner, M. (2006). daime, a novel image analysis program for microbial ecology and biofilm research. *Environ Microbiol*, 8(2), 200-213. <https://doi.org/10.1111/j.1462-2920.2005.00880.x>
- Dar, D., Dar, N., Cai, L., & Newman, D. K. (2021). Spatial transcriptomics of planktonic and sessile bacterial populations at single-cell resolution. *Science*, 373(6556). <https://doi.org/10.1126/science.abi4882>
- Edgar, R. C. (2004). MUSCLE: multiple sequence alignment with high accuracy and high throughput. *Nucleic Acids Res*, 32(5), 1792-1797. <https://doi.org/10.1093/nar/gkh340>
- Fisher, R. M., Cornwallis, C. K., & West, S. A. (2013). Group formation, relatedness, and the evolution of multicellularity. *Curr Biol*, 23(12), 1120-1125. <https://doi.org/10.1016/j.cub.2013.05.004>
- Fisher, R. M., & Regenberg, B. (2019). Multicellular group formation in *Saccharomyces cerevisiae*. *Proc Biol Sci*, 286(1910), 20191098. <https://doi.org/10.1098/rspb.2019.1098>
- Geerlings, N. M. J., Karman, C., Trashin, S., As, K. S., Kienhuis, M. V. M., Hidalgo-Martinez, S., Vasquez-Cardenas, D., Boschker, H. T. S., De Wael, K., Middelburg, J. J., Polerecky, L., & Meysman, F. J. R. (2020). Division of labor and growth during electrical cooperation in multicellular cable bacteria. *Proc Natl Acad Sci U S A*, 117(10), 5478-5485. <https://doi.org/10.1073/pnas.1916244117>
- Geier, B., Sogin, E. M., Michellod, D., Janda, M., Kompauer, M., Spengler, B., Dubilier, N., & Liebeke, M. (2020). Spatial metabolomics of in situ host-microbe interactions at the micrometre scale. *Nat Microbiol*, 5(3), 498-510. <https://doi.org/10.1038/s41564-019-0664-6>
- Gevrekci, A. O. (2017). The roles of polyamines in microorganisms. *World J Microbiol Biotechnol*, 33(11), 204. <https://doi.org/10.1007/s11274-017-2370-y>
- Gilchrist, C. L. M., & Chooi, Y. H. (2021). clinker & clustermap.js: automatic generation of gene cluster comparison figures. *Bioinformatics*, 37(16), 2473-2475. <https://doi.org/10.1093/bioinformatics/btab007>
- Greening, C., & Lithgow, T. (2020). Formation and function of bacterial organelles. *Nat Rev Microbiol*, 18(12), 677-689. <https://doi.org/10.1038/s41579-020-0413-0>
- Grosberg, R. K., & Strathmann, R. R. (2007). The Evolution of Multicellularity: A Minor Major Transition? *Annual Review of Ecology, Evolution, and Systematics*, 38(1), 621-654. <https://doi.org/10.1146/annurev.ecolsys.36.102403.114735>
- Gulli, J. G., Herron, M. D., & Ratcliff, W. C. (2019). Evolution of altruistic cooperation among nascent multicellular organisms. *Evolution*, 73(5), 1012-1024. <https://doi.org/10.1111/evo.13727>

- Hallgren, J., Tsigirigos, K. D., Pedersen, M. D., Almagro Armenteros, J. J., Marcatili, P., Nielsen, H., Krogh, A., & Winther, O. (2022). DeepTMHMM predicts alpha and beta transmembrane proteins using deep neural networks *bioRxiv*.  
<https://doi.org/10.1101/2022.04.08.487609>
- Hatzenpichler, R., Scheller, S., Tavormina, P. L., Babin, B. M., Tirrell, D. A., & Orphan, V. J. (2014). In situ visualization of newly synthesized proteins in environmental microbes using amino acid tagging and click chemistry. *Environ Microbiol*, *16*(8), 2568-2590.  
<https://doi.org/10.1111/1462-2920.12436>
- Herrero, A., Stavans, J., & Flores, E. (2016). The multicellular nature of filamentous heterocyst-forming cyanobacteria. *FEMS Microbiol Rev*, *40*(6), 831-854.  
<https://doi.org/10.1093/femsre/fuw029>
- Herron, M. D., Borin, J. M., Boswell, J. C., Walker, J., Chen, I. K., Knox, C. A., Boyd, M., Rosenzweig, F., & Ratcliff, W. C. (2019). De novo origins of multicellularity in response to predation. *Sci Rep*, *9*(1), 2328. <https://doi.org/10.1038/s41598-019-39558-8>
- Hu, D., Cui, Y., Markillie, L. M., Chrisler, W. B., Wang, Q., Hatzenpichler, R., & Orr, G. (2021). Counting mRNA Copies in Intact Bacterial Cells by Fluctuation Localization Imaging-Based Fluorescence In Situ Hybridization (fliFISH). *Methods Mol Biol*, *2246*, 237-247.  
[https://doi.org/10.1007/978-1-0716-1115-9\\_15](https://doi.org/10.1007/978-1-0716-1115-9_15)
- Hyatt, D., Chen, G.-L., LoCascio, P. F., Land, M. L., Larimer, F. W., & Hauser, L. J. (2010). Prodigal: prokaryotic gene recognition and translation initiation site identification. *BMC bioinformatics*, *11*, 1-11.
- Islam, S. T., Vergara Alvarez, I., Saidi, F., Guiseppi, A., Vinogradov, E., Sharma, G., Espinosa, L., Morrone, C., Basseur, G., Guillemot, J. F., Benarouche, A., Bridot, J. L., Ravicoularamin, G., Cagna, A., Gauthier, C., Singer, M., Fierobe, H. P., Mignot, T., & Mauriello, E. M. F. (2020). Modulation of bacterial multicellularity via spatio-specific polysaccharide secretion. *PLoS Biol*, *18*(6), e3000728.  
<https://doi.org/10.1371/journal.pbio.3000728>
- Jain, C., Rodriguez, R. L., Phillippy, A. M., Konstantinidis, K. T., & Aluru, S. (2018). High throughput ANI analysis of 90K prokaryotic genomes reveals clear species boundaries. *Nat Commun*, *9*(1), 5114. <https://doi.org/10.1038/s41467-018-07641-9>
- Jurenas, D., Fraikin, N., Goormaghtigh, F., & Van Melderen, L. (2022). Biology and evolution of bacterial toxin-antitoxin systems. *Nat Rev Microbiol*, *20*(6), 335-350.  
<https://doi.org/10.1038/s41579-021-00661-1>
- Kaiser, D. (2001). Building a multicellular organism. *Annual Review of Genetics*, *35*(1), 103-123.

- Kanehisa, M., Furumichi, M., Sato, Y., Kawashima, M., & Ishiguro-Watanabe, M. (2023). KEGG for taxonomy-based analysis of pathways and genomes. *Nucleic Acids Res*, 51(D1), D587-D592. <https://doi.org/10.1093/nar/gkac963>
- Kang, D. D., Li, F., Kirton, E., Thomas, A., Egan, R., An, H., & Wang, Z. (2019). MetaBAT 2: an adaptive binning algorithm for robust and efficient genome reconstruction from metagenome assemblies. *PeerJ*, 7, e7359. <https://doi.org/10.7717/peerj.7359>
- Kassambara, A. (2019). *Comparing groups: Numerical variables* (Vol. 192). Datanovia.
- Keim CN, Martins JL, de Barros HL, Lins U, & M., F. (2006). Structure, behavior, ecology and diversity of multicellular magnetotactic prokaryotes. *Magnetoreception and magnetosomes in bacteria*(Springer, Berlin, Heidelberg), 103-132.
- Keim, C. N., Abreu, F., Lins, U., de Barros, H. L., & Farina, M. (2004). Cell organization and ultrastructure of a magnetotactic multicellular organism. *Journal of structural biology*, 145(3), 254-262.
- Keim, C. N., Abreu, F., Lins, U., de Barros, L., & Farina, M. (2004). Cell organization and ultrastructure of a magnetotactic multicellular organism. *J Struct Biol*, 145(3), 254-262. <https://doi.org/10.1016/j.jsb.2003.10.022>
- Keim, C. N., Farina, M., & Lins, U. (2007). Magnetoglobus, Magnetic Aggregates in Anaerobic Environments. *Microbe 2*, 437-445.
- Keim, C. N., Martins, J. L., Abreu, F., Rosado, A. S., de Barros, H. L., Borojevic, R., Lins, U., & Farina, M. (2004). Multicellular life cycle of magnetotactic prokaryotes. *FEMS Microbiol Letters*, 240(2), 203-208. <https://doi.org/10.1016/j.femsle.2004.09.035>
- Kim, W., Levy, S. B., & Foster, K. R. (2016). Rapid radiation in bacteria leads to a division of labour. *Nat Commun*, 7, 10508. <https://doi.org/10.1038/ncomms10508>
- Kolinko, S., Richter, M., Glockner, F. O., Brachmann, A., & Schuler, D. (2014). Single-cell genomics reveals potential for magnetite and greigite biomineralization in an uncultivated multicellular magnetotactic prokaryote. *Environ Microbiol Rep*, 6(5), 524-531. <https://doi.org/10.1111/1758-2229.12198>
- Leao, P., Chen, Y. R., Abreu, F., Wang, M., Zhang, W. J., Zhou, K., Xiao, T., Wu, L. F., & Lins, U. (2017). Ultrastructure of ellipsoidal magnetotactic multicellular prokaryotes depicts their complex assemblage and cellular polarity in the context of magnetotaxis. *Environ Microbiol*, 19(6), 2151-2163. <https://doi.org/10.1111/1462-2920.13677>
- Leclerc, J., Rosenfeld, E., Trainini, M., Martin, B., Meuric, V., Bonnaure-Mallet, M., & Baysse, C. (2015). The Cytochrome bd Oxidase of *Porphyromonas gingivalis* Contributes to Oxidative Stress Resistance and Dioxygen Tolerance. *PLoS One*, 10(12), e0143808. <https://doi.org/10.1371/journal.pone.0143808>

- Lefèvre, C. T., & Bazylinski, D. A. (2013). Ecology, Diversity, and Evolution of Magnetotactic Bacteria. *Microbiology and Molecular Biology Reviews*, 77(3), 497-526. <https://doi.org/10.1128/membr.00021-13>
- Lefevre, C. T., Bernadac, A., Yu-Zhang, K., Pradel, N., & Wu, L. F. (2009). Isolation and characterization of a magnetotactic bacterial culture from the Mediterranean Sea. *Environ Microbiol*, 11(7), 1646-1657. <https://doi.org/10.1111/j.1462-2920.2009.01887.x>
- Lefevre, C. T., Trubitsyn, D., Abreu, F., Kolinko, S., Jogler, C., de Almeida, L. G., de Vasconcelos, A. T., Kube, M., Reinhardt, R., Lins, U., Pignol, D., Schuler, D., Bazylinski, D. A., & Ginet, N. (2013). Comparative genomic analysis of magnetotactic bacteria from the Deltaproteobacteria provides new insights into magnetite and greigite magnetosome genes required for magnetotaxis. *Environ Microbiol*, 15(10), 2712-2735. <https://doi.org/10.1111/1462-2920.12128>
- Lu, S., Wang, J., Chitsaz, F., Derbyshire, M. K., Geer, R. C., Gonzales, N. R., Gwadz, M., Hurwitz, D. I., Marchler, G. H., Song, J. S., Thanki, N., Yamashita, R. A., Yang, M., Zhang, D., Zheng, C., Lanczycki, C. J., & Marchler-Bauer, A. (2020). CDD/SPARCLE: the conserved domain database in 2020. *Nucleic Acids Res*, 48(D1), D265-D268. <https://doi.org/10.1093/nar/gkz991>
- Ludwig, W., Strunk, O., Westram, R., Richter, L., Meier, H., Yadhukumar, Buchner, A., Lai, T., Steppi, S., Jobb, G., Forster, W., Brettske, I., Gerber, S., Ginhart, A. W., Gross, O., Grumann, S., Hermann, S., Jost, R., König, A., . . . Schleifer, K. H. (2004). ARB: a software environment for sequence data. *Nucleic Acids Res*, 32(4), 1363-1371. <https://doi.org/10.1093/nar/gkh293>
- Lynes, M. M., Krukenberg, V., Jay, Z. J., Kohtz, A. J., Gobrogge, C. A., Spietz, R. L., & Hatzenpichler, R. (2023). Diversity and function of methyl-coenzyme M reductase-encoding archaea in Yellowstone hot springs revealed by metagenomics and mesocosm experiments. *ISME Commun*, 3(1), 22. <https://doi.org/10.1038/s43705-023-00225-9>
- Maier, B., & Wong, G. C. L. (2015). How Bacteria Use Type IV Pili Machinery on Surfaces. *Trends Microbiol*, 23(12), 775-788. <https://doi.org/10.1016/j.tim.2015.09.002>
- Martins, J. L., Silveira, T.S., Silva, K.T. and Lins, U. (2009). Salinity dependence of the distribution of multicellular magnetotactic prokaryotes in a hypersaline lagoon. *International Microbiology*, 12(3), 193. <https://doi.org/10.2436/20.1501.01.98>
- McNamara, A. (2018). Key attributes of a modern statistical computing tool. *The American Statistician*.
- McNamara, J. T., Morgan, J. L., & Zimmer, J. (2015). A molecular description of cellulose biosynthesis. *Annu Rev Biochem*, 84, 895-921. <https://doi.org/10.1146/annurev-biochem-060614-033930>

- Mizuno, K., Maree, M., Nagamura, T., Koga, A., Hirayama, S., Furukawa, S., Tanaka, K., & Morikawa, K. (2022). Novel multicellular prokaryote discovered next to an underground stream. *Elife*, *11*. <https://doi.org/10.7554/eLife.71920>
- Mukhopadhyay, A., He, Z., Alm, E. J., Arkin, A. P., Baidoo, E. E., Borglin, S. C., Chen, W., Hazen, T. C., He, Q., Holman, H. Y., Huang, K., Huang, R., Joyner, D. C., Katz, N., Keller, M., Oeller, P., Redding, A., Sun, J., Wall, J., . . . Keasling, J. D. (2006). Salt stress in *Desulfovibrio vulgaris* Hildenborough: an integrated genomics approach. *J Bacteriol*, *188*(11), 4068-4078. <https://doi.org/10.1128/JB.01921-05>
- Namba, A., Mano, N., Takano, H., Beppu, T., Ueda, K., & Hirose, H. (2008). OmpA is an adhesion factor of *Aeromonas veronii*, an optimistic pathogen that habituates in carp intestinal tract. *J Appl Microbiol*, *105*(5), 1441-1451. <https://doi.org/10.1111/j.1365-2672.2008.03883.x>
- Nawrocki, E. P., Kolbe, D. L., & Eddy, S. R. (2009). Infernal 1.0: inference of RNA alignments. *Bioinformatics*, *25*(10), 1335-1337.
- Niklas, K. J., & Newman, S. A. (2013). The origins of multicellular organisms. *Evolution & development*, *15*(1), 41-52.
- Omadjela, O., Narahari, A., Strumillo, J., Melida, H., Mazur, O., Bulone, V., & Zimmer, J. (2013). BcsA and BcsB form the catalytically active core of bacterial cellulose synthase sufficient for in vitro cellulose synthesis. *Proc Natl Acad Sci U S A*, *110*(44), 17856-17861. <https://doi.org/10.1073/pnas.1314063110>
- Parks, D. H., Imelfort, M., Skennerton, C. T., Hugenholtz, P., & Tyson, G. W. (2015). CheckM: assessing the quality of microbial genomes recovered from isolates, single cells, and metagenomes. *Genome Res*, *25*(7), 1043-1055. <https://doi.org/10.1101/gr.186072.114>
- Perantoni, M., Esquivel, D. M., Wajnberg, E., Acosta-Avalos, D., Cernicchiaro, G., & Lins de Barros, H. (2009). Magnetic properties of the microorganism *Candidatus Magnetoglobus multicellularis*. *Naturwissenschaften*, *96*(6), 685-690. <https://doi.org/10.1007/s00114-009-0520-2>
- Popa, R., Weber, P. K., Pett-Ridge, J., Finzi, J. A., Fallon, S. J., Hutcheon, I. D., Nealson, K. H., & Capone, D. G. (2007). Carbon and nitrogen fixation and metabolite exchange in and between individual cells of *Anabaena oscillarioides*. *ISME J*, *1*(4), 354-360. <https://doi.org/10.1038/ismej.2007.44>
- Prasad, S. M., Yin, Y., Rodzinski, E., Tuomanen, E. I., & Masure, H. R. (1993). Identification of a carbohydrate recognition domain in filamentous hemagglutinin from *Bordetella pertussis*. *Infection and Immunity*, *61*(7), 2780-2785.
- Price, M. N., Dehal, P. S., & Arkin, A. P. (2010). FastTree 2—approximately maximum-likelihood trees for large alignments. *PLoS One*, *5*(3), e9490.

- Qi, Y., Rao, F., Luo, Z., & Liang, Z. X. (2009). A flavin cofactor-binding PAS domain regulates c-di-GMP synthesis in AxDGC2 from *Acetobacter xylinum*. *Biochemistry*, *48*(43), 10275-10285. <https://doi.org/10.1021/bi901121w>
- Qian, X., Zhao, Y., Santini, C.-L., Pan, H., Xiao, T., Chen, H., Song, T., Li, J., Alberto, F., Brustlein, S., & Wu, L.-F. (2021). How light affect the magnetotactic behavior and reproduction of ellipsoidal multicellular magnetoglobules? *Journal of Oceanology and Limnology*, *39*(6), 2005-2014. <https://doi.org/10.1007/s00343-021-0493-3>
- Qian, X. X., Santini, C. L., Kosta, A., Menguy, N., Le Guenno, H., Zhang, W., Li, J., Chen, Y. R., Liu, J., Alberto, F., Espinosa, L., Xiao, T., & Wu, L. F. (2020). Juxtaposed membranes underpin cellular adhesion and display unilateral cell division of multicellular magnetotactic prokaryotes. *Environ Microbiol*, *22*(4), 1481-1494. <https://doi.org/10.1111/1462-2920.14710>
- Quast, C., Pruesse, E., Yilmaz, P., Gerken, J., Schweer, T., Yarza, P., Peplies, J., & Glockner, F. O. (2013). The SILVA ribosomal RNA gene database project: improved data processing and web-based tools. *Nucleic Acids Res*, *41*(Database issue), D590-596. <https://doi.org/10.1093/nar/gks1219>
- Rinke, C., Lee, J., Nath, N., Goudeau, D., Thompson, B., Poulton, N., Dmitrieff, E., Malmstrom, R., Stepanauskas, R., & Woyke, T. (2014). Obtaining genomes from uncultivated environmental microorganisms using FACS-based single-cell genomics. *Nat Protoc*, *9*(5), 1038-1048. <https://doi.org/10.1038/nprot.2014.067>
- Rokas, A. (2008). The origins of multicellularity and the early history of the genetic toolkit for animal development. *Annu Rev Genet*, *42*, 235-251. <https://doi.org/10.1146/annurev.genet.42.110807.091513>
- Schaible, G. A., Kohtz, A. J., Cliff, J., & Hatzenpichler, R. (2022). Correlative SIP-FISH-Raman-SEM-NanoSIMS links identity, morphology, biochemistry, and physiology of environmental microbes. *ISME Communications*, *2*(1). <https://doi.org/10.1038/s43705-022-00134-3>
- Schirrmeister, B. E., Antonelli, A., & Bagheri, H. C. (2011). The origin of multicellularity in cyanobacteria. *BMC evolutionary biology*, *11*, 1-21.
- Schramm, A., Fuchs, B. M., Nielsen, J. L., Tonolla, M., & Stahl, D. A. (2002). Fluorescence in situ hybridization of 16S rRNA gene clones (Clone-FISH) for probe validation and screening of clone libraries. *Environmental Microbiology*, *4*, 713-720.
- Schwartzman, J. A., Ebrahimi, A., Chadwick, G., Sato, Y., Roller, B. R. K., Orphan, V. J., & Cordero, O. X. (2022). Bacterial growth in multicellular aggregates leads to the emergence of complex life cycles. *Curr Biol*, *32*(14), 3059-3069 e3057. <https://doi.org/10.1016/j.cub.2022.06.011>

- Serra, D. O., Conover, M. S., Arnal, L., Sloan, G. P., Rodriguez, M. E., Yantorno, O. M., & Deora, R. (2011). FHA-mediated cell-substrate and cell-cell adhesions are critical for *Bordetella pertussis* biofilm formation on abiotic surfaces and in the mouse nose and the trachea. *PLoS One*, *6*(12), e28811. <https://doi.org/10.1371/journal.pone.0028811>
- Serra, D. O., & Hengge, R. (2019). *Cellulose in bacterial biofilms*.
- Serra, D. O., & Hengge, R. (2021). Bacterial Multicellularity: The Biology of *Escherichia coli* Building Large-Scale Biofilm Communities. *Annu Rev Microbiol*, *75*, 269-290. <https://doi.org/10.1146/annurev-micro-031921-055801>
- Serra, D. O., Richter, A. M., & Hengge, R. (2013). Cellulose as an architectural element in spatially structured *Escherichia coli* biofilms. *J Bacteriol*, *195*(24), 5540-5554. <https://doi.org/10.1128/JB.00946-13>
- Shapiro, O. H., Hatzepichler, R., Buckley, D. H., Zinder, S. H., & Orphan, V. J. (2011). Multicellular photo-magnetotactic bacteria. *Environmental Microbiology Reports*, *3*(2), 233-238. <https://doi.org/10.1111/j.1758-2229.2010.00215.x>
- Silva, K. T., Abreu, F., Keim, C. N., Farina, M., & Lins, U. (2008). Ultrastructure and cytochemistry of lipid granules in the many-celled magnetotactic prokaryote, 'Candidatus Magnetoglobus multicellularis'. *Micron*, *39*(8), 1387-1392. <https://doi.org/10.1016/j.micron.2008.05.009>
- Simmons, S. L., Bazylinski, D. A., & Edwards, K. J. (2007). Population dynamics of marine magnetotactic bacteria in a meromictic salt pond described with qPCR. *Environ Microbiol*, *9*(9), 2162-2174. <https://doi.org/10.1111/j.1462-2920.2007.01330.x>
- Simmons, S. L., & Edwards, K. J. (2007). Unexpected diversity in populations of the many-celled magnetotactic prokaryote. *Environ Microbiol*, *9*(1), 206-215. <https://doi.org/10.1111/j.1462-2920.2006.01129.x>
- Simmons, S. L., Sievert, S. M., Frankel, R. B., Bazylinski, D. A., & Edwards, K. J. (2004). Spatiotemporal distribution of marine magnetotactic bacteria in a seasonally stratified coastal salt pond. *Appl Environ Microbiol*, *70*(10), 6230-6239. <https://doi.org/10.1128/AEM.70.10.6230-6239.2004>
- Sobrinho, R. L., Lins, U., & Bernardes, M. C. (2011). Geochemical Characteristics Related to the Gregite-Producing Multicellular Magnetotactic Prokaryote *Candidatus Magnetoglobus multicellularis* in a Hypersaline Lagoon. *Geomicrobiology Journal*, *28*(8), 705-713. <https://doi.org/10.1080/01490451.2010.514027>
- Sondergaard, D., Pedersen, C. N., & Greening, C. (2016). HydDB: A web tool for hydrogenase classification and analysis. *Sci Rep*, *6*, 34212. <https://doi.org/10.1038/srep34212>

- Stepanauskas, R., Fergusson, E. A., Brown, J., Poulton, N. J., Tupper, B., Labonte, J. M., Becraft, E. D., Brown, J. M., Pachiadaki, M. G., Povilaitis, T., Thompson, B. P., Mascena, C. J., Bellows, W. K., & Lubys, A. (2017). Improved genome recovery and integrated cell-size analyses of individual uncultured microbial cells and viral particles. *Nat Commun*, 8(1), 84. <https://doi.org/10.1038/s41467-017-00128-z>
- Stoecker, K., Dorninger, C., Daims, H., & Wagner, M. (2010). Double labeling of oligonucleotide probes for fluorescence in situ hybridization (DOPE-FISH) improves signal intensity and increases rRNA accessibility. *Appl Environ Microbiol*, 76(3), 922-926. <https://doi.org/10.1128/AEM.02456-09>
- Tan, L., & Jiang, J. (2018). *Digital signal processing: fundamentals and applications*. Academic press.
- Tang, G., Peng, L., Baldwin, P. R., Mann, D. S., Jiang, W., Rees, I., & Ludtke, S. J. (2007). EMAN2: an extensible image processing suite for electron microscopy. *J Struct Biol*, 157(1), 38-46. <https://doi.org/10.1016/j.jsb.2006.05.009>
- Taoka, A., Eguchi, Y., Shimoshige, R., & Fukumori, Y. (2023). Recent advances in studies on magnetosome-associated proteins composing the bacterial geomagnetic sensor organelle. *Microbiol Immunol*, 67(5), 228-238. <https://doi.org/10.1111/1348-0421.13062>
- Team, R. C. (2023). *A language and environment for statistical computing*. <http://R-project.org/>.
- Teng, Z., Zhang, Y., Zhang, W., Pan, H., Xu, J., Huang, H., Xiao, T., & Wu, L. F. (2018). Diversity and Characterization of Multicellular Magnetotactic Prokaryotes From Coral Reef Habitats of the Paracel Islands, South China Sea. *Front Microbiol*, 9, 2135. <https://doi.org/10.3389/fmicb.2018.02135>
- Van Dongen, S. (2008). Graph clustering via a discrete uncoupling process. *SIAM Journal on Matrix Analysis and Applications*, 30(1), 121-141.
- Velicer, G. J., & Vos, M. (2009). Sociobiology of the myxobacteria. *Annu Rev Microbiol*, 63, 599-623. <https://doi.org/10.1146/annurev.micro.091208.073158>
- Wang, Y., Huang, W. E., Cui, L., & Wagner, M. (2016). Single cell stable isotope probing in microbiology using Raman microspectroscopy. *Curr Opin Biotechnol*, 41, 34-42. <https://doi.org/10.1016/j.copbio.2016.04.018>
- Wenter, R., Wanner, G., Schuler, D., & Overmann, J. (2009). Ultrastructure, tactic behaviour and potential for sulfate reduction of a novel multicellular magnetotactic prokaryote from North Sea sediments. *Environ Microbiol*, 11(6), 1493-1505. <https://doi.org/10.1111/j.1462-2920.2009.01877.x>
- Wielgoss, S., Wolfensberger, R., Sun, L., Fiegna, F., & Velicer, G. J. (2019). Social genes are selection hotspots in kin groups of a soil microbe. *Science*, 363(6433), 1342-1345.

- Winklhofer, M., Abracado, L. G., Davila, A. F., Keim, C. N., & Lins de Barros, H. G. (2007). Magnetic optimization in a multicellular magnetotactic organism. *Biophys J*, 92(2), 661-670. <https://doi.org/10.1529/biophysj.106.093823>
- Wrótniak-Drzewiecka, W., Brzezińska, A. J., Dahm, H., Ingle, A. P., & Rai, M. (2015). Current trends in myxobacteria research. *Annals of Microbiology*, 66(1), 17-33. <https://doi.org/10.1007/s13213-015-1104-3>
- Yilmaz, L. S., Parnerkar, S., & Noguera, D. R. (2011). mathFISH, a web tool that uses thermodynamics-based mathematical models for in silico evaluation of oligonucleotide probes for fluorescence in situ hybridization. *Appl Environ Microbiol*, 77(3), 1118-1122. <https://doi.org/10.1128/AEM.01733-10>
- Zimmermann, L., Stephens, A., Nam, S. Z., Rau, D., Kubler, J., Lozajic, M., Gabler, F., Soding, J., Lupas, A. N., & Alva, V. (2018). A Completely Reimplemented MPI Bioinformatics Toolkit with a New HHpred Server at its Core. *J Mol Biol*, 430(15), 2237-2243. <https://doi.org/10.1016/j.jmb.2017.12.007>

## CHAPTER FIVE

## CONCLUSION AND FUTURE DIRECTIONS

Conclusions

The emergence of multicellular lifeforms represents a pivotal milestone in Earth's history, ushering in a new era of biological complexity. Because of the relative scarcity of multicellularity in the domains Bacteria and Archaea, research on the evolution of multicellularity has predominantly focused on eukaryotic model organisms. To address this shortcoming, the work presented in his thesis focuses on exploring the evolution of multicellularity in Bacteria by studying multicellular magnetotactic bacteria (MMB), the only known bacteria without a unicellular stage in their life cycle. Because of their unique biology, MMB consortia are ideally suited to become a model system to explore the underpinnings of bacterial multicellularity.

The MMB used for studies within this thesis were collected from Little Sippewissett salt marsh (LSSM), an estuary located on Buzzards Bay in Falmouth, MA. This site has been the focus of research regarding magnetotactic bacteria and has been shown to harbor large amounts of MMB (Shapiro et al., 2011; Simmons & Edwards, 2007). Research has shown that at least five genus level populations of MMB exist in the site (Simmons & Edwards, 2007), with at least ten species of MMB present (Chapter 5). While MMB are abundant in the site and can be magnetically enriched to >99%, they still have never been successfully brought into culture, limiting experiments on these organisms to 16S clone studies and microscopy.

Due to the current inability to cultivate MMB, investigations into the mechanisms driving the evolution and maintenance of MMB multicellularity required the development of

methodologies employing culture-independent techniques. Furthermore, because the different populations of MMB in LSSM appear morphologically similar, fluorescence *in situ* hybridization (FISH) was required to differentiate between the different groups of MMB (Schaible et al., 2022; Simmons & Edwards, 2007). Chapter 2 of this thesis presents the correlative workflow that was developed for species specific analysis of organisms using stable isotope probing (SIP), FISH, scanning electron microscopy (SEM), backscatter electron microscopy (BSE), energy dispersive X-ray spectroscopy (EDS), confocal Raman microscopy (Raman), and nano-scale secondary ion mass spectrometry (NanoSIMS). This correlative approach allowed for a comprehensive analysis of single MMB taxonomic identity, structure, physiology, and metabolic activity, allowing us to overcome the limitation of using single techniques at one time. It is likely that the use of the correlative methodology presented here will be used for further studies of microbes in environments such as salt marshes, hot springs, and the human gut, allowing researchers to better understand the interplay between microbes and their environment.

The utilization of SIP for studying microbe interactions and activity is progressively gaining prevalence (Hatzenpichler, 2020; Lee et al., 2021; Musat et al., 2016). In order to facilitate meaningful comparisons of isotope uptake, it proves advantageous to assess the comparability of measurements obtained through both Raman and NanoSIMS. The work performed in Chapter 3 seeks to establish a standard for comparison of these techniques by making direct comparisons of deuterium ( $^2\text{H}$ ) uptake into cellular biomass of *Escherichia coli* cells. The analysis revealed that measurements of  $^2\text{H}$  are highly comparable between Raman and NanoSIMS, thus allowing researcher to compare results across studies. Furthermore, the study explored the pre-processing methods for Raman data, showing there is little statistical difference in baselining methods of

Raman data when measuring  $^2\text{H}$  uptake in *E. coli* cells. Beyond this, the study provides open source GNU R code for researchers seeking to process Raman data in R. We anticipate this to be of help as open sourced R code for processing Raman data is surprisingly lacking in the field. Additionally, the study explored the outcome of  $^2\text{H}$  measurements in NanoSIMS when using  $^2\text{H}/^1\text{H}$ ,  $^{12}\text{C}^2\text{H}/^{12}\text{C}^1\text{H}$ , and  $^{12}\text{C}_2^2\text{H}/^{12}\text{C}_2^1\text{H}$  mass ratios, showing that  $^{12}\text{C}_2^2\text{H}/^{12}\text{C}_2^1\text{H}$  yielded reliable and comparable results to the Raman data. Together, the analysis presented in Chapter 3 seeks to further establish a foundation for the use of powerful culture independent techniques used in microbiology, further enabling studies employing SIP.

The methods and techniques developed in Chapters 2 and 3 of this thesis were of paramount importance for the work performed in Chapter 4. The fourth chapter focused on addressing two key questions regarding MMB: are they clonal and are they metabolically differentiated. To address these questions, the genomes of 22 individual MMB consortia were sequenced, allowing for the metabolic potential MMB found in LSSM to be mapped. The 16S rRNA sequences recovered from the genomes were used to phylogenetically show there are five genera of MMB and ten distinct species of MMB in the sample site. Previous studies have assumed that MMB are clonal (Kolinko et al., 2014; Simmons & Edwards, 2007), but we were able to show they are in fact not clonal, containing a range of 157-789 single nucleotide polymorphisms (SNP) per genome. Additionally, the metabolic map was used to identify carbon substrates that could be used in SIP-NanoSIMS experiments successfully showing MMB in LSSM are mixotrophic sulfate reducers. The SIP-NanoSIMS also revealed that MMB are metabolically differentiated. Finally, bioorthogonal non-canonical amino acid tagging (BONCAT) was used to show that MMB appear to localize proteins around the acellular center of the organism, raising questions regarding the

purpose of this acellular center. Together, the analysis presented in Chapter 4 shows that MMB have a higher level of complexity than previously assumed.

### Future Directions

The methodological advancements outlined in Chapters 2 and 3, coupled with the comprehensive exploration of MMB physiology in Chapter 4, establish a robust foundation for future investigations into bacterial multicellularity using MMB as a model organism. Successfully cultivating MMB for the first time remains a significant challenge, yet this endeavor stands to benefit significantly from the genomes and SIP experiments presented in this thesis. While attempts to cultivate MMB have been continuously performed in the Hatzenpichler lab, MMB have only been sustained in defined media for 15 days, after which no MMB could be identified or recovered (Appendix D). The media tailored for MMB incorporates nutrients and pH specifications based on genomic analysis and geochemistry of LSSM water but seems to be deficient in some unknown chemical(s) or element(s) (Appendix D, Tables S1 and S2). Currently, all cultivation attempts have been performed in anoxic environments as oxygen has been shown to have a toxic effect on MMB (Keim et al., 2007). However, cultivation of closely related single celled *Magnetospirillum* requires microaerophilic conditions (Le Nagard et al., 2018), indicating that trace amounts of oxygen could be beneficial for growth of MMB. Further experiments testing microaerobic environments for the growth of MMB are warranted. Microfluidics has been used to grow bacteria in defined microenvironments (Burmeister et al., 2019) and isolate and grow novel un-cultured bacteria (Tan et al., 2020), offering a possible solution to cultivating MMB for the first time. Researchers have already used microfluidics to sort live magnetotactic bacteria, offering fundamental approaches to using microfluidics to cultivate MMB (Tay et al., 2018). Regardless of

what approach is used, the ability to grow MMB in the lab offers a multitude of possibilities, removing the need for fresh sediment samples to perform experiments and allowing the opportunity to establish a genomic system to learn more about the genetic underpinning of MMB multicellularity.

Because of the recalcitrance of MMB to cultivation efforts, many studies have employed electron microscopy to further elucidate the ultrastructure of the organism. Keim *et al.* used freeze-fracture and transmission electron microscopy (TEM) to show that individual cells within MMB consortia have pyramidal shape with four membranes at the contact between two cells (Keim *et al.*, 2004). The authors also made observations of membrane vesicles inside the acellular center of the organism, prompting the hypothesis that the function of this space is for cell communication. Freeze-fracture and TEM has also been used to study the large storage granules found within individual MMB cells showing they contain polyhydroxyalkanoate, lipids, or phosphate (Silva *et al.*, 2008). Focused-ion beam (FIB) SEM and TEM have been used to construct three-dimensional models of the organism, providing insight into the organization of cells and the distribution of magnetosomes across the entire consortium (Abreu *et al.*, 2013; Leao *et al.*, 2017). These studies and others have revealed that consortia of MMB have complex ultrastructure that is important for maintaining the multicellular structure of the organism but there are many components for which the function is still not yet known, prompting further exploration of MMB ultrastructure (Qian *et al.*, 2020).

The Hatzenpichler lab has begun to explore the ultrastructure of MMB using serial block face electron microscopy (SBF-EM), a technique that successively removes ~100 nm of sample in between which a TEM image taken, allowing for three dimensional reconstructions of samples

(Fig. 1). This dataset has yet to be fully analyzed but will provide insight into the ultrastructure of MMB from LSSM. Analysis of the SBF-EM images will be done using 3DMOD, an auxiliary package of the image modeling (IMOD) software (Kremer, 1996), and will allow for subcellular compartments to be modeled in a three-dimensional space, providing further insight into the structure of MMB.

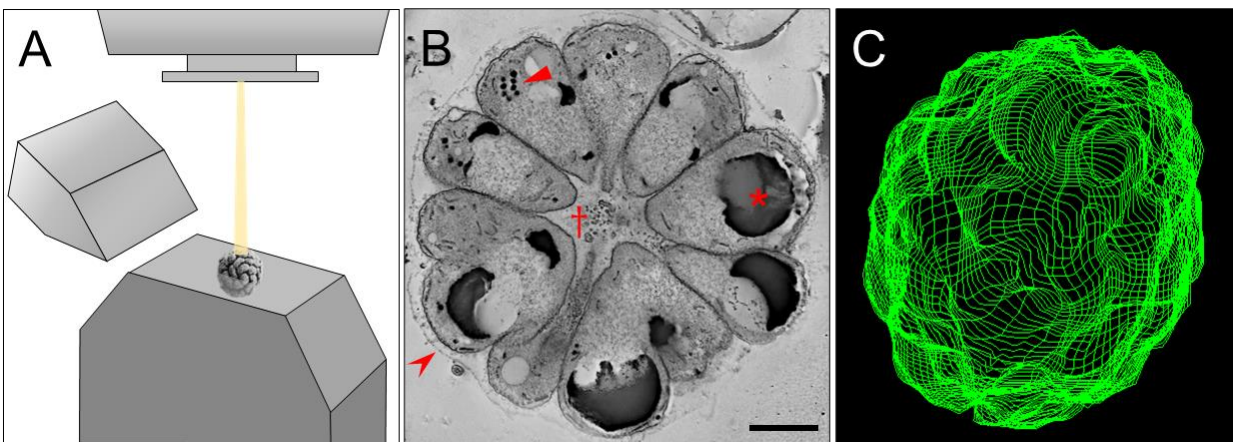


Fig. 1. SBF-EM analysis of MMB. **A** Diagram showing the set up of SBF-EM where the sample is mounted on a pedestal and a diamond blade removes nm thin section of samples, between which a TEM image is taken. **B** Single z-stack TEM image of an MMB. The defining features of the organism can be seen including the acellular center (dagger), the carbon/energy storage granules (asterisk), the magnetosomes (triangle), and the exopolysaccharide layer (arrow). Small electron dense objects appear to be in the acellular center that are postulated to be small lipid droplets possibly involved in cell to cell exchange. Size bar is 1  $\mu\text{m}$ . **C** Preliminary analysis of SBF-EM data showing the three-dimensional shape. Further analysis is needed to refine the model for a full analysis of the ultrastructure.

In addition to SBF-EM, preliminary Cryo-EM data has been obtained to establish protocols for future experiments aimed at further exploring MMB ultrastructure (Fig. 2). Because entire MMB consortium have a large spherical diameter ( $> 3 \mu\text{m}$ ), they are too large for Cryo-EM studies as the electrons are unable to pass through the whole organism. To overcome this, MMB were magnetically enriched and treated with milliQ water (1:10 MMB to milliQ) for 5 minutes, resulting

in the disaggregation of the consortia to single cells, as has been previously shown (Abreu et al., 2006). The treatment was halted by the addition of 20% paraformaldehyde (PFA) to a final concentration of 4% PFA and the cells stored indefinitely at 4 °C. A 50  $\mu$ L of sample was vitrified

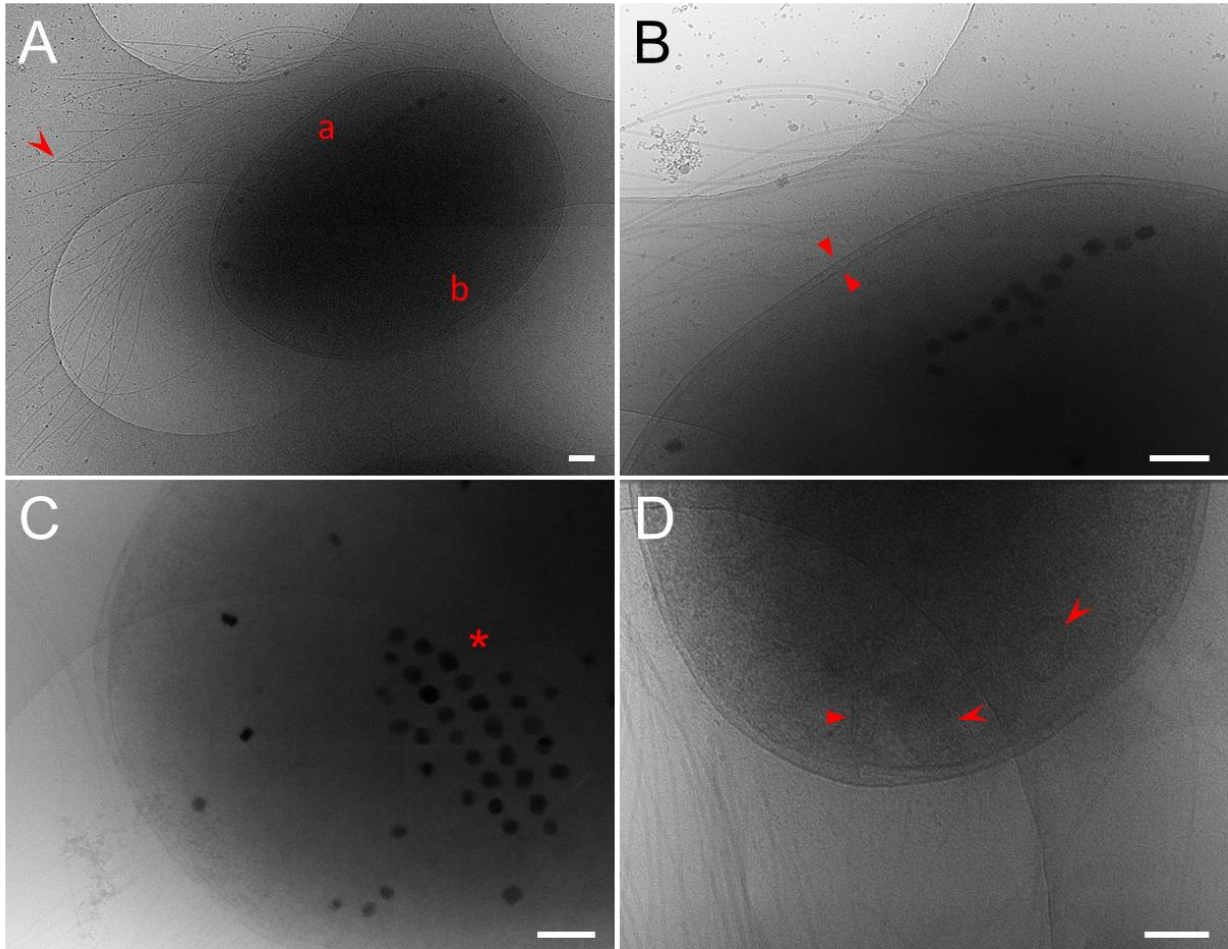


Fig. 2. Preliminary Cryo-EM data of single MMB cells that have been dislodged from the consortium. A Single MMB cell showing the localization of flagella (arrow) to a single side of the cell (a), providing orientation of the cell and indicating that side (b) faces the acellular center of the consortium. B A clear image of the double membrane (triangles) of the cell. C Clear organization of the magnetosomes (asterisk) within the cell. D Though difficult to see without further processing of images, unique internal structures were observed in the MMB including filaments (triangle) and icosahedral shapes (arrows). Processing of the tomography data is warranted to further analyze these shapes. All size bars are 200 nm. Images taken by Colin Gauvin in the Montana State University Cryo-EM facility.

on a carbon grid and cells imaged using the Montana State University Talos Arctica Cryo-EM using the Gatan K3 Direct Electron Detector. This analysis provided detailed images of MMB cells and allowed for several tilt-series to be acquired for tomography (data not shown). The images showed that the MMB dislodged from consortia had lost their pyramidal shape and become oblong shaped, suggesting that turgor pressure plays a role in maintaining the cell shape within the consortium. Additionally, the analysis showed the localization flagella to a single side of cells, presumably the exterior side of the consortium as has been previously observed (Silva et al., 2007). The organization of the electron dense magnetosome mineral, greigite ( $\text{Fe}^{2+}\text{Fe}^{3+}_2\text{S}_4$ ), was apparent in the cells along with other unidentified internal structures. Some internal structures appeared to be icosahedral in shape, a common geometric shape of viruses, possibly suggesting MMB are infected by viruses. This is of interest as research has shown that a single virus can be responsible for inducing a multicellular morphology, as observed in *Methanosarcina barkeri* (Weidenbach et al., 2017). Altogether, the analysis of MMB using Cryo-EM, while informative, highlights the need for FIB milling to improve the quality of EM data aimed at modeling the ultrastructure of MMB, as this has proved successful in studying other MMB (Abreu et al., 2013; Leao et al., 2017) and the multicellular cyanobacterium *Anabaena* (Weiss et al., 2022).

The genome analysis performed in Chapter 4 identified Type I, Type III-A, and Type III-B CRISPR (clustered regularly interspaced short palindromic repeats) systems, providing support that MMB interact with viruses. Furthermore, CRISPR-Cas systems have been suggested as a vehicle for the evolution of complexity as they allow for the acquisition and incorporation of new information (Koonin & Wolf, 2012). The CRISPR-Cas system responds to environmental cues (e.g. foreign DNA) and initiates an adaptive immune response that incorporates new genetic

information into the genome of the organism (Hille et al., 2018). In this way, viruses are in part responsible for an organism's increase in genomic complexity (if defined as amount of genetic information). Computational modeling has been used to suggest that viruses are a driving force in the evolution of programmed cell death and multicellularity in communities of single cells (Iranzo et al., 2014). The role of CRISPR systems in biological complexity and multicellularity becomes even more intriguing when considering clonality, as CRISPR systems inherently drive the evolution of genomes. Wielgoss *et al.* found that SNPs accumulate in CRISPR loci of cells in the fruiting bodies of the aggregative multicellular bacterium *Myxococcus xanthus* (Wielgoss et al., 2019). The accumulation of SNPs increased the deviation of the organism's genome from its ancestral genotype, favoring the selection of genes pertinent to social cooperation. Our analysis found that MMB are not clonal (section 2.2 Chapter 4), although no SNPs were identified in CRISPR loci. Regardless, the role of viruses and CRISPR systems in MMB multicellularity requires further study to elucidate the impact of CRISPR systems on the evolution of multicellularity.

The non-clonal state of MMB is an enigma. MMB must continually purge genomic diversity, otherwise mutations would continue to accumulate leading to extreme genetic mutations within several generations. This suggests that MMB maintain genomic heterogeneity, possibly as a benefit to the organism allowing for specific proteins to evolve. Future studies exploring the mechanisms that drive genomic heterogeneity in MMB are needed. A possible mechanism could be diversity generating retroelements (DGR), a process where an error-prone reverse transcriptase generates hypervariable regions in proteins (Medhekar & Miller, 2007). This process occurs when a mutagenized complimentary DNA is reverse transcribed from a template region and is replaced

with a segment similar to the template region called variable region. Future studies will be needed to identify if DGRs are responsible for the genomic diversity in MMB.

Another area in need of further exploration is the cell-to-cell differentiation identified in MMB (sections 2.7 and 2.8 in Chapter 4). SIP-NanoSIMS showed different area of MMB had assimilated the SIP label more than others, indicating some cells are more metabolically active than others. Moreover, the BONCAT study unveiled a spatial gradient of protein activity within cells, with the highest levels concentrated near the acellular center of the organism. While these studies provide more information about the cell-to-cell differentiation within MMB, further analysis is needed to establish if a true division of labor exists within the organism. Studies probing the distribution of specific messenger RNA within the consortium could shed light on the activity and function of specific cells. The Hatzenpichler lab has been developing protocols for mRNA FISH to allow for specific transcripts to be identified (Hu et al., 2021). An additional approach could be to use Lanthanide-FISH and NanoSIMS (Parker et al., 2019), a methodology that labels sequences with an oligo tagged with a lanthanide metal that can then be identified using NanoSIMS. If both approaches fail to succeed, co-detection by indexing (CODEX) using DNA-conjugated antibodies to fluorescently label mRNA *in situ* could be explored (Black et al., 2021; Cheng et al., 2022; Kuswanto et al., 2023). Potential targets for mRNA studies could include dissimilatory sulfate reduction and acetyl CoA synthetase genes to probe metabolic activity.

Over the course of studying the MMB at LSSM, a unique morphotype of MMB has been identified in some samples. Attempts to label this species of MMB with the designed FISH probes have failed (data not shown), suggesting it is yet another novel species of MMB (nMMB) that has evaded detection in 16S rRNA and metagenomic studies. The organism has distinct morphological

and ultrastructural features, unlike the majority of MMB in the sample site. The nMMB appear to have smaller cells and magnetosomes are contained in only half of the cells within the consortium (Fig. 4). The distribution of magnetosomes could be the result of a division of labor within the

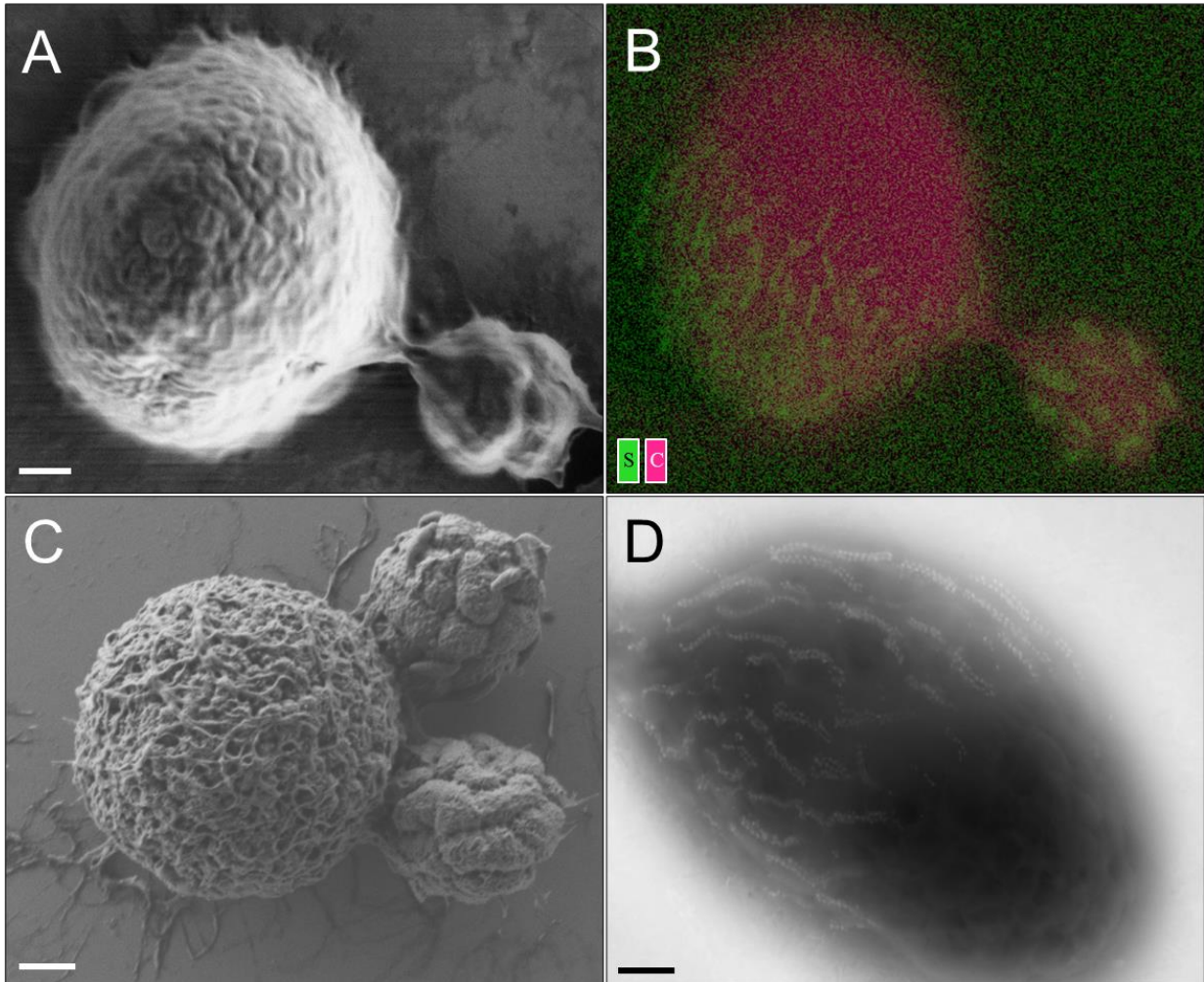


Fig. 4. nMMB isolated from LSSM. **A** nMMB containing smaller cells and exhibiting a generally larger size than other MMB from the sample site. **B** EDS image of the same nMMB in **A** showing the sulfur in the greigite magnetosomes localized to one side of the consortium. **C** SEM image of the nMMB (left) and two other common MMB morphotypes. The novel MMB appears to generally have smaller cells as compared. **D** BSE showing the organization and localization of magnetosomes in the nMMB.

consortium or possibly occur during the division process of the consortium. If magnetosome localization within the consortium was a result of the lifecycle, it would suggest that new cells only form at one polar end of the consortium before the entire nMMB divides. Correlative microscopy approaches may be of use for further analysis of nMMB but will likely require FISH, indicating the need to sequence the 16S rRNA of this organism.

The work presented in this thesis focuses on MMB isolated from LSSM but MMB have been found across the globe in South and North America, Asia, and Europe (Keim et al., 2007; Schaible et al., 2022; Simmons & Edwards, 2007; Teng et al., 2018; Wenter et al., 2009; Zhou et al., 2011). A comprehensive geographical study of MMB has yet to be performed but the organism has generally been found in coastal environments, indicating the importance of salinity. It should be mentioned that non-magnetotactic bacteria have been isolated in low saline non-marine aquatic environments (Lefevre et al., 2010), suggesting that MMB may be wider spread than assumed. MMB have been identified in Santa Barbra California (Hatzenpichler personal observation) and in Seaside Oregon (Fig. 3, Schaible personal observation), providing opportunity to further explore this unique organism.

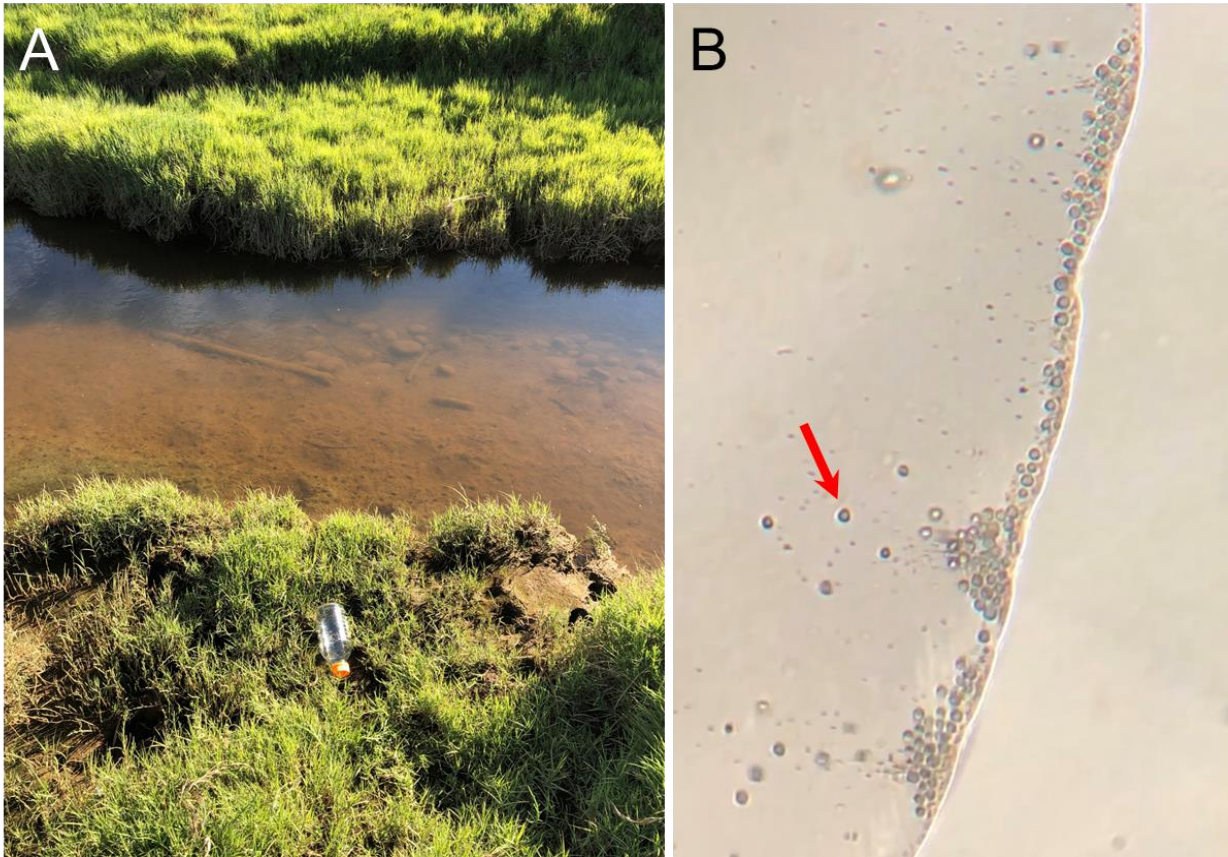


Fig. 3. MMB inhabiting an estuary in Seaside, OR. **A** Image showing where a sediment sample was collected. The location was subject to tidal fluxing from the Pacific Ocean with minimal freshwater input. **B** A hanging water droplet containing MMB from Seaside (arrow indicates a single MMB) viewed under 20x magnification.

References

- Abreu, F., Silva, K. T., Leao, P., Guedes, I. A., Keim, C. N., Farina, M., & Lins, U. (2013). Cell adhesion, multicellular morphology, and magnetosome distribution in the multicellular magnetotactic prokaryote *Candidatus Magnetoglobus multicellularis*. *Microsc Microanal*, *19*(3), 535-543. <https://doi.org/10.1017/S1431927613000329>
- Abreu, F., Silva, K. T., Martins, J. L., & Lins, U. (2006). Cell viability in magnetotactic multicellular prokaryotes. *International Microbiology*, *9*, 267-272.
- Black, S., Phillips, D., Hickey, J. W., Kennedy-Darling, J., Venkatarahaman, V. G., Samusik, N., Goltsev, Y., Schurch, C. M., & Nolan, G. P. (2021). CODEX multiplexed tissue imaging with DNA-conjugated antibodies. *Nat Protoc*, *16*(8), 3802-3835. <https://doi.org/10.1038/s41596-021-00556-8>
- Burmeister, A., Hilgers, F., Langner, A., Westerwalbesloh, C., Kerkhoff, Y., Tenhaef, N., Drepper, T., Kohlheyer, D., von Lieres, E., & Noack, S. (2019). A microfluidic co-cultivation platform to investigate microbial interactions at defined microenvironments. *Lab on a Chip*, *19*(1), 98-110.
- Cheng, Y., Burrack, R. K., & Li, Q. (2022). Spatially Resolved and Highly Multiplexed Protein and RNA In Situ Detection by Combining CODEX With RNAscope In Situ Hybridization. *J Histochem Cytochem*, *70*(8), 571-581. <https://doi.org/10.1369/00221554221114174>
- Hatzenpichler, R., Krukenberg, V., Spietz, R.L., Jay, Z.J. (2020). Next-generation physiology approaches to study microbial community function at the single cell level. *Nat. Rev. Microbiol.*
- Hille, F., Richter, H., Wong, S. P., Bratovic, M., Ressel, S., & Charpentier, E. (2018). The Biology of CRISPR-Cas: Backward and Forward. *Cell*, *172*(6), 1239-1259. <https://doi.org/10.1016/j.cell.2017.11.032>
- Hu, D., Cui, Y., Markillie, L. M., Chrisler, W. B., Wang, Q., Hatzenpichler, R., & Orr, G. (2021). Counting mRNA Copies in Intact Bacterial Cells by Fluctuation Localization Imaging-Based Fluorescence In Situ Hybridization (fliFISH). *Methods Mol Biol*, *2246*, 237-247. [https://doi.org/10.1007/978-1-0716-1115-9\\_15](https://doi.org/10.1007/978-1-0716-1115-9_15)
- Iranzo, J., Lobkovsky, A. E., Wolf, Y. I., & Koonin, E. V. (2014). Virus-host arms race at the joint origin of multicellularity and programmed cell death. *Cell Cycle*, *13*(19), 3083-3088. <https://doi.org/10.4161/15384101.2014.949496>
- Keim, C. N., Abreu, F., Lins, U., de Barros, H. L., & Farina, M. (2004). Cell organization and ultrastructure of a magnetotactic multicellular organism. *Journal of structural biology*, *145*(3), 254-262.

- Keim, C. N., Martins, J. L., de Barros, H. L., Lins, U., & Farina, M. (2007). Structure, behavior, ecology and diversity of multicellular magnetotactic prokaryotes. In *Magnetoreception and magnetosomes in bacteria*. Springer, 103-132.  
[https://doi.org/10.1007/7171\\_040/Published](https://doi.org/10.1007/7171_040/Published)
- Kolinko, S., Richter, M., Glockner, F. O., Brachmann, A., & Schuler, D. (2014). Single-cell genomics reveals potential for magnetite and greigite biomineralization in an uncultivated multicellular magnetotactic prokaryote. *Environ Microbiol Rep*, 6(5), 524-531.  
<https://doi.org/10.1111/1758-2229.12198>
- Koonin, E. V., & Wolf, Y. I. (2012). Evolution of microbes and viruses: a paradigm shift in evolutionary biology? *Front Cell Infect Microbiol*, 2, 119.  
<https://doi.org/10.3389/fcimb.2012.00119>
- Kremer, J. R., Mastronarde, D. N., & McIntosh, J. R. (1996). Computer visualization of three-dimensional image data using IMOD. *Journal of structural biology*, 116, 71-76.
- Kuswanto, W., Nolan, G., & Lu, G. (2023). Highly multiplexed spatial profiling with CODEX: bioinformatic analysis and application in human disease. *Semin Immunopathol*, 45(1), 145-157. <https://doi.org/10.1007/s00281-022-00974-0>
- Le Nagard, L., Morillo-López, V., Fradin, C., & Bazylinski, D. A. (2018). Growing magnetotactic bacteria of the genus magnetospirillum: strains msr-1, amb-1 and ms-1. *JoVE (Journal of Visualized Experiments)*(140), e58536.
- Leao, P., Chen, Y. R., Abreu, F., Wang, M., Zhang, W. J., Zhou, K., Xiao, T., Wu, L. F., & Lins, U. (2017). Ultrastructure of ellipsoidal magnetotactic multicellular prokaryotes depicts their complex assemblage and cellular polarity in the context of magnetotaxis. *Environ Microbiol*, 19(6), 2151-2163. <https://doi.org/10.1111/1462-2920.13677>
- Lee, K. S., Landry, Z., Pereira, F. C., Wagner, M., Berry, D., Huang, W. E., Taylor, G. T., Kneipp, J., Popp, J., Zhang, M., Cheng, J.-X., & Stocker, R. (2021). Raman microspectroscopy for microbiology. *Nature Reviews Methods Primers*, 1(1). <https://doi.org/10.1038/s43586-021-00075-6>
- Lefevre, C. T., Abreu, F., Lins, U., & Bazylinski, D. A. (2010). Nonmagnetotactic multicellular prokaryotes from low-saline, nonmarine aquatic environments and their unusual negative phototactic behavior. *Applied and Environmental Microbiology*, 76(10), 3220-3227.
- Medhekar, B., & Miller, J. F. (2007). Diversity-generating retroelements. *Curr Opin Microbiol*, 10(4), 388-395. <https://doi.org/10.1016/j.mib.2007.06.004>
- Musat, N., Musat, F., Weber, P. K., & Pett-Ridge, J. (2016). Tracking microbial interactions with NanoSIMS. *Curr Opin Biotechnol*, 41, 114-121.  
<https://doi.org/10.1016/j.copbio.2016.06.007>

- Parker, L. M., Sayyadi, N., Staikopoulos, V., Shrestha, A., Hutchinson, M. R., & Packer, N. H. (2019). Visualizing neuroinflammation with fluorescence and luminescent lanthanide-based in situ hybridization. *Journal of Neuroinflammation*, *16*(1), 1-13.
- Qian, X. X., Santini, C. L., Kosta, A., Menguy, N., Le Guenno, H., Zhang, W., Li, J., Chen, Y. R., Liu, J., Alberto, F., Espinosa, L., Xiao, T., & Wu, L. F. (2020). Juxtaposed membranes underpin cellular adhesion and display unilateral cell division of multicellular magnetotactic prokaryotes. *Environ Microbiol*, *22*(4), 1481-1494. <https://doi.org/10.1111/1462-2920.14710>
- Schaible, G. A., Kohtz, A. J., Cliff, J., & Hatzenpichler, R. (2022). Correlative SIP-FISH-Raman-SEM-NanoSIMS links identity, morphology, biochemistry, and physiology of environmental microbes. *ISME Communications*, *2*(1). <https://doi.org/10.1038/s43705-022-00134-3>
- Shapiro, O. H., Hatzenpichler, R., Buckley, D. H., Zinder, S. H., & Orphan, V. J. (2011). Multicellular photo-magnetotactic bacteria. *Environmental Microbiology Reports*, *3*(2), 233-238. <https://doi.org/10.1111/j.1758-2229.2010.00215.x>
- Silva, K. T., Abreu, F., Almeida, F. P., Keim, C. N., Farina, M., & Lins, U. (2007). Flagellar apparatus of south-seeking many-celled magnetotactic prokaryotes. *Microscopy research and technique*, *70*(1), 10-17.
- Silva, K. T., Abreu, F., Keim, C. N., Farina, M., & Lins, U. (2008). Ultrastructure and cytochemistry of lipid granules in the many-celled magnetotactic prokaryote, 'Candidatus Magnetoglobus multicellularis'. *Micron*, *39*(8), 1387-1392. <https://doi.org/10.1016/j.micron.2008.05.009>
- Simmons, S. L., & Edwards, K. J. (2007). Unexpected diversity in populations of the many-celled magnetotactic prokaryote. *Environ Microbiol*, *9*(1), 206-215. <https://doi.org/10.1111/j.1462-2920.2006.01129.x>
- Tan, J. Y., Wang, S., Dick, G. J., Young, V. B., Sherman, D. H., Burns, M. A., & Lin, X. N. (2020). Co-cultivation of microbial sub-communities in microfluidic droplets facilitates high-resolution genomic dissection of microbial 'dark matter'. *Integrative Biology*, *12*(11), 263-274.
- Tay, A., Pfeiffer, D., Rowe, K., Tannenbaum, A., Popp, F., Strangeway, R., Schüler, D., & Di Carlo, D. (2018). High-throughput microfluidic sorting of live magnetotactic bacteria. *Applied and Environmental Microbiology*, *84*(17), e01308-01318.
- Teng, Z., Zhang, Y., Zhang, W., Pan, H., Xu, J., Huang, H., Xiao, T., & Wu, L. F. (2018). Diversity and Characterization of Multicellular Magnetotactic Prokaryotes From Coral Reef Habitats of the Paracel Islands, South China Sea. *Front Microbiol*, *9*, 2135. <https://doi.org/10.3389/fmicb.2018.02135>

- Weidenbach, K., Nickel, L., Neve, H., Alkhnabashi, O. S., Künzel, S., Kupczok, A., Bauersachs, T., Cassidy, L., Tholey, A., & Backofen, R. (2017). Methanosarcina spherical virus, a novel archaeal lytic virus targeting Methanosarcina strains. *Journal of Virology*, *91*(22), 10.1128/jvi.00955-00917.
- Weiss, G. L., Eisenstein, F., Kieninger, A.-K., Xu, J., Minas, H. A., Gerber, M., Feldmüller, M., Maldener, I., Forchhammer, K., & Pilhofer, M. (2022). Structure of a thylakoid-anchored contractile injection system in multicellular cyanobacteria. *Nature microbiology*, *7*(3), 386-396.
- Wenter, R., Wanner, G., Schuler, D., & Overmann, J. (2009). Ultrastructure, tactic behaviour and potential for sulfate reduction of a novel multicellular magnetotactic prokaryote from North Sea sediments. *Environ Microbiol*, *11*(6), 1493-1505.  
<https://doi.org/10.1111/j.1462-2920.2009.01877.x>
- Wielgoss, S., Wolfensberger, R., Sun, L., Fiegna, F., & Velicer, G. J. (2019). Social genes are selection hotspots in kin groups of a soil microbe. *Science*, *363*(6433), 1342-1345.
- Zhou, K., Pan, H., Zhang, S., Yue, H., Xiao, T., & Wu, L. (2011). Occurrence and microscopic analyses of multicellular magnetotactic prokaryotes from coastal sediments in the Yellow Sea. *Chinese Journal of Oceanology and Limnology*, *29*(2), 246-251.  
<https://doi.org/10.1007/s00343-011-0032-8>

CUMULATIVE REFERENCES CITED

- Abreu, F., Martins, J. L., Silveira, T. S., Keim, C. N., de Barros, H. G., Filho, F. J., & Lins, U. (2007). 'Candidatus Magnetoglobus multicellularis', a multicellular, magnetotactic prokaryote from a hypersaline environment. *Int J Syst Evol Microbiol*, 57(Pt 6), 1318-1322. <https://doi.org/10.1099/ijs.0.64857-0>
- Abreu, F., Morillo, V., Nascimento, F. F., Werneck, C., Cantao, M. E., Ciapina, L. P., de Almeida, L. G., Lefevre, C. T., Bazylinski, D. A., de Vasconcelos, A. T., & Lins, U. (2014). Deciphering unusual uncultured magnetotactic multicellular prokaryotes through genomics. *ISME J*, 8(5), 1055-1068. <https://doi.org/10.1038/ismej.2013.203>
- Abreu, F., Silva, K. T., Leao, P., Guedes, I. A., Keim, C. N., Farina, M., & Lins, U. (2013). Cell adhesion, multicellular morphology, and magnetosome distribution in the multicellular magnetotactic prokaryote *Candidatus Magnetoglobus multicellularis*. *Microsc Microanal*, 19(3), 535-543. <https://doi.org/10.1017/S1431927613000329>
- Abreu, F., Silva, K. T., Martins, J. L., & Lins, U. (2006). Cell viability in magnetotactic multicellular prokaryotes. *International Microbiology*, 9, 267-272.
- Adami, C., Ofria, C., & Collier, T. C. (1999). Evolution of biological complexity. *Proceedings of the National Academy of Sciences*, 97, 4463-4468.
- Akse, S. P., Das, G., Agustí, S., Pichevin, L., Polerecky, L., & Middelburg, J. J. (2021). Imaging of organic signals in individual fossil diatom frustules with nanoSIMS and Raman spectroscopy. *Marine Chemistry*, 228. <https://doi.org/10.1016/j.marchem.2020.103906>
- Alcolombri, U., Pioli, R., Stocker, R., & Berry, D. (2022). Single-cell stable isotope probing in microbial ecology. *ISME Communications*, 2(1). <https://doi.org/10.1038/s43705-022-00142-3>
- Allwood, A. C., Walter, M. R., Kamber, B. S., Marshall, C. P., & Burch, I. W. (2006). Stromatolite reef from the Early Archaean era of Australia. *Nature*, 441(7094), 714-718.
- Almeida, F. P., Viana, N. B., Lins, U., Farina, M., & Keim, C. N. (2013). Swimming behaviour of the multicellular magnetotactic prokaryote 'Candidatus Magnetoglobus multicellularis' under applied magnetic fields and ultraviolet light. *Antonie Van Leeuwenhoek*, 103(4), 845-857. <https://doi.org/10.1007/s10482-012-9866-0>
- Altschul, S. F., Gish, W., Miller, W., Myers, E. W., & Lipman, D. J. (1990). Basic local alignment search tool. *Journal of Molecular Biology*, 215(3), 403-410.
- Amann, R., & Fuchs, B. M. (2008). Single-cell identification in microbial communities by improved fluorescence in situ hybridization techniques. *Nat Rev Microbiol*, 6(5), 339-348. <https://doi.org/10.1038/nrmicro1888>

- Amor, M., Tharaud, M., Gelabert, A., & Komeili, A. (2020). Single-cell determination of iron content in magnetotactic bacteria: implications for the iron biogeochemical cycle. *Environ Microbiol*, 22(3), 823-831. <https://doi.org/10.1111/1462-2920.14708>
- Ando, T., Bhamidimarri, S. P., Brending, N., Colin-York, H., Collinson, L., De Jonge, N., De Pablo, P. J., Debroye, E., Eggeling, C., & Franck, C. a. F., M., . (2018). The 2018 correlative microscopy techniques roadmap. *Journal of physics D: Applied physics*, 51.
- Araujo, A. C., Abreu, F., Silva, K. T., Bazylnski, D. A., & Lins, U. (2015). Magnetotactic bacteria as potential sources of bioproducts. *Mar Drugs*, 13(1), 389-430. <https://doi.org/10.3390/md13010389>
- Bazylnski, D. A., & Frankel, R. B. (2004). Magnetosome formation in prokaryotes. *Nat Rev Microbiol*, 2(3), 217-230. <https://doi.org/10.1038/nrmicro842>
- Behrens, S., Ruhland, C., Inacio, J., Huber, H., Fonseca, A., Spencer-Martins, I., Fuchs, B. M., & Amann, R. (2003). In situ accessibility of small-subunit rRNA of members of the domains Bacteria, Archaea, and Eucarya to Cy3-labeled oligonucleotide probes. *Appl Environ Microbiol*, 69(3), 1748-1758. <https://doi.org/10.1128/AEM.69.3.1748-1758.2003>
- Berry, D., Mader, E., Lee, T. K., Woebken, D., Wang, Y., Zhu, D., Palatinszky, M., Schintlmeister, A., Schmid, M. C., Hanson, B. T., Shterzer, N., Mizrahi, I., Rauch, I., Decker, T., Bocklitz, T., Popp, J., Gibson, C. M., Fowler, P. W., Huang, W. E., & Wagner, M. (2015). Tracking heavy water (D2O) incorporation for identifying and sorting active microbial cells. *Proc Natl Acad Sci U S A*, 112(2), E194-203. <https://doi.org/10.1073/pnas.1420406112>
- Betts, H. C., Puttick, M. N., Clark, J. W., Williams, T. A., Donoghue, P. C., & Pisani, D. (2018). Integrated genomic and fossil evidence illuminates life's early evolution and eukaryote origin. *Nature ecology & evolution*, 2(10), 1556-1562.
- Betzig, E., Patterson, G. H., Sougrat, R., Lindwasser, O. W., Olenych, S., Bonifacino, J. S., Davidson, M. W., Lippincott-Schwartz, J., & Hess, H. F. (2006). Imaging intracellular fluorescent proteins at nanometer resolution. *Science*, 313(5793), 1642-1645. <https://doi.org/10.1126/science.1127344>
- Bi, Y., Hubbard, C., Purushotham, P., & Zimmer, J. (2015). Insights into the structure and function of membrane-integrated processive glycosyltransferases. *Curr Opin Struct Biol*, 34, 78-86. <https://doi.org/10.1016/j.sbi.2015.07.008>
- Black, S., Phillips, D., Hickey, J. W., Kennedy-Darling, J., Venkatarahaman, V. G., Samusik, N., Goltsev, Y., Schurch, C. M., & Nolan, G. P. (2021). CODEX multiplexed tissue imaging with DNA-conjugated antibodies. *Nat Protoc*, 16(8), 3802-3835. <https://doi.org/10.1038/s41596-021-00556-8>

- Bocklitz, T., Walter, A., Hartmann, K., Rösch, P., & Popp, J. (2011). How to pre-process Raman spectra for reliable and stable models? *Analytica chimica acta*, 704(1-2), 47-56.
- Bonner, J. T. (1998). The origins of multicellularity. *Integrative Biology*, 1, 27-36.
- Bonner, J. T. (2004). Perspective: the size-complexity rule. *Evolution*, 58(9), 1883-1890.
- Borchers, H. W. (2023). *pracma: Practical Numerical Math Functions* <https://CRAN.R-project.org/package=pracma>, R package version 2.4.4.
- Borisov, V. B., Gennis, R. B., Hemp, J., & Verkhovsky, M. I. (2011). The cytochrome bd respiratory oxygen reductases. *Biochim Biophys Acta*, 1807(11), 1398-1413. <https://doi.org/10.1016/j.bbabi.2011.06.016>
- Bourdoiseau, J.-A., Jeannin, M., Rémazeilles, C., Sabot, R., & Refait, P. (2011). The transformation of mackinawite into greigite studied by Raman spectroscopy. *Journal of Raman Spectroscopy*, 42(3), 496-504. <https://doi.org/10.1002/jrs.2729>
- Bowen, J. L., Morrison, H. G., Hobbie, J. E., & Sogin, M. L. (2012). Salt marsh sediment diversity: a test of the variability of the rare biosphere among environmental replicates. *ISME Journal*, 6(11), 2014-2023. <https://doi.org/10.1038/ismej.2012.47>
- Bozdag, G. O., Libby, E., Pineau, R., Reinhard, C. T., & Ratcliff, W. C. (2021). Oxygen suppression of macroscopic multicellularity. *Nat Commun*, 12(1), 2838. <https://doi.org/10.1038/s41467-021-23104-0>
- Bozdag, G. O., Szeinbaum, N., Conlin, P., Chen, K., Fos, S. M., Garcia, A., Penev, P., Schaible, G. A., & Trubl, G. (2023). Major biological innovations that had an impact on the diversity and complexity of life on Earth. *Astrobiology*.
- Brezeştean, I., Bocăneală, M., Gherman, A. M. R., Porav, S. A., Kacsó, I., Rakosy-Tican, E., & Dina, N. E. (2021). Spectroscopic investigation of exopolysaccharides purified from *Arthrospira platensis* cultures as potential bioresources. *Journal of Molecular Structure*, 1246. <https://doi.org/10.1016/j.molstruc.2021.131228>
- Brooks, D. R., & Wiley, E. O. (1988). *Evolution as entropy*. University of Chicago Press Chicago.
- Brunet, T., & King, N. (2017). The Origin of Animal Multicellularity and Cell Differentiation. *Dev Cell*, 43(2), 124-140. <https://doi.org/10.1016/j.devcel.2017.09.016>
- Bull, L. (2020). The Evolution of Complexity: Simple Simulations of Major Innovations. *Springer Nature*, 37.
- Burmeister, A., Hilgers, F., Langner, A., Westerwalbesloh, C., Kerkhoff, Y., Tenhaef, N., Drepper, T., Kohlheyer, D., von Lieres, E., & Noack, S. (2019). A microfluidic co-

- cultivation platform to investigate microbial interactions at defined microenvironments. *Lab on a Chip*, 19(1), 98-110.
- Bushnell, B. (2014). BBMap: a fast, accurate, splice-aware aligner. *Lawrence Berkeley National Lab*.
- Butterfield, N. J. (2000). Bangiomorpha pubescens n. gen., n. sp.: implications for the evolution of sex, multicellularity, and the Mesoproterozoic/Neoproterozoic radiation of eukaryotes. *Paleobiology*, 26(3), 386-404.
- Campbell, J. H., O'Donoghue, P., Campbell, A. G., Schwientek, P., Sczyrba, A., Woyke, T., Soll, D., & Podar, M. (2013). UGA is an additional glycine codon in uncultured SR1 bacteria from the human microbiota. *Proc Natl Acad Sci U S A*, 110(14), 5540-5545. <https://doi.org/10.1073/pnas.1303090110>
- Carroll, S. B. (2001). Chance and necessity: the evolution of morphological complexity and diversity. *Nature*, 409(6823), 1102-1109.
- Chavhan, Y., Dey, S., & Lind, P. A. (2023). Bacteria evolve macroscopic multicellularity by the genetic assimilation of phenotypically plastic cell clustering. *Nat Commun*, 14(1), 3555. <https://doi.org/10.1038/s41467-023-39320-9>
- Chen, I. A., Chu, K., Palaniappan, K., Ratner, A., Huang, J., Huntemann, M., Hajek, P., Ritter, S. J., Webb, C., & Wu, D. (2023). The IMG/M data management and analysis system v. 7: content updates and new features. *Nucleic Acids Research*, 51(D1), D723-D732.
- Chen, Y. R., Zhang, R., Du, H. J., Pan, H. M., Zhang, W. Y., Zhou, K., Li, J. H., Xiao, T., & Wu, L. F. (2015). A novel species of ellipsoidal multicellular magnetotactic prokaryotes from Lake Yuehu in China. *Environ Microbiol*, 17(3), 637-647. <https://doi.org/10.1111/1462-2920.12480>
- Cheng, Y., Burrack, R. K., & Li, Q. (2022). Spatially Resolved and Highly Multiplexed Protein and RNA In Situ Detection by Combining CODEX With RNAscope In Situ Hybridization. *J Histochem Cytochem*, 70(8), 571-581. <https://doi.org/10.1369/00221554221114174>
- Chiyomaru, K., & Takemoto, K. (2020). Revisiting the hypothesis of an energetic barrier to genome complexity between eukaryotes and prokaryotes. *R Soc Open Sci*, 7(2), 191859. <https://doi.org/10.1098/rsos.191859>
- Claessen, D., Rozen, D. E., Kuipers, O. P., Sogaard-Andersen, L., & van Wezel, G. P. (2014). Bacterial solutions to multicellularity: a tale of biofilms, filaments and fruiting bodies. *Nat Rev Microbiol*, 12(2), 115-124. <https://doi.org/10.1038/nrmicro3178>
- Colizzi, E. S. V., R. M.; Merks, R. M. (2020). Evolution of multicellularity by collective integration of spatial information. *Elife*, 9. <https://doi.org/10.7554/eLife.56349>

- Collier, J. (1986). Entropy in evolution. *Biology and Philosophy*, 1, 5-24.
- Collin, R., & Miglietta, M. P. (2008). Reversing opinions on Dollo's Law. *Trends in ecology & evolution*, 23(11), 602-609.
- Comolli, L. R., Baker, B. J., Downing, K. H., Siegerist, C. E., & Banfield, J. F. (2009). Three-dimensional analysis of the structure and ecology of a novel, ultra-small archaeon. *The ISME journal*, 3(2), 159-167.
- Cope, E. (1887). *The origin of the fittest*: New York. *Appleton and Co.*
- Cope, E. D. (1904). *The primary factors of organic evolution*. Open Court Publishing Company.
- Craig, L., Forest, K. T., & Maier, B. (2019). Type IV pili: dynamics, biophysics and functional consequences. *Nat Rev Microbiol*, 17(7), 429-440. <https://doi.org/10.1038/s41579-019-0195-4>
- Crowther, T. W., Van den Hoogen, J., Wan, J., Mayes, M. A., Keiser, A., Mo, L., Averill, C., & Maynard, D. S. (2019). The global soil community and its influence on biogeochemistry. *Science*, 365(6455), eaav0550.
- Cruickshank, R. H., & Paterson, A. M. (2006). The great escape: do parasites break Dollo's law? *TRENDS in Parasitology*, 22(11), 509-515.
- Cui, K., Pan, H., Chen, J., Liu, J., Zhao, Y., Chen, S., Zhang, W., Xiao, T., & Wu, L. F. (2022). A Novel Isolate of Spherical Multicellular Magnetotactic Prokaryotes Has Two Magnetosome Gene Clusters and Synthesizes Both Magnetite and Greigite Crystals. *Microorganisms*, 10(5). <https://doi.org/10.3390/microorganisms10050925>
- Cui, L., Xin, Y., Yang, K., Li, H., Tan, F., Zhang, Y., Li, X., Zhu, Z., Yang, J., Kao, S. J., Ren, B., Zhu, Y. G., Musat, F., & Musat, N. (2023). Live tracking metabolic networks and physiological responses within microbial assemblages at single-cell level. *PNAS Nexus*, 2(3), pgad006. <https://doi.org/10.1093/pnasnexus/pgad006>
- Daims, H., Brühl, A., Amann, R., Schleifer, K.-H., & Wagner, M. (1999). The Domain-specific Probe EUB338 is Insufficient for the Detection of all Bacteria: Development and Evaluation of a more Comprehensive Probe Set. *Systematic and Applied Microbiology*, 22(3), 434-444. [https://doi.org/10.1016/s0723-2020\(99\)80053-8](https://doi.org/10.1016/s0723-2020(99)80053-8)
- Daims, H., Lucker, S., & Wagner, M. (2006). daime, a novel image analysis program for microbial ecology and biofilm research. *Environ Microbiol*, 8(2), 200-213. <https://doi.org/10.1111/j.1462-2920.2005.00880.x>
- Daims, H., Stoecker, K., & Wagner, M. (2004). Fluorescence in situ hybridization for the detection of prokaryotes. *Taylor & Francis, Molecular microbial ecology*, 208-228.

- Dar, D., Dar, N., Cai, L., & Newman, D. K. (2021). Spatial transcriptomics of planktonic and sessile bacterial populations at single-cell resolution. *Science*, 373(6556). <https://doi.org/10.1126/science.abi4882>
- Darwin, C. (1859). On the Origin of Species by Means of Natural Selection, or, The Preservation of Favoured Races in the Struggle for Life. *J. Murray*.
- Davila, A. F., Winklhofer, M., McKay, C. . (2007). Multicellular magnetotactic prokaryote as a target for life search on Mars. *38th Lunar and Planetary Science Conference*, 1338. <https://doi.org/10.1007/7171>
- Dawkins, R. (2016). *The selfish gene*. Oxford university press.
- Dobro, M. J., Oikonomou, C. M., Piper, A., Cohen, J., Guo, K., Jensen, T., Tadayon, J., Donermeyer, J., Park, Y., & Solis, B. A. (2017). Uncharacterized bacterial structures revealed by electron cryotomography. *Journal of bacteriology*, 199(17), 10.1128/jb.00100-00117.
- Dollo, L. (1893). Les lois de l'évolution. *Bull. Soc. Belge Geol. Pal. Hydr*, VII, 164-166.
- Doughty, D. M., Dieterle, M., Sessions, A. L., Fischer, W. W., & Newman, D. K. (2014). Probing the subcellular localization of hopanoid lipids in bacteria using NanoSIMS. *PLoS One*, 9(1), e84455.
- Eder, S. H., Gigler, A. M., Hanzlik, M., & Winklhofer, M. (2014). Sub-micrometer-scale mapping of magnetite crystals and sulfur globules in magnetotactic bacteria using confocal Raman micro-spectrometry. *PLoS One*, 9(9), e107356. <https://doi.org/10.1371/journal.pone.0107356>
- Edgar, R. C. (2004). MUSCLE: multiple sequence alignment with high accuracy and high throughput. *Nucleic Acids Res*, 32(5), 1792-1797. <https://doi.org/10.1093/nar/gkh340>
- Eichorst, S. A., Strasser, F., Woyke, T., Schintlmeister, A., Wagner, M., & Wobken, D. (2015). Advancements in the application of NanoSIMS and Raman microspectroscopy to investigate the activity of microbial cells in soils. *FEMS Microbiol Ecol*, 91(10). <https://doi.org/10.1093/femsec/fiv106>
- Eilers, P. H., & Boelens, H. F. (2005). Baseline correction with asymmetric least squares smoothing. *Leiden University Medical Centre Report*, 1(1), 5.
- Endesfelder, U. (2015). Advances in Correlative Single-Molecule Localization Microscopy and Electron Microscopy. *NanoBioImaging*, 1(1). <https://doi.org/10.2478/nbi-2014-0002>
- Esquivel, D. M. S., Lins de Barros, H. G. P., Farina, M., Aragão, P. H. A., & Danon, J. (1983). Microorganismes magnétotactiques de la region de Rio de Janeiro. *Biology of the cell*, 47, 227-234.

- Faivre, D., & Schuler, D. (2008). Magnetotactic bacteria and magnetosomes. *Chem Rev*, *108*(11), 4875-4898. <https://doi.org/10.1021/cr078258w>
- Farina, M., Esquivel, D. M. S., & Debarros, H. G. P. L. (1990). Magnetic Iron-Sulfur Crystals from a Magnetotactic Microorganism. *Nature*, *343*(6255), 256-258. <https://doi.org/DOI10.1038/343256a0>
- Farina, M., Lins de Barros, H., Esquivel, D. M. S., & Danon, J. (1983). Ultrastructure of a magnetotactic bacterium. *Biol Cell*, *48*, 85-88.
- Fisher, R. M., Cornwallis, C. K., & West, S. A. (2013). Group formation, relatedness, and the evolution of multicellularity. *Curr Biol*, *23*(12), 1120-1125. <https://doi.org/10.1016/j.cub.2013.05.004>
- Fisher, R. M., & Regenberg, B. (2019). Multicellular group formation in *Saccharomyces cerevisiae*. *Proc Biol Sci*, *286*(1910), 20191098. <https://doi.org/10.1098/rspb.2019.1098>
- Frankel, R. B., Bazylnski, D. A., Johnson, M. S., & Taylor, B. L. (1997). Magneto-aerotaxis in marine coccoid bacteria. *Biophysical journal*, *73*, 994-1000.
- Frerebeau, N. (2023). alkahest: Pre-Processing XY Data from Experimental Methods. <https://CRAN.R-project.org/package=alkahest> R package version 1.1.1.9000.
- Friedman, I. (1953). Deuterium content of natural waters and other substances. *Geochimica et cosmochimica acta*, *4*(1-2), 89-103.
- Gautam, R., Vanga, S., Ariese, F., & Umapathy, S. (2015). Review of multidimensional data processing approaches for Raman and infrared spectroscopy. *EPJ Techniques and Instrumentation*, *2*, 1-38.
- Geerlings, N. M. J., Karman, C., Trashin, S., As, K. S., Kienhuis, M. V. M., Hidalgo-Martinez, S., Vasquez-Cardenas, D., Boschker, H. T. S., De Wael, K., Middelburg, J. J., Polerecky, L., & Meysman, F. J. R. (2020). Division of labor and growth during electrical cooperation in multicellular cable bacteria. *Proc Natl Acad Sci U S A*, *117*(10), 5478-5485. <https://doi.org/10.1073/pnas.1916244117>
- Geier, B., Sogin, E. M., Michellod, D., Janda, M., Kompauer, M., Spengler, B., Dubilier, N., & Liebeke, M. (2020). Spatial metabolomics of in situ host-microbe interactions at the micrometre scale. *Nat Microbiol*, *5*(3), 498-510. <https://doi.org/10.1038/s41564-019-0664-6>
- Gevrekci, A. O. (2017). The roles of polyamines in microorganisms. *World J Microbiol Biotechnol*, *33*(11), 204. <https://doi.org/10.1007/s11274-017-2370-y>
- Gibson, T. M., Shih, P. M., Cumming, V. M., Fischer, W. W., Crockford, P. W., Hodgskiss, M. S., Wörndle, S., Creaser, R. A., Rainbird, R. H., & Skulski, T. M. (2018). Precise age of

- Bangiomorpha pubescens dates the origin of eukaryotic photosynthesis. *Geology*, 46(2), 135-138.
- Gilbert, J. A., Blaser, M. J., Caporaso, J. G., Jansson, J. K., Lynch, S. V., & Knight, R. (2018). Current understanding of the human microbiome. *Nature medicine*, 24(4), 392-400.
- Gilchrist, C. L. M., & Chooi, Y. H. (2021). clinker & clustermap.js: automatic generation of gene cluster comparison figures. *Bioinformatics*, 37(16), 2473-2475. <https://doi.org/10.1093/bioinformatics/btab007>
- Golubic, S., Sergeev, V. N., & Knoll, A. H. (1995). Mesoproterozoic Archaeoellipsoides: akinetes of heterocystous cyanobacteria. *Lethaia*, 28(4), 285-298.
- Gould, S. J. (1966). Allometry and size in ontogeny and phylogeny. *Biological Reviews*, 41, 587-638.
- Gould, S. J. (1970). Dollo on Dollo's law: irreversibility and the status of evolutionary laws. *Journal of the History of Biology*, 3, 189-212.
- Gould, S. J. (1996). *Full house: The spread of excellence from Plato to Darwin*. Harvard University Press.
- Grant, C. R., Wan, J., & Komeili, A. (2018). Organelle Formation in Bacteria and Archaea. *Annu Rev Cell Dev Biol*, 34, 217-238. <https://doi.org/10.1146/annurev-cellbio-100616-060908>
- Greenberg, M., Canter, K., Mahler, I., & Tornheim, A. (2005). Observation of magnetoreceptive behavior in a multicellular magnetotactic prokaryote in higher than geomagnetic fields. *Biophys J*, 88(2), 1496-1499. <https://doi.org/10.1529/biophysj.104.047068>
- Greening, C., & Lithgow, T. (2020). Formation and function of bacterial organelles. *Nat Rev Microbiol*, 18(12), 677-689. <https://doi.org/10.1038/s41579-020-0413-0>
- Greilhuber, J., Dolezel, J., Lysak, M. A., & Bennett, M. D. (2005). The origin, evolution and proposed stabilization of the terms 'genome size' and 'C-value' to describe nuclear DNA contents. *Ann Bot*, 95(1), 255-260. <https://doi.org/10.1093/aob/mci019>
- Grieb, A., Bowers, R. M., Oggerin, M., Goudeau, D., Lee, J., Malmstrom, R. R., Woyke, T., & Fuchs, B. M. (2020). A pipeline for targeted metagenomics of environmental bacteria. *Microbiome*, 8(1), 21. <https://doi.org/10.1186/s40168-020-0790-7>
- Grosberg, R. K., & Strathmann, R. R. (2007). The Evolution of Multicellularity: A Minor Major Transition? *Annual Review of Ecology, Evolution, and Systematics*, 38(1), 621-654. <https://doi.org/10.1146/annurev.ecolsys.36.102403.114735>

- Gulli, J. G., Herron, M. D., & Ratcliff, W. C. (2019). Evolution of altruistic cooperation among nascent multicellular organisms. *Evolution*, *73*(5), 1012-1024.  
<https://doi.org/10.1111/evo.13727>
- Guo, S., Popp, J., & Bocklitz, T. (2021). Chemometric analysis in Raman spectroscopy from experimental design to machine learning–based modeling. *Nature protocols*, *16*(12), 5426-5459.
- Hallgren, J., Tsirigos, K. D., Pedersen, M. D., Almagro Armenteros, J. J., Marcatili, P., Nielsen, H., Krogh, A., & Winther, O. (2022). DeepTMHMM predicts alpha and beta transmembrane proteins using deep neural networks *bioRxiv*.  
<https://doi.org/10.1101/2022.04.08.487609>
- Hanke, D. (2004). Teleology: The explanation that bedevils biology. *Explanations: Styles of explanation in science*, *143*, 155.
- Hao, L., McIlroy, S. J., Kirkegaard, R. H., Karst, S. M., Fernando, W. E. Y., Aslan, H., Meyer, R. L., Albertsen, M., Nielsen, P. H., & Dueholm, M. S. (2018). Novel prosthecate bacteria from the candidate phylum Acetothermia. *ISME J*, *12*(9), 2225-2237.  
<https://doi.org/10.1038/s41396-018-0187-9>
- Hapca, S., Baveye, P. C., Wilson, C., Lark, R. M., & Otten, W. (2015). Three-Dimensional Mapping of Soil Chemical Characteristics at Micrometric Scale by Combining 2D SEM-EDX Data and 3D X-Ray CT Images. *PLoS One*, *10*(9), e0137205.  
<https://doi.org/10.1371/journal.pone.0137205>
- Hatzenpichler, R., Krukenberg, V., Spietz, R.L., Jay, Z.J. (2020). Next-generation physiology approaches to study microbial community function at the single cell level. *Nat. Rev. Microbiol.*
- Hatzenpichler, R., Scheller, S., Tavormina, P. L., Babin, B. M., Tirrell, D. A., & Orphan, V. J. (2014). In situ visualization of newly synthesized proteins in environmental microbes using amino acid tagging and click chemistry. *Environ Microbiol*, *16*(8), 2568-2590.  
<https://doi.org/10.1111/1462-2920.12436>
- Heim, N. A., Knope, M. L., Schaal, E. K., Wang, S. C., & Payne, J. L. (2015). Cope's rule in the evolution of marine animals. *Science*, *347*(6224), 867-870.
- Heim, N. A., Payne, J. L., Finnegan, S., Knope, M. L., Kowalewski, M., Lyons, S. K., McShea, D. W., Novack-Gottshall, P. M., Smith, F. A., & Wang, S. C. (2017). Hierarchical complexity and the size limits of life. *Proc Biol Sci*, *284*(1857).  
<https://doi.org/10.1098/rspb.2017.1039>
- Henderson, G. P., Gan, L., & Jensen, G. J. (2007). 3-D ultrastructure of *O. tauri*: electron cryotomography of an entire eukaryotic cell. *PLoS One*, *2*(8), e749.

- Herrero, A., Stavans, J., & Flores, E. (2016). The multicellular nature of filamentous heterocyst-forming cyanobacteria. *FEMS Microbiol Rev*, *40*(6), 831-854. <https://doi.org/10.1093/femsre/fuw029>
- Herron, M. D., Borin, J. M., Boswell, J. C., Walker, J., Chen, I. K., Knox, C. A., Boyd, M., Rosenzweig, F., & Ratcliff, W. C. (2019). De novo origins of multicellularity in response to predation. *Sci Rep*, *9*(1), 2328. <https://doi.org/10.1038/s41598-019-39558-8>
- Hille, F., Richter, H., Wong, S. P., Bratovic, M., Ressel, S., & Charpentier, E. (2018). The Biology of CRISPR-Cas: Backward and Forward. *Cell*, *172*(6), 1239-1259. <https://doi.org/10.1016/j.cell.2017.11.032>
- Hu, D., Cui, Y., Markillie, L. M., Chrisler, W. B., Wang, Q., Hatzenpichler, R., & Orr, G. (2021). Counting mRNA Copies in Intact Bacterial Cells by Fluctuation Localization Imaging-Based Fluorescence In Situ Hybridization (fliFISH). *Methods Mol Biol*, *2246*, 237-247. [https://doi.org/10.1007/978-1-0716-1115-9\\_15](https://doi.org/10.1007/978-1-0716-1115-9_15)
- Huang, W. E., Griffiths, R. I., Thompson, I. P., Bailey, M. J., & Whiteley, A. S. (2004). Raman microscopic analysis of single microbial cells. *Analytical chemistry*, *76*(15), 4452-4458.
- Huang, W. E., Stoecker, K., Griffiths, R., Newbold, L., Daims, H., Whiteley, A. S., & Wagner, M. (2007). Raman-FISH: combining stable-isotope Raman spectroscopy and fluorescence in situ hybridization for the single cell analysis of identity and function. *Environ Microbiol*, *9*(8), 1878-1889. <https://doi.org/10.1111/j.1462-2920.2007.01352.x>
- Hug, L. A., Baker, B. J., Anantharaman, K., Brown, C. T., Probst, A. J., Castelle, C. J., Butterfield, C. N., HERNSDORF, A. W., Amano, Y., & Ise, K. (2016). A new view of the tree of life. *Nature microbiology*, *1*(5), 1-6.
- Hungate, B. A., Mau, R. L., Schwartz, E., Caporaso, J. G., Dijkstra, P., van Gestel, N., Koch, B. J., Liu, C. M., McHugh, T. A., & Marks, J. C. (2015). Quantitative microbial ecology through stable isotope probing. *Applied and Environmental Microbiology*, *81*(21), 7570-7581.
- Hyatt, D., Chen, G.-L., LoCascio, P. F., Land, M. L., Larimer, F. W., & Hauser, L. J. (2010). Prodigal: prokaryotic gene recognition and translation initiation site identification. *BMC bioinformatics*, *11*, 1-11.
- Iranzo, J., Lobkovsky, A. E., Wolf, Y. I., & Koonin, E. V. (2014). Virus-host arms race at the joint origin of multicellularity and programmed cell death. *Cell Cycle*, *13*(19), 3083-3088. <https://doi.org/10.4161/15384101.2014.949496>
- Islam, S. T., Vergara Alvarez, I., Saidi, F., Guiseppi, A., Vinogradov, E., Sharma, G., Espinosa, L., Morrone, C., Brasseur, G., Guillemot, J. F., Benarouche, A., Bridot, J. L., Ravicoularamin, G., Cagna, A., Gauthier, C., Singer, M., Fierobe, H. P., Mignot, T., & Mauriello, E. M. F. (2020). Modulation of bacterial multicellularity via spatio-specific

- polysaccharide secretion. *PLoS Biol*, 18(6), e3000728.  
<https://doi.org/10.1371/journal.pbio.3000728>
- Jain, C., Rodriguez, R. L., Phillippy, A. M., Konstantinidis, K. T., & Aluru, S. (2018). High throughput ANI analysis of 90K prokaryotic genomes reveals clear species boundaries. *Nat Commun*, 9(1), 5114. <https://doi.org/10.1038/s41467-018-07641-9>
- Jennings, R. C., Belgio, E., & Zucchelli, G. (2020). Does maximal entropy production play a role in the evolution of biological complexity? A biological point of view. *Rendiconti Lincei. Scienze Fisiche e Naturali*, 31(2), 259-268. <https://doi.org/10.1007/s12210-020-00909-7>
- Joosten, B., Willemse, M., Fransen, J., Cambi, A., & van den Dries, K. (2018). Super-Resolution Correlative Light and Electron Microscopy (SR-CLEM) Reveals Novel Ultrastructural Insights Into Dendritic Cell Podosomes. *Frontiers in Immunology*, 9. <https://doi.org/ARTN 1908>  
 10.3389/fimmu.2018.01908
- Jurenas, D., Fraikin, N., Goormaghtigh, F., & Van Melderen, L. (2022). Biology and evolution of bacterial toxin-antitoxin systems. *Nat Rev Microbiol*, 20(6), 335-350.  
<https://doi.org/10.1038/s41579-021-00661-1>
- Justice, N. B., Li, Z., Wang, Y., Spaulding, S. E., Mosier, A. C., Hettich, R. L., Pan, C., & Banfield, J. F. (2014). 15 N-and 2 H proteomic stable isotope probing links nitrogen flow to archaeal heterotrophic activity. *Environmental Microbiology*, 16(10), 3224-3237.
- Kaiser, D. (1986). Control of multicellular development: Dictyostelium and Myxococcus. *Annual Review of Genetics*, 20, 539-566.
- Kaiser, D. (2001). Building a multicellular organism. *Annual Review of Genetics*, 35(1), 103-123.
- Kanehisa, M., Furumichi, M., Sato, Y., Kawashima, M., & Ishiguro-Watanabe, M. (2023). KEGG for taxonomy-based analysis of pathways and genomes. *Nucleic Acids Res*, 51(D1), D587-D592. <https://doi.org/10.1093/nar/gkac963>
- Kang, D. D., Li, F., Kirton, E., Thomas, A., Egan, R., An, H., & Wang, Z. (2019). MetaBAT 2: an adaptive binning algorithm for robust and efficient genome reconstruction from metagenome assemblies. *PeerJ*, 7, e7359. <https://doi.org/10.7717/peerj.7359>
- Karnkowska, A., Vacek, V., Zubáčová, Z., Treitli, S. C., Petrželková, R., Eme, L., Novák, L., Žárský, V., Barlow, L. D., & Herman, E. K. (2016). A eukaryote without a mitochondrial organelle. *Current Biology*, 26(10), 1274-1284.
- Kassambara, A. (2019). *Comparing groups: Numerical variables* (Vol. 192). Datanovia.

- Katayama, T., Nobu, M. K., Kusada, H., Meng, X. Y., Yoshioka, H., Kamagata, Y., & Tamaki, H. (2019). Membrane-bounded nucleoid discovered in a cultivated bacterium of the candidate phylum 'Atribacteria'. *bioRxiv*, 728279. <https://doi.org/10.1101/728279>
- Katsnelson, M. I., Wolf, Y. I., & Koonin, E. V. (2018). Towards physical principles of biological evolution. *Physica Scripta*, 93(4). <https://doi.org/10.1088/1402-4896/aaaba4>
- Keim CN, Martins JL, de Barros HL, Lins U, & M., F. (2006). Structure, behavior, ecology and diversity of multicellular magnetotactic prokaryotes. *Magnetoreception and magnetosomes in bacteria*(Springer, Berlin, Heidelberg), 103-132.
- Keim, C. N., Abreu, F., Lins, U., de Barros, H. L., & Farina, M. (2004). Cell organization and ultrastructure of a magnetotactic multicellular organism. *Journal of structural biology*, 145(3), 254-262.
- Keim, C. N., Abreu, F., Lins, U., de Barros, L., & Farina, M. (2004). Cell organization and ultrastructure of a magnetotactic multicellular organism. *J Struct Biol*, 145(3), 254-262. <https://doi.org/10.1016/j.jsb.2003.10.022>
- Keim, C. N., Abreu, F., Lins, U., Lins de Barros, H., & Farina, M. (2004). Cell organization and ultrastructure of a magnetotactic multicellular organism. *J Struct Biol*, 145(3), 254-262. <https://doi.org/10.1016/j.jsb.2003.10.022>
- Keim, C. N., Farina, M., & Lins, U. (2007). Magnetoglobus, Magnetic Aggregates in Anaerobic Environments. *Microbe* 2, 437-445.
- Keim, C. N., Martins, J. L., Abreu, F., Rosado, A. S., de Barros, H. L., Borojevic, R., Lins, U., & Farina, M. (2004a). Multicellular life cycle of magnetotactic prokaryotes. *FEMS Microbiol Letters*, 240(2), 203-208. <https://doi.org/10.1016/j.femsle.2004.09.035>
- Keim, C. N., Martins, J. L., Abreu, F., Rosado, A. S., de Barros, H. L., Borojevic, R., Lins, U., & Farina, M. (2004b). Multicellular life cycle of magnetotactic prokaryotes. *FEMS Microbiology Letters*, 240(2), 203-208.
- Keim, C. N., Martins, J. L., de Barros, H. L., Lins, U., & Farina, M. (2007). Structure, behavior, ecology and diversity of multicellular magnetotactic prokaryotes. In *Magnetoreception and magnetosomes in bacteria*. Springer, 103-132. [https://doi.org/10.1007/7171\\_040/Published](https://doi.org/10.1007/7171_040/Published)
- Kim, W., Levy, S. B., & Foster, K. R. (2016). Rapid radiation in bacteria leads to a division of labour. *Nat Commun*, 7, 10508. <https://doi.org/10.1038/ncomms10508>
- Kirk, D. L. (2005). A twelve-step program for evolving multicellularity and a division of labor. *Bioessays*, 27(3), 299-310. <https://doi.org/10.1002/bies.20197>

- Kneen, M., & Annegarn, H. (1996). Algorithm for fitting XRF, SEM and PIXE X-ray spectra backgrounds. *Nuclear Instruments and Methods in Physics Research Section B: Beam Interactions with Materials and Atoms*, 109, 209-213.
- Knoll, A. H. (1999). *Size limits of very small microorganisms: proceedings of a workshop*. National Academies Press.
- Knoll, A. H., & Bambach, R. K. (2000). Directionality in the history of life: diffusion from the left wall or repeated scaling of the right? *Paleobiology*, 26(S4), 1-14.
- Knott, C. G. (1911). *Life and scientific work of Peter Guthrie Tait* (Vol. 1). Рипол Классик.
- Kolinko, S., Richter, M., Glockner, F. O., Brachmann, A., & Schuler, D. (2014). Single-cell genomics reveals potential for magnetite and greigite biomineralization in an uncultivated multicellular magnetotactic prokaryote. *Environ Microbiol Rep*, 6(5), 524-531. <https://doi.org/10.1111/1758-2229.12198>
- Komeili, A., Li, Z., Newman, D. K., & Jensen, G. J. (2006). Magnetosomes are cell membrane invaginations organized by the actin-like protein MamK. *Science*, 311, 242-245.
- Koonin, E. V. (2010). The origin and early evolution of eukaryotes in the light of phylogenomics. *Genome biology*, 11, 209.
- Koonin, E. V. (2011). The logic of chance: the nature and origin of biological evolution. *FT press*.
- Koonin, E. V., & Wolf, Y. I. (2012). Evolution of microbes and viruses: a paradigm shift in evolutionary biology? *Front Cell Infect Microbiol*, 2, 119. <https://doi.org/10.3389/fcimb.2012.00119>
- Kremer, J. R., Mastronarde, D. N., & McIntosh, J. R. (1996). Computer visualization of three-dimensional image data using IMOD. *Journal of structural biology*, 116, 71-76.
- Kuswanto, W., Nolan, G., & Lu, G. (2023). Highly multiplexed spatial profiling with CODEX: bioinformatic analysis and application in human disease. *Semin Immunopathol*, 45(1), 145-157. <https://doi.org/10.1007/s00281-022-00974-0>
- Ladyman, J., Lambert, J., & Wiesner, K. (2012). What is a complex system? *European Journal for Philosophy of Science*, 3(1), 33-67. <https://doi.org/10.1007/s13194-012-0056-8>
- Lane, N., & Martin, W. (2010). The energetics of genome complexity. *Nature*, 467(7318), 929-934. <https://doi.org/10.1038/nature09486>
- Lange, F., Agui-Gonzalez, P., Riedel, D., Phan, N. T. N., Jakobs, S., & Rizzoli, S. O. (2021). Correlative fluorescence microscopy, transmission electron microscopy and secondary

- ion mass spectrometry (CLEM-SIMS) for cellular imaging. *PLoS One*, 16(5).  
<https://doi.org/ARTN e0240768>  
 10.1371/journal.pone.0240768
- Larsen, S., Nielsen, L. P., & Schramm, A. (2015). Cable bacteria associated with long-distance electron transport in New England salt marsh sediment. *Environmental Microbiology Reports*, 7(2), 175-179. <https://doi.org/10.1111/1758-2229.12216>
- Le Nagard, L., Morillo-López, V., Fradin, C., & Bazylinski, D. A. (2018). Growing magnetotactic bacteria of the genus magnetospirillum: strains msr-1, amb-1 and ms-1. *JoVE (Journal of Visualized Experiments)*(140), e58536.
- Leao, P., Chen, Y. R., Abreu, F., Wang, M., Zhang, W. J., Zhou, K., Xiao, T., Wu, L. F., & Lins, U. (2017). Ultrastructure of ellipsoidal magnetotactic multicellular prokaryotes depicts their complex assemblage and cellular polarity in the context of magnetotaxis. *Environ Microbiol*, 19(6), 2151-2163. <https://doi.org/10.1111/1462-2920.13677>
- Leclerc, J., Rosenfeld, E., Trainini, M., Martin, B., Meuric, V., Bonnaure-Mallet, M., & Baysse, C. (2015). The Cytochrome bd Oxidase of *Porphyromonas gingivalis* Contributes to Oxidative Stress Resistance and Dioxygen Tolerance. *PLoS One*, 10(12), e0143808. <https://doi.org/10.1371/journal.pone.0143808>
- Lee, K. S., Landry, Z., Pereira, F. C., Wagner, M., Berry, D., Huang, W. E., Taylor, G. T., Kneipp, J., Popp, J., Zhang, M., Cheng, J.-X., & Stocker, R. (2021). Raman microspectroscopy for microbiology. *Nature Reviews Methods Primers*, 1(1). <https://doi.org/10.1038/s43586-021-00075-6>
- Lefevre, C. T., Abreu, F., Lins, U., & Bazylinski, D. A. (2010). Nonmagnetotactic multicellular prokaryotes from low-saline, nonmarine aquatic environments and their unusual negative phototactic behavior. *Applied and Environmental Microbiology*, 76(10), 3220-3227.
- Lefèvre, C. T., & Bazylinski, D. A. (2013). Ecology, Diversity, and Evolution of Magnetotactic Bacteria. *Microbiology and Molecular Biology Reviews*, 77(3), 497-526. <https://doi.org/10.1128/mubr.00021-13>
- Lefevre, C. T., Bernadac, A., Yu-Zhang, K., Pradel, N., & Wu, L. F. (2009). Isolation and characterization of a magnetotactic bacterial culture from the Mediterranean Sea. *Environ Microbiol*, 11(7), 1646-1657. <https://doi.org/10.1111/j.1462-2920.2009.01887.x>
- Lefevre, C. T., Trubitsyn, D., Abreu, F., Kolinko, S., Jogler, C., de Almeida, L. G., de Vasconcelos, A. T., Kube, M., Reinhardt, R., Lins, U., Pignol, D., Schuler, D., Bazylinski, D. A., & Ginet, N. (2013). Comparative genomic analysis of magnetotactic bacteria from the Deltaproteobacteria provides new insights into magnetite and greigite magnetosome genes required for magnetotaxis. *Environ Microbiol*, 15(10), 2712-2735. <https://doi.org/10.1111/1462-2920.12128>

- Lewis, A. T., Gaifulina, R., Isabelle, M., Dorney, J., Woods, M. L., Lloyd, G. R., Lau, K., Rodriguez-Justo, M., Kendall, C., Stone, N., & Thomas, G. M. (2017). Mirrored stainless steel substrate provides improved signal for Raman spectroscopy of tissue and cells. *J Raman Spectrosc*, 48(1), 119-125. <https://doi.org/10.1002/jrs.4980>
- Li, J., Liu, P., Tamaxia, A., Zhang, H., Liu, Y., Wang, J., Menguy, N., Zhao, X., Roberts, A. P., & Pan, Y. (2021). Diverse intracellular inclusion types within magnetotactic bacteria: implications for biogeochemical cycling in aquatic environments. *Journal of Geophysical Research: Biogeosciences*, 126(7).
- Li, J., Zhang, H., Menguy, N., Benzerara, K., Wang, F., Lin, X., Chen, Z., & Pan, Y. (2017). Single-Cell Resolution of Uncultured Magnetotactic Bacteria via Fluorescence-Coupled Electron Microscopy. *Appl Environ Microbiol*, 83(12). <https://doi.org/10.1128/AEM.00409-17>
- Li, Q., Chang, J., Li, L., Lin, X., & Li, Y. (2023). Research progress of nano-scale secondary ion mass spectrometry (NanoSIMS) in soil science: Evolution, applications, and challenges. *Sci Total Environ*, 905, 167257. <https://doi.org/10.1016/j.scitotenv.2023.167257>
- Libby, E., and William C. Ratcliff. (2014). Ratcheting the evolution of multicellularity. *Science*, 346, 426-427.
- Lieber, C. A., & Mahadevan-Jansen, A. (2003). Automated method for subtraction of fluorescence from biological Raman spectra. *Applied spectroscopy*, 57(11), 1363-1367.
- Lins, U., & Farina, M. (1999). Organization of cells in magnetotactic multicellular aggregates. *Microbiological Research*, 154(1), 9-13. [https://doi.org/10.1016/s0944-5013\(99\)80028-7](https://doi.org/10.1016/s0944-5013(99)80028-7)
- Loussert-Fonta, C., Toullec, G., Paraecattil, A. A., Jeangros, Q., Krueger, T., Escrig, S., & Meibom, A. (2020). Correlation of fluorescence microscopy, electron microscopy, and NanoSIMS stable isotope imaging on a single tissue section. *Commun Biol*, 3(1), 362. <https://doi.org/10.1038/s42003-020-1095-x>
- Lu, S., Wang, J., Chitsaz, F., Derbyshire, M. K., Geer, R. C., Gonzales, N. R., Gwadz, M., Hurwitz, D. I., Marchler, G. H., Song, J. S., Thanki, N., Yamashita, R. A., Yang, M., Zhang, D., Zheng, C., Lanczycki, C. J., & Marchler-Bauer, A. (2020). CDD/SPARCLE: the conserved domain database in 2020. *Nucleic Acids Res*, 48(D1), D265-D268. <https://doi.org/10.1093/nar/gkz991>
- Ludwig, W., Strunk, O., Westram, R., Richter, L., Meier, H., Yadhukumar, Buchner, A., Lai, T., Steppi, S., Jobb, G., Forster, W., Brettske, I., Gerber, S., Ginhart, A. W., Gross, O., Grumann, S., Hermann, S., Jost, R., Konig, A., . . . Schleifer, K. H. (2004). ARB: a software environment for sequence data. *Nucleic Acids Res*, 32(4), 1363-1371. <https://doi.org/10.1093/nar/gkh293>

- Lynch, M. (2006). Streamlining and simplification of microbial genome architecture. *Annu Rev Microbiol*, 60, 327-349. <https://doi.org/10.1146/annurev.micro.60.080805.142300>
- Lynch, M., & Conery, J. S. (2003). The origins of genome complexity. *Science*, 302, 1401-1404.
- Lynch, M., & Marinov, G. K. (2017). Membranes, energetics, and evolution across the prokaryote-eukaryote divide. *Elife*, 6. <https://doi.org/10.7554/eLife.20437>
- Lynes, M. M., Krukenberg, V., Jay, Z. J., Kohtz, A. J., Gobrogge, C. A., Spietz, R. L., & Hatzenpichler, R. (2023). Diversity and function of methyl-coenzyme M reductase-encoding archaea in Yellowstone hot springs revealed by metagenomics and mesocosm experiments. *ISME Commun*, 3(1), 22. <https://doi.org/10.1038/s43705-023-00225-9>
- Lyons, N. A., & Kolter, R. (2015). On the evolution of bacterial multicellularity. *Curr Opin Microbiol*, 24, 21-28. <https://doi.org/10.1016/j.mib.2014.12.007>
- Mackey, K. R. M., Hunter-Cevera, K., Britten, G. L., Murphy, L. G., Sogin, M. L., & Huber, J. A. (2017). Seasonal Succession and Spatial Patterns of Synechococcus Microdiversity in a Salt Marsh Estuary Revealed through 16S rRNA Gene Oligotyping. *Frontiers in Microbiology*, 8. <https://doi.org/ARTN 1496>  
10.3389/fmicb.2017.01496
- Maier, B., & Wong, G. C. L. (2015). How Bacteria Use Type IV Pili Machinery on Surfaces. *Trends Microbiol*, 23(12), 775-788. <https://doi.org/10.1016/j.tim.2015.09.002>
- Mann, S., Sparks, N. H., & Board, R. G. (1990). Magnetotactic bacteria: microbiology, biomineralization, palaeomagnetism and biotechnology. *Adv Microb Physiol*, 31, 125-181. [https://doi.org/10.1016/s0065-2911\(08\)60121-6](https://doi.org/10.1016/s0065-2911(08)60121-6)
- Marlow, J., Spietz, R., Kim, K. Y., Ellisman, M., Girguis, P., & Hatzenpichler, R. (2021). Spatially resolved correlative microscopy and microbial identification reveal dynamic depth- and mineral-dependent anabolic activity in salt marsh sediment. *Environ Microbiol*, 23(8), 4756-4777. <https://doi.org/10.1111/1462-2920.15667>
- Martins, J. L., Silveira, T.S., Silva, K.T. and Lins, U. (2009). Salinity dependence of the distribution of multicellular magnetotactic prokaryotes in a hypersaline lagoon. *International Microbiology*, 12(3), 193. <https://doi.org/10.2436/20.1501.01.98>
- Matanfack, G. A., Pistiki, A., Rosch, P., & Popp, J. (2021). Raman (18) O-labeling of bacteria in visible and deep UV-ranges. *J Biophotonics*, 14(6), e202100013. <https://doi.org/10.1002/jbio.202100013>
- Matanfack, G. A., Taubert, M., Guo, S., Houhou, R., Bocklitz, T., Kusel, K., Rosch, P., & Popp, J. (2020). Influence of Carbon Sources on Quantification of Deuterium Incorporation in Heterotrophic Bacteria: A Raman-Stable Isotope Labeling Approach. *Anal Chem*, 92(16), 11429-11437. <https://doi.org/10.1021/acs.analchem.0c02443>

- McGlynn, S. E., Chadwick, G. L., O'Neill, A., Mackey, M., Thor, A., Deerinck, T. J., Ellisman, M. H., & Orphan, V. J. (2018). Subgroup characteristics of marine methane-oxidizing ANME-2 archaea and their syntrophic partners revealed by integrated multimodal analytical microscopy. *Appl Environ Microbiol*. <https://doi.org/10.1128/AEM.00399-18>
- McNamara, A. (2018). Key attributes of a modern statistical computing tool. *The American Statistician*.
- McNamara, J. T., Morgan, J. L., & Zimmer, J. (2015). A molecular description of cellulose biosynthesis. *Annu Rev Biochem*, *84*, 895-921. <https://doi.org/10.1146/annurev-biochem-060614-033930>
- McShea, D. W. (1991). Complexity and evolution: what everybody knows. *Biology and Philosophy*, *6*, 303-324.
- McShea, D. W. (1996). Metazoan complexity and evolution: is there a trend? *Evolution*, *5*, 477-492.
- McShea, D. W. (2012). Upper-directed systems: a new approach to teleology in biology. *Biology & Philosophy*, *27*, 663-684.
- McShea, D. W. (2023). Evolutionary trends and goal directedness. *Synthese*, *201*(5), 178.
- McShea, D. W., & Brandon, R. N. (2010). *Biology's first law: the tendency for diversity and complexity to increase in evolutionary systems*. University of Chicago Press.
- McShea, D. W., Wang, S. C., & Brandon, R. N. (2019). A quantitative formulation of biology's first law. *Evolution*, *73*(6), 1101-1115.
- Medhekar, B., & Miller, J. F. (2007). Diversity-generating retroelements. *Curr Opin Microbiol*, *10*(4), 388-395. <https://doi.org/10.1016/j.mib.2007.06.004>
- Meyer, N. R., Fortney, J. L., & Dekas, A. E. (2021). NanoSIMS sample preparation decreases isotope enrichment: magnitude, variability and implications for single-cell rates of microbial activity. *Environ Microbiol*, *23*(1), 81-98. <https://doi.org/10.1111/1462-2920.15264>
- Mizuno, K., Maree, M., Nagamura, T., Koga, A., Hirayama, S., Furukawa, S., Tanaka, K., & Morikawa, K. (2022). Novel multicellular prokaryote discovered next to an underground stream. *Elife*, *11*. <https://doi.org/10.7554/eLife.71920>
- Monod, J. (1974). *On chance and necessity*. Springer.
- Mukhopadhyay, A., He, Z., Alm, E. J., Arkin, A. P., Baidoo, E. E., Borglin, S. C., Chen, W., Hazen, T. C., He, Q., Holman, H. Y., Huang, K., Huang, R., Joyner, D. C., Katz, N., Keller, M., Oeller, P., Redding, A., Sun, J., Wall, J., . . . Keasling, J. D. (2006). Salt stress

- in *Desulfovibrio vulgaris* Hildenborough: an integrated genomics approach. *J Bacteriol*, 188(11), 4068-4078. <https://doi.org/10.1128/JB.01921-05>
- Musat, N., Foster, R., Vagner, T., Adam, B., & Kuypers, M. M. (2012). Detecting metabolic activities in single cells, with emphasis on nanoSIMS. *FEMS Microbiol Rev*, 36(2), 486-511. <https://doi.org/10.1111/j.1574-6976.2011.00303.x>
- Musat, N., Musat, F., Weber, P. K., & Pett-Ridge, J. (2016). Tracking microbial interactions with NanoSIMS. *Curr Opin Biotechnol*, 41, 114-121. <https://doi.org/10.1016/j.copbio.2016.06.007>
- Musat, N., Stryhanyuk, H., Bombach, P., Adrian, L., Audinot, J. N., & Richnow, H. H. (2014). The effect of FISH and CARD-FISH on the isotopic composition of (13)C- and (15)N-labeled *Pseudomonas putida* cells measured by nanoSIMS. *Syst Appl Microbiol*, 37(4), 267-276. <https://doi.org/10.1016/j.syapm.2014.02.002>
- Namba, A., Mano, N., Takano, H., Beppu, T., Ueda, K., & Hirose, H. (2008). OmpA is an adhesion factor of *Aeromonas veronii*, an optimistic pathogen that habituates in carp intestinal tract. *J Appl Microbiol*, 105(5), 1441-1451. <https://doi.org/10.1111/j.1365-2672.2008.03883.x>
- Nawrocki, E. P., Kolbe, D. L., & Eddy, S. R. (2009). Infernal 1.0: inference of RNA alignments. *Bioinformatics*, 25(10), 1335-1337.
- Niklas, K. J., & Newman, S. A. (2013). The origins of multicellular organisms. *Evolution & development*, 15(1), 41-52.
- Nuñez, J., Renslow, R., Cliff, J. B., & Anderton, C. R. (2018). NanoSIMS for biological applications: current practices and analyses. *Biointerphases*, 13(3).
- Nutman, A. P., Bennett, V. C., Friend, C. R., Van Kranendonk, M. J., & Chivas, A. R. (2016). Rapid emergence of life shown by discovery of 3,700-million-year-old microbial structures. *Nature*, 537(7621), 535-538.
- Omadjela, O., Narahari, A., Strumillo, J., Melida, H., Mazur, O., Bulone, V., & Zimmer, J. (2013). BcsA and BcsB form the catalytically active core of bacterial cellulose synthase sufficient for in vitro cellulose synthesis. *Proc Natl Acad Sci U S A*, 110(44), 17856-17861. <https://doi.org/10.1073/pnas.1314063110>
- Osborn, M., Webster, R. E., & Weber, K. (1978). Individual microtubules viewed by immunofluorescence and electron microscopy in the same PtK2 cell. *The Journal of cell biology*, 77(3).
- Ozyamak, E., Kollman, J., Agard, D. A., & Komeili, A. (2013). The bacterial actin MamK: in vitro assembly behavior and filament architecture. *J Biol Chem*, 288(6), 4265-4277. <https://doi.org/10.1074/jbc.M112.417030>

- Parker, L. M., Sayyadi, N., Staikopoulos, V., Shrestha, A., Hutchinson, M. R., & Packer, N. H. (2019). Visualizing neuroinflammation with fluorescence and luminescent lanthanide-based in situ hybridization. *Journal of Neuroinflammation*, *16*(1), 1-13.
- Parks, D. H., Chuvochina, M., Rinke, C., Mussig, A. J., Chaumeil, P.-A., & Hugenholtz, P. (2022). GTDB: an ongoing census of bacterial and archaeal diversity through a phylogenetically consistent, rank normalized and complete genome-based taxonomy. *Nucleic Acids Research*, *50*(D1), D785-D794.
- Parks, D. H., Imelfort, M., Skennerton, C. T., Hugenholtz, P., & Tyson, G. W. (2015). CheckM: assessing the quality of microbial genomes recovered from isolates, single cells, and metagenomes. *Genome Res*, *25*(7), 1043-1055. <https://doi.org/10.1101/gr.186072.114>
- Perantoni, M., Esquivel, D. M., Wajnberg, E., Acosta-Avalos, D., Cernicchiaro, G., & Lins de Barros, H. (2009). Magnetic properties of the microorganism *Candidatus Magnetoglobus multicellularis*. *Naturwissenschaften*, *96*(6), 685-690. <https://doi.org/10.1007/s00114-009-0520-2>
- Perkovic, M., Kunz, M., Endesfelder, U., Bunse, S., Wigge, C., Yu, Z., Hodirnau, V. V., Scheffer, M. P., Seybert, A., Malkusch, S., Schuman, E. M., Heilemann, M., & Frangakis, A. S. (2014). Correlative Light- and Electron Microscopy with chemical tags. *Journal of structural biology*, *186*(2), 205-213. <https://doi.org/10.1016/j.jsb.2014.03.018>
- Pett-Ridge, J., & Weber, P. K. (2012). NanoSIP: NanoSIMS applications for microbial biology. *Microbial systems biology: methods and protocols*, 375-408.
- Pirozzi, N. M., Hoogenboom, J. P., & Giepmans, B. N. G. (2018). ColorEM: analytical electron microscopy for element-guided identification and imaging of the building blocks of life. *Histochemistry and Cell Biology*, *150*(5), 509-520. <https://doi.org/10.1007/s00418-018-1707-4>
- Popa, R., Weber, P. K., Pett-Ridge, J., Finzi, J. A., Fallon, S. J., Hutcheon, I. D., Nealson, K. H., & Capone, D. G. (2007). Carbon and nitrogen fixation and metabolite exchange in and between individual cells of *Anabaena oscillarioides*. *ISME J*, *1*(4), 354-360. <https://doi.org/10.1038/ismej.2007.44>
- Posfai M., Buseck PR., Bazylinski DA., & RB., F. (1998). Iron sulfides from magnetotactic bacteria: structure, composition, and phase transitions. *American Mineralogist*, *83*(11), 1469-1481.
- Prasad, S. M., Yin, Y., Rodzinski, E., Tuomanen, E. I., & Masure, H. R. (1993). Identification of a carbohydrate recognition domain in filamentous hemagglutinin from *Bordetella pertussis*. *Infection and Immunity*, *61*(7), 2780-2785.
- Price, M. N., Dehal, P. S., & Arkin, A. P. (2010). FastTree 2—approximately maximum-likelihood trees for large alignments. *PLoS One*, *5*(3), e9490.

- Qi, Y., Rao, F., Luo, Z., & Liang, Z. X. (2009). A flavin cofactor-binding PAS domain regulates c-di-GMP synthesis in AxDGC2 from *Acetobacter xylinum*. *Biochemistry*, *48*(43), 10275-10285. <https://doi.org/10.1021/bi901121w>
- Qian, X., Zhao, Y., Santini, C.-L., Pan, H., Xiao, T., Chen, H., Song, T., Li, J., Alberto, F., Brustlein, S., & Wu, L.-F. (2021). How light affect the magnetotactic behavior and reproduction of ellipsoidal multicellular magnetoglobules? *Journal of Oceanology and Limnology*, *39*(6), 2005-2014. <https://doi.org/10.1007/s00343-021-0493-3>
- Qian, X. X., Santini, C. L., Kosta, A., Menguy, N., Le Guenno, H., Zhang, W., Li, J., Chen, Y. R., Liu, J., Alberto, F., Espinosa, L., Xiao, T., & Wu, L. F. (2020). Juxtaposed membranes underpin cellular adhesion and display unilateral cell division of multicellular magnetotactic prokaryotes. *Environ Microbiol*, *22*(4), 1481-1494. <https://doi.org/10.1111/1462-2920.14710>
- Quast, C., Pruesse, E., Yilmaz, P., Gerken, J., Schweer, T., Yarza, P., Peplies, J., & Glockner, F. O. (2013). The SILVA ribosomal RNA gene database project: improved data processing and web-based tools. *Nucleic Acids Res*, *41*(Database issue), D590-596. <https://doi.org/10.1093/nar/gks1219>
- Regenberg, B., Hanghoj, K. E., Andersen, K. S., & Boomsma, J. J. (2016). Clonal yeast biofilms can reap competitive advantages through cell differentiation without being obligatorily multicellular. *Proc Biol Sci*, *283*(1842). <https://doi.org/10.1098/rspb.2016.1303>
- Richard, B. (1975). Magnetotactic Bacteria. *Science*, *190*, 377-379.
- Rinke, C., Lee, J., Nath, N., Goudeau, D., Thompson, B., Poulton, N., Dmitrieff, E., Malmstrom, R., Stepanauskas, R., & Woyke, T. (2014). Obtaining genomes from uncultivated environmental microorganisms using FACS-based single-cell genomics. *Nat Protoc*, *9*(5), 1038-1048. <https://doi.org/10.1038/nprot.2014.067>
- Rodgers, F. G., Blakemore, R. P., Blakemore, N. A., Frankel, R. B., Bazyliński, D. A., Maratea, D., & Rodgers, C. (1990). Intercellular structure in a many-celled magnetotactic prokaryote. *Archives of Microbiology*, *154*, 18-22.
- Rodrigues-Oliveira, T., Wollweber, F., Ponce-Toledo, R. I., Xu, J., Rittmann, S. K.-M., Klingl, A., Pilhofer, M., & Schleper, C. (2023). Actin cytoskeleton and complex cell architecture in an Asgard archaeon. *Nature*, *613*(7943), 332-339.
- Rokas, A. (2008). The origins of multicellularity and the early history of the genetic toolkit for animal development. *Annu Rev Genet*, *42*, 235-251. <https://doi.org/10.1146/annurev.genet.42.110807.091513>
- Rust, M. J., Bates, M., & Zhuang, X. (2006). Sub-diffraction-limit imaging by stochastic optical reconstruction microscopy (STORM). *Nat Methods*, *3*(10), 793-795. <https://doi.org/10.1038/nmeth929>

- Ryabchikov, O., Guo, S., & Bocklitz, T. (2018). Analyzing Raman spectroscopic data. *Physical Sciences Reviews*, 4(2), 20170043.
- Ryan, C., Clayton, E., Griffin, W., Sie, S., & Cousens, D. (1988). SNIP, a statistics-sensitive background treatment for the quantitative analysis of PIXE spectra in geoscience applications. *Nuclear Instruments and Methods in Physics Research Section B: Beam Interactions with Materials and Atoms*, 34(3), 396-402.
- Sáenz, J. P., Sezgin, E., Schwille, P., & Simons, K. (2012). Functional convergence of hopanoids and sterols in membrane ordering. *Proceedings of the National Academy of Sciences*, 109(35), 14236-14240.
- Salman, V., Yang, T. T., Berben, T., Klein, F., Angert, E., & Teske, A. (2015). Calcite-accumulating large sulfur bacteria of the genus *Achromatium* in Sippewissett Salt Marsh. *ISME Journal*, 9(11), 2503-2514. <https://doi.org/10.1038/ismej.2015.62>
- Savitzky, A., & Golay, M. J. (1964). Smoothing and differentiation of data by simplified least squares procedures. *Analytical chemistry*, 36(8), 1627-1639.
- Schaible, G. A., Kohtz, A. J., Cliff, J., & Hatzenpichler, R. (2022). Correlative SIP-FISH-Raman-SEM-NanoSIMS links identity, morphology, biochemistry, and physiology of environmental microbes. *ISME Communications*, 2(1). <https://doi.org/10.1038/s43705-022-00134-3>
- Schirrmeister, B. E., Antonelli, A., & Bagheri, H. C. (2011). The origin of multicellularity in cyanobacteria. *BMC evolutionary biology*, 11, 1-21.
- Schirrmeister, B. E., de Vos, J. M., Antonelli, A., & Bagheri, H. C. (2013). Evolution of multicellularity coincided with increased diversification of cyanobacteria and the Great Oxidation Event. *Proc Natl Acad Sci U S A*, 110(5), 1791-1796. <https://doi.org/10.1073/pnas.1209927110>
- Schluter, S., Eickhorst, T., & Mueller, C. W. (2019). Correlative Imaging Reveals Holistic View of Soil Microenvironments. *Environ Sci Technol*, 53(2), 829-837. <https://doi.org/10.1021/acs.est.8b05245>
- Schramm, A., Fuchs, B. M., Nielsen, J. L., Tonolla, M., & Stahl, D. A. (2002). Fluorescence in situ hybridization of 16S rRNA gene clones (Clone-FISH) for probe validation and screening of clone libraries. *Environmental Microbiology*, 4, 713-720.
- Schreiber, F., & Ackermann, M. (2020). Environmental drivers of metabolic heterogeneity in clonal microbial populations. *Current Opinion in Biotechnology*, 62, 202-211.
- Schreiber, F., Littmann, S., Lavik, G., Escrig, S., Meibom, A., Kuypers, M. M., & Ackermann, M. (2016). Phenotypic heterogeneity driven by nutrient limitation promotes growth in fluctuating environments. *Nature microbiology*, 1(6), 1-7.

- Schrödinger, E. (1992). *What is life?: With mind and matter and autobiographical sketches.* Cambridge University Press.
- Schwartzman, J. A., Ebrahimi, A., Chadwick, G., Sato, Y., Roller, B. R. K., Orphan, V. J., & Cordero, O. X. (2022). Bacterial growth in multicellular aggregates leads to the emergence of complex life cycles. *Curr Biol*, *32*(14), 3059-3069 e3057. <https://doi.org/10.1016/j.cub.2022.06.011>
- Serra, D. O., Conover, M. S., Arnal, L., Sloan, G. P., Rodriguez, M. E., Yantorno, O. M., & Deora, R. (2011). FHA-mediated cell-substrate and cell-cell adhesions are critical for *Bordetella pertussis* biofilm formation on abiotic surfaces and in the mouse nose and the trachea. *PLoS One*, *6*(12), e28811. <https://doi.org/10.1371/journal.pone.0028811>
- Serra, D. O., & Hengge, R. (2019). *Cellulose in bacterial biofilms.*
- Serra, D. O., & Hengge, R. (2021). Bacterial Multicellularity: The Biology of *Escherichia coli* Building Large-Scale Biofilm Communities. *Annu Rev Microbiol*, *75*, 269-290. <https://doi.org/10.1146/annurev-micro-031921-055801>
- Serra, D. O., Richter, A. M., & Hengge, R. (2013). Cellulose as an architectural element in spatially structured *Escherichia coli* biofilms. *J Bacteriol*, *195*(24), 5540-5554. <https://doi.org/10.1128/JB.00946-13>
- Shannon, C. E. (1948). A mathematical theory of communication. *Bell system technical journal*, *27*, 379-423.
- Shapiro, J. A. (1988). Bacteria as Multicellular Organisms. *Scientific American*, *258*, 82-89.
- Shapiro, J. A. (1998). Thinking about bacterial populations as multicellular organisms. *Annu. Rev. Microbiol.*, *52*, 81-104.
- Shapiro, O. H., Hatzenpichler, R., Buckley, D. H., Zinder, S. H., & Orphan, V. J. (2011). Multicellular photo-magnetotactic bacteria. *Environmental Microbiology Reports*, *3*(2), 233-238. <https://doi.org/10.1111/j.1758-2229.2010.00215.x>
- Siegrist, M. S., Whiteside, S., Jewett, J. C., Aditham, A., Cava, F., & Bertozzi, C. R. (2013). (D)-Amino acid chemical reporters reveal peptidoglycan dynamics of an intracellular pathogen. *ACS Chem Biol*, *8*(3), 500-505. <https://doi.org/10.1021/cb3004995>
- Silva, K. T., Abreu, F., Almeida, F. P., Keim, C. N., Farina, M., & Lins, U. (2007). Flagellar apparatus of south-seeking many-celled magnetotactic prokaryotes. *Microscopy research and technique*, *70*(1), 10-17.
- Silva, K. T., Abreu, F., Keim, C. N., Farina, M., & Lins, U. (2008). Ultrastructure and cytochemistry of lipid granules in the many-celled magnetotactic prokaryote, 'Candidatus

- Magnetoglobus multicellularis'. *Micron*, 39(8), 1387-1392.  
<https://doi.org/10.1016/j.micron.2008.05.009>
- Simmons, S. L., Bazylinski, D. A., & Edwards, K. J. (2007). Population dynamics of marine magnetotactic bacteria in a meromictic salt pond described with qPCR. *Environ Microbiol*, 9(9), 2162-2174. <https://doi.org/10.1111/j.1462-2920.2007.01330.x>
- Simmons, S. L., & Edwards, K. J. (2007). Unexpected diversity in populations of the many-celled magnetotactic prokaryote. *Environ Microbiol*, 9(1), 206-215.  
<https://doi.org/10.1111/j.1462-2920.2006.01129.x>
- Simmons, S. L., Sievert, S. M., Frankel, R. B., Bazylinski, D. A., & Edwards, K. J. (2004). Spatiotemporal distribution of marine magnetotactic bacteria in a seasonally stratified coastal salt pond. *Appl Environ Microbiol*, 70(10), 6230-6239.  
<https://doi.org/10.1128/AEM.70.10.6230-6239.2004>
- Simoës, M. F., Ottoni, C. A., & Antunes, A. (2020). Biogenic Metal Nanoparticles: A New Approach to Detect Life on Mars? *Life (Basel)*, 10(3).  
<https://doi.org/10.3390/life10030028>
- Slotznick, S. P., Egli, R., & Lascu, I. (2023). Magnetofossils: relicts and records of deep time and space. *Elements*, 19(4), 215-221.
- Smith, J. M., & Szathmary, E. (1997). *The major transitions in evolution*. OUP Oxford.
- Smruga, S., Samo, T. J., Malfatti, F., Villareal, J., & Azam, F. (2014). Individual cell DNA synthesis within natural marine bacterial assemblages as detected by 'click' chemistry. *Aquatic Microbial Ecology*, 72(3), 269-280. <https://doi.org/10.3354/ame01698>
- Sobrinho, R. L., Lins, U., & Bernardes, M. C. (2011). Geochemical Characteristics Related to the Gregite-Producing Multicellular Magnetotactic Prokaryote Candidatus Magnetoglobus multicellularis in a Hypersaline Lagoon. *Geomicrobiology Journal*, 28(8), 705-713.  
<https://doi.org/10.1080/01490451.2010.514027>
- Sondergaard, D., Pedersen, C. N., & Greening, C. (2016). HydDB: A web tool for hydrogenase classification and analysis. *Sci Rep*, 6, 34212. <https://doi.org/10.1038/srep34212>
- Srivastava, P. (2005). Vindhyan akinites: an indicator of mesoproterozoic biospheric evolution. *Origins of Life and Evolution of Biospheres*, 35, 175-185.
- Stahl, D. A., & Amann, R. I. (1991). Development and application of nucleic acid probes. In E. Stackebrandt and M. Goodfellow (ed.), *Nucleic acid techniques in bacterial systematics* (John Wiley & Sons), 205-248

- Staley, J. T. (1999). Bacteria, Their Smallest Representatives and Subcellular Structures, and the Purported Precambrian Fossil “Metallogenium”. Size Limits of Very Small Microorganisms: Proceedings of a Workshop,
- Stanley, S. M. (1973). An explanation for Cope's rule. *Evolution*, 27, 1-26.
- Stepanauskas, R., Fergusson, E. A., Brown, J., Poulton, N. J., Tupper, B., Labonte, J. M., Becraft, E. D., Brown, J. M., Pachiadaki, M. G., Povilaitis, T., Thompson, B. P., Mascena, C. J., Bellows, W. K., & Lubys, A. (2017). Improved genome recovery and integrated cell-size analyses of individual uncultured microbial cells and viral particles. *Nat Commun*, 8(1), 84. <https://doi.org/10.1038/s41467-017-00128-z>
- Stoecker, K., Dorninger, C., Daims, H., & Wagner, M. (2010). Double labeling of oligonucleotide probes for fluorescence in situ hybridization (DOPE-FISH) improves signal intensity and increases rRNA accessibility. *Appl Environ Microbiol*, 76(3), 922-926. <https://doi.org/10.1128/AEM.02456-09>
- Tan, J. Y., Wang, S., Dick, G. J., Young, V. B., Sherman, D. H., Burns, M. A., & Lin, X. N. (2020). Co-cultivation of microbial sub-communities in microfluidic droplets facilitates high-resolution genomic dissection of microbial ‘dark matter’. *Integrative Biology*, 12(11), 263-274.
- Tan, L., & Jiang, J. (2018). *Digital signal processing: fundamentals and applications*. Academic press.
- Tang, G., Peng, L., Baldwin, P. R., Mann, D. S., Jiang, W., Rees, I., & Ludtke, S. J. (2007). EMAN2: an extensible image processing suite for electron microscopy. *J Struct Biol*, 157(1), 38-46. <https://doi.org/10.1016/j.jsb.2006.05.009>
- Taoka, A., Eguchi, Y., Shimoshige, R., & Fukumori, Y. (2023). Recent advances in studies on magnetosome-associated proteins composing the bacterial geomagnetic sensor organelle. *Microbiol Immunol*, 67(5), 228-238. <https://doi.org/10.1111/1348-0421.13062>
- Tay, A., Pfeiffer, D., Rowe, K., Tannenbaum, A., Popp, F., Strangeway, R., Schöler, D., & Di Carlo, D. (2018). High-throughput microfluidic sorting of live magnetotactic bacteria. *Applied and Environmental Microbiology*, 84(17), e01308-01318.
- Team, R. C. (2023). *A language and environment for statistical computing*. <http://R-project.org/>.
- Teng, Z., Zhang, Y., Zhang, W., Pan, H., Xu, J., Huang, H., Xiao, T., & Wu, L. F. (2018). Diversity and Characterization of Multicellular Magnetotactic Prokaryotes From Coral Reef Habitats of the Paracel Islands, South China Sea. *Front Microbiol*, 9, 2135. <https://doi.org/10.3389/fmicb.2018.02135>
- Tong, K., Bozdag, G. O., & Ratcliff, W. C. (2022). Selective drivers of simple multicellularity. *Curr Opin Microbiol*, 67, 102141. <https://doi.org/10.1016/j.mib.2022.102141>

- Uebe, R., & Schuler, D. (2016). Magnetosome biogenesis in magnetotactic bacteria. *Nat Rev Microbiol*, *14*(10), 621-637. <https://doi.org/10.1038/nrmicro.2016.99>
- Van Dongen, S. (2008). Graph clustering via a discrete uncoupling process. *SIAM Journal on Matrix Analysis and Applications*, *30*(1), 121-141.
- Vanchurin, V., Wolf, Y. I., Koonin, E. V., & Katsnelson, M. I. (2022). Thermodynamics of evolution and the origin of life. *Proceedings of the National Academy of Sciences*, *119*(6), e2120042119.
- Velicer, G. J., & Vos, M. (2009). Sociobiology of the myxobacteria. *Annu Rev Microbiol*, *63*, 599-623. <https://doi.org/10.1146/annurev.micro.091208.073158>
- Waite, D. W., Chuvochina, M., Pelikan, C., Parks, D. H., Yilmaz, P., Wagner, M., Loy, A., Naganuma, T., Nakai, R., Whitman, W. B., Hahn, M. W., Kuever, J., & Hugenholtz, P. (2020). Proposal to reclassify the proteobacterial classes Deltaproteobacteria and Oligoflexia, and the phylum Thermodesulfobacteria into four phyla reflecting major functional capabilities. *Int J Syst Evol Microbiol*, *70*(11), 5972-6016. <https://doi.org/10.1099/ijsem.0.004213>
- Wallner, G., Amann, R., & Beisker, W. (1993). Optimizing Fluorescent Insitu Hybridization with Ribosomal-Rna-Targeted Oligonucleotide Probes for Flow Cytometric Identification of Microorganisms. *Cytometry*, *14*(2), 136-143. <https://doi.org/DOI.10.1002/cyto.990140205>
- Wang, X., Li, Y., Zhao, J., Yao, H., Chu, S., Song, Z., He, Z., & Zhang, W. (2020). Magnetotactic bacteria: Characteristics and environmental applications. *Frontiers of Environmental Science & Engineering*, *14*(4). <https://doi.org/10.1007/s11783-020-1235-z>
- Wang, Y., Huang, W. E., Cui, L., & Wagner, M. (2016). Single cell stable isotope probing in microbiology using Raman microspectroscopy. *Curr Opin Biotechnol*, *41*, 34-42. <https://doi.org/10.1016/j.copbio.2016.04.018>
- Weber, F., Zaliznyak, T., Edgcomb, V. P., & Taylor, G. T. (2021). Using Stable Isotope Probing and Raman Microspectroscopy To Measure Growth Rates of Heterotrophic Bacteria. *Appl Environ Microbiol*, *87*(22), e0146021. <https://doi.org/10.1128/AEM.01460-21>
- Webster, R. E., Osborn, M., & Weber, K. (1978). Visualization of the same PtK2 cytoskeletons by both immunofluorescence and low power electron microscopy. *Experimental cell research*, *117*(1), 47-61.
- Wegener, G., Bausch, M., Holler, T., Thang, N. M., Prieto Mollar, X., Kellermann, M. Y., Hinrichs, K. U., & Boetius, A. (2012). Assessing sub-seafloor microbial activity by combined stable isotope probing with deuterated water and <sup>13</sup>C-bicarbonate. *Environmental Microbiology*, *14*(6), 1517-1527.

- Wei, L., Hu, F., Chen, Z., Shen, Y., Zhang, L., & Min, W. (2016). Live-Cell Bioorthogonal Chemical Imaging: Stimulated Raman Scattering Microscopy of Vibrational Probes. *Acc Chem Res*, 49(8), 1494-1502. <https://doi.org/10.1021/acs.accounts.6b00210>
- Weidenbach, K., Nickel, L., Neve, H., Alkhnabshi, O. S., Künzel, S., Kupczok, A., Bauersachs, T., Cassidy, L., Tholey, A., & Backofen, R. (2017). Methanosarcina spherical virus, a novel archaeal lytic virus targeting Methanosarcina strains. *Journal of Virology*, 91(22), 10.1128/jvi.00955-00917.
- Weiss, G. L., Eisenstein, F., Kieninger, A.-K., Xu, J., Minas, H. A., Gerber, M., Feldmüller, M., Maldener, I., Forchhammer, K., & Pilhofer, M. (2022). Structure of a thylakoid-anchored contractile injection system in multicellular cyanobacteria. *Nature microbiology*, 7(3), 386-396.
- Wenter, R., Wanner, G., Schuler, D., & Overmann, J. (2009). Ultrastructure, tactic behaviour and potential for sulfate reduction of a novel multicellular magnetotactic prokaryote from North Sea sediments. *Environ Microbiol*, 11(6), 1493-1505. <https://doi.org/10.1111/j.1462-2920.2009.01877.x>
- Wielgoss, S., Wolfensberger, R., Sun, L., Fiegna, F., & Velicer, G. J. (2019). Social genes are selection hotspots in kin groups of a soil microbe. *Science*, 363(6433), 1342-1345.
- Wilbanks, E. G., Jaekel, U., Salman, V., Humphrey, P. T., Eisen, J. A., Facciotti, M. T., Buckley, D. H., Zinder, S. H., Druschel, G. K., Fike, D. A., & Orphan, V. J. (2014). Microscale sulfur cycling in the phototrophic pink berry consortia of the Sippewissett Salt Marsh. *Environmental Microbiology*, 16(11), 3398-3415. <https://doi.org/10.1111/1462-2920.12388>
- Wilbanks, E. G., Salman-Carvalho, V., Jaekel, U., Humphrey, P. T., Eisen, J. A., Buckley, D. H., & Zinder, S. H. (2017). The Green Berry Consortia of the Sippewissett Salt Marsh: Millimeter-Sized Aggregates of Diazotrophic Unicellular Cyanobacteria. *Frontiers in Microbiology*, 8. <https://doi.org/ARTN162310.3389/fmicb.2017.01623>
- Winklhofer, M., Abracado, L. G., Davila, A. F., Keim, C. N., & Lins de Barros, H. G. (2007). Magnetic optimization in a multicellular magnetotactic organism. *Biophys J*, 92(2), 661-670. <https://doi.org/10.1529/biophysj.106.093823>
- Woehl, T. J., Kashyap, S., Firlar, E., Perez-Gonzalez, T., Faivre, D., Trubitsyn, D., Bazylinski, D. A., & Prozorov, T. (2014). Correlative electron and fluorescence microscopy of magnetotactic bacteria in liquid: toward in vivo imaging. *Sci Rep*, 4, 6854. <https://doi.org/10.1038/srep06854>
- Wolf, Y. I., Katsnelson, M. I., & Koonin, E. V. (2018). Physical foundations of biological complexity. *Proc Natl Acad Sci U S A*, 115(37), E8678-E8687. <https://doi.org/10.1073/pnas.1807890115>

- Wolpert, L., & Szathmáry, E. (2002). Multicellularity: evolution and the egg. *Nature*, *420*, 745-745.
- Wrótniak-Drzewiecka, W., Brzezińska, A. J., Dahm, H., Ingle, A. P., & Rai, M. (2015). Current trends in myxobacteria research. *Annals of Microbiology*, *66*(1), 17-33. <https://doi.org/10.1007/s13213-015-1104-3>
- Yilmaz, L. S., Parnerkar, S., & Noguera, D. R. (2011). mathFISH, a web tool that uses thermodynamics-based mathematical models for in silico evaluation of oligonucleotide probes for fluorescence in situ hybridization. *Appl Environ Microbiol*, *77*(3), 1118-1122. <https://doi.org/10.1128/AEM.01733-10>
- Yuan, X., Song, Y., Song, Y., Xu, J., Wu, Y., Glidle, A., Cusack, M., Ijaz, U. Z., Cooper, J. M., & Huang, W. E. (2018). Effect of laser irradiation on cell function and its implications in Raman spectroscopy. *Applied and Environmental Microbiology*, *84*(8), e02508-02517.
- Zhang, R., Chen, Y. R., Du, H. J., Zhang, W. Y., Pan, H. M., Xiao, T., & Wu, L. F. (2014). Characterization and phylogenetic identification of a species of spherical multicellular magnetotactic prokaryotes that produces both magnetite and greigite crystals. *Res Microbiol*, *165*(7), 481-489. <https://doi.org/10.1016/j.resmic.2014.07.012>
- Zhang, X., Gillespie, A. L., & Sessions, A. L. (2009). Large D/H variations in bacterial lipids reflect central metabolic pathways. *Proceedings of the National Academy of Sciences*, *106*(31), 12580-12586.
- Zhou, K., Pan, H., Zhang, S., Yue, H., Xiao, T., & Wu, L. (2011). Occurrence and microscopic analyses of multicellular magnetotactic prokaryotes from coastal sediments in the Yellow Sea. *Chinese Journal of Oceanology and Limnology*, *29*(2), 246-251. <https://doi.org/10.1007/s00343-011-0032-8>
- Zhou, K., Zhang, W. Y., Pan, H. M., Li, J. H., Yue, H. D., Xiao, T., & Wu, L. F. (2013). Adaptation of spherical multicellular magnetotactic prokaryotes to the geochemically variable habitat of an intertidal zone. *Environ Microbiol*, *15*(5), 1595-1605. <https://doi.org/10.1111/1462-2920.12057>
- Zhou, K., Zhang, W. Y., Yu-Zhang, K., Pan, H. M., Zhang, S. D., Zhang, W. J., Yue, H. D., Li, Y., Xiao, T., & Wu, L. F. (2012). A novel genus of multicellular magnetotactic prokaryotes from the Yellow Sea. *Environ Microbiol*, *14*(2), 405-413. <https://doi.org/10.1111/j.1462-2920.2011.02590.x>
- Zimin, A. V., Puiu, D., Hall, R., Kingan, S., Clavijo, B. J., & Salzberg, S. L. (2017). The first near-complete assembly of the hexaploid bread wheat genome, *Triticum aestivum*. *Gigascience*, *6*(11), gix097.
- Zimmermann, L., Stephens, A., Nam, S. Z., Rau, D., Kubler, J., Lozajic, M., Gabler, F., Soding, J., Lupas, A. N., & Alva, V. (2018). A Completely Reimplemented MPI Bioinformatics

Toolkit with a New HHpred Server at its Core. *J Mol Biol*, 430(15), 2237-2243.  
<https://doi.org/10.1016/j.jmb.2017.12.007>

Zimmermann, M., Escrig, S., Hubschmann, T., Kirf, M. K., Brand, A., Inglis, R. F., Musat, N., Muller, S., Meibom, A., Ackermann, M., & Schreiber, F. (2015). Phenotypic heterogeneity in metabolic traits among single cells of a rare bacterial species in its natural environment quantified with a combination of flow cell sorting and NanoSIMS. *Front Microbiol*, 6, 243. <https://doi.org/10.3389/fmicb.2015.00243>

APPENDICES

APPENDIX A

CHAPTER TWO SUPPORTING MATERIAL

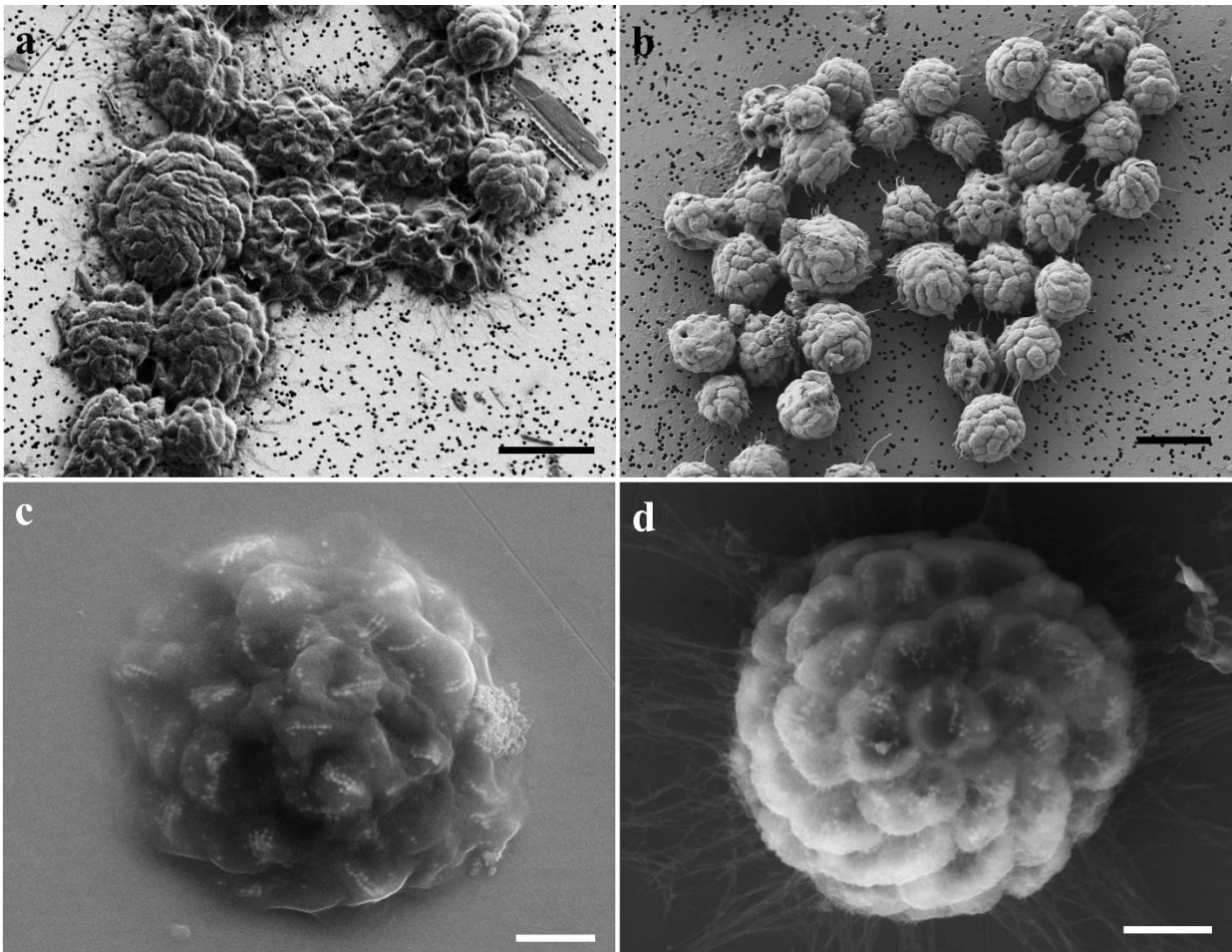


Fig. S1. SEM images showing the loss of structural integrity of MMB when FISH is performed prior to SEM. (a-b) MMB deposited on a 0.22  $\mu\text{m}$  filter and imaged using SEM (a) post and (b) prior to FISH. (c-d) MMB on a stainless steel coupon imaged using back scatter electrons with the secondary electron detector (c) post and (d) prior to FISH. Scale bars in a and b equal to 5  $\mu\text{m}$ , c and d equal to 1  $\mu\text{m}$ .

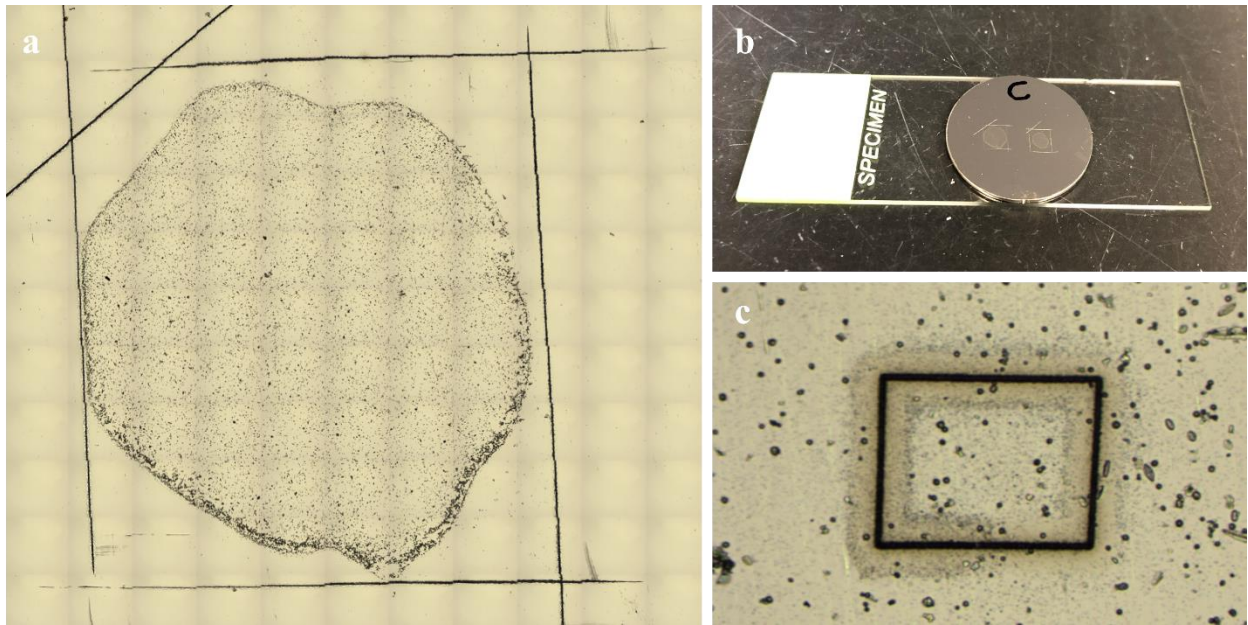


Fig. S2. Slide design and sample orientation. (a) A mosaic image showing the sample dried within an asymmetric square etched into the stainless steel coupon with a razor blade. (b) The stainless steel coupon attached to a standard 60x20 mm microscope slide. (c) An ROI that had been traced using a laser dissection microscope to assist in locating the ROI during nanoSIMS analysis.

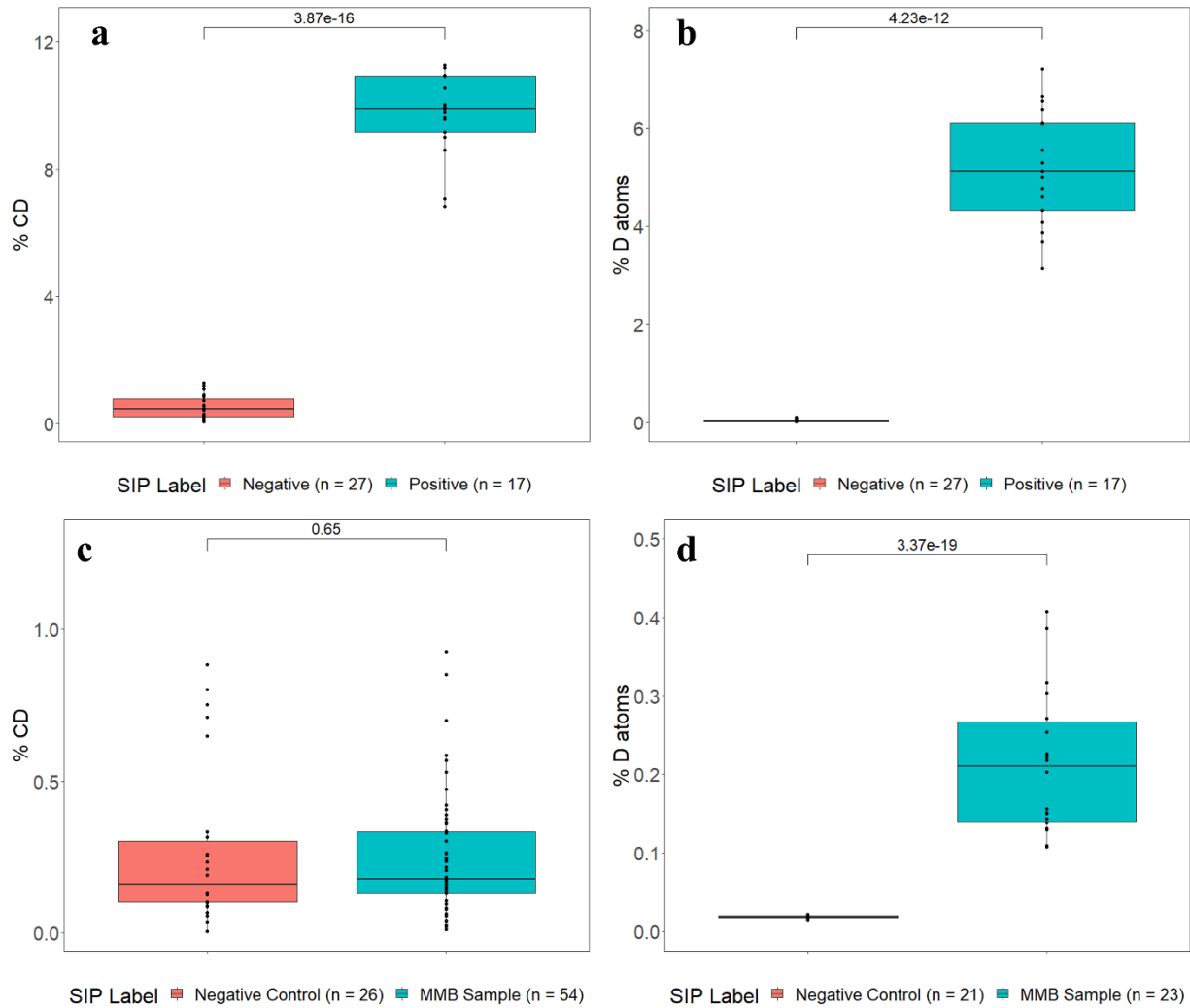


Fig. S3. Comparison of D-labeled and non-labeled cells. (a) Analysis of D-incorporation within the mock community calculated from Raman C–H ( $2,800\text{--}3,100\text{ cm}^{-1}$ ) and C–D ( $2,040\text{--}2,300\text{ cm}^{-1}$ ) data (p-value =  $3.87 \times 10^{-16}$ ). (b) Comparison of the NanoSIMS m/z 2/1 (D/H) data for the same cells within the mock community shown in panel (a) (p-value =  $4.23 \times 10^{-12}$ ). (c) Analysis of D-incorporation within the MMB calculated from Raman C–H ( $2,800\text{--}3,100\text{ cm}^{-1}$ ) and C–D ( $2,040\text{--}2,300\text{ cm}^{-1}$ ) data (p-value = 0.65). (d) Corresponding analysis of D incorporated into the cells using NanoSIMS; p-value =  $3.37 \times 10^{-19}$ ) for the same MMB in panel (c). The black line represents the mean value and individual data points (*i.e.*, individual cells/MMB) are shown as black dots. Significant differences (p-value shown in plots) were determined by Student's t-test.

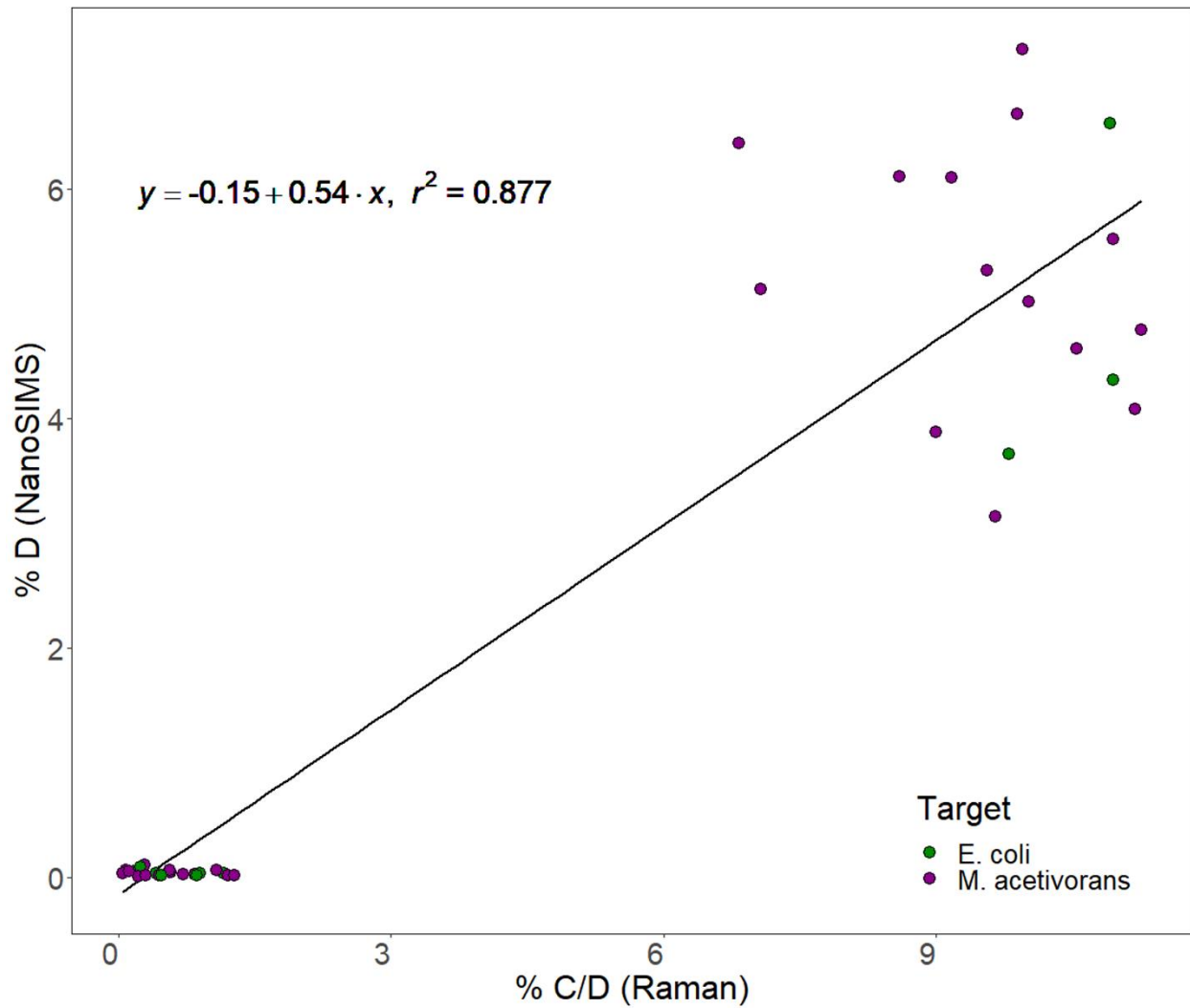


Fig. S4. Comparison of Raman and NanoSIMS atom percent of deuterium in the mock community. Both Raman and NanoSIMS were used to detect deuterium within individual cells of the mock community shown in Figure 2. Comparison of data revealed that Raman and NanoSIMS did not yield identical results on individual cells for deuterium incorporation.

APPENDIX B

CHAPTER THREE SUPPORTING MATERIAL

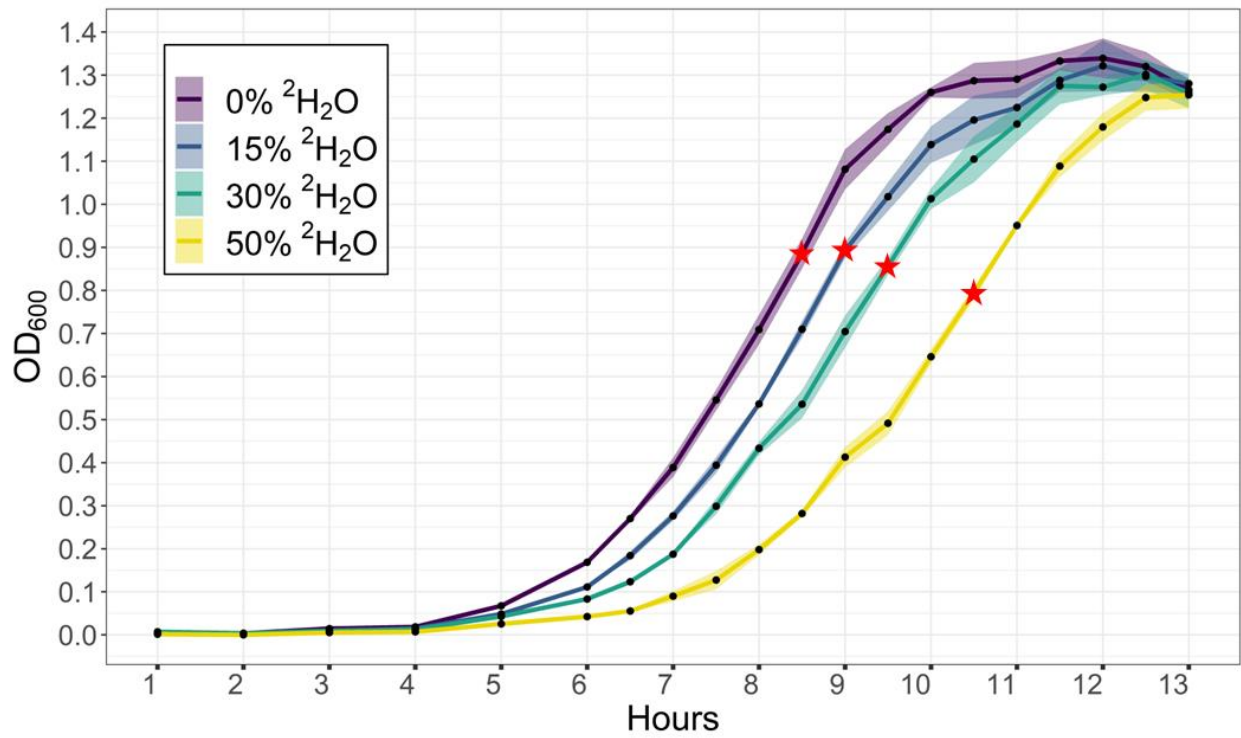


Fig. S1. Growth curve of *E. coli* cultures grown in varying  $^2\text{H}$ -water concentrations. Shaded region behind line shows the minimum and maximum  $\text{OD}_{600}$  of each measurement. Red stars highlight the time and  $\text{OD}_{600}$  at which cells fixed for Raman and NanoSIMS analysis. The effect of  $^2\text{H}_2\text{O}$  on *E. coli* growth can be seen by a delayed logarithmic growth upon the increased addition of heavy water to the growth media.

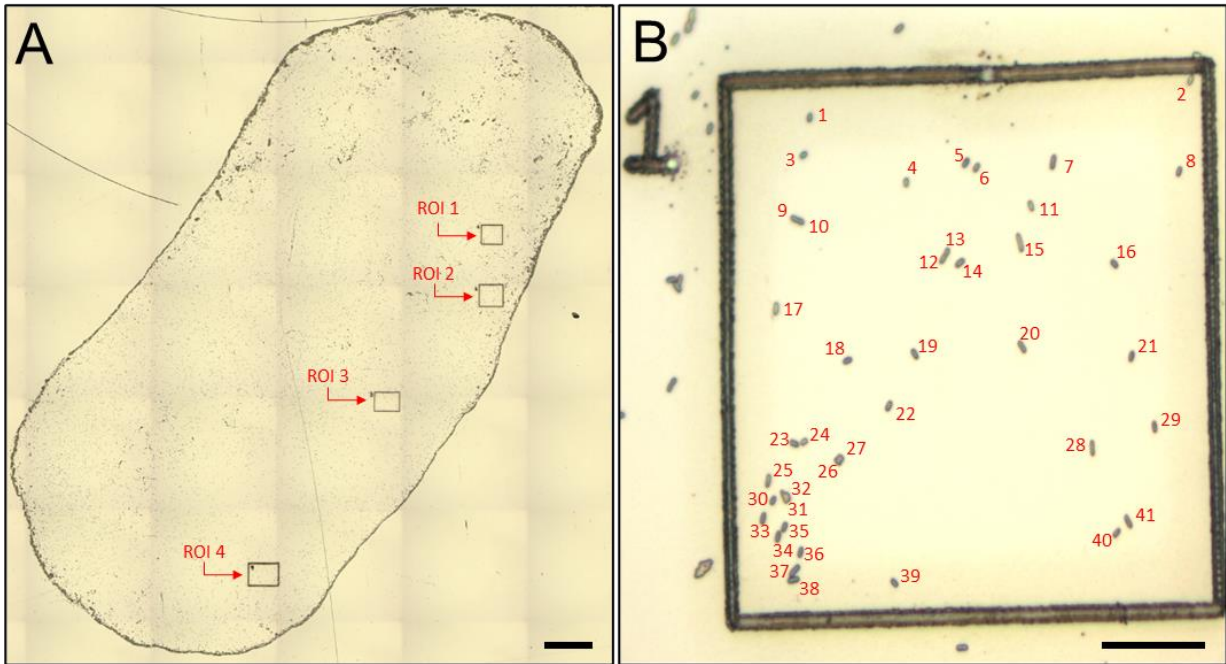


Fig. S2. Example of the mapping of ROIs and cells for correlative workflow. **A** Shows the individual ROIs etched into the surface of the stainless steel coupon using a laser microdissection microscope. Scale bar, 100  $\mu\text{m}$ . **B** Catalogued *E. coli* cells located within ROI 1 shown in A. Scale bar, 10  $\mu\text{m}$ .

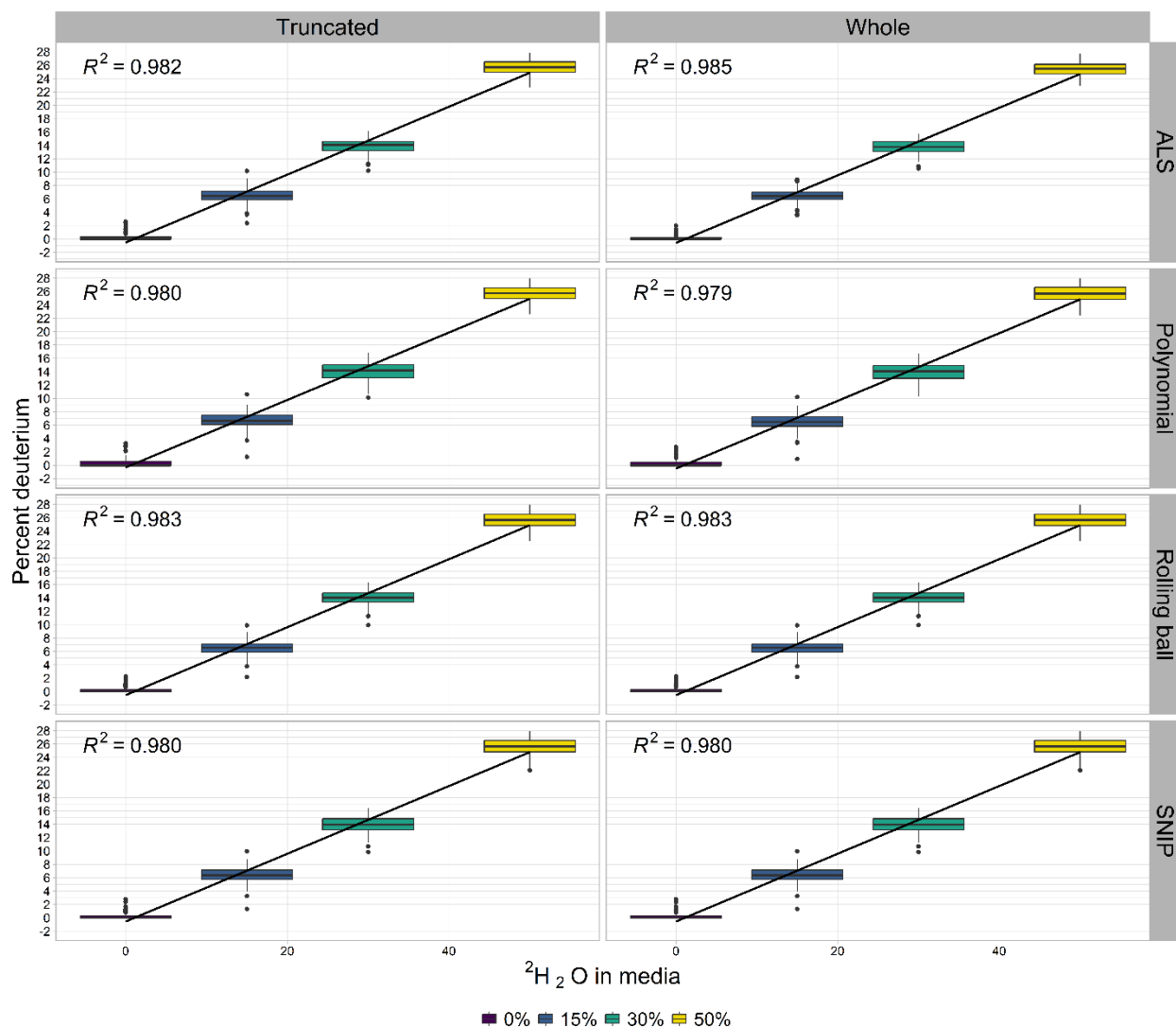


Fig. S3. Analysis of baselining methods for Raman spectra. The percent deuterium was calculated by comparing the ratio between CD and CH of the vibrational bands. Spectra were either analyzed as a whole ( $250\text{-}3,200\text{ cm}^{-1}$ ) or truncated ( $1,800\text{-}3,200\text{ cm}^{-1}$ ) with each of the four baselining methods. No statistical differences were observed between the samples and treatment methods (whole vs. truncated).

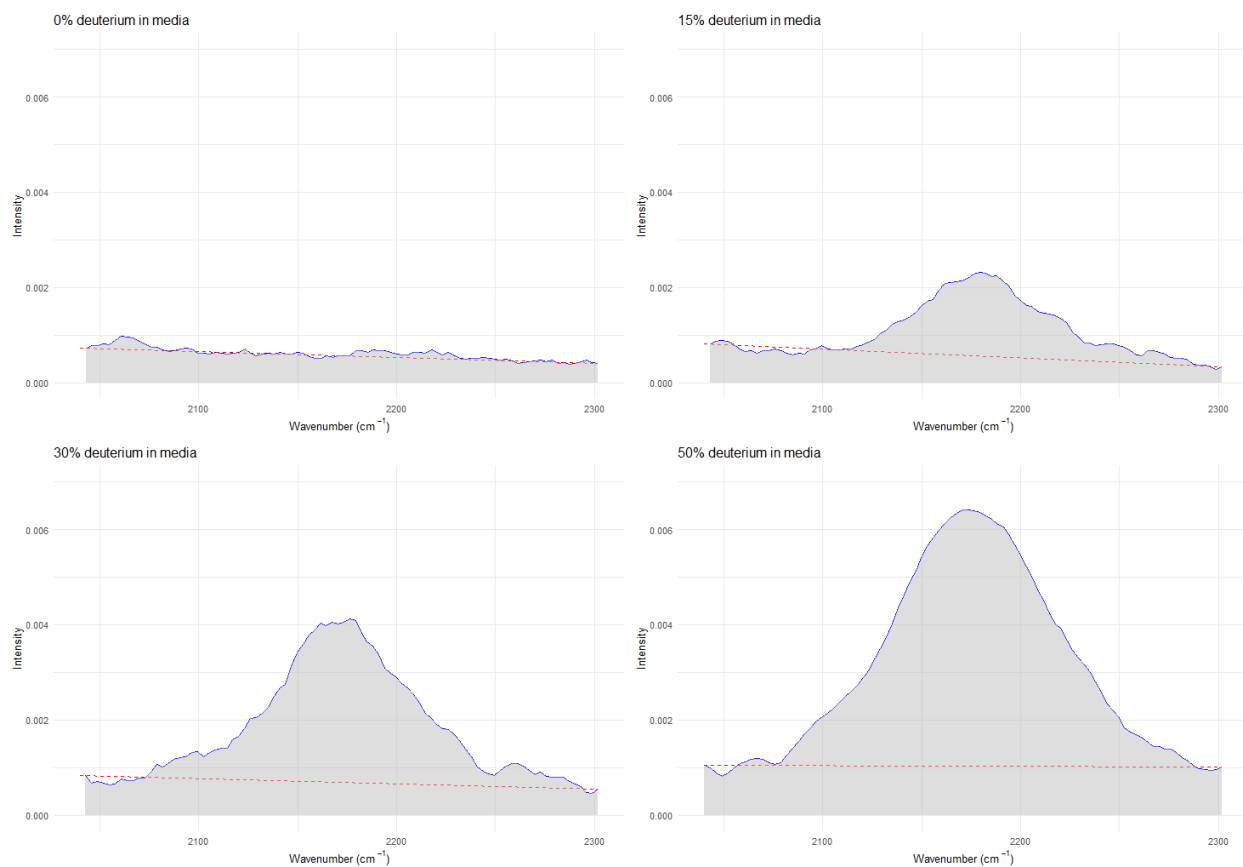


Fig. S4. Calculating the AUC for  $^{12}\text{C}-^2\text{H}$ . A baseline is drawn from the starting wavenumber ( $2,040\text{ cm}^{-1}$ ) to the ending wavenumber ( $2,300\text{ cm}^{-1}$ ) and only the area above that line and below the curve is calculated. The same method was applied to the  $^{12}\text{C}-^1\text{H}$  peak ( $2,800\text{--}3,100\text{ cm}^{-1}$ ).

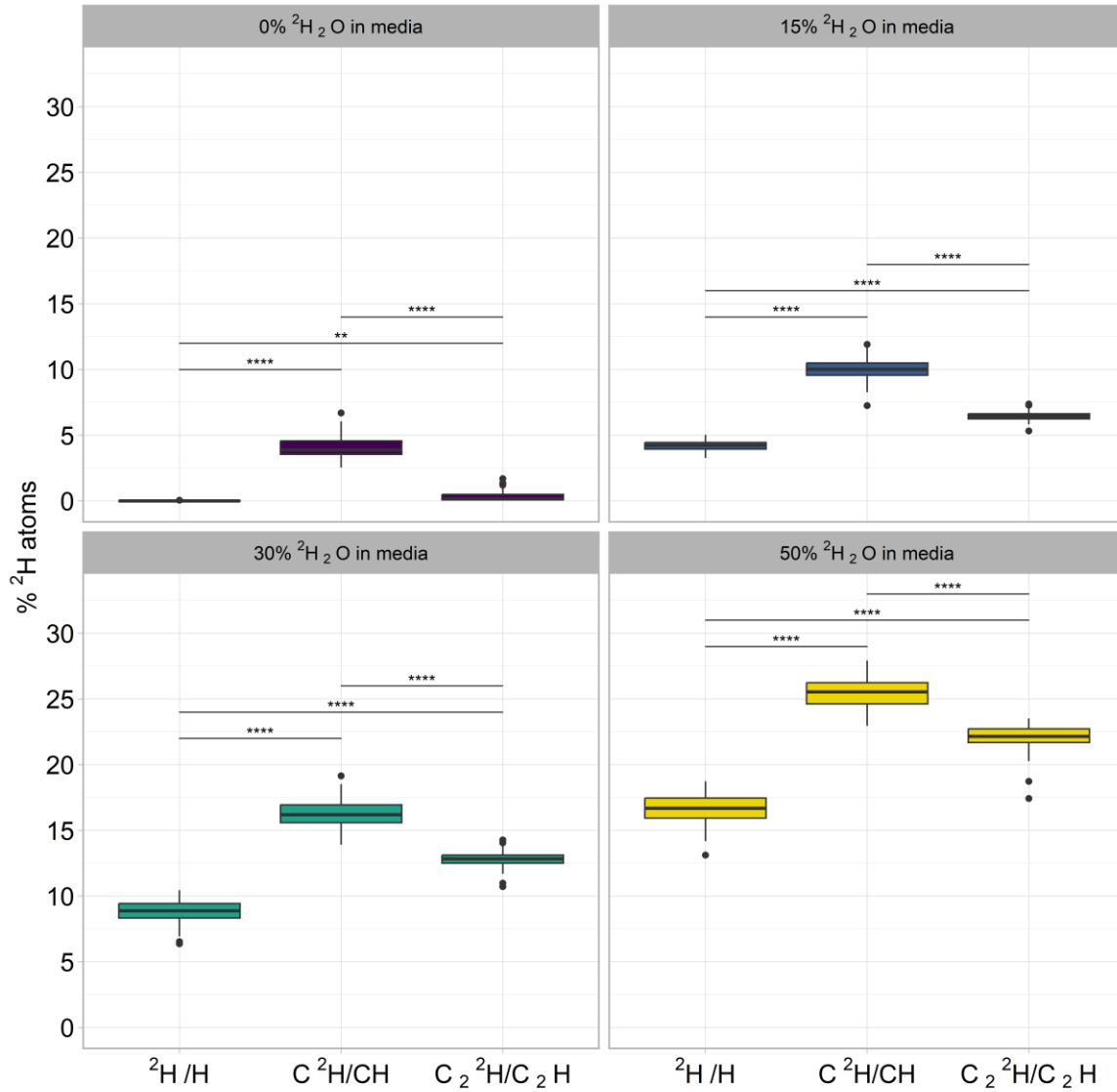


Fig. S5. Percent  $^2\text{H}$  as measured by the different atomic mass ratios using NanoSIMS across the four heavy water incubations. All statistically differences are shown: \*\* =  $p\text{-value} < 5.0 \times 10^{-3}$ , \*\*\*\* =  $p\text{-value} < 1.0 \times 10^{-10}$ .

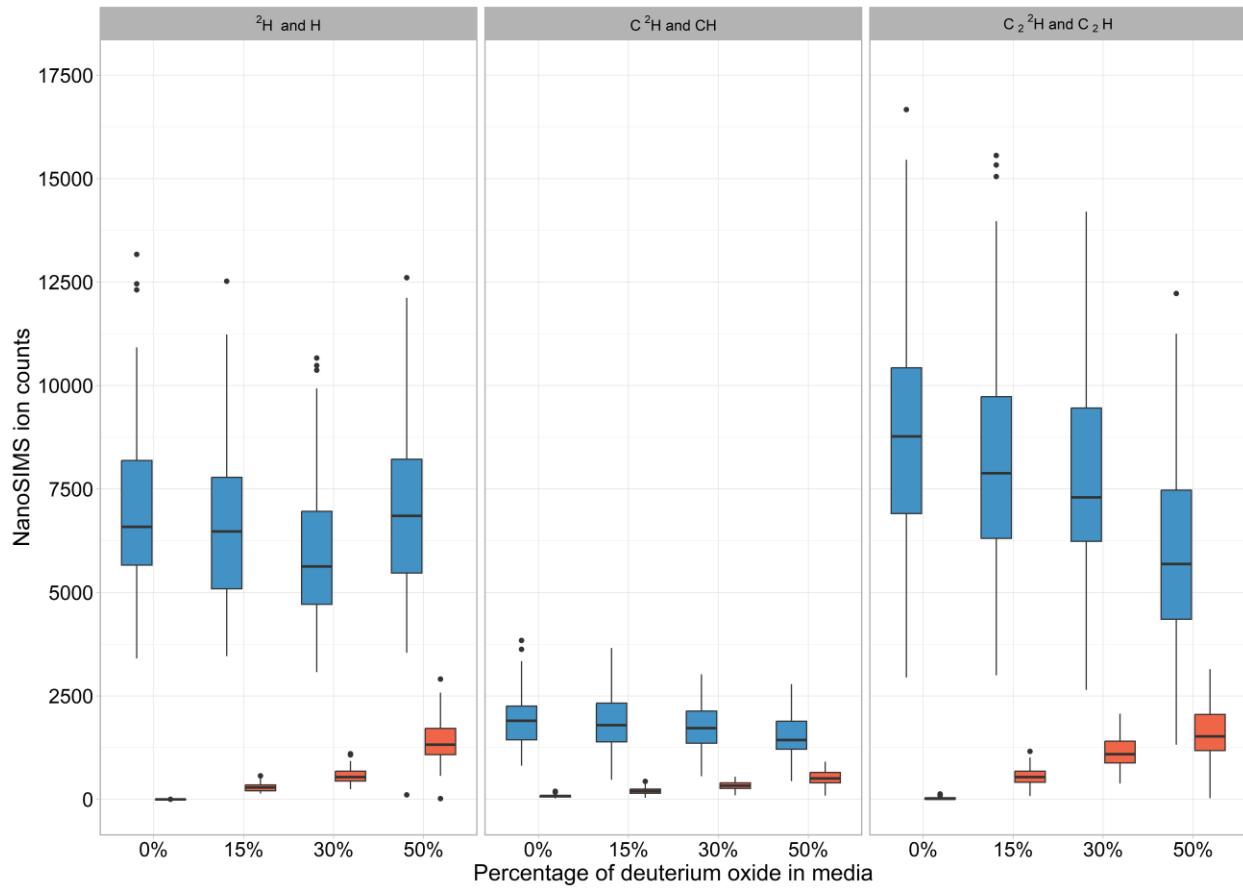


Fig. S6. Comparison of NanoSIMS ion counts for each ion mass analyzed. Blue bars show the mass measured for the H count and orange bars show the mass measured for the  $^2\text{H}$  count. Both  $\text{C}^2\text{H}/\text{C}^1\text{H}$  and  $\text{C}_2^2\text{H}/\text{C}_2^1\text{H}$  were measured on the same cells, indicating that differences in counts are likely due to instrument drift or kinetic isotope/electron affinity effects.

<sup>2</sup> H in media	Variable 1	Variable 2	P-value
0%	ALS	Polynomial	*0.040
0%	ALS	Rolling ball	0.420
0%	Polynomial	Rolling ball	0.213
0%	ALS	SNIP	0.100
0%	Polynomial	SNIP	0.683
0%	Rolling ball	SNIP	0.402
15%	ALS	Polynomial	0.674
15%	ALS	Rolling ball	0.616
15%	Polynomial	Rolling ball	0.935
15%	ALS	SNIP	0.860
15%	Polynomial	SNIP	0.551
15%	Rolling ball	SNIP	0.498
30%	ALS	Polynomial	0.298
30%	ALS	Rolling ball	0.175
30%	Polynomial	Rolling ball	0.751
30%	ALS	SNIP	0.511
30%	Polynomial	SNIP	0.702
30%	Rolling ball	SNIP	0.483
50%	ALS	Polynomial	0.216
50%	ALS	Rolling ball	0.194
50%	Polynomial	Rolling ball	0.950
50%	ALS	SNIP	0.241
50%	Polynomial	SNIP	0.948
50%	Rolling ball	SNIP	0.898

Table S1. Pairwise t-tests of baselining methods applied to Raman spectra for each <sup>2</sup>H<sub>2</sub>O incubation. There was no statistical difference found except for ALS vs. Polynomial in the 0% <sup>2</sup>H<sub>2</sub>O incubation, denoted by the asterisk.

APPENDIX C

CHAPTER FOUR SUPPORTING MATERIAL

We assign type genomes for eight newly discovered species of MMB and propose the following provisional taxonomic assignments. All researchers were contacted and gave permission to name new MMB species after them. See SI Appendix Table S4.

*Candidatus Magnetoglobus abreuianus* sp. nov.

a.bre.u.i.a'nus N.L. masc. adj. abreuianus; named in honor of Fernanda Abreu, who described the first species of MMB, *Magnetoglobus multicellularis* (Abreu et al., 2007). This uncultured species is represented by bin 3300034485, which has an estimated completeness of 89.22%, a contamination of 2.09%, with no 16S rRNA, 23S rRNA or 5S rRNA genes.

*Candidatus Magnetoglobus debarrosii* sp. nov.

de.bar.ro'si.i N.L. gen. n. debarrosii, of de Barros; named in honor of Henrique Lins de Barros, who shaped understanding of MMB for the past four decades. This uncultured species is represented by bin 3300034500, which has an estimated completeness of 90.62%, a contamination of 1.94%, and contains 16S rRNA, 23S rRNA and 5S rRNA genes.

*Candidatus Magnetoglobus farinai* sp. nov.

fa.ri.'na.i N.L. gen. n. farinai, of Farina; named in honor of Marcos Farina, who co-discovered MMB in 1983 (Esquivel et al., 1983; Farina et al., 1983). This uncultured species is represented by bin 3300034494, which has an estimated completeness of 90.65%, a contamination of 0.86%, and contains 16S rRNA, 23S rRNA and 5S rRNA genes.

*Candidatus Magnetoglobus keimiae* sp. nov.

ke.i'mi.æ N.L. gen. n. keimiae, of Keim; named in honor of Carolina Keim, who first demonstrated the multicellular life cycle of MMB (Keim et al., 2004). This uncultured species is represented by bin 3300034495, which has an estimated completeness of 94.77%, a contamination of 1.53%, and contains 16S rRNA, 23S rRNA and 5S rRNA genes.

*Candidatus Magnetoglobus linsii* sp. nov.

lin'si.i N.L. gen. n. linsii, of Lins; named in honor of the late Ulysses Lins, whose pursuit of pure, “romantic” scientific questions (Keim et al., 2007) shaped our understanding of MMB. This uncultured species is represented by bin 3300034496, which has an estimated completeness of 93.56%, a contamination of 1.29%, and contains 16S rRNA, 23S rRNA and 5S rRNA genes.

*Candidatus Magnetoglobus martinsiae* sp. nov.

mar.tin'si.æ N.L. gen. n. martinsiae, of Martins; named in honor of Juliana Lopes Martins' contributions to the study of MMB. This uncultured species is represented by bin 330034493, which has an estimated completeness of 91.77%, a contamination of 0.86%, with no 16S rRNA, 23S rRNA or 5S rRNA genes.

*Candidatus Magnetoglobus simmonsiae* sp. nov.

sim.mon'si.æ N.L. gen. n. simmonsiae, of Simmons; named in honor of Sherri Simmons, whose research on MMB in Little Sippewissett Salt Marsh laid the foundation for much of our analysis (Simmons & Edwards, 2007). This uncultured species is represented by bin 3300034505, which

has an estimated completeness of 85.37%, a contamination of 1.31%, and contains 16S rRNA, 23S rRNA and 5S rRNA genes.

*Candidatus* Magnetomorum sippewissettense sp. nov.

sip.pe.wis.set.ten'se N.L. neut. adj. sippewissettense; pertaining to Sippewissett, named after Little Sippewissett Salt Marsh, Falmouth, MA, USA, where this study was conducted. This uncultured species is represented by bin 3300034504, which has an estimated completeness of 86.63%, a contamination of 0.32%, and contains 16S rRNA, 23S rRNA and 5S rRNA genes.

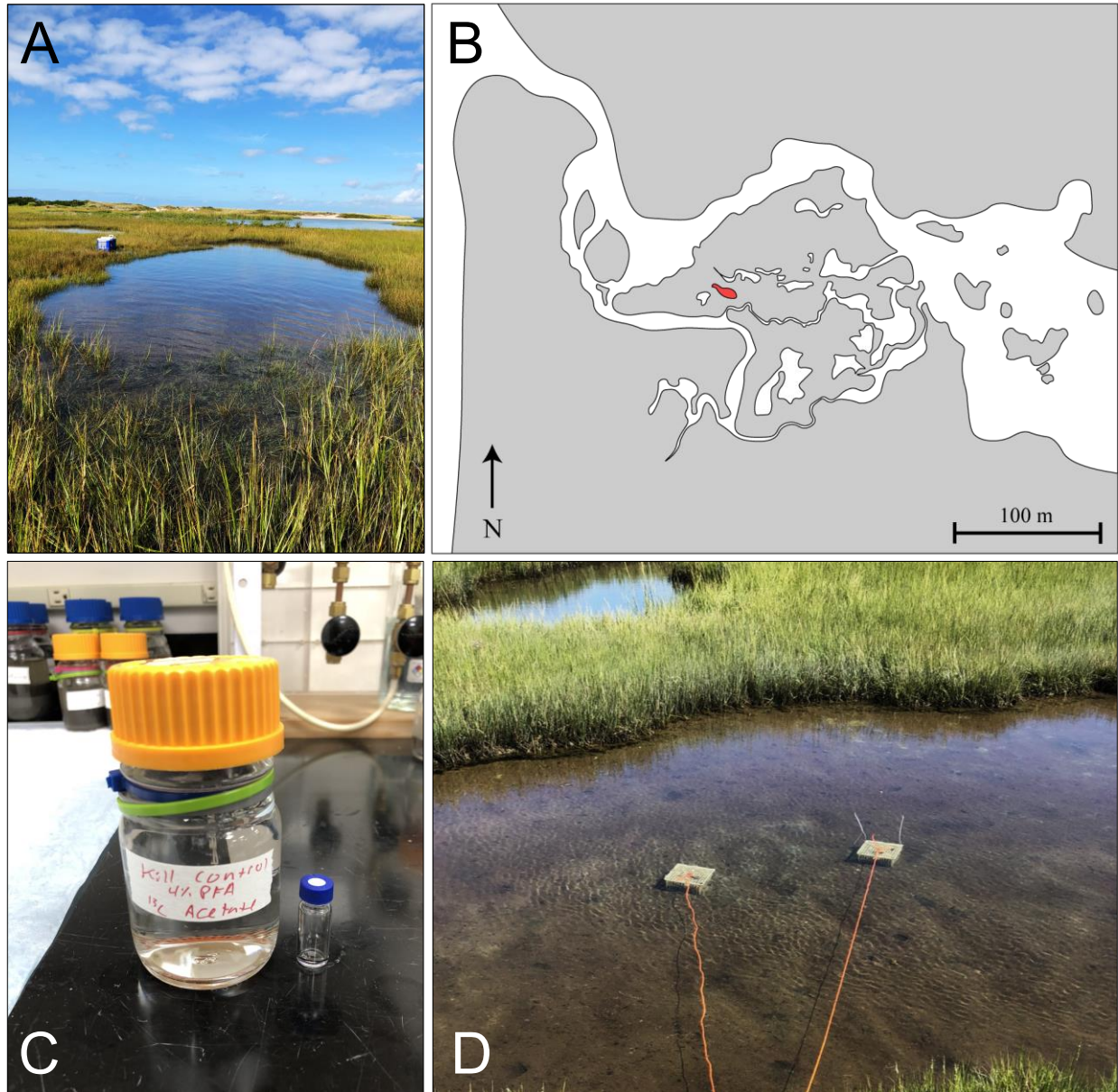


Fig. S1. Little Sippewissett salt marsh, Falmouth MA. (A) Photo of the tidal pool from which sulfidic sediments were obtained, facing west towards Buzzards Bay. (B) Map of the salt marsh showing the tidal pool in red and water in white. (C) Each sample was incubated in a 200 mL bottle filled to the top with the sediment slurry and tightly capped. Because no MMB could be recovered post-fixation from the the kill control sample, 200  $\mu$ L of sample were incubated in a small glass vial inside of the 200 mL bottle. (D) Samples were incubated *in situ* below the sediment at the site for 24 hours.



Fig. S2. Phylogenetic analysis of MMB using near-full length 16S rRNA genes (length listed next to name) found in 14 of the 22 SCGs and in reference genomes. Tree reconstructed using maximum likelihood method with bootstrap values calculated using 500 replicates. Bootstrap values above 50 are shown. *Ca. M. abreuianus* is not shown in this analysis because no 16S rRNA gene was recovered from the SCG. Color coded sequences belong to their respective SCG, as shown in supplemental table 1. Bars on right show specificities of our newly designed FISH probes that target genus-level groups of MMB in LSSM (SI Appendix Table S9).

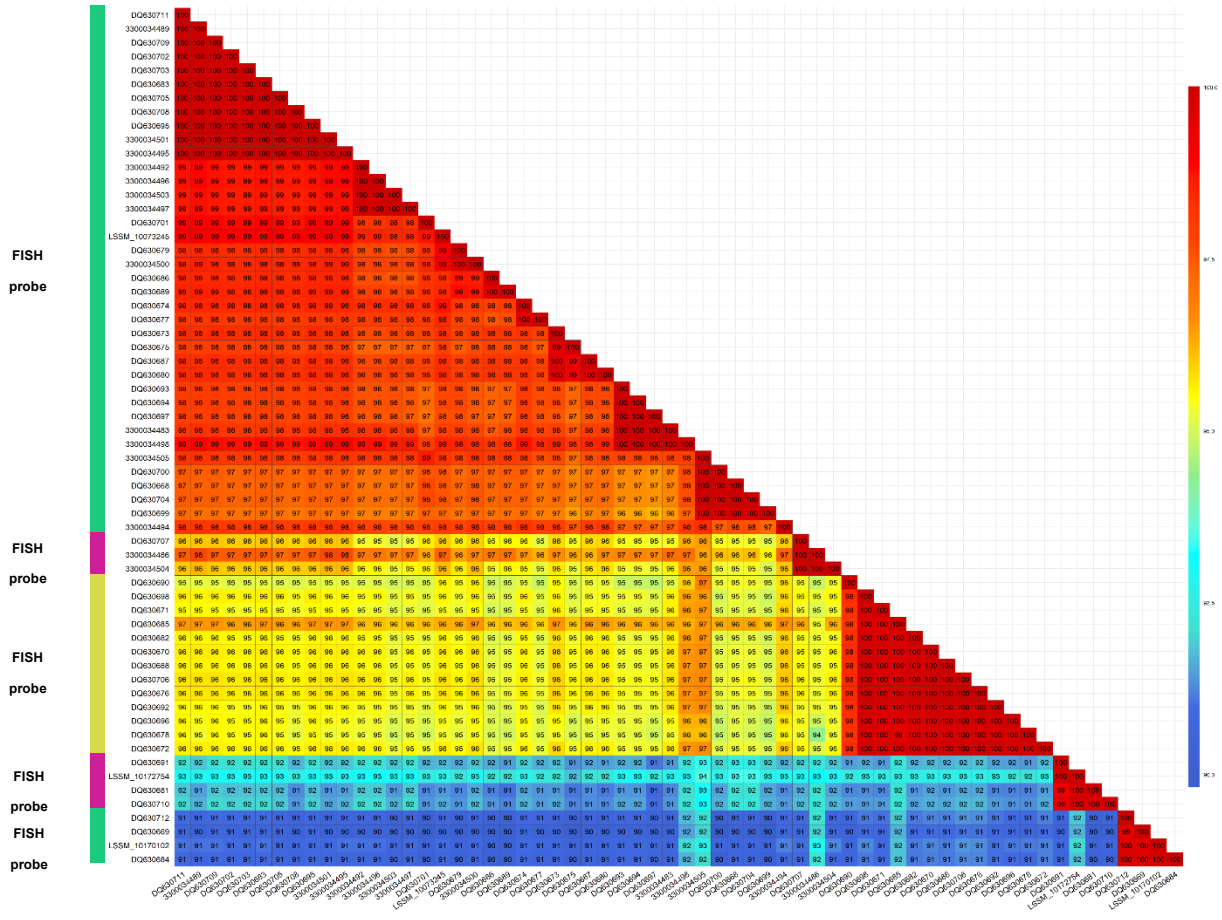


Fig. S3. Near-full length 16S rRNA gene comparison of all sequences recovered in this study and previous studies at LSSM (Simmons and Edwards 2007). Percent identity values are shown within boxes. Bars on left highlight MMB groups for which genus-level FISH probes designed (SI Appendix Table S9).

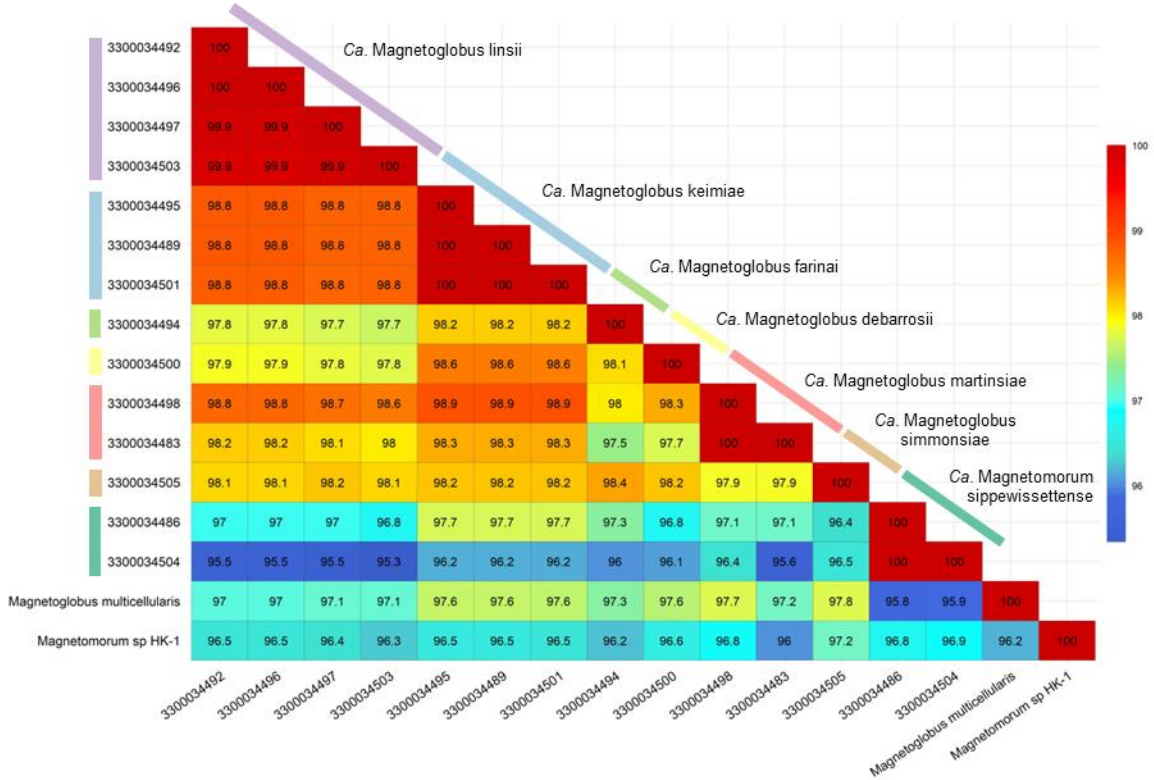


Fig. S4. Near-full length 16S rRNA identity comparison for the 14 sequences recovered from SCGs and the two MMB reference genomes (*Ca. M. multicellularis* and *Ca. Magnetomorum sp. HK-1*). Percent identity values are shown within boxes.

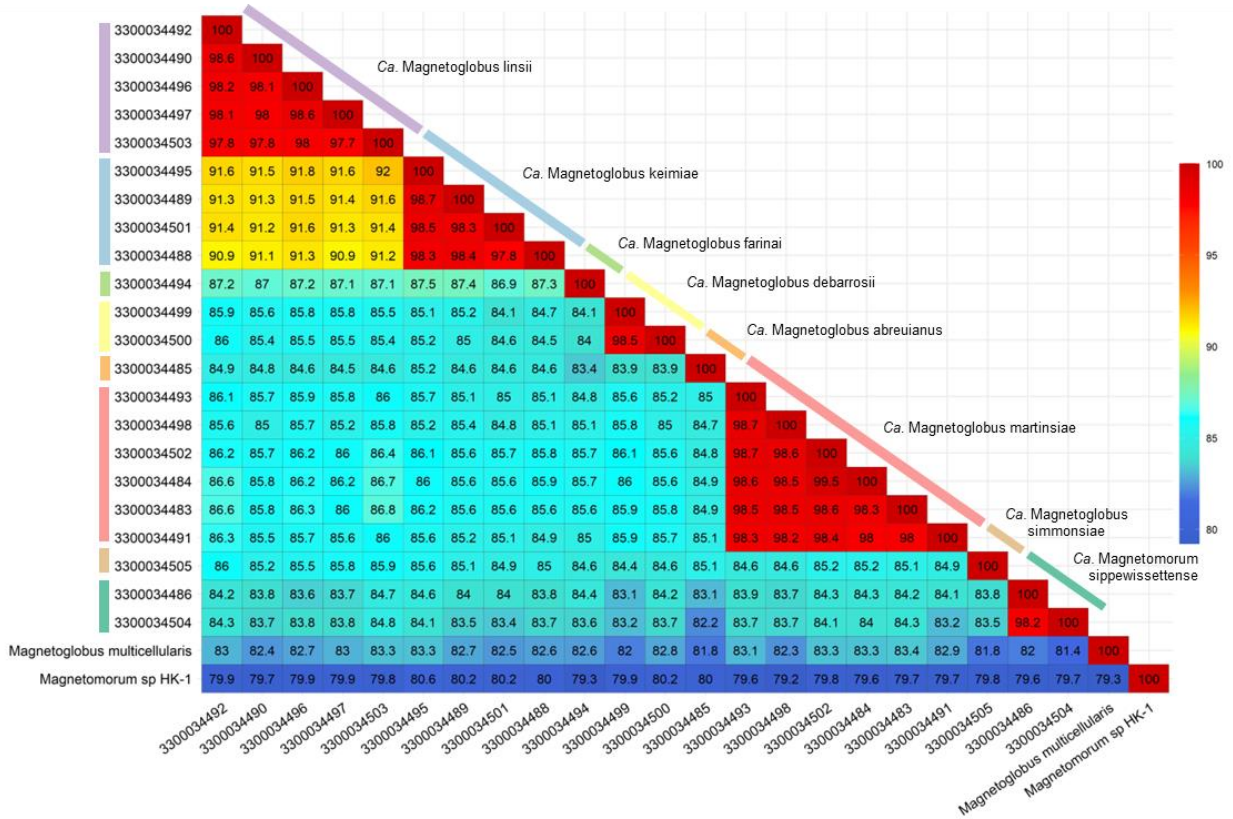


Fig. S5. Genome ANI comparing each of the 22 individual SCGs with the two publicly available reference genomes (*Ca. M. multicellularis* and *Ca. Magnetomorum sp. HK-1*). ANI values are shown within boxes.

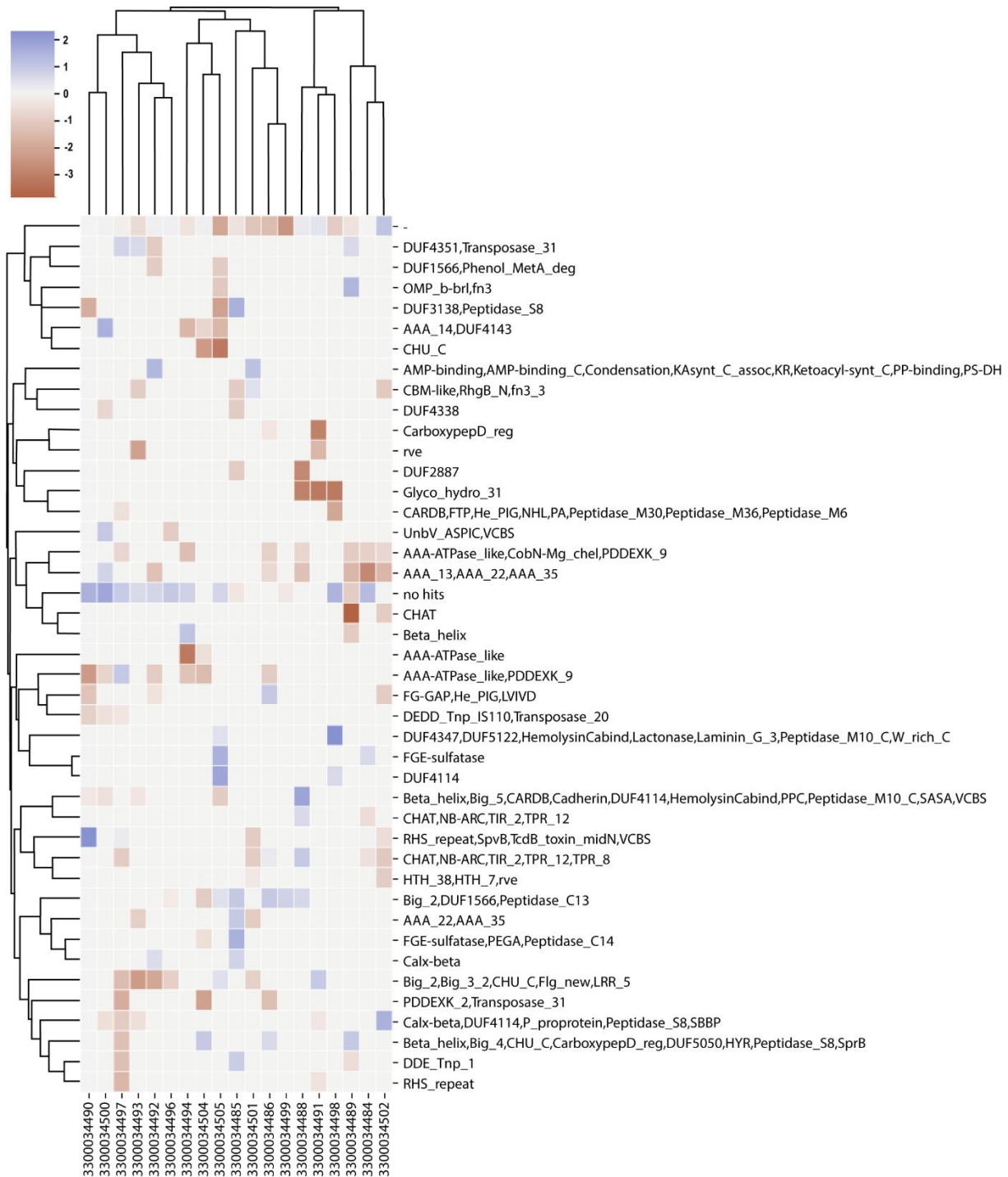


Fig. S6. Heatmap and cluster analysis of pfams annotation of individual SNPs showing the log<sub>2</sub> ratio of non-synonymous to synonymous substitutions (dN/dS) for the SNP differences contained within each SCG. The analysis suggested there was no positive selection of the protein-coding genes in which the SNPs were found.

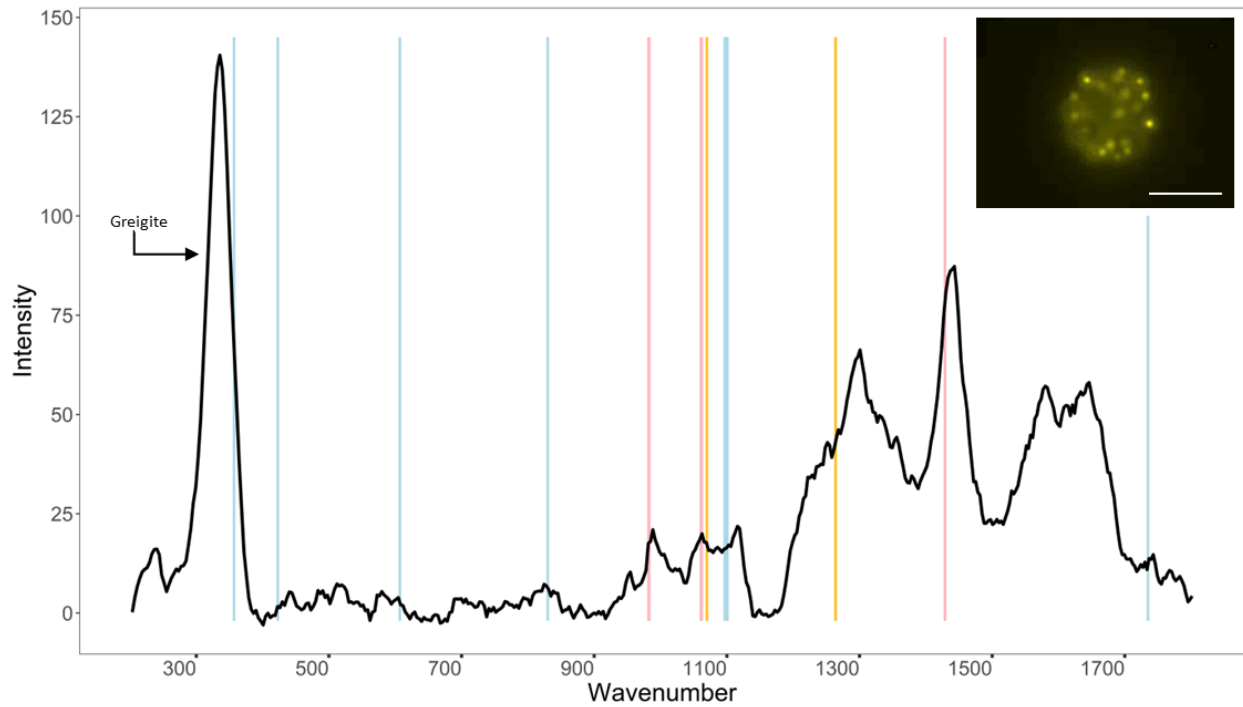


Fig. S7. Representative Raman spectrum of a MMB using a 532 nm laser. Vertical lines show peaks corresponding to polyhydroxybutyrate (blue), triglycerides (gold), and exopolysaccharides (pink). Wavenumbers corresponding to peaks are listed in SI Appendix Table S6. The large peak at  $\sim 335 \text{ cm}^{-1}$  is assigned to the magnetosome crystal greigite, which has previously been shown for MMB from the same site (Schaible *et al.*, 2022). Inset image shows a MMB consortium stained with Nile Red, indicating C-H rich droplets within cells. The contrast and brightness of the image has been increased for better visualization. Scale bar is 5  $\mu\text{m}$ .

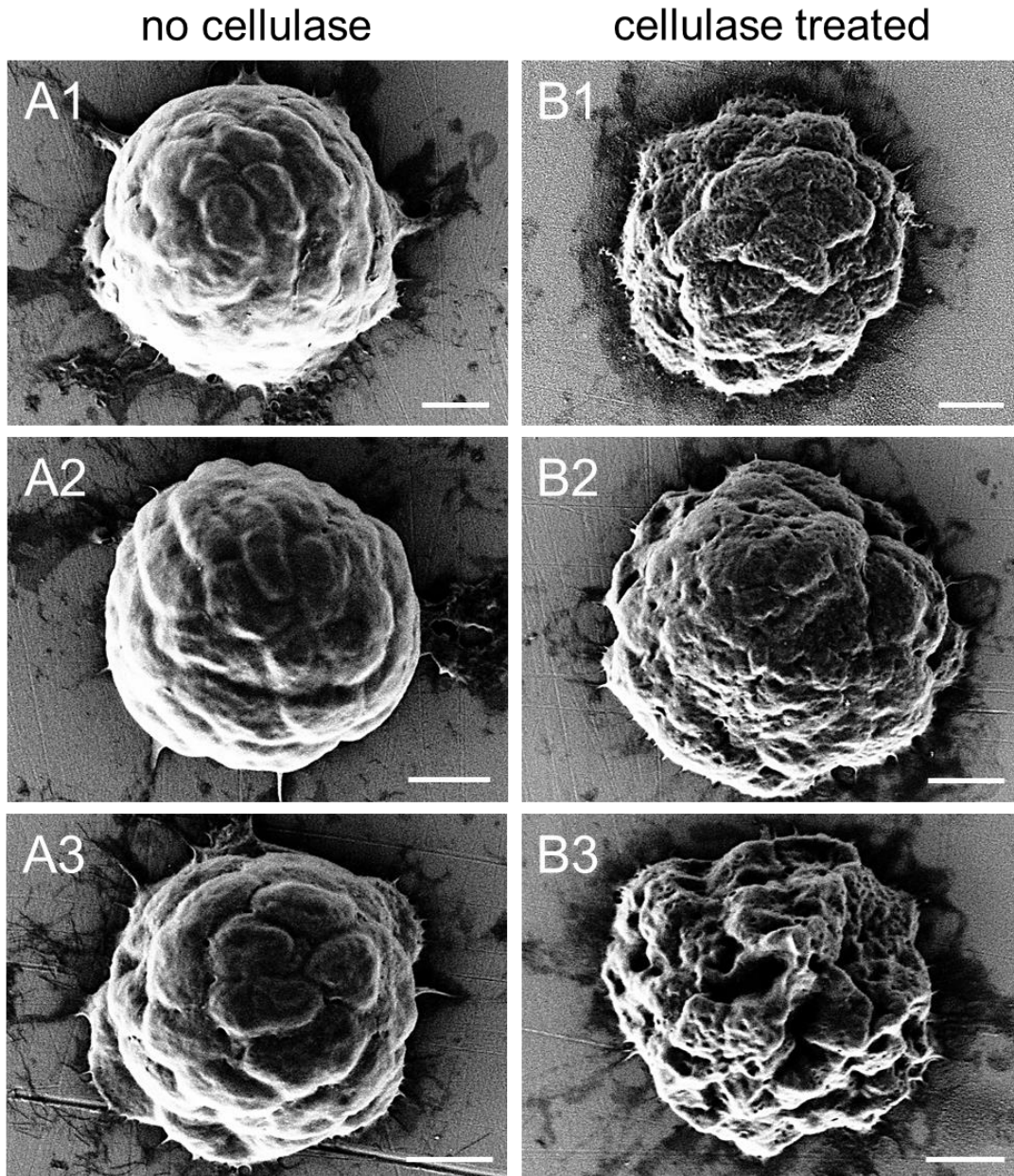


Fig. S8. Cellulase treatment of MMB. (A1-3) Control sample of MMB incubated without cellulase. (B1-3) After treatment with cellulase the surface of MMB consortia was noticeably eroded as compared to the control. Both samples were incubated for 1 hr under otherwise identical conditions (pH, temperature, and osmolarity). All scale bars are 1  $\mu\text{m}$ .

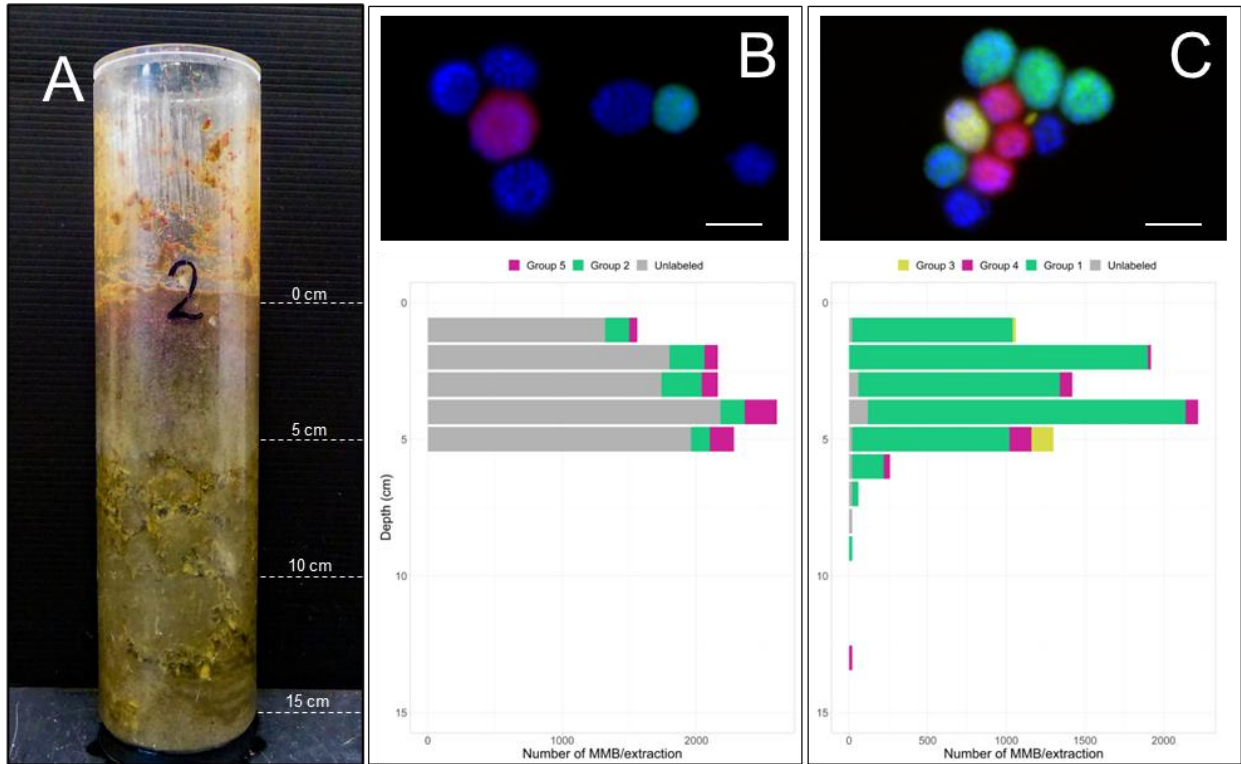


Fig. S9. Fractional abundance of MMB groups by depth in LSSM. (A) Image of the 15 cm core taken from the West end of sampling site prior to being sectioned into 1 cm horizons from which MMB were enriched for quantification by FISH. (B) DOPE-FISH analysis of MMB Groups 2 (red) and 5 (green) shown in panel (B) and Groups 1 (green), 3 (yellow) and 4 (red) shown in panel (C). MMB not detected by the respective FISH probes are shown in the blue DAPI counterstain in the microscopy images. Scale bars are 5  $\mu\text{m}$ . Bar plots show the abundance of each MMB group as determined by DOPE-FISH for each centimeter of the sediment core shown in panel (A). Unlabeled populations are MMB that were stained with DAPI but were not detected by the FISH probes used in the two separate experiments and are shown in gray. Consistent with results from SCG and previous 16S rRNA gene abundance studies (Simmons and Edwards 2007) in LSSM, Group 1 numerically dominate the MMB population. FISH probes used in this experiment are detailed in SI Appendix Table S9.

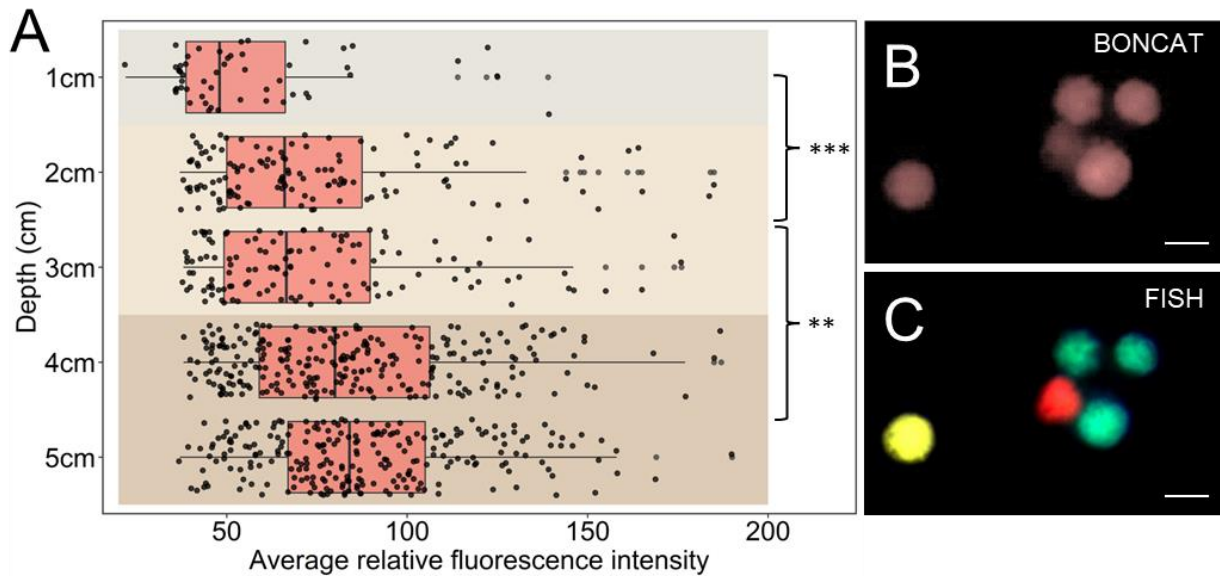


Fig. S10. Anabolic activity of MMB inhabiting the top 6 cm of LSSM sediment as measured by BIONCAT. (A) 1 cm sediment core horizons were incubated in the presence of the methionine analogue HPG and magnetically enriched MMB stained via azide-alkyne click chemistry with Alexa Fluor 405 to show relative activity of Group 1 MMB as a factor of depth in the sediment. The vertical line within each box shows the median and the whisker shows the range of the data. Dots represent individual MMB that were measured and analyzed using the software package Daimé. Data points that were more than two standard deviations of the mean are shown as individual points past the whicker. The analysis showed that there is a statistically relevant difference in the activity of MMB from 1 cm depth to 2-3 cm and again from 2-3 cm to the 4-5 cm depth. (B) Exemplary epifluorescence microscopy image of click-stained MMB. (C) Overlay epifluorescence microscopy image of FISH-labeled MMB shown in panel B. Group 1 is shown in green, Group 3 in yellow, and Group 4 in red. All scale bars are 5  $\mu\text{m}$ . All statistically differences are shown: \*\* =  $p < 3.9 \times 10^{-3}$ , \*\*\* =  $p < 3.5 \times 10^{-4}$ . FISH probes used in this experiment are detailed in SI Appendix Table S9.

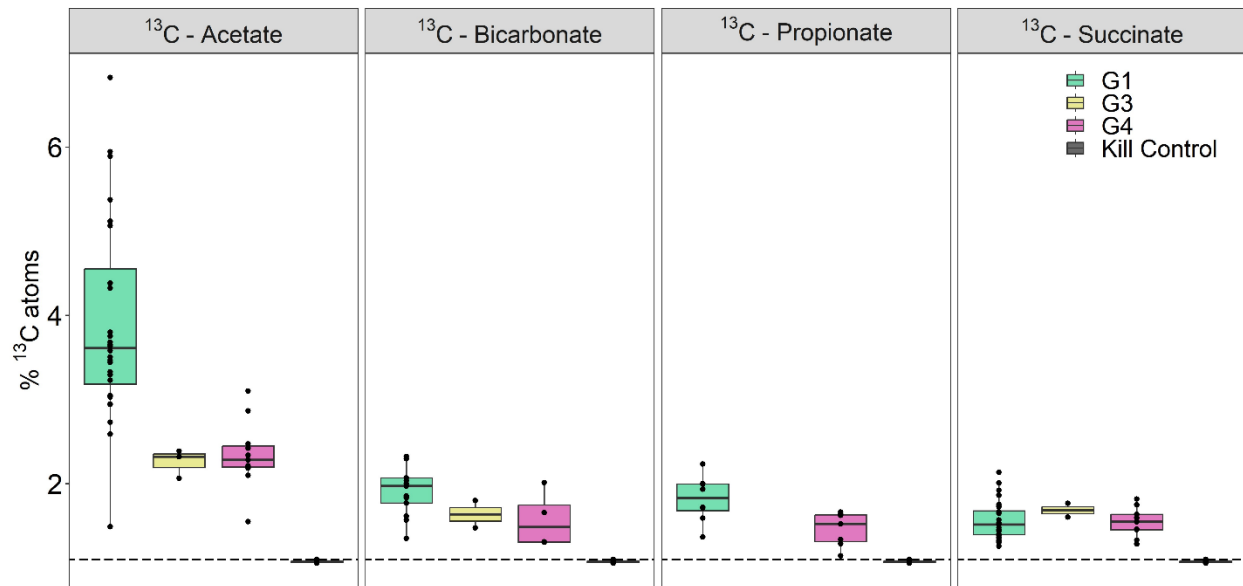


Fig. S11. Comparison of  $^{13}\text{C}$ -labeled substrate incorporation by MMB Groups 1, 3, and 4 using NanoSIMS analysis of mass ratio  $^{13}\text{C}^{12}\text{C}/^{12}\text{C}_2$ . The analysis shows that MMB in Group 1 anabolize acetate at a statistically greater rate than Groups 3 and 4 ( $p < 8.9 \times 10^{-3}$ ). Group 1 also incorporated more bicarbonate than Group 4 ( $p < 2.4 \times 10^{-2}$ ), although Group 4 only contained four samples to compare.

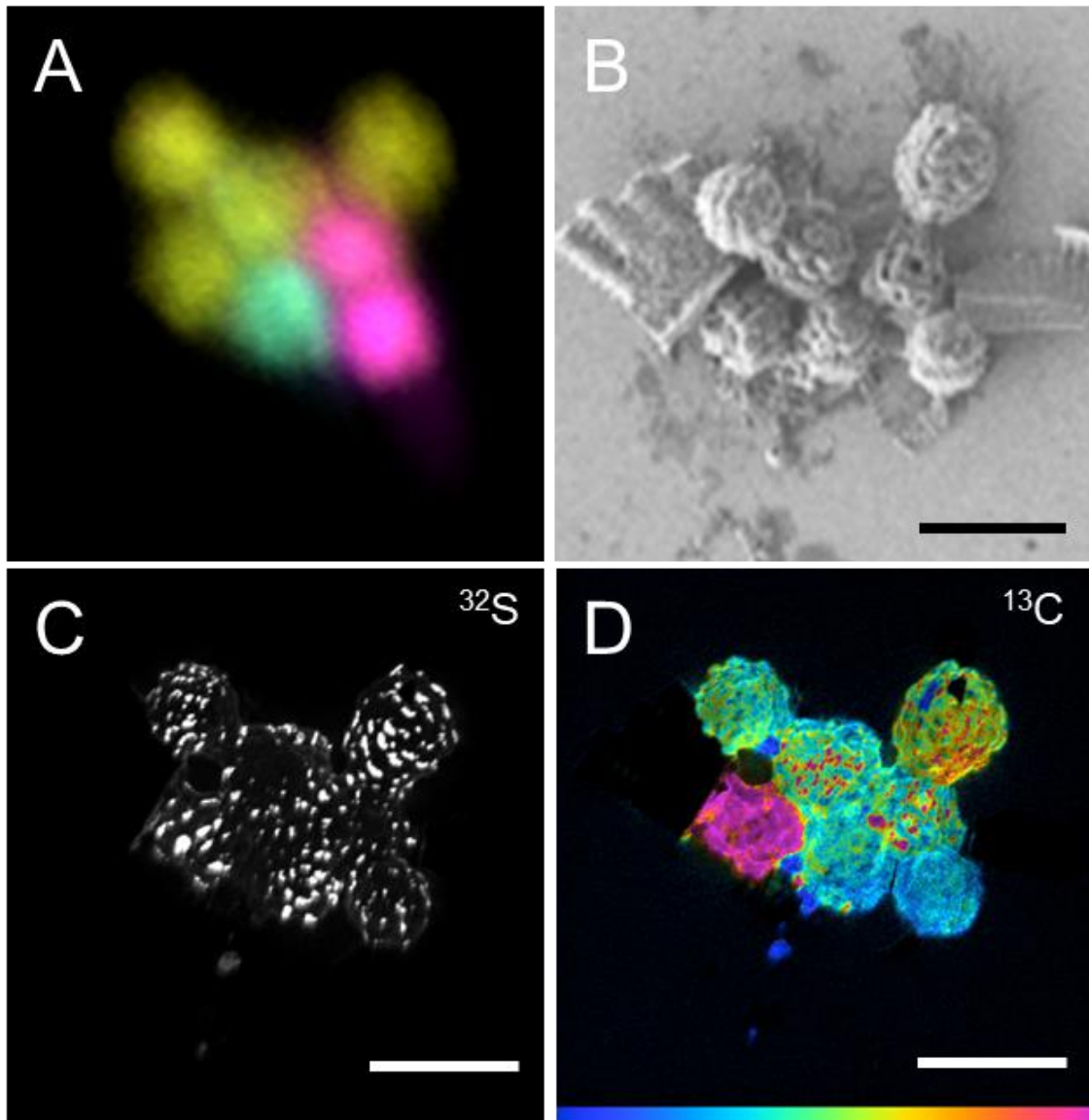


Fig. S12. Correlative imaging of MMB to identify their (A) taxonomy (DOPE-FISH), (B) morphology (SEM), (C) distribution of sulfur (NanoSIMS, mass 32; a proxy for the presence of sulfur-containing magnetosomes) and (D) uptake of 1,2-<sup>13</sup>C<sub>2</sub>-labeled acetate (NanoSIMS, HSI image showing mass ratio  $^{13}\text{C}^{12}\text{C}/^{12}\text{C}_2$ ). Scale bars are 5 μm. The HSI mass ratio color scale in D is 1.1% - 5% atom percent.

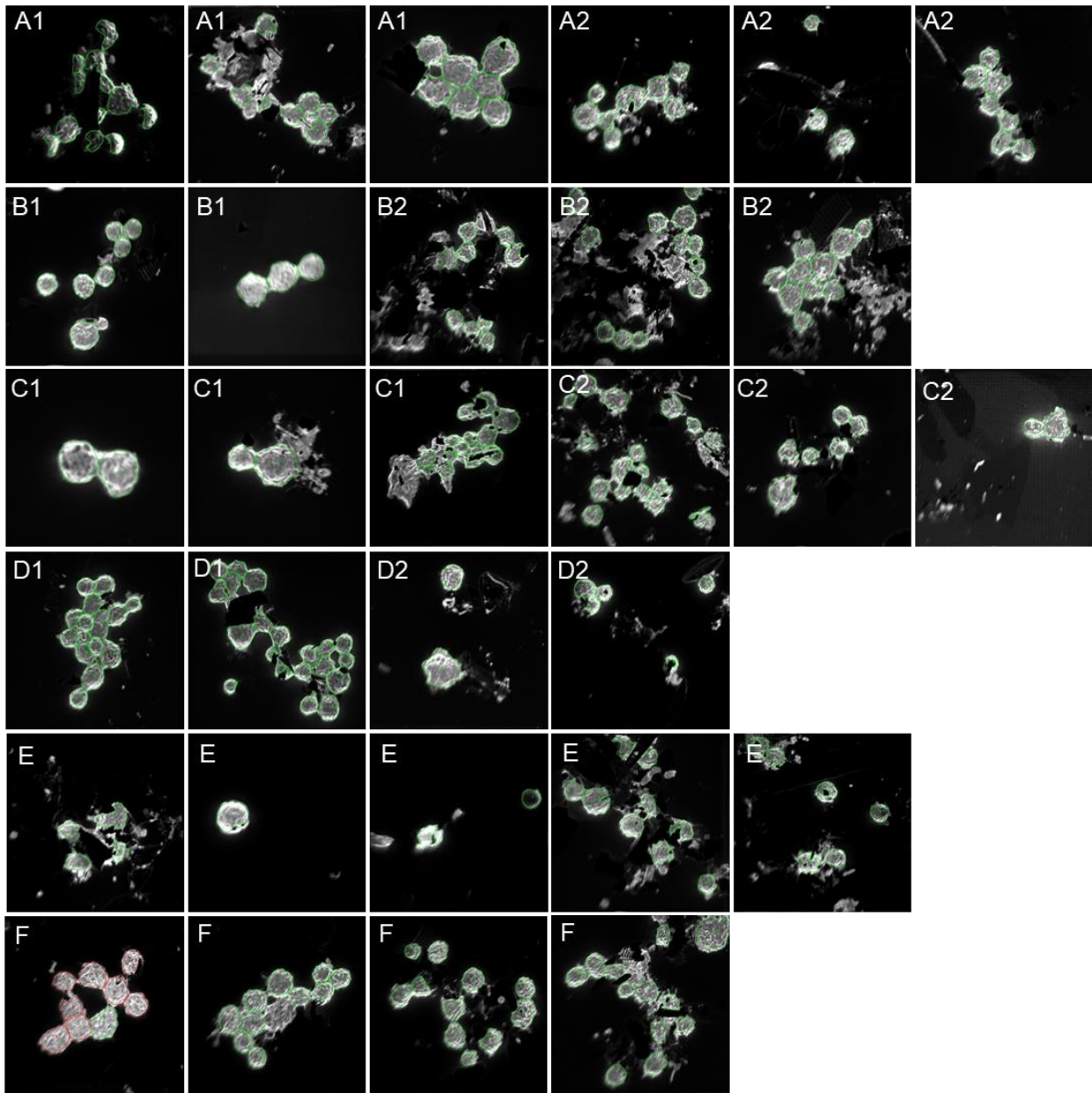


Fig. S13. ROIs for NanoSIMS substrate analysis shown in Fig. 5 of main text. Because the *in situ* incubation incurred particles that were not of interest (*e.g.*, diatoms and particulates), the ROIs were hand drawn around each MMB using the mass 26.00 ( $^{12}\text{C}^{14}\text{N}$ ) channel as to avoid incorporation of exogenous material in the analysis. (A1)  $^{13}\text{C}$ -acetate, (A2)  $^{12}\text{C}$ -acetate, (B1)  $^{13}\text{C}$ -bicarbonate, (B2)  $^{12}\text{C}$ -bicarbonate, (C1)  $^{13}\text{C}$ -propionate, (C2)  $^{12}\text{C}$ -propionate, (D1)  $^{13}\text{C}$ -succinate, (D2)  $^{12}\text{C}$ -succinate, (E)  $^{13}\text{C}$ -acetate kill control, (F) negative control. ROIs are shown in green and red outlines.

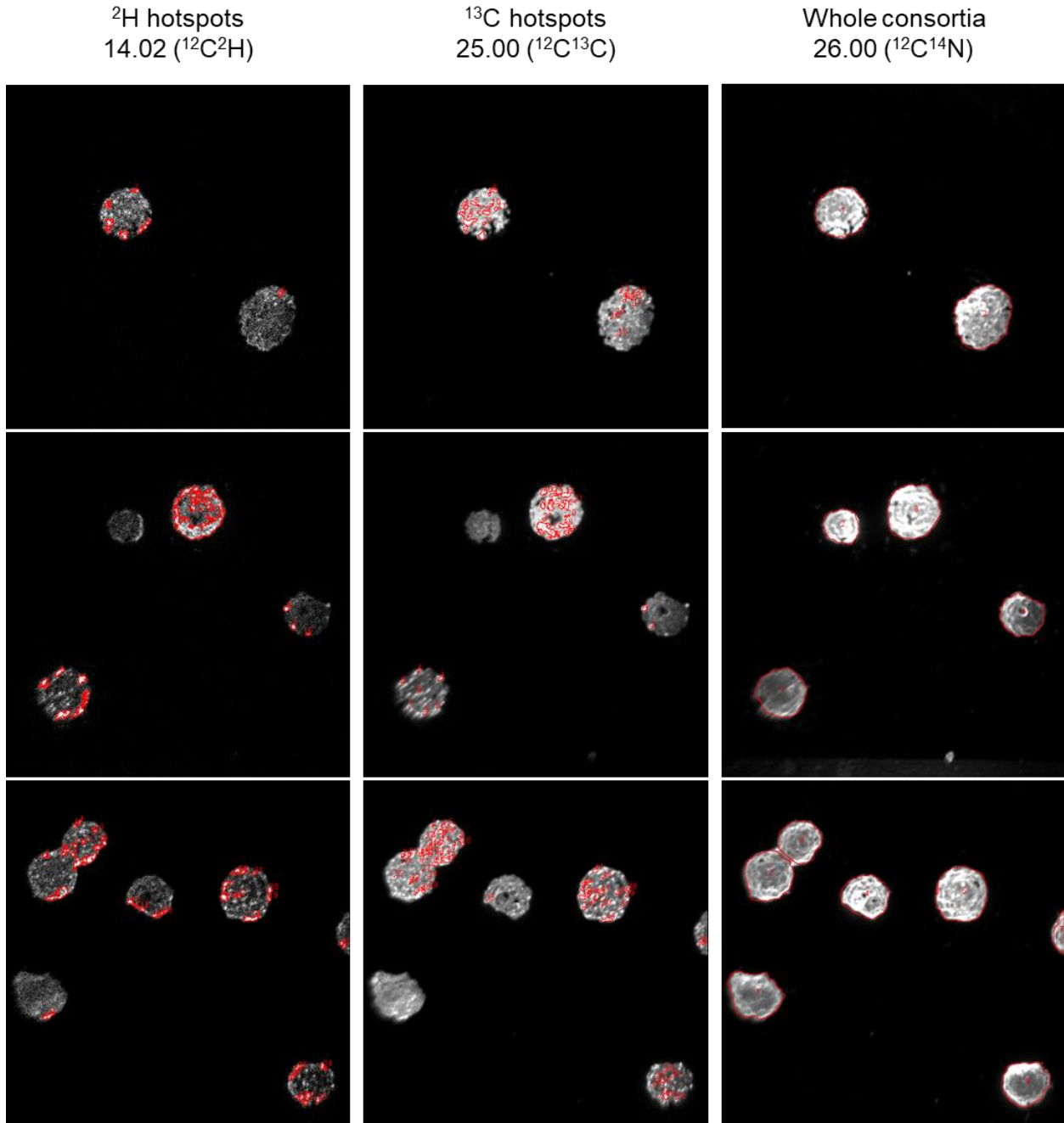


Fig. S14. ROIs for NanoSIMS hotspot analysis shown in Fig. 6 of main text. As to avoid introducing bias into the selection of hotspot ROIs, thresholding in ImageJ was used to automatically select for ROIs, as outlined in the methods. The respective mass image was used for hotspot thresholding and ROI selection. ROIs for whole consortia were hand drawn. All ROIs are show in red outlines.

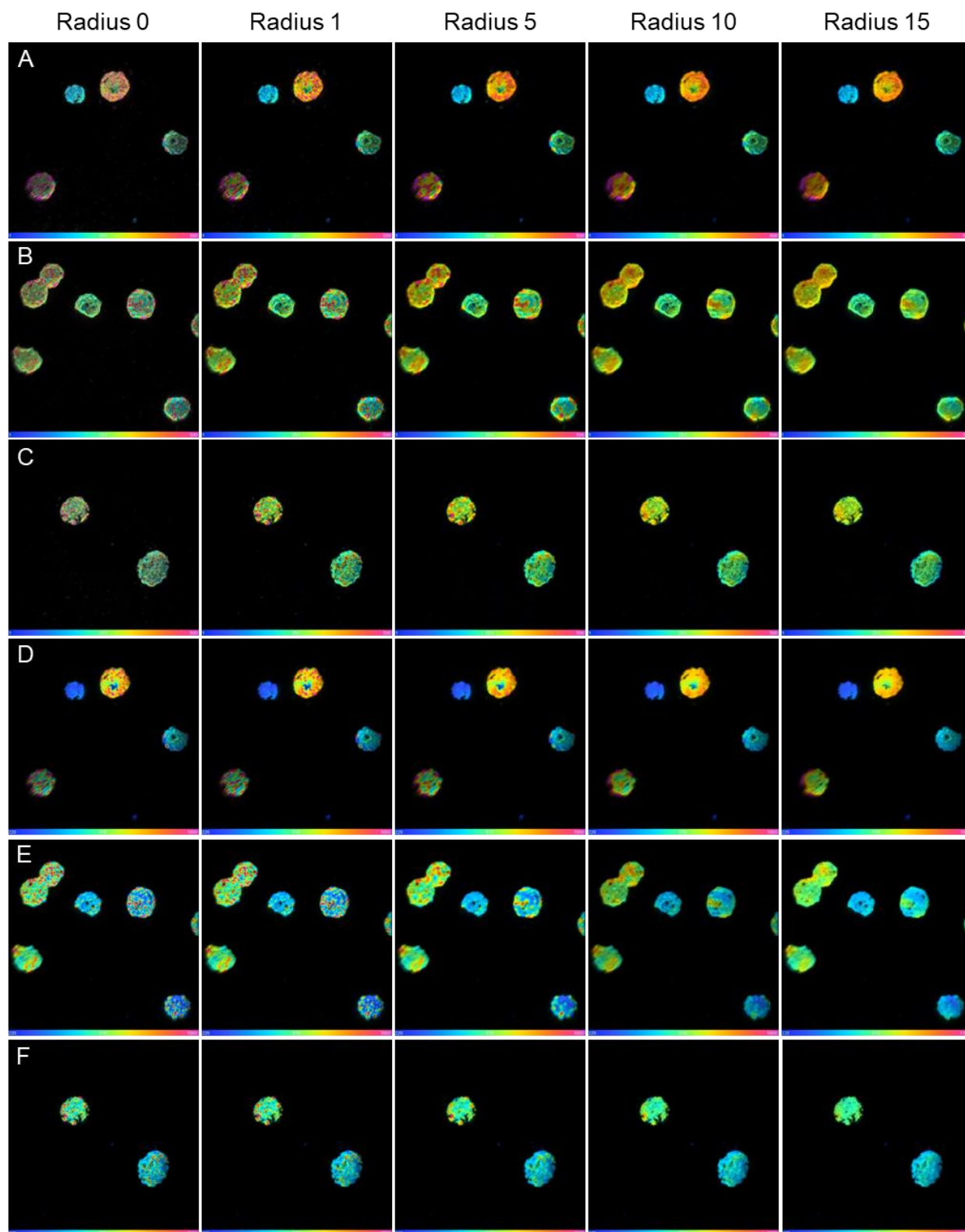


Fig. S15. Median filter ratio radius effect on HSI NanoSIMS images of  $^{13}\text{C}$  and  $^2\text{H}$  hotspots (*A-C*) Mass ratio ( $^2\text{H}^{12}\text{C}/^1\text{H}^{12}\text{C}$ ) of MMB labeled with deuterium oxide ( $^2\text{H}_2\text{O}$ ). (*D-F*) Mass ratio ( $^{13}\text{C}^{12}\text{C}/^{12}\text{C}_2$ ) of the same MMB shown in *A-C* but labeled with 1,2- $^{13}\text{C}_2$ -labeled acetate. For these images, the median filter ratio radius was increased to show the effect of noise reduction and localization of isotope label within consortia. A higher filter radius reveals isolated areas of the respective isotope label within MMB, though for a radius  $> 5$ , the label is averaged over an area greater than the size of a single cell within the consortium, thus losing cellular resolution. Independent of the radius chosen, hot spots remain visible.

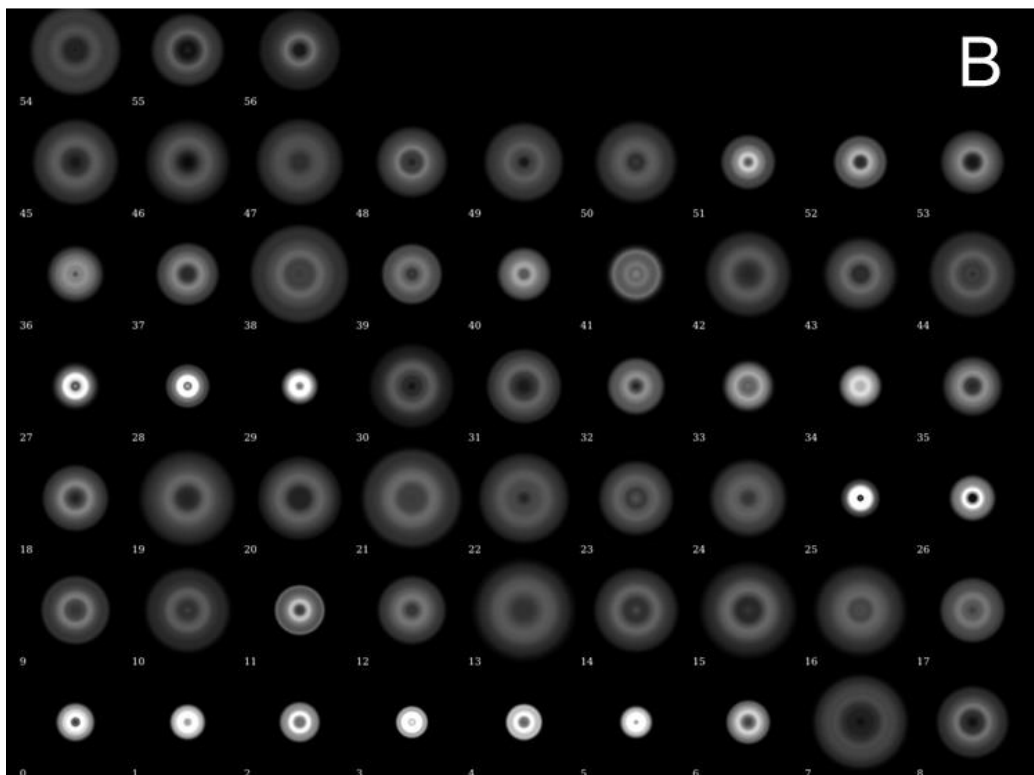
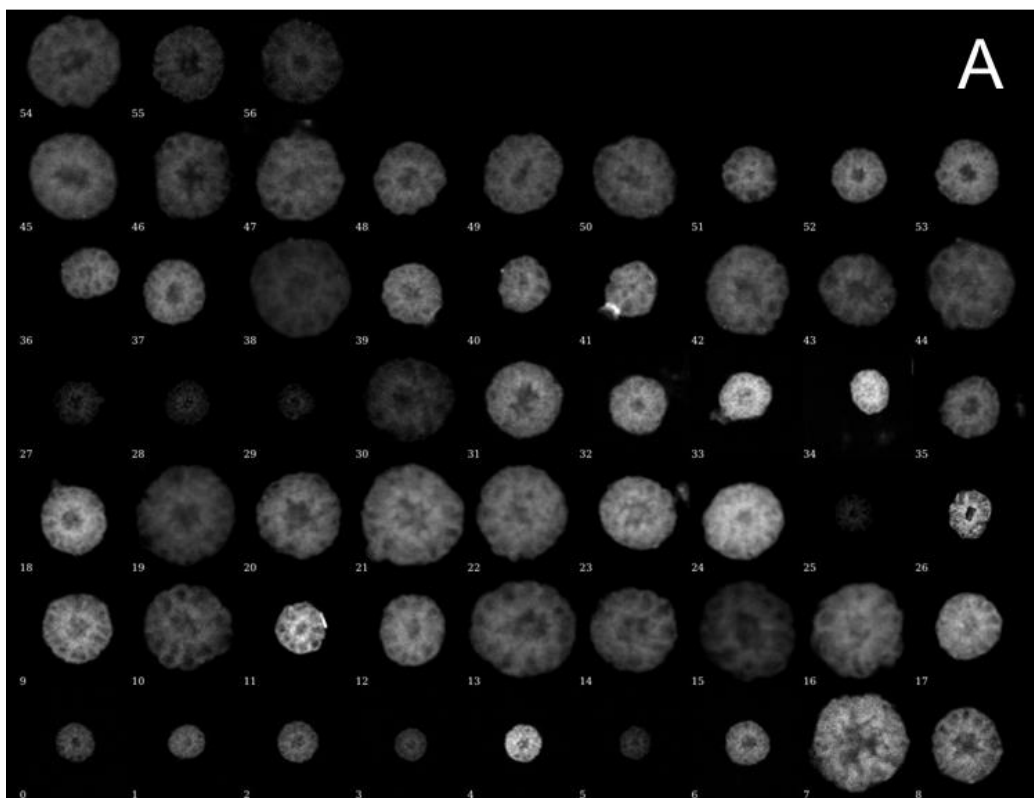


Fig. S16. Anabolic activity within individual consortia. (A) Gray-scale images of individual MMB stained via azide-alkyne click chemistry with Alexa Fluor 488. (B) The same consortia shown in A that have been rotationally averaged in Eman2 software. The relative fluorescence intensity was standardized for all samples prior to analysis.

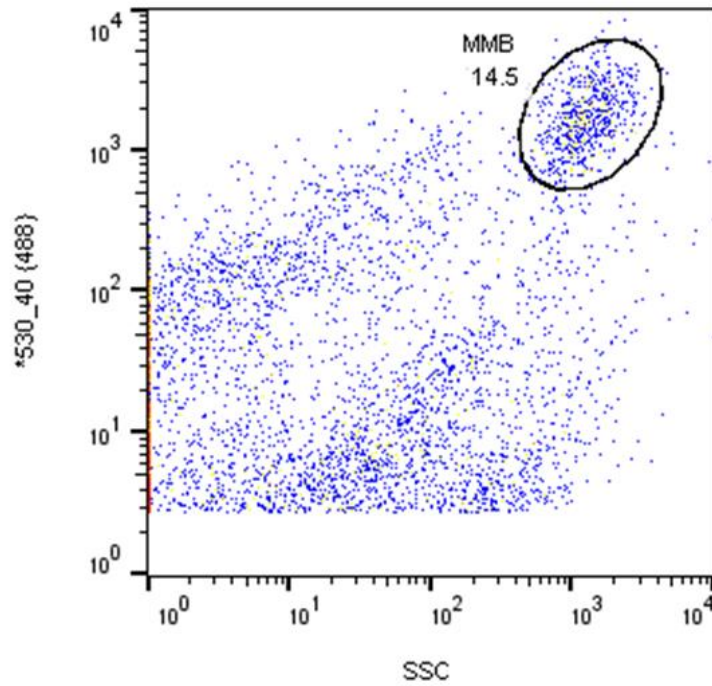


Fig. S17. Fluorescence activated cell sorting of a magnetically enriched sample from tidal pond sediment stained with SYBR Green. A sorting gate, presumed to contain MMB consortia, was set around particles with a strong 488 nm signal and high side scatter (SSC), indicating a large cell size. Other particles likely are single cell magnetotactic bacteria or non-magnetotactic bacteria present in the pond water. MMB consortia were sorted into individual wells of a microtiter well plate and 22 MMB consortia were genome sequenced.

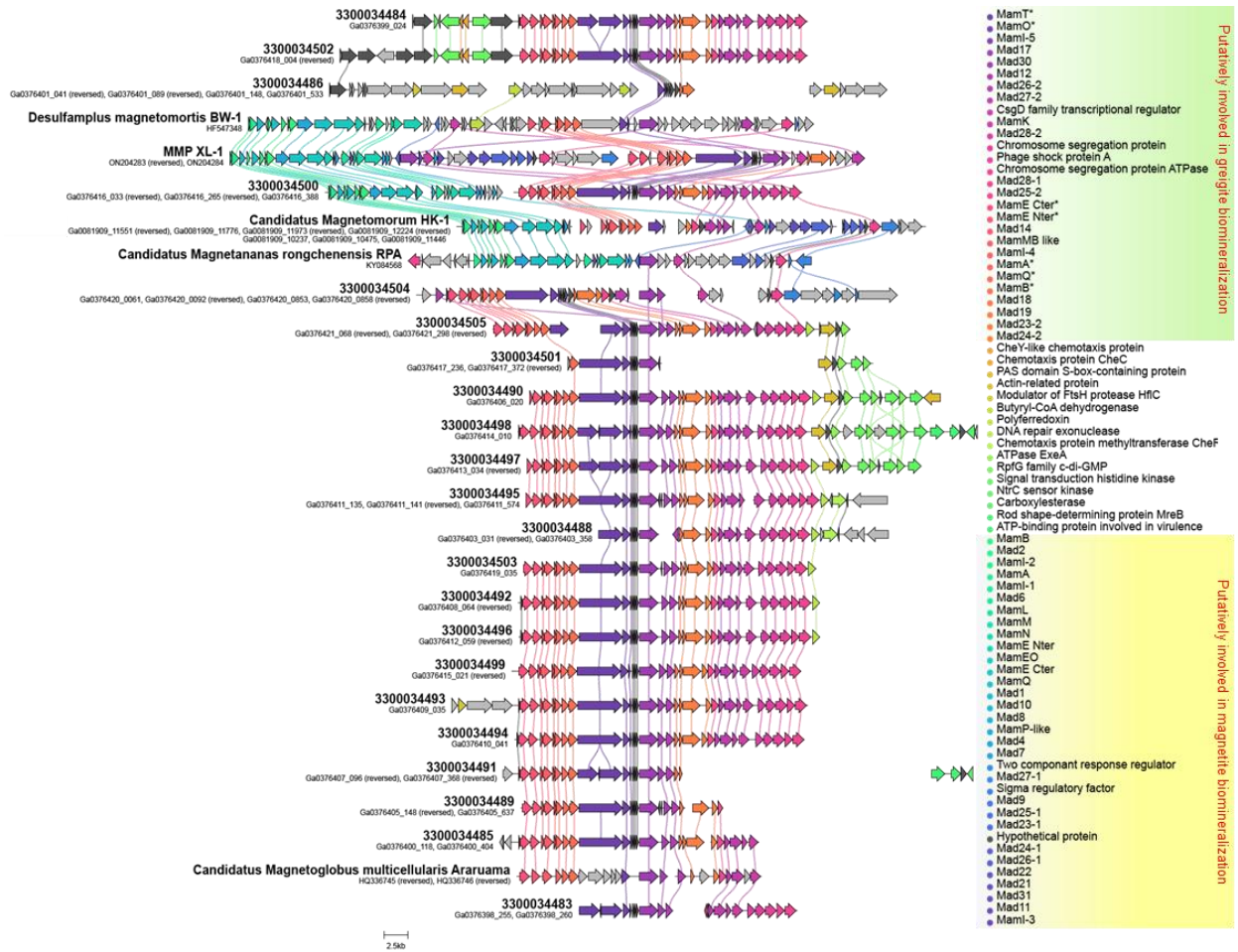


Fig. S18. Gene synteny for scaffolds containing the magnetosome gene clusters compared. The corresponding annotations of colored genes are shown in the legend to the right.

APPENDIX D

CHAPTER FIVE SUPPORTING MATERIAL

### Failure to establish an enrichment culture

Previous studies have attempted to cultivate magnetically enriched MMB in defined media but so far there has been no success despite the ability to magnetically enrich them to >99% purity (Abreu et al., 2014; Wenter et al., 2009). In an attempt to bring MMB into cultivation, we designed a medium (Appendix D Table S1) informed by the geochemical composition of the water at LSSM (Appendix D Table S2), the metabolic predictions derived from genomic data (Chapter 4 Fig. 4; Appendix C Table S7), and the results of SIP-NanoSIMS experiments (Chapter 4 Fig. 5; Appendix C Table S10). Incubations were performed under anoxic conditions at 27 °C and a pH of 7.4. MMB were found to maintain their magnetotaxis and could be recovered from the media for up to 15 days, after which no MMB could be magnetically enriched nor identified using FISH.

Reagent	Final Concentration
NaCl	376.45 mM
Na <sub>2</sub> SO <sub>4</sub>	7.96 mM
MgCl <sub>2</sub> •6H <sub>2</sub> O	45.00 mM
CaCl <sub>2</sub> •2H <sub>2</sub> O	8.75 mM
PO <sub>4</sub> buffer (K <sub>2</sub> HPO <sub>4</sub> /KH <sub>2</sub> PO <sub>4</sub> )	1.40 mM
NaHCO <sub>3</sub>	2.00 mM
KCl	4.02 mM
NH <sub>4</sub> Cl	5.00 mM
Na-Acetate	5.00 mM
Na-Propionate	2.50 mM
Na-Succinate	2.00 mM
Cysteine	1.00 mM
Methionine	1.00 mM
Glycine betaine	2.00 mM
Peptone	0.01 mg/mL
Ferric Citrate	0.10 mM
Fe-quinatate	0.10 mM
DSMZ 318 trace metal	1x
Wolfe's vitamins (DSMZ 141)	1x
KOH (pH adjustment to ~7.2)	1.50 mM
Resazurin	1.00 mg/L

Table S1. Media recipe for cultivation attempts of MMB

Ion	8/1/2021		9/1/2021 Sample 1		9/1/2021 Sample 2		Average	Chemical Reagent
	mg/L	mM	mg/L	mM	mg/L	mM	mM	
Cl	19029.0	536.7	17555.2	495.2	17401.6	490.8	507.6	NaCl/CaCl2/MgCl2
SO4	815.0	8.5	761.4	7.9	762.4	7.9	8.1	MgSO4
<b>Element</b>								
K	271.2	6.9	235.1	6.0	259.3	6.6	6.5	KBr/KH2PO4
Mg	1216.0	50.0	1028.0	42.3	1063.0	43.7	45.4	MgSO4
Na	6284.0	273.3	5296.0	230.4	5415.0	235.5	246.4	NaCl/NaHCO3
Ca	401.8	10.0	304.7	7.6	345.0	8.6	8.7	CaCl2
Al	bd	-	bd	-	bd	-	-	-
Sr	10.0	0.1	7.0	0.1	6.7	0.1	0.1	SrCl2
S	806.0	25.1	666.0	20.8	678.0	21.1	22.4	MgSO4
P	bd	-	bd	-	bd	-	-	-
<b>Measurment</b>								
pH	na	7.0	na	7.0	na	7.0		
NH4 (mg/L)	4.5E-02	2.5E-03	0.0E+00	0.0E+00	0.0E+00	0.0E+00	8.3E-04	
DIC (mg C/L)	17.9	1.5	23.0	1.9	23.1	1.9	1.8	NaHCO3
DOC (mg C/L)	7.0	0.6	2.8	0.2	2.1	0.2	0.3	
TC (mg C/L)	28.1	2.3	28.9	2.4	26.6	2.2	2.3	

Table S2. Water chemistry of LSSM sample site at two time points. Water collected above sediment during low tide. bd = below detection.